Title
Computational Fluid Dynamics Modeling of Secondary Settling Tank

Author
GAO, HAIWEN

Publication Date
2019

Peer reviewed|Thesis/dissertation

UNIVERSITY OF CALIFORNIA

Los Angeles

Computational Fluid Dynamics Modeling of Secondary Settling Tank

A dissertation submitted in partial satisfaction of the

requirements for the degree Doctor of Philosophy

in Civil Engineering

by

Haiwen Gao

2019

ABSTRACT OF THE DISSERTATION

Computational Fluid Dynamics Modeling of Secondary Settling Tank

by

Haiwen Gao

Doctor of Philosophy in Civil Engineering

University of California, Los Angeles, 2019

Professor Michael K. Stenstrom, Chair

Secondary settling tanks (SSTs) are a very crucial process that determines the performance of the activated sludge process (ASP). Due to the importance of its performance, computational fluid dynamics (CFD) models have been employed for the designing new SSTs, the modifying the geometries of existing SSTs and improving control techniques in wastewater treatment plants. However, the practical application of SST CFD models remains challenges due to several difficulties, such as the uncertainty of model structures and the accuracy of different sub-models. To facilitate the practical application of CFD SST models, this dissertation focuses on the numerical analysis of SST models, including the evaluation of different turbulence sub-models and investigation the impact of different parameters in modeling structures and the application of CFD models on the design and operation of SSTs, including improving the understanding the effects of different operation parameters, and surface wind conditions on the performance of SSTs.

To improve the understanding of CFD modeling of SSTs, this dissertation provides a comprehensive literature review of different multiphase approaches and the widely applied single-phase approach to model the motion of the particle in SSTs. The literature review also provides a thorough introduction of current CFD research and engineering practice, focusing on the formation and the effect of density currents, effects of different design variables, parameter uncertainties in modeling structures and atmospheric conditions.

Also, the widely applied standard k-ε (SKE) turbulence sub-model is investigated with two more advanced turbulence models (RNG k-ε and Realizable k-ε models). The results show that turbulence sub-model selection has a strong influence on the prediction of hydrodynamics of an SST, especially inside the inlet zone, and on the prediction of flow capacity. Moreover, due to the inconsistency of coupling or decoupling the buoyancy-term in the turbulence model structure among different studies as well as the discrepancies observed in other modeling structures, including in the sludge transport model, sludge settling model, dry solids density and different inlet turbulence boundary conditions, their impact on the prediction accuracy of an SST are all investigated.

This dissertation also investigates CFD applications on the design and operation of SSTs, including improving the understanding of the effects of different operation parameters, and surface wind conditions on the performance of SSTs. The effects of different operation parameters, such as surface overflow rate (SOR), sludge loading rate (SLR), the concentration of mixed liquid suspended solids (MLSS), and returned activated sludge (RAS) concentration, are firstly evaluated

with professor McCorquodale's Quasi-3D SST model. Next, the operational strategy to these operating parameters is investigated with Ansys Fluent-based model in order to maximize the SST capacity. The maximum capacity predicted by the Fluent-based CFD model is then compared with the prediction of one-dimensional idealized flux theory (1DFT) model. Also, the performance of the McKinney baffle on the SST performance is evaluated and shows significant improvement on the SST performance. Finally, instead of focusing on the influential factors inside SSTs, the effects of wind on the performance of both circular and rectangular SSTs are studied. Due to the strong negative impact of wind on the SST performance, the prediction results suggest that in strong windy climates covering SSTs or protecting them from strong winds may be justified.

The dissertation of Haiwen Gao is approved by:

Panagiotis D Christofides

Timu Gallien

William W Yeh

Michael K. Stenstrom, Committee Chair

University of California, Los Angeles

2019

Dedication to my parents Junjie Zhou and Guolong Gao

Table of Contents

List of Figures

List of Tables

Acknowledgements

This dissertation would have not been possible without the support of my professors, friends and family.

I would like to express my deep gratitude to my advisor Dr. Michael K. Stenstrom. Without his patience and encouragement, I would have not overcome many challenges I faced along the way. I appreciate him not only as my academic advisor, but also as my mentor in my life in the last five years. His guidance and attitude dealing with challenge inspires me and will always be assets in my life.

To all the members of my academic committee, personal learning network and communities of practice, who connect, inspire, collaborate, interact, challenge, and share with me personally, academically and professionally, I am thankful for your passion.

Finally, I would like to thank my family for their unconditional love and support. I am thankful for my beloved wife, Geer Chen, being there with me during difficult time. I am luck to meet my Mrs. Right at the right place and right time.

VITA

Education

2010.09 – 2014.06 B.E. in Water Supply and Sewage Engineering, Xihua University, China

2014.09 – 2016.06 M.S. in Civil Engineering, University of California, Los Angeles

Employment

2015.09 – 2019.06 Teaching Fellow in the Department of Civil and Environmental Engineering at UCLA

2018.06 – 2018.09 CFD Modeling Specialist intern at Carollo Engineers, Inc.

Publications

1. **Gao, H** and Stenstrom. M. K. (2017). Computational Fluid Dynamics Applied to Secondary Clarifier Analysis. In Proceeding of the 17th Annual World Environmental and Water Resources Congress, Sacramento, CA, USA, pp. 301-315. https://doi.org/10.1061/9780784480632.
2. **Gao, H** and Stenstrom. M. K. (2018a). Evaluation of three turbulence models in predicting of the hydrodynamics of a secondary sedimentation tank. *Water Res*. 143, 445-456. https://doi.org/10.1016/j.watres.2018.06.067.
3. **Gao, H** and Stenstrom. M. K. (2018b). Evaluation of turbulence and inter-phase mass diffusion assumptions on the performance of a secondary settling tank. *Water Environ Res*. 91, 101-110. DOI: 10.1002/wer.1003.
4. **Gao, H** and Stenstrom. M. K. (2019a). Generalizing the effects of the baffling structures on the buoyancy-induced turbulence in secondary settling tanks with eleven different geometries using CFD models. *Chem. Eng. Res. Des*. 143, 215-225. https://doi.org/10.1016/j.cherd.2019.01.015
5. **Gao, H** and Stenstrom. M. K. (2019b). Evaluating the effects of inlet geometry on the flux capacity of secondary settling tanks with computational fluid dynamics model and one-dimensional flux theory model. *J. Environ. Eng- Special Collection on CFD*. 2019, 145(10), 04019065-1-9. DOI: 10.1061/(ASCE)EE.1943-7870.0001582.
6. **Gao, H** and Stenstrom. M. K. (2019c). The influence of wind in secondary settling tanks for wastewater treatment- A computational fluid dynamics study. Part I: circular secondary settling tanks (Under Review-2nd round)
7. **Gao, H** and Stenstrom. M. K. (2019d). The influence of wind in secondary settling tanks for wastewater treatment- A computational fluid dynamics study. Part II: rectangular secondary settling tanks (Under Review-2nd round)
8. **Gao, H** and Stenstrom. M. K. (2019e). Uncertainty analysis of the model parameters and inlet turbulence boundary specification methods of secondary settling tank. (Under Review-2nd round).
9. **Gao, H** and Stenstrom. M. K. (2019f). Development and applications in CFD modeling for secondary settling tanks: A review (Under Review)

Chapter 1 Introduction

1.1. Background

In conventional wastewater treatment plants (WWTPs), the activated sludge process (ASP) is widely used to remove organic matter and remove nutrients such as nitrogen and phosphorus. The aeration tank effluent is a concentrated slurry and must be separated from the liquid. Gravity sedimentation is the most commonly used treatment methods for solids separation in WWTPs and the process used to remove the highly concentrated suspended solids from the bioreactor effluent is a secondary settling tank (SST), also known as a sedimentation tank or a secondary clarifier (Ramin et al., 2014).

There are three crucial parameters describing the performance of an SST: (1) effluent suspended solids (ESS) concentration, (2) returned activated sludge (RAS) concentration, and (3) sludge blanket height (SBH) (Krebs, 1995). As noted by Kleine and Reddy (2005) there are two different functions of SSTs: clarification and thickening. Clarification is used to separate the suspended solids (SS) from the effluent. Thickening is used to concentrate the sludge for recycle or disposal in a small volume. These two functions are influenced by six interrelated processes in SSTs described by McCorquodale et al. (2004): (1) hydrodynamics, (2) sludge settling, (3) sludge rheology, (4) turbulence, (5) flocculation, and (6) heat exchange and temperature changes. In summary, failure in clarification or thickening processes usually results from a poor understanding of these interrelated processes.

Previously, SSTs were designed based on empirical hydraulic criteria, such as surface

overflow rate (SOR) (Parker, 1983; Parker and Stenquist, 1986; Parker et al., 1996). However, this design procedure assumes that the flow in the SST is ideal and ignores other influential factors in SSTs such as (1) internal geometries; (2) sludge properties; (3) atmospheric conditions, including wind and temperature effects (Stamou et al., 2009). With the increase of computational power and the development of the computational fluid dynamics (CFD) models, which were initially associated with aerospace and mechanical engineering, much interest now exists in the environmental engineering field to understand non-ideal flow in SSTs and other processes. Compared with traditional design approaches, techniques based on CFD are high-precision, allowing evaluation and prediction of SST performance (Karpinska and Bridgeman, 2016).

In the last two decades, CFD has been applied to simulate multiphase flow in wastewater treatment facilities, such as primary settling tanks (Liu and Garcia, 2011), aeration tanks (Karpinska and Bridgeman, 2016), SSTs (Zhou et al., 1992a, b, c; Vitasovic et al.,1997; Weiss et al., 2007; Wicklein and Samstag, 2009; Ramalingam et al., 2012; Patziger et al., 2012; Xanthos et al., 2013; Das et al., 2016; Gao and Stenstrom, 2017), sludge digestions (Craig et al., 2013), disinfection (Zhang et al., 2014a). Among these applications, SSTs have been most widely studied. Therefore, CFD-aided modeling is becoming a robust tool for the optimization of existing SSTs and design of new SSTs.

Developments and applications of SST CFD models over the past 30 years can be divided into three main periods:

(1) The 1980s to the early 1990s: developing the numerical model under neutral density

condition (Imam et al., 1983; Imam and McCorquodale, 1983; Abdel-Gawad and McCorquodale, 1984; Abdel-Gawad and McCorquodale, 1985a; Adam and Rodi, 1990).

(2) The late 1980s to early 1990s: developing the numerical model for the density-driven flow (DeVantier and Larock, 1986; 1987; McCorquodale et al, 1991; Zhou and McCorquodale, 1992a, b, c; Zhou and McCorquodale, 1993).

(3) The mid-1990s to present: studying different influential factors, optimizing the internal baffling structures of existing SSTs and designing new SSTs (Krebs, 1995; Vitasovic et al.,1997; De Clercq, 2003; McCorquodale et al., 2004; Patziger et al., 2012).

Before the early 2000s, SST CFD models were limited to the two-dimensional (2D) scale because of the limited computational speed of computers. McCorquodale et al. (2004) extended the 2D model to a Quasi-3D (Q3D) model and verified the model results with the data from three different treatment plants. Compared with other early models developed before the 2000s, Q3D is more robust, which couples the flocculation sub-model, the effect of temperature and allows modifications of internal baffling structures of SSTs. Since then, more and more researchers are developing 3D SST models and studying the optimization of the SSTs' performance based on the commercial CFD models (Fan et al., 2007; Wang et al., 2008; Ramalingam et al., 2009; Xanthos et al., 2011; Gong et al., 2011; Ramalingam et al., 2012; Xanthos et al., 2013). In the last two decades, commercial CFD solution-codes, such as ANSYS FLUENT, have been widely used for SST modeling due to their advantages of easy-learning, friendly interface, and stability (Zhang et al., 2014a). Free software, user-coded programs, and open-source codes have been employed in

previous studies. A summary of CFD codes used in previous SST CFD studies is presented in Table 1.1.

In spite of the significant and rapid advances in the development and applications of SST CFD models over the last 30 years, great challenges to create accurate and fast CFD simulations of SSTs still exist.

1.2. Objectives

In order to improve the CFD model reliability as well as facilitate its practical application, the three main objectives of this dissertation are (1) to provide a comprehensive literature review, which includes the significant research topics related to the CFD SST modeling, such as modeling strategies of sludge settling, underflow hydrodynamics analysis, investigation the effects of primary design variables and atmospheric conditions, and evaluation the parameters in modeling structures; (2) to focus on the numerical analysis of CFD SST models with the aim of investigating the performance of different turbulence models and the effects of different parameters in CFD modeling structures; (3) to investigate the application of CFD models on the design and operation of SSTs, including improving the understanding the effects of different operation parameters, and surface wind conditions on the performance of SSTs.

1.3. Outline

Chapter 2 of this dissertation focus on the first objective, which is to provide a comprehensive literature review of the CFD modeling of SSTs. This chapter starts with a review of different modeling strategies of sludge settling process, including multi-phase and single-phase

models. The second part of this chapter is a review of different CFD models in current research and engineering practice, including the analysis of underflow hydrodynamics, effects of design variables, parameters in modeling structures and atmospheric conditions. The third part is a discussion of challenges in CFD SSTs simulation.

Chapters 3 to 5 of this dissertation mainly focus on the second objective, which is the numerical analysis of SST models, including different turbulence models and parameters in CFD modeling structures. The standard k-ε (SKE) turbulence model has been widely used to describe the turbulent flow in SSTs in the last 30 years. In Chapter 3, the performance of the SKE model is investigated with two more advanced turbulence models (RNG k-ε and Realizable k-ε models). Also, since there are some discrepancies in SKE model structures in different studies, these discrepancies are summarized in Chapter 4 and their effects on the performance of SSTs are analyzed in Chapters 4 and 5. Additionally, the discrepancies in other modeling structures, including sludge transport model, sludge settling model, dry solids density and different inlet turbulence boundary conditions are investigated in Chapters 4 and 6.

Chapters 7 to 9 mainly focus on the third objective, which is the investigation of CFD applications on the design and operation of SSTs. The effects of different operation parameters, including surface overflow rate (SOR), sludge loading rate (SLR), concentration of mixed liquid suspended solids (MLSS), and returned activated sludge (RAS) concentration, are studied in Chapter 7 with professor McCorquodale's Quasi-3D SST model. Furthermore, the strategy to operate these operation parameters in order to maximum the SST capacity is investigated in

Chapter 8 with Ansys Fluent-based model. Then, the maximum capacity predicted by the Fluent-based CFD model is compared with the prediction of one-dimensional idealized flux theory (1DFT) model. Also, the performance of the McKinney baffle on the SST performance is evaluated in Chapter 8. In Chapter 9, instead of focusing on the influential factors inside SSTs, the effects of surface wind on the performance of both circular and rectangular SSTs are studied.

Table 1-1. Summary of CFD codes used in previous studies of secondary settling tanks

Category	CFD Codes	References
Commercial software	ANSYS Fluent	Laine et al. (1999), De Clercq (2003), Jayanti and Narayanan (2004), Shaw et al. (2005), Weiss et al. (2007), Fan et al. (2007), Ramalingam et al. (2009), Xanthos et al. (2011), Gong et al. (2011), Patziger et al. (2012), Ramalingam et al. (2012), Tarpagkou et al. (2013), Xanthos et al. (2013), Wicklein and Samstag (2014), Das et al. (2016), Patziger (2016), Gao and Stenstrom (2018a, b, 2019a, b)
	ANSYS CFX	Matko (1997), Mohanarangam and Stephens (2009), Stamou et al. (2009), Burt (2010)
	PHOENICS	Krebs (1991), Dahl et al. (1994), Krebs et al. (1992, 1995), Brouckaert and Buckley (1999)
	STAR-CD	Wang et al. (2008), Wang et al. (2011)
	SettlerSIMs	Narayanan et al (2002), Samstag et al. (2010), Zhou et al. (2010)
	HACM	Gerges and McCorquodale (2008)
Free software	Quasi-3D	McCorquodale et al. (2004), Winkler et al. (2015), Gao and Stenstrom (2017)
	SettlerCAD	Vitasovic et al. (1997), Ekama and Marais (2004), Wahlberg et al. (1998)
	FAST-2D	Lakehal et al. (1999), Armbruster et al. (2001), Saffarian et al. (2010, 2011)
Open-source code	OpenFOAM	Ramin et al. (2014)
User-coded program	----------	Godo and McCorquodale (1991), Zhou and McCorquodale (1992a, b, c), Zhou et al. (1992), Kleine and Reddy (2005)

Chapter 2 Literature review

Secondary settling tanks (SSTs) are a very crucial process that determines the performance of the activated sludge process (ASP). However, their performance is often far from satisfactory. In the last 30 years, computational fluid dynamics (CFD) has become a robust and cost-efficient tool for the designing new SSTs, the modifying the geometries of existing SSTs and developing new and improved control techniques in wastewater treatment plants. The first part of this review paper discusses the different approaches to model the motion of the particle in SSTs. The applications of different multiphase approaches and the widely applied single-phase approach in different SST studies are reviewed. The second part of this paper reviews current CFD research and engineering practice, focusing on the formation and the effect of density currents, effects of different design variables (loading, geometry, and sludge settling characteristics), parameter uncertainties in modeling structures and atmospheric conditions. Finally, challenges and future improvements of sub-models (sludge settling, rheology, turbulence, and flocculation) in the SST model framework are identified.

2.1. Modeling strategies of sludge settling process

The sludge settling process is a multi-phase problem in SSTs. The accurate numerical simulation of the sludge settling process relies on the accurate assessment of the sludge transport phenomena and the character of interaction between the phases.

Table 2-1. Summary of multiphase approaches used in settling tanks modeling

Model	Concept	Modeling	Applications	Comments in settling tanks modeling
Euler-Lagrange	Liquid phase treated with Eulerian approach. Every particle tracked along trajectory.	A set of averaged NS equations for the liquid phase. A set of Newton's 2nd law (N2L) equations applied to all particles. Momentum transfer terms in both NS and N2L to be modeled.	Jayanti and Narayanan (2004); Goula et al. (2008a, b); Tarpagkou and Pantokratoras (2013)	It does not consider the interparticle interaction and is computational expensive to track a large number of particles (De Clercq, 2003).
Eulerian	Each phase modeled as a separate fluid.	A set of averaged, volume fractionated weighted NS equations for each phase. Momentum transfer terms and constitutive equations to be modeled.	Fan et al. (2007); Liu and Garcia (2011)	None of the calculated particle concentration field was compared with the observed particle concentration distribution.
Mixture	Both phases treated as a single phase.	Single set of NS equations. Effective mixture density and viscosity to be modeled.	Wicklein and Samstag (2009); Sammarraee-Al and Chan (2009); Liu et al (2016)	Unrealistic for most wastewater modeling applications where a wide range of particle diameters are existence and change as they flow through a tank (Wicklein and Samstag, 2009).
VOF	Each phase modeled as a separate fluid. The interface between the phases is tracked.	Interface tracked via a continuity equation and the domains of the single phases are defined. A set of phase-specific NS equations with momentum exchange terms are solved for each domain.	Rostami et al. (2011)	Due to the strong effect of surface wind shown in Gao and Stenstrom (2019c, d), VOF model can be used to simulate the water surface fluctuation and simulate the effect of surface baffling structures.

Table 2.1 summarizes the descriptions of different multi-phase approaches used in modeling of WWTP processes shown in Karpinska and Bridgeman (2016) and their applications in settling tanks.

2.1.1. Multiphase modeling

2.1.1.1 Euler-Lagrange model

In the Euler-Lagrange (EL) model, the governing phase (fluid) is treated as a continuum by solving the Navier-Stokes (NS) equations, while the behavior of the dispersed phase (e.g. solids) is solved by tracking a large number of particles through the calculated flow field. The trajectories of particles are predicted by integrating the force balance on the single particle. This force balance equates the particle inertia with the forces acting on the particle and is defined as (Bridgeman et al., 2009):

$$\frac{\partial p}{\partial t} = \frac{v - v_p}{t_r} + \frac{g(\rho_p - \rho)}{\rho_p} + F \qquad (2.1)$$

where F is an additional acceleration term, v_p is particle velocity and v is fluid phase velocity, $\frac{v - v_p}{t_r}$ represents drag force per unit particle mass, t_r is particle relaxation time.

The Euler-Lagrange model is often used to evaluate the behavior of individual particles or particles with specific characteristics (Karpinsha Portela, 2013). The model allows for one-way coupling where the discrete phase follows the continuous phase flow field or two-way coupling, where the effect of the discrete phase on the continuous phase is included. One-way coupling EL model has been used to model the solids transport in full-scale settling tanks in water treatment plants (WTPs).

Jayanti and Narayanan (2004) applied the one-way EL model to study the effect of flow field on solids distribution in a pilot scale settling tank. The turbulent flow was modeled by the Reynolds-averaged Navier-Stokes (RANS) equations with the standard k-ε (SKE) turbulence closure. The experimental studies conducted by McCorquodale (1976) and Szalai et al. (1994) in a centrally fed settling tank were used to validate the prediction of the flow field for neutrally buoyant flow. The study showed that particles smaller than a lower cut-off size (100 μm in this case) would be difficult to settle while whose large than the upper cut-off size (300 μm in this case) would settle easily.

Goula et al. (2008a) applied a CFD model coupled with the one-way EL model to study the influence of the inlet baffle for a full-scale circular settling tank in an WTP. The turbulent flow was accounted by the shear stressed transport (SST) k-ω turbulence model. The grid independent test was performed to eliminate numerical diffusion and to determine the best compromise between simulation accuracy and computational time. The experimental measurements and the simulated values of the floc size distribution in the tank effluent was compared to validate the CFD model. Their study showed that the addition of a vertical baffle at the feed section of the settling tank reduced the effluent solid concentration by 85%. The validated CFD model was further used to assess the effect of a warmer influent on the performance of the settling tank (Goula et al., 2008b). The study showed that a temperature difference of only 1 ºC is sufficient to induce a temperature-driven density current and reduce the detention time as well as the solids removal efficiency.

Tarpagkou and Pantokratoras (2013) used CFD models coupled with the EL model to

simulate the 3D hydrodynamics and flow behavior in a settling tank. Unlike most of the previous numerical investigations, the EL model with two-way coupled calculations was applied to identify the influence between the discrete and the continuous phases over a change of particle diameters and volume fractions. The RNG k-ε model was used to describe turbulence flow. The study provided detailed procedures on the application of two-way coupled EL model which are valuable to researchers to learn how to use the EL model. The depth-average velocity magnitude along the radial direction of the tank was compared among three different mesh densities to demonstrate grid independent. Next, the prediction of the depth-average velocity magnitude along the radial direction of the tank on the optimal mesh density was compared with experimental measurements.

The study showed that the effect of particles on the fluid phase is higher as the particle size and volume fraction increases.

However, a number of factors such as the effects of density currents, sludge flocculation and hindered settling were neglected in those studies, the results were appropriate in water treatment settling tanks but not in SSTs in WWTPs. Currently, the EL model has not been used in a full-scale SST study. The application of the EL model in full-scale SSTs needs extensive interparticle interactions which requires large computational resources (De Clercq, 2003). Karpinska and Bridgeman (2016) stated that the EL model is the most computational expensive multiphase model which limits its popularity in the simulation of WWTPs. Additionally, Burt (2010) stated that the EL model cannot reliably predict solids retention in SSTs which precludes it use in SSTs where the sludge bed deposition and accumulation is a vital element of the

hydrodynamics.

2.1.1.2 Euler-Lagrange model

The Eulerian-Eulerian (EE) multiphase model is a multi-fluid model, where both the governing fluid phase and dispersed particle phase are solved using NS equations. The equations for the two phases are coupled by the phase volume fraction (α_q) and the inter-phase exchanges terms are defined as sources or sinks to represent the exchange of mass, momentum and heat between the two phases (Jayanti and Narayanan, 2004). The sum of volume fraction equals to unity.

$$\sum_{q=1}^{n} \alpha_q = 1 \tag{2.2}$$

The mass conservation equation for phase q is (Ratkovich, 2010):

$$\frac{\partial}{\partial t}\left(\alpha_q \rho_q\right) + \nabla\left(\alpha_q \rho_q v_q\right) - \sum_{p=1}^{n}\left(m_{pq} - m_{qp}\right) = 0 \tag{2.3}$$

where ρ_q is density and the term $\alpha_q \rho_q$ is the effective density of the phase q, v_q denotes its velocity, m_{pq} and m_{qp} are mass transfer mechanisms from phase p to q and from q to p, respectively.

The generalized momentum conservation equation for phase q can be written in the simplified form as (Ratkovich, 2010):

$$\frac{\partial}{\partial t}\left(\alpha_q \rho_q v_q\right) + \nabla\left(\alpha_q \rho_q v_q v_q\right) = -\alpha_q \Delta p + \nabla \mu_q\left(\nabla \alpha_q v_q + \nabla \alpha_q v_q^T\right) + \rho_g + F_q \tag{2.4}$$

where p is pressure, μ_q denotes shear viscosity of phase q, F_q represents the sum of interfacial forces between the continuous and dispersed particle phases.

In WWTPs, the EE model is often used to model the gas-liquid or solid-liquid flow in

aeration system (Karpinska and Bridgeman, 2016). Currently, there are only a few applications of the EE model in settling tanks. Fan (2007) applied a three-dimensional (3D) CFD model coupled with the EE multiphase model to investigate the hydrodynamics of a circular SST and the impact of the internal baffle. SKE model was used to describe turbulent effects.

However, sludge withdrawal and sludge settling behavior were excluded in this study which make the CFD prediction results less accurate to describe the SST's actual behavior. Also, the flow and concentration fields were not compared with experimental data. Therefore, the reliability of predictions results by the EE multiphase model in this study are unknown

Liu and Garcia (2011) applied a 3D CFD model coupled with the EE model to evaluate the hydrodynamics and identify the optimal internal structures for a primary settling tank. The SKE model with Bingham plastic model is used to simulate the turbulence and the sludge rheological behavior. Hindered settling was described via the double exponential settling equation (Takács et al., 1991). While the prediction of velocity field showed good agreements with the experimental data, the concentration field data was not calibrated with the experimental data. Therefore, the performance of the EE model on the prediction of the sludge concentration is unclear. Therefore, the further application of the EE model in settling tanks in WWTPs needs to calibrate the prediction of sludge concentration profiles with field data in order to demonstrate the model reliability. Additionally, in modeling the particle settling process, due to heavy computational effort, only a limited number of particle size classes can be considered, which is another limitation to the application of EE model for a full-scale SST.

2.1.1.3 Slip mixture or algebraic slip model

The slip mixture or algebraic slip model is a simplified multiphase model. The interracial relationships in the multiphase model are eliminated by using only one momentum equation for the complex mixture (De Clercq, 2003). The algebraic velocity equation is used to solve relative velocities to describe the dispersed phase. Therefore, the continuity equation for the mixture model is (Azzopardi et al., 2010):

$$\frac{\partial \rho_m}{\partial t} + \nabla(\rho_m v_m) = 0 \tag{2.5}$$

where ρ_m is the mixture density:

$$\rho_m = \sum_{q=1}^{n} \alpha_q \rho_q \tag{2.6}$$

and v_m is the mass-averaged mixture velocity:

$$v_m = \frac{1}{\rho_m} \sum_{q=1}^{n} \alpha_q \rho_q v_q \tag{2.7}$$

The momentum equation for the mixture model is (Azzopardi et al., 2010):

$$\frac{\partial}{\partial t}(\rho_m v_m) + \nabla(\rho_m v_m v_m) = -\Delta p + \nabla[\mu_m(\nabla v_m + \nabla v_m^T)] + \rho_m g + F + \nabla(\sum_{q=1}^{n} \alpha_q \rho_m v_{dr,q} v_{dr,q}) \tag{2.8}$$

where μ_m is the mixture viscosity:

$$\mu_m = \sum_{q=1}^{n} \alpha_q \mu_q \tag{2.9}$$

And $v_{dr,q}$ is drift velocity for the secondary phase q:

$$v_{dr,q} = v_q - v_m \tag{2.10}$$

The slip velocity of the secondary phase (p) relative to the velocity of the primary phase (q) is:

$$v_{pq} = v_p - v_q \tag{2.11}$$

The relation between drift and slip velocities can be written as:

$$v_{dr,q} = v_{pq} - \sum_{q=1}^{n} c_q v_q \tag{2.12}$$

c_q is the mass fraction of phase q:

$$c_q = \frac{\alpha_q \rho_q}{\rho_m} \tag{2.13}$$

The mixture model has been applied to simulate gas-liquid turbulent flow in bioreactors (Yang et al., 2011), solid-liquid turbulent flow for setting tanks in WTPs (Al-Sammarraee et al., 2009a, b) and for SSTs in WWTPs (Liu et al., 2011).

Al-Sammarraee et al. (2009a) compared the performance of the large eddy simulation (LES) model with the SKE model for a full-scale 3D longitudinal settling tank in a WTP. The mixture multiphase model was used to model the particle sedimentation process. Five different mesh grids were used to determine the best compromise between accuracy and computational cost. The prediction of effluent concentration of particle with different sizes showed good agreement with experimental measurements. The study showed that the SKE model in general has similar performance in predicting velocity, turbulence, particle settling efficiencies in the bulk part of the settling tank, while LES can more accurately resolve the small-scale flow patterns near the inlet, effluent weir and tank bottom. The authors further applied their model to investigate the influence of baffles on the particle sedimentation process (Al-Sammarraee et al., 2009b). Four different baffle numbers (zero, two, three, and four baffles) were compared. The study concluded that increase the number of baffles causes larger suppression of the horizontal velocities and improves

the particle settling.

Liu et al (2011) applied the mixture multiphase model with the SKE turbulence model to quantitatively investigate the effect of a baffle on the hydrodynamics and solids removal efficiency for an SST. However, since the prediction results were not validated with experimental data, the prediction accuracy of the model for the SST is unknown.

In order to understand the performance of mixture multiphase model in predicting a full-scale SST in the WWTP, Wicklein and Samstag (2009) compared its prediction of solids concentration profiles with field measurements in both rectangular and circular SSTs. The results showed that the prediction of the mixture model was poor in predicting the sludge concentration distribution. The authors explained that a wide range of particle diameters exist (Khelifa and Hill, 2006) and change as they flow through an SST that a single representative input particle size cannot be easily determined for the mixture model.

2.1.1.4 Volume of Fluid (VOF) model

The VOF model is designed to track the location and motion of a free surface between immiscible fluids. While the phases are immiscible, the fields for all variables and properties are shared and represented by volume-averaged values. Therefore, the continuity and momentum equations for the VOF model are expressed as (Ratkovich, 2010):

$$\frac{\partial \alpha_q}{\partial t} + \nabla\left(\alpha_q v_q\right) = 0 \tag{2.14}$$

$$\frac{\partial}{\partial t}(\rho v) + \nabla(\rho v v) = -\Delta p + \nabla[\mu(\nabla v + \nabla v^T)] + \rho g + F \tag{2.15}$$

For two-phase system, the density in each cell is:

$$\rho = \alpha_q \rho_q + (1 - \alpha_q)\rho_p \quad (2.16)$$

All other variables, such as μ are computed in the similar fashion.

Karpinska and Bridgeman (2016) noted that this model can be used to model stratified and free-surface flows, filling, sloshing and motion of large bubbles (slug flow). However, it is very rare to find the application of the VOF model in settling tanks modeling studies. Rostami et al. (2011) applied the VOF model to study the effect of the free surface in a primary settling tank (PST). They compared the velocity distribution predicted by the VOF method and confined surface with experimental results and showed that the VOF method predicted more accurate velocity field than the confined surface method. However, the flow was treated as pure water without particles; therefore, the effect of the particles on the velocity distribution was neglected. An application of the VOF model was recommended by Gao and Stenstrom (2019c, d) in their surface wind effect on the performance of both circular and rectangular SSTs. The VOF model has advantages to study how the surface baffling structures influence the surface wind.

2.1.2. Single-phase modeling

Although sludge settling is a multi-phase problem, a single-phase flow model has become the most widely applied approach in the academic (e.g. De Clercq, 2003; Lakehal et al., 1999; Patziger et al., 2012; Ramin et al., 2014; Saffarian et al., 2010; Vitasovic et al., 1997; Weiss et al., 2007) and non-academic SST projects (e.g. Morse et al., 2016; Shaw et al., 2005; Wicklein and Samstag, 2014) because of its economy and accuracy for the prediction of sludge distribution. Additionally, Wicklein and Samstag (2009) quantitatively compared the performance of this

single-phase modeling approach with the mixture multi-phase model in both full-scale circular and rectangular SSTs. Their results showed that this single-phase modeling approach outperforms multi-phase models in predicting the sludge concentration distribution in both rectangular and circular SSTs.

This approach assumes the solids follow the advective flow by coupling a separate solids transport equation (Nopens et al., 2012). Also, additional equations related with density state and the sludge settling velocity (usually the settling function of Vesilind (1968) or the Takács et al (1991)) need to be included to achieve this coupling. The sludge transport equation, density state equation, and Takács settling function are shown in the following formula (Patziger et al., 2012):

Sludge transport equation:

$$\frac{\partial C}{\partial t} + \frac{\partial \rho(\overrightarrow{u_i}+V_s)C}{\partial x_i} = \rho \frac{\partial}{\partial x_i}(\frac{v_t}{\sigma_c}\frac{\partial C}{\partial x_i}) \tag{2.17}$$

t is time, *C* is sludge concentration.

Density state equation:

$$\rho = \rho_r + C(1 - \frac{\rho_r}{\rho_p}) \tag{2.18}$$

where ρ is the local fluid-solid mixture density, ρ_p is dry particle density, ρ_r is reference density (clear water).

Takács settling function:

$$V_s = V_o(e^{-r_h(C-C_{min})} - e^{-r_p(C-C_{min})}) \tag{2.19}$$

where V_o is Stokes velocity, r_h and r_p account for rapidly and poorly settling floc, respectively. The constant C_{min} is the concentration of non-settleable solids in the effluent of the

SST.

The single-phase modeling approach, due to its accuracy and modest need for computing resources, has become the most popular approach for CFD SST modeling. In the next section we review the applications of CFD SST models and how they are improving SST design and operation.

2.2. Applications of CFD modeling research and engineering practice

In the last two decades, multiple applications of CFD models to existing SSTs have been made. These applications include: (1) studying the underflow hydromechanics, such as the occurrence and effects of density currents; (2) studying the primary design variables on the performance of SSTs (tank loadings, tank geometry and sludge management); and (3) studying the variation of ambient environmental factors (temperature and wind).

2.2.1 Underflow hydromechanics (turbulent flow and buoyancy effects)

Since the influent to the SST is a high concentration of mixed liquor suspended solids (MLSS), the flow in SSTs is driven by density. However, the causes of density currents were controversial (Taebi-harandy and Schroeder, 2000) and were studied in some early CFD research (Godo and McCorquodale, 1991; Lyn et al., 1992; Moursi et al., 1995; Vitasovic et al., 1997; Gerges and McCorquodale, 2000; McCorquodale et al., 2004). Moursi et al. (1995) suggested that the density currents (bottom or surface) may occur from the temperature difference, concentration effects, and the release of gas bubbles. Also, Gerges and McCorquodale (2000) concluded that there were two types of thermal density currents in SSTs: (1) heat exchange between water surface and the surroundings and (2) temperature variance between the influent and ambient water. Both

effects may occur at the same time. Godo and McCorquodale (1991) studied the effect of the temperature difference between influent and effluent on the formation of density currents in a lab-scale rectangular settling tank and concluded that a temperature difference, as small as 0.2°C, could result in the formation of density currents.

McCorquodale et al. (2004) conducted the most thorough numerical study on the formation of density currents (surface and bottom) and their effects of on the SST performance. The numerical studies were tested on different influent temperature variations, surface heat exchange and on two MLSS concentrations (300 and 2800 mg/L). The lower MLSS was used to simulate the loading condition in PSTs. McCorquodale's et al. (2004) findings on the formation of the density currents and their effects on PSTs and SSTs are summarized in Table 2.2.

Table 2-2. Formation of the density current and its effect on PSTs and SSTs (McCorquodale et al. 2004).

	Density current type		Performance	
	MLSS (300 mg/L)	MLSS (2800 mg/L)	MLSS (300 mg/L)	MLSS (2800 mg/L)
Cooler inflow	Bottom	Bottom	Decrease	Decrease
Warmer inflow	Surface	Bottom	Decrease	Increase
Surface cooling	Not shown	Bottom	Decrease	Increase
Surface heating	Not shown	Bottom	Decrease	Decrease

For the case of low suspended solids concentration, corresponding to a PST, warmer

influent temperatures tend to create surface density currents, which is consistent with the Taebi-harandy and Schroeder's (2000) observations in a lab-scale SST. McCorquodale et al. (2004) showed that surface density currents form in PSTs with warmer influent and bottom density currents form with cooler influent. This indicates that the temperature-induced buoyant effect is stronger than the gravitational effect caused by the low concentration of MLSS. Also, the performance of PSTs deteriorates with temperature variations. Therefore, the temperature is the dominate factor affecting the performance of PSTs and the type of density currents produced.

Table 2.2 also shows that only bottom density currents form in SSTs, which indicates that the gravitational effect caused by the high concentration of MLSS is stronger than the temperature-induced buoyancy effect. Therefore, MLSS concentration is the dominate factor in producing density currents (surface or bottom), with or without the consideration of temperature effects (Lyn et al., 1992; Zhou et al., 1992; Zhou and McCorquodale, 1992b, 1992c; Krebs, 1996; McCorquodale et al., 2004; Gao and Stenstrom, 2017).

Some researchers have suggested that density currents cause a negative effect on the SSTs' performance by reducing their volume usage efficiency (Lyn et al., 1992; Vitasovic et al., 1997). However, Table 2.2 indicates that the performance of SSTs under different influent temperatures and surface heat exchange is different. The cooler inflow and surface heating reduce the performance of SSTs by increasing the upflow velocities and vertical mixing close to the side wall. which increases the ESS. Warmer inflow and surface cooling tend to have the opposite effect by reducing upflow velocities and mixing. McCorquodale's et al. (2004) numerical results are

consistent with the Wells and LaLiberte's (1998) field observations of three different SSTs during the winter.

Samstag et al. (1992) although ignoring temperature change and heat exchange, indicated that stable density stratification in the settling and effluent zone contributed to significant damping of vertical mixing, concluding that concentration-induced density currents do not reduce ESS removal efficiency. An exception occurs where there is a sudden increase of the inlet MLSS concentration, which increases the upward currents near the side wall, changing the flow pattern. These observations and numerical results show that influent temperature variations, surface heat exchange, and MLSS concentrations are all major factors on the affecting the performance of SSTs.

2.2.2 Effects of primary design variables on the performance of SSTs

The Clarifier Research Technical Committee (CRTC) recommended a comprehensive protocol for analysis of the hydraulic efficiency of SSTs (Wahlberg et al., 1994). In the CRTC study, the following aspects of SSTs were considered (Vitasovic et al., 1997):

1. Tank loading, including hydraulic and solids loading and returned activated sludge (RAS) flow rate.
2. Tank geometry, including radius and depths, size of the flocculating well, bottom slope, sludge removal mechanisms, launder arrangements.
3. Sludge settling characteristics.

2.2.2.1. Effects of hydraulic and solids loading

The effects of hydraulic and solids loading rates on the performance of SSTs have been

studied and debated based on the observations by different researchers from different WWTPs in the last three decades. These observations have not been extensively analyzed in previous CFD studies and are discussed in this review. A particularly controversial finding is the relationship between surface overflow rate (SOR), SST depth and performance.

Parker (1983) indicated that the ESS concentration is usually assumed to directly relate to SOR. The results of his field measurements showed an obvious effect of high SOR on ESS. Therefore, he recommended a lower the SOR from 1.7 m/h to 1.4 m/h (1003 to 826 gallons/ft^2-day) to improve effluent quality. However, field measurements conducted by Wahlberg et al. (1993) did not find a significant influence of SOR on ESS. Similarly, Parker et al. (1996) studied the performance of flocculator-SSTs in several different WWTPs. The combined experience suggests that the performance of SSTs is stable over a very broad range in overflow rates.

Parker et al. (2001) compared the operating performances of SSTs in three different studies (Parker and Stenquistt, 1986; Stahl and Chen, 1996; Okuno and Fukuda, 1992) and showed that deep SSTs, no matter circular or rectangular, were more stable than shallow SSTs, over a wide range of SORs. For shallower units, the poor SOR performance may relate to the higher sludge blanket. This problem can be mitigated by building deeper SSTs or changing operating conditions to increase separation between the sludge blanket and the effluent weirs (Ekama et al., 1997). Therefore, Parker et al. (2001) concluded that the existence of a correlation between SOR and ESS indicates either a design problem or poor operation. Vestner and Günthert (2004) investigated four operating parameters: SOR, sludge volume loading rate, MLSS and flocculation time in two SSTs.

They concluded that at appropriate loading, the influence of SOR and sludge loading rate (SLR) on ESS is very small, and it is important to consider the effect of inlet MLSS concentration and flocculation time.

To explain the contradictory results of the effects of SOR on ESS observed at different WWTPs, we summarized the relationship between ESS and SOR from ten different SSTs in Figure 1. In order to simplify the figure, raw data points from the first eight studies are not shown and best fit lines are shown for the first eight studies. Three sets of data points from two SSTs and their best fits from our previous studies (Gao and Stenstrom, 2017, 2019b) are also shown in Figure 2.1. It shows that in observations of three previous researchers and predictions from three of our previous studies that ESS increases with the increase of SOR. For five other sets of observations show a relatively constant ESS over a large range of SORs. These five sets of observations are for deeper SSTs, ranging from 4.3m to 5.5m SSTs. The observations showing an increasing relationship between ESS and SOR are all for shallow SSTs ranging from 1.8m to 3.3m except for Gao and Stenstrom (2017), which is 4.1m deep. The dependence of ESS on SOR seems to be related to the depth, with deeper SSTs performing much better.

In order to compare the performance of an SST with different SWDs without other geometric differences, the modified Witney SST studied in Burt (2010) and Gao and Stenstrom (2019b) was simulated with different SWDs. Burt (2010) measured r_h in a series of batch settling tests. An SVI corresponding to the measured r_h was calculated as 110 using the Daigger (1995) correlation, which indicates a good settling sludge. The original SWD was 1.8m and was simulated

over a range 0.8m, 2.8m, 3.8m and 4.8m. Figure 2.2 shows the prediction of ESS, RAS and SBH as the variation of SWD.

It shows that the ESS increases from 12.5 to 33.1 mg/L as the SWD increases from 0.8 to 2.8m and then decreases from 33.1 to 10 mg/L as the SWD increases from 2.8 to 4.8m. The variation of the RAS concentration is negligible and the SBH from the water surface increases as the increase of SWD from 0.8 to 4.8m. Figure 2.3 shows the concentration and velocity profiles of the modified Witney SST as SWD is increased. It shows that when the SDW is only 0.8m, currents from the inlet zone flow directly to the sludge blanket without the formation of density currents. The sludge blanket dissipates the flow energy coming from the inlet zone. Therefore, the upward velocity to the effluent weir is weak and the ESS is very low. However, as the SDW increases from 0.8 to 2.8m, sludge blanket is below the McKinney baffle, and the density current flows across the top of the sludge blanket level scouring particles to the effluent weir along the side wall. As the SWD is further increased, density currents do not have enough energy to rise to the level of the effluent weirs, and the ESS decreases. Gao and Stenstrom (2017) simulations at 4.1m SWD showed a trend of increasing ESS with SOR, similar to the shallow SSTs. This case has poor sludge settling properties (SVI=280, calculated from Daigger's (1995) correlation) making the SBH higher, which impacted the density currents and allowed particles to be transported to the effluent. The simulation results are supported by Ekama et al. (1997) observations.

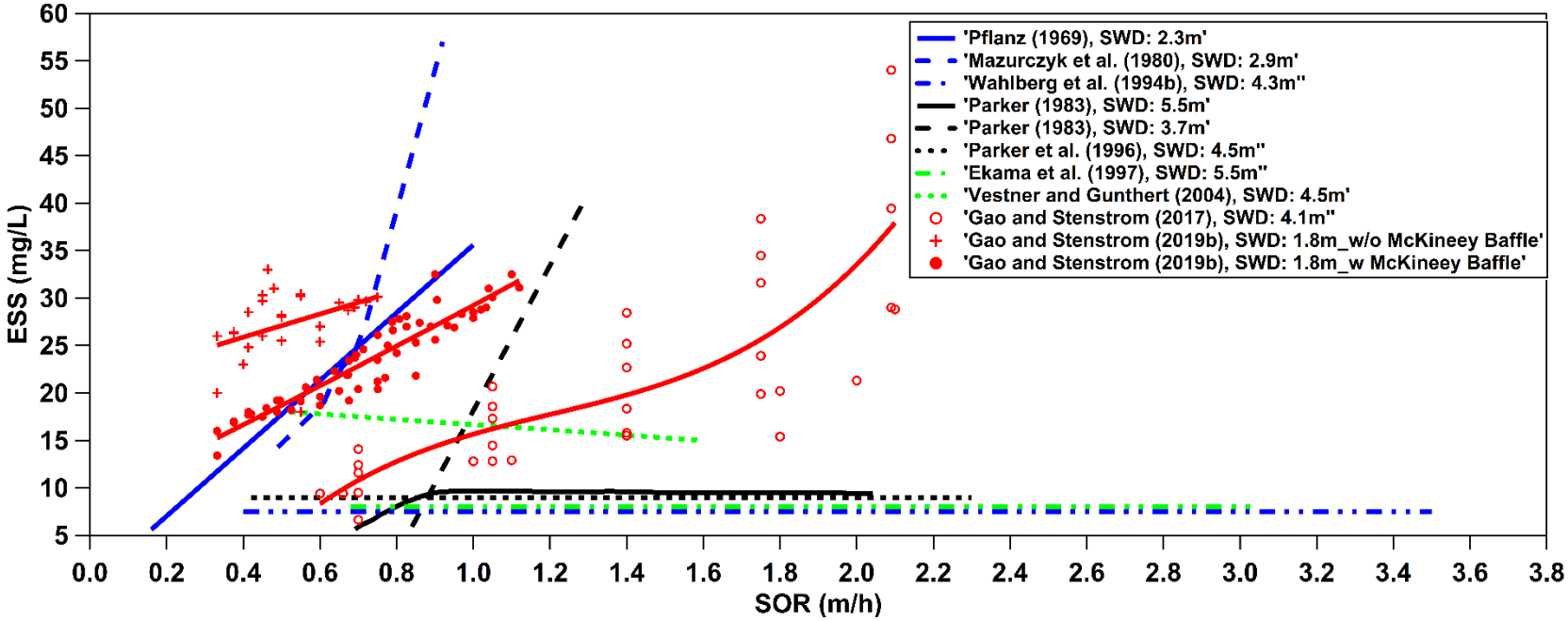

Figure 2-1. Relationship between SOR and ESS

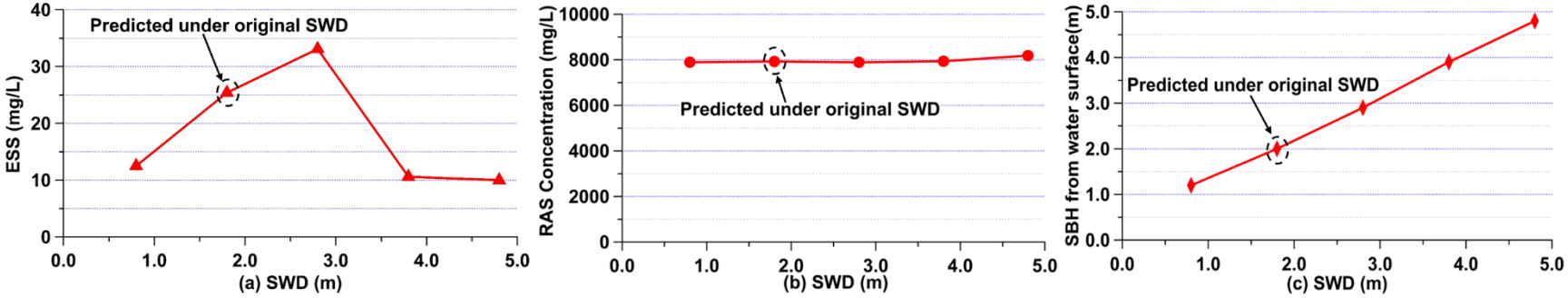

Figure 2-2. Variation of SWD (m) on the performance of modified Witney SST (SBH is 850 mg/L contour followed by Burt (2010). The depth of the Witney SST at the center is 6.15m. The original SWD of Witney SST is 1.8m)

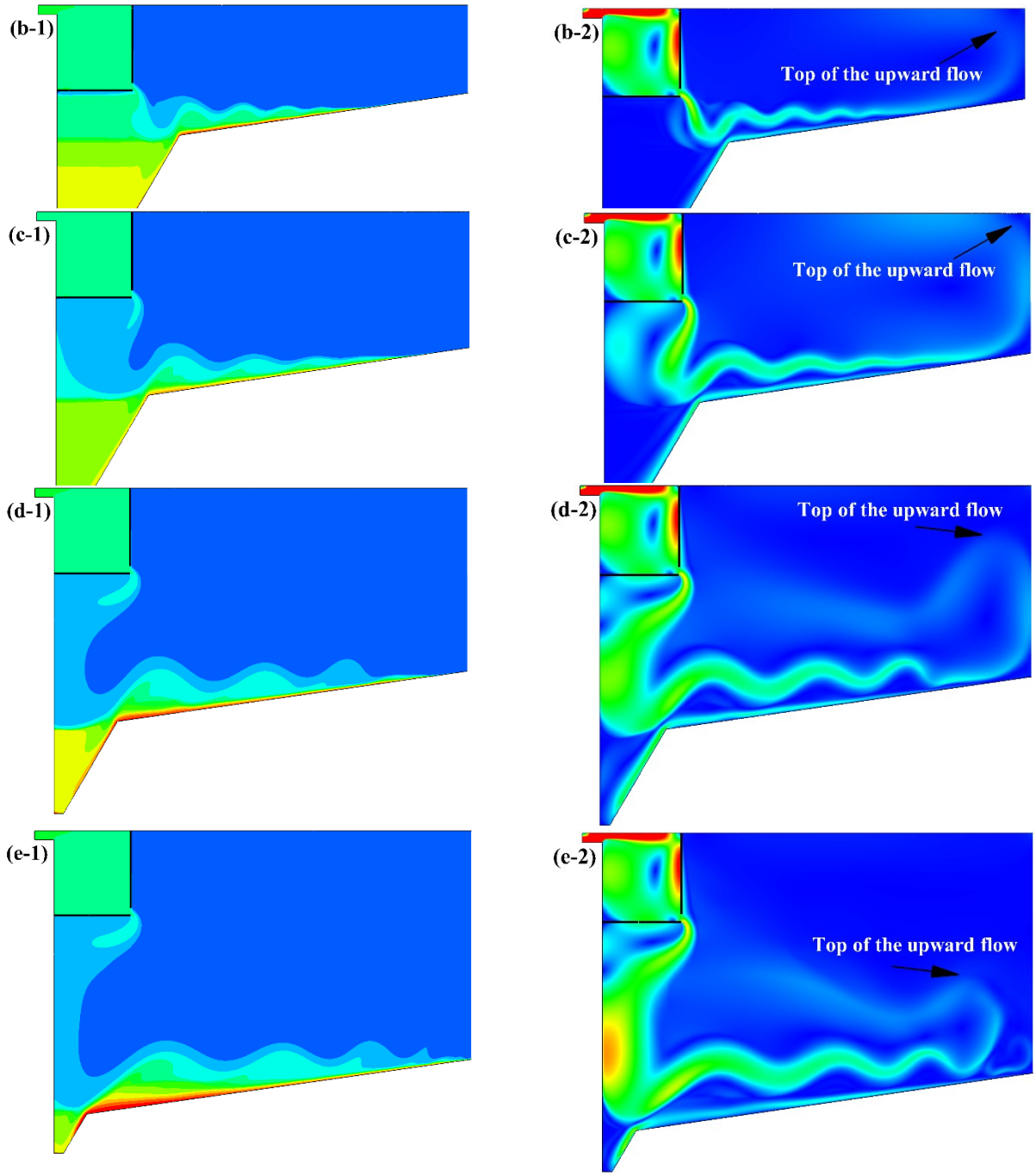

Figure 2-3. Concentration (left) and velocity (right) profiles for the modified Witney SST with different SWD (SWD=0.8, 1.8, 2.8, 3.8, 4.8m for profiles (a) to (e), respectively)

The overall conclusion of these simulations is that while the McKinney baffle improves SST performance and increases its flow capacity, if a density current is produced at the same height as the top of the sludge blanket, the current can scour particles into the effluent. For very shallow SSTs, density currents may impact the middle or lower part of sludge blanket, dissipating the velocity. For deep SSTs density currents never reach the height of the effluent weirs. These simulations showed that ESS is not a simple function of SOR and that different geometries can complicate the results.

The simulations support the conclusion that deeper SSTs are able to produce the highest quality effluent. First of all, it can separate the ESS from the highly concentrated sludge at the bottom with larger distance. Also, more energy of density currents can be dissipated when density currents turning to flow upward along deeper side wall to the effluent weir. Therefore, the effect of density currents can be reduced. The deeper SSTs also have greater capacity to store sludge which can be important when treating peak flows.

The controversy over traditional design parameters such as SOR and loading rate is of continuing interest among CFD researchers and has resulted in an increased used of CFD models by practical engineers. A number of CFD modeling case studies have been presented at the Water Environment Federation's Annual Technical Exhibition and Conference (WEFTEC) (Griborio et al. (2010); Winkler et al. (2015); Esping et al. (2015); Chu et al. (2015); Griborio and McCorquodale (2016)).

2.2.2.2 Tank geometry and construction features

After Zhou and McCorquodale (1992a) overcame the local numerical instabilities near the reaction baffle lip and successfully simulated the entire flow domain from inlet zone to effluent weirs in an SST, SST CFD models have been widely applied to study the effect of geometric features (dimensions and internal baffling structures) and to optimize the geometry. The structural optimization for the inlet zone includes optimizing the location and submergence of the inlet baffle (a cylinder surrounding the feed zone for circular SSTs, or a wall across the width of rectangular SSTs, either solid or porous). These inlet baffles have since become known as energy dissipating inlets (EDI). An influent floor baffle (McKinney baffle) if located below inlet structure and flocculating well, if present, can (1) dissipate the strong inflow energy, (2) reduce recirculation and avoid the re-entrainment of already clarified liquid into the inlet zone, (3) avoid the scouring on the thickened sludge at the bottom of the SST. The structure optimization for the outlet zone includes optimizing the arrangement (length and location) of the outlet weirs and adding various baffles on the side wall, especially Stamford baffle, to reduce the upward flow to the effluent weir. Table 2.3 summarizes previous CFD studies of SST geometry features. Figure 2.4 shows different SST geometry features.

Table 2-3. Configuration optimizations in previous studies

	References	Baffle types	Scale	Dim.	Model	Validation	Remarks
Inlet structures	Krebs (1991)	inlet solid baffle	Pilot	2D	RANS+ constant eddy viscosity	N/A	Optimized the inlet baffle location
	Zhou et al. (1992)	Inlet solid baffle	Full	2D	URANS+ *sk-ε*	Velocity	Inlet baffle improved SST performance
	Wang et al. (2011)	Inlet solid baffle	Full	3D	URANS+ *sk-ε*	Velocity	Optimized the baffle depth and location
	Patziger (2016)	Inlet solid baffle	Full	2D	URANS+ *sk-ε*	Velocity	Optimized the baffle depth and location
	Kreb et al. (1992)	Porous wall	Pilot	2D	RANS+ constant eddy viscosity	N/A	Simulated porous walls with various porosity fraction
	Xanthos et al. (2011)	Porous wall	Full	3D	URANS+ *sk-ε*	N/A	Perforated baffle reduced flow recirculation
	Vitasovic et al. (1997)	Flocculation well	Full	2D	URANS+ *sk-ε*	ESS	Optimized the flocculating well size
	Narayanan et al. (2002)	EDI	Full	3D	URANS+ *sk-ε*	N/A	SST without an EDI bottom performed better
	Ghawi and Kris (2011)	EDI	Full	3D	URANS+*sk-ε*	N/A	LA-EDI improved SST performance
	Burt (2010)	McKinney baffle	Full	2D	URANS+*sk-w*	Concentration and velocity	McKinney baffle reduced ESS

	Gao and Stenstrom (2019b)	McKinney baffle	Full	2D	URANS+ *sk-ε*	Concentration and velocity	McKinney baffle increased the SST capacity
Outlet structures	Gerges and McCorquodale (2008)	Stamford baffle	Full	2D	URANS+ mixing length model	N/A	60º version of the Stamford baffle could be more effective than a typical 45º baffle
	Xanthos et al. (2013)	Effluent weirs	Full	3D	URANS+ *sk-ε*	ESS	Optimized effluent weir locations
	Wicklein and Samstag (2014)	Surface lamella plates	Full	2D/ 3D	URANS+ *k-ε*	N/A	Lamella plates didn't show any benefit
Comprehensive evaluations	Shaw et al. (2005)	Inlet geometries (Tangential EDI; LA EDI; Concentric plates; no EDI)	Full	3D	URANS+ RNG *k-ε*	N/A	EDI provided the best performance at high flows
	Zhou S.P et al. (2010)	EDI, flocculating well	Full	3D	URANS+ *sk-ε*	Field data	Comprehensive evaluation of SST inlet geometries
	Stamstag et al. (2010)	EDI, flocculating well	Full	3D	URANS+ *sk-ε*	Velocity and concentration	Comprehensive evaluation of SST inlet geometries
	Das et al. (2015)	Inlet geometries (inward baffle; EDI; submerged skirt; no EDI)	Full	3D	URANS+ Realizable *k-ε*	N/A	inward baffle was added
	Chu et al. (2015)	Inlet baffle; flocculating well; Stamford baffle	Full	2D	URANS+ mixing length model	ESS	Comprehensive evaluation of SST inlet geometries
	Winkler et al. (2015)	Inlet baffle; flocculating well; Stamford baffle; effluent weir location	Full	2D	URANS+ mixing length model	SBH	Comprehensive evaluation of different SST geometries

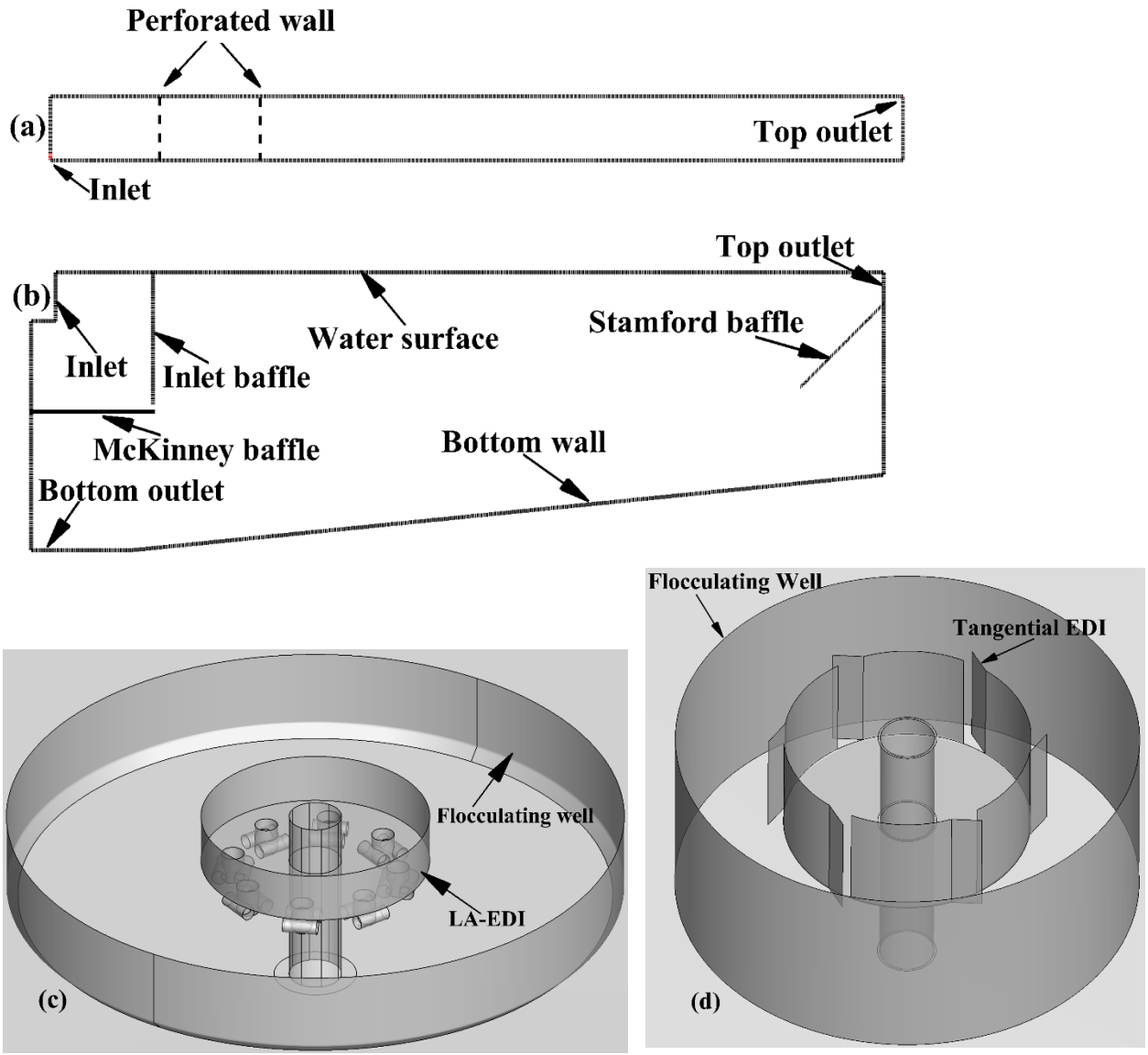

Figure 2-4. SST geometry features (a: perforated wall in a rectangular SST; b: inlet baffle, McKinney baffle and 45º Stamford baffle in a circular SST; c: LA-EDI and flocculating well in a circular SST; d: tangential EDI and flocculating well in a circular SST)

2.2.2.2.1 *The structure optimization for the inlet zone*

Imam et al. (1983) indicated that a solid, cylindrical inlet baffle, enclosing the inflow zone, can be used to dissipate the kinetic energy of the inlet flow and to stabilize the flow. They studied the effect of baffle submergence on the solids removal and found that the removal rate increased at a specific range of baffle submergence. However, because of the limitation of their model, they could solve only the hydrodynamics of a rectangular settling tank operating under neutral density conditions. Zhou and McCorquodale (1992b) and Zhou et al. (1992) applied a 2D unsteady-state model to study the effect of a solid inlet baffle under the density-driven flow and showed that the baffle reduced the entrainment compensating flow and improved the tank performance. Wang et al. (2011) applied a 3D unsteady-state model to optimize the optimal baffling location and length. Patziger et al. (2016) applied a Fluent-based 2D unsteady-state model to optimize the inlet structure of an SST in the Graz Municipal WWTP. The results showed that the optimized inlet structure can reduce the density jet length by 18% and decrease the ESS by 70% under wet weather conditions.

In addition to the study of a solid baffle for the inlet zone, CFD models have also been used to study a perforated inlet baffle. A porous baffle can not only dissipate the inlet energy, reducing the density waterfall, but also can enhance flocculation (Krebs et al., 1992). Kawamura (1981) was the pioneer in studying perforated baffle in the sedimentation process. His study indicated that hole shapes, porosity fractions and numbers of porous walls are the three main influential factors to the performance of a porous wall. Krebs et al. (1992) applied a 2D steady-state model to study porous

baffles with various porosity fraction for a pilot SST. The most significant contribution from this study was that their study provided a design guidance to the application of porous walls. However, the sludge was modeled by a non-flocculent, clay suspension in their research and the effect of the porous wall on the flocculation enhancement cannot be verified. Baumuer et al. (1996) followed Krebs et al.'s (1992) research and compared the effect of a solid and perforated baffles with different porosity on the performance of a pilot SST under dynamic loadings. The results showed that the perforated baffle performed better than the solid baffle under dynamic loading conditions, which can be helpful to maintain the stable performance of the SST during the wet-weather. However, because of limited computational capacity, previous CFD researchers could only study the effect of perforated baffles on a 2D scale model and simplified orifice distributions and shapes to several horizontal slots. For the perforated baffle which cannot be easily simplified into a wall with several horizontal slots, a 3D model should be applied to improve the prediction accuracy of the perforated baffle with various porosity fractions and orifice distribution. Zhou et al. (1997) conducted a comprehensive modification for the SST in the Passaic Valley Sewerage Commission, including the addition of a perforated wall with two different porosities. A 3D unsteady-state model was used to predict ESS in CFD stress tests. The predicted results showed the modified SST with the perforated wall reduced the ESS by at least 20%. Ramalingam et al. (2009) and Xanthos et al. (2011) applied a 3D unsteady-state model to optimize the performance of an SST with a perforated wall in New York City water pollution control plants and was especially concerned with performance during periods of poor settling and peak flow conditions. The perforated baffle

reduced flow recirculation into the inlet zone and provided plug flow pattern immediately after the baffle, which promotes effluent quality.

Burt and Ganeshalingam (2005) were the first to study the effect of an inlet floor baffle or McKinney baffle. The addition of a McKinney baffle placed below the inlet circular baffle separates the inlet zone from the settling zone and sludge thickening zone. They found that the baffle reduces the re-entrainment of already clarified liquid into the inlet baffle and avoids density currents impinging the thickened sludge blanket. It can also reduce the fluctuation of ESS during dynamic hydraulic loading. Burt (2010) optimized the inlet of the SST at the Witney sewage treatment works in Oxfordshire with the addition of a McKinney baffle. Gao and Stenstrom (2019b) conducted a series of CFD stress tests on the original Witney SST without McKinney baffle and on the new SST with the addition of the McKinney baffle. Their simulation results showed that the flow capacity in the new SST can be approximately 1.4 to 2 times the capacity of the old SST.

More effective EDIs evolved from inlet baffles to improve the SST performance and much of the recent SST design and development work has focused on the installation and modification of the EDIs (Shaw et al., 2005). The EDI can confine the high turbulent energy and spread the load uniformly near the top of the flocculating well. The most common EDI has tangential outlets which can generate a swirling flow pattern. However, Burt and Ganeshalingam (2005) indicated that the combination of slot size and vane angle can produce excessive swirl and cause re-suspension of the sludge below the flocculating well. Therefore, they suggested that the size of the slot and the vane angle should generate strong momentum in the flocculating well to improve

sludge flocculation, but not too strong to produce sludge re-suspension. Narayanan et al (2002) conducted side-by-side full-scale hydraulic testing and hydrodynamic modeling of SSTs at the Laguna Subregional Water Reclamation Facility of the City of Santa Rosa. Their CFD model confirmed the results obtained in field work that the SST without the tangential EDI bottom has significantly higher capacity at peak flows. Shaw et al. (2005) applied a 3D transient model to compare the performance of four different inlet geometries (Tangential EDI; LA EDI; Concentric plates EDI; no EDI). They indicated that the poor performance of the tangential EDI can also be improved by breaking up the spiral motion by the inclusion of baffles within the flocculating well. Their comparison showed that these four different inlet geometries performed similarly at low flows and that the LA EDI provided the best performance at high flows. Ghawi and Kris (2011) showed that the LA-EDI can maintain high removal efficiency even when the sludge has a poor settling ability (SVI>200 ml/g). Zhou et al. (2010) applied a 3D transient model to upgrade an existing SST in Tai Po Sewage Treatment Plant, Hong Kong. The existing tangential EDI was replaced by an innovative 'multilayer energy dissipating inlet column' (MEDIC, US Patent No. 7378027). Perforated concentric circular baffles sufficiently dissipated the inflow energy and distributed the influent flow jets along the vertical and tangential direction before entering the flocculating well. After comprehensive field-testing and CFD modeling evaluation (Samstag et al., 2010). the MEDIC EDI was also a recommended for North San Mateo County Sanitation District wastewater treatment plant.

In order to improve the usage of the entire flocculating well, Vitasovic et al. (1997)

simulated the reduction the size of the flocculating well from 46% to 28% of the tank diameter. The simulations showed that the smaller well reduced the ESS from 87 mg/L to 15 mg/L. Parker et al. (1996), based on plant-scale observations, concluded that the optimum size of the flocculating well to produce lowest ESS is between 32 and 35% of SST radius. Burt and Ganeshalingam (2005) using simulations found that a flocculating well radius of 20% SST radius and half the SST depth produced the lowest ESS.

2.2.2.2.2 *The structure optimization of the effluent weirs and Stamford Baffle*

The outlet optimization includes optimizing the arrangement (length and location) of the outlet weirs and adding various baffles on the side wall, especially the Stamford baffle. Krebs et al. (1996) developed a 2D model for a rectangular SST using three different lengths (short, medium, long) to compare different effluent weir positions. The first weir position was at the end of the tank and perpendicular to the tank length. The other position was a single launder, parallel to the tank length, and located at varying distances from the end, based on the overall tank length. The study showed that the weir greatly affected performance position with weirs in the middle of the SST being best. The perpendicular weir at the end of the SST tended to produce a bottom current at the end wall.

Zhou et al. (1997) in their study of rectangular SSTs proposed eight longitudinal effluent weirs to replace the six surrounding effluent launders (two on each side and two perpendicular all towards the effluent end of the SST). The total length of the new launders was 33% longer than the original launders. Xanthos et al. (2013) followed Zhou et al. (1997)'s study and simulated the

SST with both 2D and 3D transient models. The 3D model results were more illustrative of the impacts and were able to show that concentration contours along weir width.

The 2D simulations have shown the effects various baffles, such as the Stamford baffle at the side wall to reduce ESS. Burt and Ganeshalingam (2005) listed five different types of baffles, but only the Stamford baffle was studied in their numerical model. Their simulation results showed that since the effluent flow bypasses the Stamford baffle in shallow SSTs, which limits its influence in shallow SSTs. The Stamford baffle predicted to perform better in SSTs with deeper sidewall depths and flat bottoms. Gerges and McCorquodale (2008) indicated that the 60-degree down angel version of the Stamford baffle could be more effective than the standard 45-degree Stamford baffle.

2.2.2.3 Sludge settling characteristics

Sludge settling properties are one of the major processes impacting the performance of an SST. Based on the sludge concentration and particle or floc interactions, sludge settling can be described in four different zones: (1) discrete; (2) flocculent; (3) hindered or zone; (4) compression (Kynch, 1952). De Clercq (2003) and McCorquodale et al. (2004) reviewed the development of sludge settling models based on these four zones. Also, Li and Stenstrom (2014) critically reviewed the development of 1D SST models, including the advantage and disadvantage of various settling behaviors, the numerical techniques required to solve the 1D model and the important 1D modeling challenges. Therefore, this review includes the impacts of the settling velocity sub-model on 2D and 3D CFD simulations, but does not discuss the mathematics of the 1D hyperbolic equation

The Takács et al. (1991) (Equation. 19) and the Vesilind (1968) (Equation. 20) are the most

widely applied sub-models coupled in SST CFD models in the last 30 years and many recent developments of sludge settling models are based on these two models (e.g. Guo et al. 2009; Ramin et al. 2014; Diehl et al., 2015; Bürger et al., 2017; Torfs et al., 2017; Daigger et al., 2018).

$$V_s = V_o(e^{-r_h(C-C_{min})} - e^{-r_p(C-C_{min})}) \quad (19)$$

$$V_s = V_o e^{-r_h C} \quad (20)$$

The first exponential term in the Takács settling model is the same as the Vesilind model, which is used to describe the sludge settling in hindered and compression settling zones, while the addition of the second exponential term is used to describe the slow and non-settling in discrete and flocculent settling zones (Ekama and Marais, 2004). Different sludge settling characteristics directly determine the coefficient (r_h) in the first exponential term, which can be obtained from a series of batch tests over a concentration range, by measuring the zone settling velocities as the linear descending rate of the liquid/solid interface (Ramin, 2014). However, the calibration procedure requires a series of time-consuming batch tests; therefore, it is often used for research but seldom used in field investigations (De Clercq, 2003; McCorquodale et al., 2004; Burt, 2010; Ramin, 2014). An alternative method which is widely used in field and consulting projects (e.g. Winkler et al. (2015); Esping et al. (2015); Chu et al. (2015); Griborio and McCorquodale (2016)) is to correlate r_h with easily measurable parameters in WWTPs (Daigger et al., 2018), including SVI, stirred sludge volume index (SSVI), and diluted sludge volume index (DSVI).

There have also been efforts to develop the settling velocity from fundamental analysis of force action on activated sludge. Xu et al. (2017) developed a force-based mechanistic model for

the standard EE multi-phase model. Compared with the standard EE multi-phase model, he developed new equations for modeling the drag force, solids pressure and shear stress. The prediction results were validated by the experimental data from their own tests and from De Clercq et al. (2008) and Ramin et al. (2014). The results demonstrated that this mechanistic model can be directly executed in CFD software. Therefore, this force-based model can be the alternative approach to simulate the sludge settling.

2.2.3 Parameters in modeling structures

Although CFD models have been applied to study SSTs in the last three decades, there are some uncertainties of model parameters and only three recent papers (Gao and Stenstrom, 2018b; Gao and Stenstrom, 2019a) studied the uncertainty of these parameters on the performance of SSTs. These model parameters are (1) generation of turbulent kinetic energy (TKE) due to buoyancy ($\boldsymbol{G_b}$) in the TKE equation of the *k*-*ε* family turbulence models; (2) buoyancy coefficient ($\boldsymbol{C_3}$) in the turbulent dissipation rate (TDR) equation of the *k*-*ε* family turbulence models; (3) turbulent Schmidt number ($\boldsymbol{\sigma_c}$) in the sludge transport equation; (4) the coefficient in the second exponential term of the Takács settling equation ($\boldsymbol{r_p}$) and (5) dry solids density ($\boldsymbol{\rho_p}$). Table 2.4 shows the values of $\boldsymbol{C_3}$, $\boldsymbol{\sigma_c}$, $\boldsymbol{r_p}$, and $\boldsymbol{\rho_p}$ used in previous studies. These parameters area coupled in the sludge transport equation, density state equation and Takács settling equation shown in section 2.2 and the turbulence model shown below:

For simplicity, only the standard *k*-*ε* turbulence (SKE) model is shown here:

$$\rho\frac{\partial k}{\partial t}+\rho\nabla(\overrightarrow{u_i}k)=\rho\nabla\left[\left(v+\frac{v_t}{\sigma_k}\right)\nabla k\right]+G_k+G_b-\rho\varepsilon \tag{2.21}$$

$$\rho\frac{\partial k}{\partial t}+\rho\nabla(\overrightarrow{u_i}\varepsilon)=\rho\nabla\left[\left(v+\frac{v_t}{\sigma_\varepsilon}\right)\nabla\varepsilon\right]+C_1\frac{\varepsilon}{k}(G_k-C_3G_b)-C_2\rho\frac{\varepsilon^2}{k} \quad (2.22)$$

G_k represents the generation of TKE due to the mean velocity gradients, and G_b corresponds to the generation of TKE due to buoyancy. The dimensionless empirical constants are given the standard values suggested by Rodi (1993). $C_\mu = 0.09$, $C_1 = 1.44$, $C_2 = 1.92$, $\sigma_k = 1.0$, and $\sigma_\varepsilon = 1.3$.

Table 2-4. Ranges of parameters in modeling structures in previous studies

No.	Parameters in modeling		References
	Turbulent Schmidt number		
	σ_y	σ_r	
1	0.5	0.5	
2	0.7	0.7	Stamou et al. (1989)
3	1.0	1.0	
4	1.0	0.5	Zhou and McCorquodale (1992a)
5	1.0	1.0	Zhou and McCorquodale (1992c)
6	0.5	1.0	
7	1.0	1.0	Dahl (1993)
8	0.7	0.7	Lakehal et al. (1999)
9	0.5-0.9	0.7	Saffarian et al. (2010)
10	1.0	1.0	Ramin et al. (2014)
	Coefficient of Buoyancy Term (C_3)		
1	0.15		Ramin et al. (2014)
2	0.2		Dahl (1993); Shahrokhi et al. (2013)
3	0-0.2		Lakehal et al. (1999); Saffarian et al. (2010)
4	0.8		Xanthos et al. (2010)
	r_p (L/g)		
1	4		McCorquodale et al. (2004)
2	5		McCorquodale et al. (2004)
3	10		Ekama and Marais (2004); Vitasovic et al. (1997)
4	$10r_h^*$		Ekama et al. (1997); Weiss et al. (2007)
5	15-30		Zhou and McCorquodale (1992a)
6	20		Tamayol et al. (2009)

	ρ_p (kg/m^3)	
1	1100	Deininger et al. (1998)
2	1450	Larsen (1977); Lakehal et al. (1999)
3	1500	Tarpagkou and Pantokratoras (2013)
4	1600	Weiss et al. (2007)
5	1360-1660	Zhou and McCorquodale (1992a)
6	1700-1800	Kinnear (2002)
7	1907 / 1743 / 2070	Xu et al. (2017)

* r_h: the coefficient in the first exponential term of the Takács settling equation

2.2.3.1 Generation of TKE due to buoyancy (G_b)

Many early CFD SST studies ignored the G_b in the TKE equation of the turbulence model. For example, DeVantier and Larock (1986, 1987) ignored the G_b due to the convergence difficulty in modeling the flow with a high MLSS concentration and the limited computational resources. Zhou and McCorquodale (1992a, b) used the G_b-decoupled SKE model to study the hydrodynamics of SSTs. However, simulated MLSS in the study was only 1400 mg/L. Vitasovic et al. (1997) studied the effect of SOR and the internal baffling structure of the SST with a 2D CFD model. The buoyancy term was also ignored in their SKE model. The latest CFD SST model decoupling the buoyancy term in the turbulence model was in Tamayol et al. (2009). In this study, the effects of Reynolds number and Froude number on the optimal baffle location and the flow field were studied. However, the study did not show the calibration of their CFD prediction results with experimental data; therefore, the reliability of their model results is unknown.

More recent CFD SST studies coupled G_b in the turbulence model (Lakehal et al., 1999; Xanthos et al., 2010; Ramalingam et al., 2012; Shahrokhi et al., 2013; Ramin et al., 2014). However, none have simulated the same cases with and without G_b coupling. Therefore, Gao and

Stenstrom (2018b, 2019a) studied the need for coupling the G_b by simulating same cases with and without coupling G_b.

Gao and Stenstrom (2018b) used a Fluent-based 2D SST model to study the effects of G_b at Darvill SST reported by McCorquodale et al. (2004). The inlet baffling structure of the Darvill SST is very poor and has only a center well. The effect of the G_b was analyzed under different MLSS concentration, and sludge settling properties. The study showed that the G_b should be coupled in the TKE equation to correctly predict the Darvill SST performance, unless both MLSS is very low and sludge settling is very high.

In order to generalize the effects of baffling structures on the buoyancy-induced turbulence in SSTs, the authors used eleven SST geometries, including four circular SSTs and seven rectangular SSTs in their further study (Gao and Stenstrom, 2019a). The results show that the G_b has strong impacts on the prediction of the performance of an SST with similar poor baffling structures to the Darvill SST. For an SST with good baffling structures, the prediction of G_b-decoupled and G_b-coupled turbulence model is similar. Therefore, G_b is a buoyancy correction term to correctly predict the performance of an SST with poor baffling structures.

2.2.3.2 Buoyancy coefficient C_3 and turbulent Schmidt number (σ_c)

The application of C_3 in the TDR equation and σ_c in the sludge transport equation has varied widely among different studies. Gao and Stenstrom (2018b) showed that among the performance indicators (ESS, SBH, RAS concentration), none of them is sensitive to the change of C_3 and only SBH is sensitive to the variation of the σ_c. Therefore, C_3 can be removed from the

TDR equation to improve the rate of convergence and reduce computing time and $\boldsymbol{\sigma_c}$ can be used to adjust SBH, when ESS and RAS are well calibrated to the field data.

2.2.3.3 Coefficient $\boldsymbol{r_p}$ in the Takács settling equation and dry solids density ($\boldsymbol{\rho_p}$)

Ekama and Marais (2004) noted that the value of $\boldsymbol{r_p}$ in the Takács settling equation affects the CFD prediction of ESS. Also, since $\boldsymbol{\rho_p}$ is coupled in every governing equation, different values of $\boldsymbol{\rho_p}$ may influence CFD prediction of the entire SST hydrodynamics. As shown in Table 2.4, there is a large range of values of these two parameters. Gao and Stenstrom (2019e) studied the influence of these two parameters under varied flow conditions. The results showed that ESS is very sensitive to the change of $\boldsymbol{r_p}$. The incorrect specification of $\boldsymbol{r_p}$ may predict clarification failure of the SST when the field measurements indicate the SST performs well. Also, the incorrect value of $\boldsymbol{r_p}$ may show that the clarification performance in the original SST outperforms the modified SST, which is opposite to the field measurements. However, the prediction of SBH and RAS concentration is not sensitive to the $\boldsymbol{r_p}$; therefore, $\boldsymbol{r_p}$ can be used to adjust ESS, when RAS and SBH are well calibrated to the field data.

Dry solids density ($\boldsymbol{\rho_p}$) also only affects the prediction of clarification and has little effect on sludge thickening. However, the effect is smaller than the effect $\boldsymbol{r_p}$. Gao and Stenstrom (2019e) indicated that the CFD model still predicts reasonable ESS compared to field data, even after doubling the $\boldsymbol{\rho_p}$; therefore, the medium value of $\boldsymbol{\rho_p}$ (1450 kg/m^3) is a good assumption.

2.2.4 Atmospheric conditions

Atmospheric conditions, including ambient and water temperature, and surface wind, are

one of the influential factors on an SST performance (McCorquodale et al., 2004). While the effect of temperature on the performance of SSTs has been studied with CFD models in the last 30 years (shown in Section 3.1), few studies show the effect of surface wind. Several recent CFD researchers studied the surface wind effect on rectangular settling tanks in WTPs (Khezri et al., 2012; Stamou and Gkesouli, 2015; Gkesouli et al., 2016; Goodarzi et al., 2017; Gkesouli and Stamou, 2018). However, the applicability of these studies to SSTs in WWTPs is limited due to (1) the structural difference between SSTs in WWTPs and settling tanks in WTPs, (2) different solids settling processes and (3) different solids concentration. Therefore, Gao and Stenstrom (2019c, d) studied the effect of surface wind on the performance of 3D circular and rectangular SSTs, respectively, under different flow conditions. Under each flow condition, the surface wind was simulated in different flow directions and surface wind velocities. The results showed that the surface wind has strong negative impacts on the performance of both rectangular and circular SSTs, especially on circular SSTs.

Gao and Stenstrom (2019c) showed that the predicted ESS can double in the circular SST between normal and windy conditions. Also, for the circular SST, surface wind along the inlet port direction resulted in much higher ESS than the surface wind at 45^{o} to the inlet direction. The difference of the predicted ESS between these two surface wind directions increases as the increase of the surface wind speed. For the rectangular SST (Gao and Stenstrom, 2019d), the CFD prediction showed that the counter-current wind has strongest negative impacts on the SST while the surface wind flowing perpendicular to the SST longitudinal direction has the least negative

impacts.

2.3. Challenges in CFD SSTs simulation

Despite the successes of CFD modeling of SSTs in the last 30 years, a significant shortcoming of the CFD modeling is the lack of a generally accepted SST modeling framework (assumptions for sludge settling, sludge rheology, turbulence, flocculation). The different assumptions implemented for these sub-models in the SST model framework still do not fully satisfy the experimental observations and need further improvements.

2.3.1. Sludge settling model

The development of an advanced sludge settling sub-model can improve the prediction of particle sedimentation in water and wastewater treatment processes. Plósz et al. (2012) provided a critical review of SST modeling techniques to identify recent developments and limitations. He noted that the lack of practical measurement technique for measuring sludge settling behavior outside the hindered settling range is the most limiting the use of advanced settling models. Although advanced techniques such as radiotracing (Vanrolleghem et al., 2006; De Clercq et al., 2008) have been used to obtain high resolution concentration and compression pressure profiles during batch settling tests, high complexity and cost may prohibit their use as a routine test method (Li and Stenstrom, 2014).

Plósz et al. (2012) also noted that the poor understanding of solids settling outside the zone settling range limits the development of the settling model. Firstly, the lack of understanding of transition behavior from zone settling into compression settling limits the accuracy in predicting

observed transient settling interface height. Also, the challenge in observing interface height change in batch tests at low initial concentration (≤500 mg/L) makes it difficult to develop a reliable flocculation velocity model (Li and Stenstrom, 2014). Therefore, although some advanced settling models have been developed based on the Takács settling equation (Equation 19), none of these advanced settling models provides sufficient confidence to make it a widely accepted engineering tool.

Because of these limitations, Vesilind (1968) and Takács et al. (1991) settling sub-models are still the most widely applied settling models. As described in Section 3.2.3, practitioners normally use SVI-based correlation equation to obtain settling parameter, r_h. Giokas et al. (2003) summarized eight different SVI correlations and two different SSVI correlations. Kelly et al. (2009) compared the predictions of maximum flow capacity in five different WWTPs by using three different SVI-based correlations (Wahlberg and Keinath (1988a); Daigger (1995); Ozinsky and Ekama (1995)) with field observations. Figure 2.5 indicates that the differences between the prediction of SVI-based correlation equations and field observations can be remarkable. For example, for the first WWTP, the prediction of Ozinsky/Ekama correlation was twice as much as the flow capacity in the field observation. In contrast, the Wahlberg/Keinath correlation under-predicted the capacity of the second WWTP by 15%. Therefore, Kelly et al. (2009) concluded that significant care must be given when using these SVI correlations to predict the maximum flow capacity.

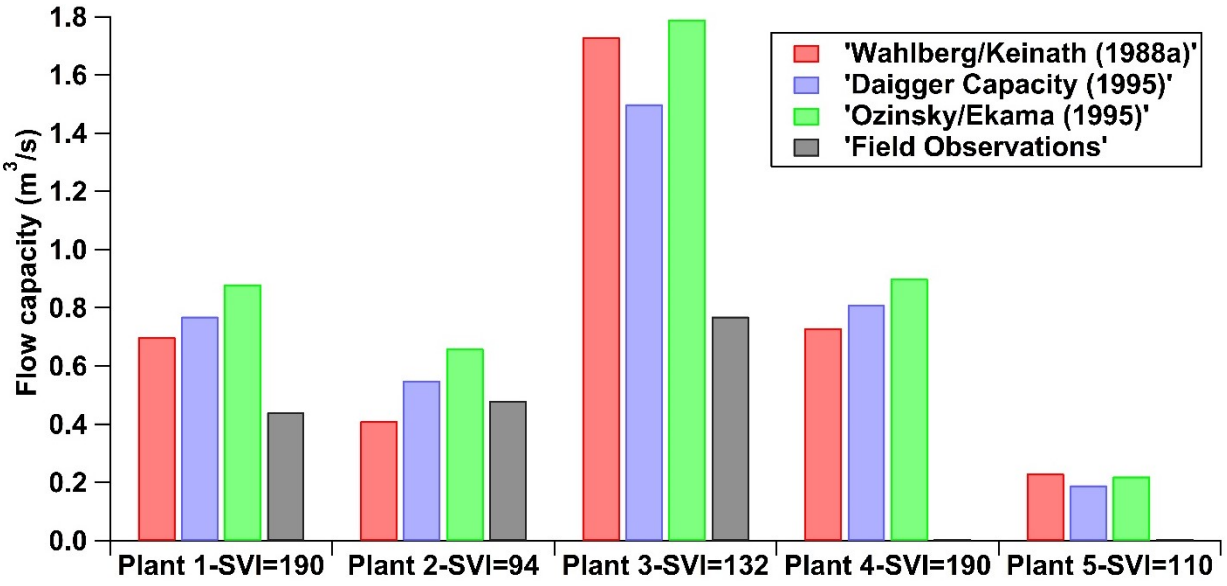

Figure 2-5. Comparison of flow capacities (m^3/s) based on different SVI-based correlations to field observations in five different WWTPs (adapted from Kelly et al., 2009).

However, the relation between SVI and compression settling is unclear and there is no practical method to identify sludge compression characteristic from the SVI (Li and Stenstrom, 2014). Given that some compression settling velocity models were developed as a function of solids concentration (e.g. McCorquodale et al. 2004; De Clercq et al. 2008; Ramin et al. 2014; Bürger et al., 2017; Torfs et al., 2017), in a similar fashion to the zone settling models, it may be feasible to develop a SVI-based correlation to obtain the sludge compression settling parameter ($\boldsymbol{r_p}$) in a similar fashion to obtain $\boldsymbol{r_h}$. In order to measure the proper SVI-based correlation to $\boldsymbol{r_p}$, longer settling time (more than 30 minutes) for the standard SVI test may be required for sludge to be sufficiently compressed into the compression zone. Also, higher initial concentration may be required to produce observation in the compression zone. (Li and Stenstrom, 2014).

Guo et al. (2009) also indicated that advanced settling models were often developed for the

one-dimensional (1D) modeling purpose and were limited to static or quasi-static conditions. However, the flow hydrodynamics of settling tanks in 2D or 3D scale is not static and the flow turbulence influences sludge settling. Therefore, Guo et al. (2009) developed a settling model based on the Vesilind equation which relates both sludge concentration and turbulent intensity. It is important to further develop and implement settling models that describe the sludge behavior across the entire concentration range with measurable parameters.

Table 2-5. Applications of different sludge rheological models in previous CFD SST studies.

Bokil-Bewtra model (Bokil, 1972)	Pseudoplastic Casson model	Bingham Plastic Model	Herschel-Bulkley model (Pseudoplastic with yield stress)	Modified Herschel-Bulkley model
Lakehal et al. (1999)	Weiss et al. (2006, 2007)	Dahl et al. (1994)	Dahl (1993)	De Clercq (2003)
Armbruster et al. (2001)	Saffarian et al. (2010)	Lakehal et al. (1999)	Saffarian et al. (2010)	Saffarian et al. (2010)
McCorquodale et al. (2004)		Armbruster et al. (2001)	Ramin et al. (2014)	
Xanthos et al. (2011)		Weiss et al. (2006)	Wagner et al. (2015)	
Ramalingam et al. (2012)		Saffarian et al. (2010, 2011)		
Das et al. (2015)				
Gao and Stenstrom (2018a, b, 2019a, b)				

Table 2-6. Comparison of turbulence models used in WWTP modeling. Adapted from Bridgeman et al. (2009)

Turbulence Models	Comments	Advantages	Disadvantages
Standard k-ε (SKE)	• Semi-empirical modeling of k and ε. • Valid for full turbulence only.	• Simplest model. • Excellent performance for many flows. • Well established.	• Poor performance in some scenarios (rotating flows, flow separation, adverse pressure gradients.) • Assumes isotropy in turbulence. • Poor prediction of lateral expansion in three-dimensional wall jets.
Renormalized Group (RNG) k-ε	• Based on statistical methods, not observed fluid behavior. • Effects of small-scale turbulence represented by means of a random forcing function in N-S equations. • Similar in form to SKE, but modified dissipation equation to describe high-strain flows better • Differential equation solved for turbulent viscosity, better for transitional flows	• Improved performance for swirling flow compared to the SKE model.	• Less stable than the SKE model.
Realizable k-ε	• A new eddy-viscosity formula involving a variable C_μ	• Suited to round jets, swirling flows and flow separation.	• Not recommended for use with multiple reference frames.

	• A new dissipation equation based on dynamic equation of the mean-square vorticity fluctuation		
Standard *k-ω*	• *ω= ε/k*=specific dissipation rate • SKE solves for dissipation of *k,* Standard *k-ω* solves for rate at which dissipation occurs. • Resolves near wall without wall functions, so can be applied through boundary layer	• Valid throughout the boundary layer, subject to sufficiently fine grid resolution.	• Separation is typically predicted to be excessive and early.
Shear Stress Transport (SST) *k-ω*	• As *k-ω* except for gradual change from *k-ω* in inner region of boundary layer to high Re version of SKE in outer part. • Modified turbulent viscosity formulation to account for transport effects of turbulent shear stress.	• Suitable for adverse pressure gradients and pressure-induced separation. • Accounts for the transport of the principal turbulent shear stress.	• Less suitable for free shear flows.
Reynolds Stress Model (RSM)	• The most general of all models.	• Accurate calculation of mean flow properties and all Reynolds stresses. • Yields superior results to *k-ε* models for flows with stagnation points.	• Computationally expensive. • Not always more accurate than two-equation models. • Harder to obtain converged results.

2.3.2. Sludge rheological model

Sludge rheology directly influences the SST hydrodynamics and the transport of sludge at the bottom of the sludge blanket to the sludge hopper. Since turbulence damping by buoyancy occurs in the sludge blanket of an SST, the sludge viscosity becomes equal to or larger than the turbulence eddy viscosity; therefore, the influence of the sludge viscosity on flow and concentration fields cannot be ignored and an appropriate rheological model should be coupled in the CFD model (De Clercq, 2003). However, previous inclusions of rheological model were chosen based on the simplicity of the model or because a particular model fit the observed results. Table 2.5 summarizes the applications of different sludge rheological models in previous CFD SST studies.

Over the last 30 years, three reviewers (Seyssiec et al., 2003; Eshtuaghi et al. 2013; Ratkovich et al. 2013) have summarized sludge rheology research progress. Seyssiec et al. (2003) reviewed the application of rheology in wastewater treatment processes and the rheological characterization of wastewater treatment sludge, such as shear-thinning, viscoplastic, thixotropy and viscoelasticity behaviors. Eshtuaghi et al. (2013) extended Seyssiec's study and reviewed the commonly used rheometers and different rheological properties of wastewater municipal sludge as well as the effect of concentration, temperature, and water content on these properties. Ratkovich et al. (2013) summarized the different forms of correlation relationships between the combinations of MLSS, shear rate, and temperature with viscosity and compared the measurement protocol from 42 different experimental setups. Their review showed that there was no consensus

on the measurement protocol and only a few authors illustrated their measurement protocol sufficiently. As a result, it seems impossible to compare the reliability of the apparent viscosity data published by different research groups which use different rheometers, sludge, and measurement procedures.

Therefore, a systematic and repeatable measurement protocol needs to be defined to improve data reliability. Then a proper rheological model should be developed in order to describe the physical process rather than to fit a qualitative model by means of parameter calibration.

2.3.3. Turbulence model

Table 2.6 summarizes the description of turbulence models commonly used for Reynold Averaged Navier-Stokes (RANS) closure (Bridgeman et al. 2009). Although the SKE model has been widely applied in the CFD SST modeling over the last 30 years, Das et al. (2016) noted that it performs poorly for complex flows with strong streamline curvature. Therefore, two modified versions of the SKE model (Realizable k-ε and RNG k-ε models) have been developed and applied in recent sedimentation studies. Additionally, Burt (2010) applied the low Reynold number k-ω turbulence model to study the performance of SSTs.

However, to the best of the authors knowledge, the RNG k-ε model was only applied in the studies of settling tanks either in drinking water treatment or primary settling tanks in wastewater treatment (Laine et al., 1999; Tamayol et al., 2008; Tarpagkou and Pantokratoras, 2013; Patziger and Kiss, 2015; Das et al., 2016), where the particle concentration is low, and its buoyancy effect can be ignored and no study applied shear stress transport and Reynolds stress models in the SST

modeling. Only Das et al. (2016) applied the Realizable k-ε model to optimize the complex inlet structure of an SST. However, the study did not show the model calibration with the field data to show the superiority of the Realizable k-ε model. Also, only Burt (2010) applied the low Reynold number k-ω turbulence model to the prediction of SSTs and showed good agreement with field observation.

Because of the limitation of the SKE model and the recent application of the more advanced Realizable k-ε and RNG k-ε turbulence models, Gao and Stenstrom (2018a) compared them in predicting the performance of SSTs. The results showed that the predictions of flow and sludge concentration fields are remarkably different inside the inlet zone of the SST. The significant different prediction among different turbulence models inside the inlet zone causes more than 10% difference in predicting the RAS concentration and SBH, which can greatly influence the operation of sludge recycle. Also, different turbulence models have a strong influence on the prediction of SST flow capacity. The Realizable k-ε model predicts more than 30% higher flow capacity than the SKE model.

Although the comparison among different turbulence models showed a significant prediction difference inside the inlet zone, previous SST CFD researchers rarely showed the velocity and concentration measurements in this area. Therefore, more data are required in this area for model calibration and turbulence model selection.

2.3.4. Flocculation model

Karpinska and Bridgeman (2016) noted that although the effect of flocculation on the

performance of SSTs and the causes which promote flocculation in SSTs have been widely acknowledged, its application in SST modeling is still scarce and limited to a very few examples.

Lyn et al. (1992) coupled the flocculation model in their CFD SST studies. They concluded that the shear-induced flocculation is relatively unimportant to the flow conditions with low MLSS concentrations. However, because of limited computational resources, floc breakup was not modeled, and only MLSS in a very low concentration (80mg/L) was considered.

McCorquodale et al. (2004) used the differential equation (Equation 23) described by Parker et al. (1970, 1971) to develop their flocculation model. The CFD results showed that this flocculation model arcuately predicted flocculation in SSTs. In the last decade, the flocculation model developed in McCorquodale et al. (2004) was applied in several three-dimensional SST studies (Gong et al., 2011; Xanthos et al., 2011; Ramalingam et al., 2012; Xanthos et al., 2013). Gong et al. (2011) conducted the jar test to compute the coefficients (K_A, K_B) under the MLSS concentrations in the range of 1400 to 1600 mg/L and in the range of the discrete particle settling (160 to 440 mg/L). The results showed that both K_A and K_B are dependent on the velocity gradient (G) and are different at different MLSS concentrations, which indicates that Equation 23 requires to be further refinement. Therefore, they modified the Equation 23 without considering the dependence of MLSS concentration on K_B. The results in Gong et al. (2011) and Ramalingam et al. (2012) showed that the K_A and K_B in the modified flocculation model (Equation 24) are independent of the MLSS concentration and fits observations better. In the future, the reliability of this modified flocculation model should be tested for a wide range of MLSS concentrations and

the CFD results of coupling this new model should be compared with field observations.

$$\frac{dX_l}{dt} = K_B \cdot X \cdot G^2 - K_A \cdot X \cdot X_l \cdot G \quad (2.23)$$

$$\frac{dX_l}{dt} = K_B \cdot G^2 - K_A \cdot X \cdot X_l \cdot G \quad (2.24)$$

where X_l is the concentration of primary particles, X is the MLSS initial concentration, G is the mean velocity gradient, K_A and K_B are the floc aggregation and break up coefficients, respectively.

2.4. Conclusions

Over the last 20 years, due to the increase of computational resources and the availability of CFD software, CFD models have been widely applied as a robust and accurate tool for design, optimization, and control of SSTs. This chapter has reviewed the early findings and the following conclusions are made.

- The controversy over the relationship between SOR and SST performance can be largely explained by the SST geometry. Shallow SSTs (< 4m) have poorer performance relative to deep SSTs (> 4m). The shallow SSTs have density currents which scour particles to the effluent zones of the SST, which makes the area available for sedimentation more important. Deep SSTs do not scour particles into the effluent zones and the area available for sedimentation is less important.
- The prediction difference between $\boldsymbol{G_b}$-decoupled and $\boldsymbol{G_b}$-coupled turbulence models is significant in an SST with poor baffling structures but negligible in an SST with good baffling structures. Therefore, $\boldsymbol{G_b}$ is a buoyancy correction term to correctly predict the

performance of an SST with poor baffling structures.

- Evaluation of parameters used in the CFD models indicates that none of the performance indicators (ESS, SBH and RAS concentration) is sensitive to the change of the values of buoyancy coefficient (C_3) in the turbulent dissipation rate (TDR) equation. Additionally, only SBH is sensitive to the change of turbulent Schmidt number (σ_c) in the sludge transport equation. Also, only ESS is sensitive to the coefficient (r_p) describing the settling of small particle in Takács settling model. Incorrect specification of r_p may predict clarification failure of the SST when the field measurements indicate the SST performs well and may predict better clarification performance in the original SST than the modified SST. Dry solids density (ρ_p) has some effect on the ESS prediction but has little effect on sludge thickening. However, the effect is smaller than the effect of r_p. Therefore, C_3 can be removed from the TDR equation to improve the rate of convergence and reduce computing time. σ_c can be used to adjust SBH, when ESS and RAS are well calibrated to the field data, while r_p can be used to adjust ESS, when RAS and SBH are well calibrated to the field data. The medium value of ρ_p (1450 kg/m^3) is a good assumption.
- Temperature is a dominate factor affecting both the performance of PSTs and the type of density currents that are produced. Surface currents are produced when the inlet temperature is higher than the temperature in PSTs, and vice-versa.
- Influent temperature variations, surface heat exchange, and MLSS concentrations are all major factors affecting the performance of SSTs. Also, high MLSS concentrations,

typically occurring in ASPs, will overcome the effect of inlet temperature, resulting in bottom currents. Therefore, MLSS concentration is the dominate factor in producing density currents in SSTs.

- The existing SVI-based correlations to predict sludge settling velocities produce different flow capacity estimates for a given plant's SVI. Great care must be given when using these SVI correlations to predict the maximum flow capacity.

The following additional research needs were identified in this critical review.

- The VOF model can be used to study the surface wind effect on the SST performance and the effect of the surface baffling structures to reduce surface wind. Due to the strong surface wind effect on the SST performance, covering the SST surface or adding some vertical baffles on the water surface to reduce the surface wind shear should be considered. Future research can compare the prediction of the SST hydrodynamics with the VOF model results in order to evaluate the benefits of covering or wind baffling.
- Velocity and concentration measurements are needed inside the inlet zone. Since different turbulence models predict significantly different flow capacities and velocity and concentration fields inside the inlet zone, more measurement data are required to select the most accurate turbulence model.
- Further development is needed for settling models that describe the sludge behavior across the entire concentration range as well as considering the turbulent hydrodynamics with measurable parameters.

- An improved sludge rheological model is needed. Instead of fitting a qualitative model by means of parameter calibration, a systematic and repeatable measurement protocol needs to be defined to improve the data reliability.
- The reliability and accuracy of an improved flocculation model such proposed by Gong et al. (2011) should be tested over a wide range of MLSS concentrations and the CFD results of coupling this new model should be compared with field observations.

Chapter 3 Evaluation of three turbulence models in predicting of the hydrodynamics of a secondary sedimentation tank

3.1. Introduction

Gravity sedimentation is one of the most commonly used treatment methods for removal of suspended solids (SS) in water or wastewater treatment plants. In addition, the cost for building the sedimentation tank is about 30% of the total investment of a treatment plant (Tamayol et al., 2008). For conventional wastewater treatment plants, sedimentation tanks are mainly divided into two categories: primary and secondary sedimentation tanks (SST). Primary sedimentation tanks have a low influent SS concentration; therefore, buoyancy effects are usually negligible. However, SSTs are used to remove and concentrate and recycle biosolids and have much higher influent SS concentrations (Tamayol et al., 2008); therefore, flow currents can be density-driven and affect the performance of SSTs. Ekama and Marais (2002) stated that SSTs are "the bottle neck limiting the capacity of the wastewater treatment plant". The placement of the two types of the sedimentation tanks is shown in the Figure. 3.1.

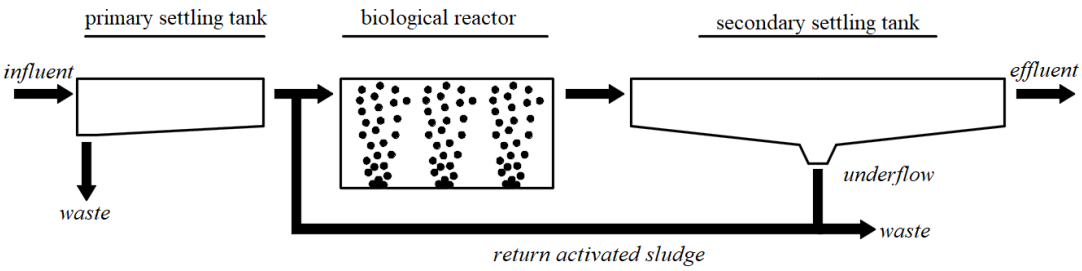

Figure 3-1. Layout of a typical AS system (adapted from De Clercq, 2003).

Previously, SSTs were designed only using empirical equations, which were based on

hydraulic criteria such as surface overflow rate (SOR) (Parker, 1983; Parker and Stenquist, 1986; Parker et al., 1996). Other influential factors such as (1) tank internal geometry, (2) solids characteristics, (3) atmospheric conditions, including wind movement and temperature were not considered (Krebs, 1995; Stamou et al., 2009). Thickening capability was often correlated to the sludge volume index (SVI) but is now usually based upon state-point analysis (Wahlberg and Keinath, 1988).

One-dimensional (1-D) models were developed to estimate solids loading rate and have evolved from conceptual models (Kynch, 1952) to numerical models. The model can solve problems such as the returned activated sludge (RAS) concentration, the sludge blanket height (SBH), and solids inventory management (Kynch, 1952; Takács et al., 1991; Li and Stenstrom, 2014). Although 1-D models are useful in evaluating loads, they cannot include non-ideal effects such as flow currents and poor geometries.

To improve the predicative capability of 1-D models and consider non-ideal conditions, CFD models have been developed over the last 40 years and have improved our knowledge of sedimentation tanks (Larsen, 1977; Zhou and McCorquodale, 1992a, 1992b, 1992c; De Clercq, 2003; Griborio, 2004; Ramin et al., 2014).

The development and the applications of the CFD model of SSTs depend on the following four parts:

(1) Improving the understanding of SSTs by relaxing assumptions for ideal behavior by including physical problems such as the impacts of turbulence and density currents (Larsen, 1977;

Adams and Rodi, 1990; Zhou et al., 1992; Wells and LaLiberte, 1998; Jayanti and Narayanan, 2004);

(2) Selecting a mathematical structure for the turbulence and buoyant flow modeling components to more accurately conform to the physical mechanisms (Adams and Rodi, 1990; Bretscher et al., 1992; Vitasovic et al., 1997; Lakehal et al., 1999; Griborio, 2004);

(3) Optimizing the solution to more quickly and accurately solve the differencing equations (Imam and McCorquodale, 1983; Imam et al., 1983; Abdel-Gawad and McCorquodale, 1984a; Abdel-Gawad and McCorquodale, 1985);

Larsen (1977) was among the first to address the physical problems of SSTs and is considered the pioneer in the CFD study of SSTs, setting the framework for the future sedimentation tank research. In his work, the Prandtl mixing length theory was applied to solve the eddy viscosity and was also used in (Abdel-Gawad and McCorquodale, 1984a, 1984b).

The complexity of solving the resulting partial differential equations was reduced with several key assumptions. Constant eddy viscosity was assumed in several early studies (Imam et al., 1983; Krebs, 1991; Krebs et al., 1992; Krebs et al., 1995). However, since eddy viscosity depends on the state of turbulence in the SSTs, the value of the eddy viscosity should vary from case to case as well as in different parts of the SSTs. The constant eddy viscosity assumption limited to the accuracy of the models. Additionally, both the mixing length theory model and constant eddy viscosity assumption imply that the turbulence is dissipated where it is generated, which cannot be used to accurately describe the transport of turbulence in the flow field (Griborio,

2004).

Therefore, a more advanced turbulence model (standard k-ε model) which is based on the transport of turbulent kinetic energy (TKE) and the turbulent dissipation rate (TDR) was used to improve many of the previously developed SST models. In the last 30 years, the standard k-ε model (SKE) has become the most widely applied turbulence model in the CFD of SSTs because of its robustness, economy and reasonable accuracy for the prediction of turbulent flow in SSTs (Stamou et al., 1989; Zhou and McCorquodale, 1992b, 1992c, 1992a; Vitasovic et al., 1997; Lakehal et al., 1999; Armbruster et al., 2001; Kleine and Reddy, 2005; Weiss et al., 2007; Tamayol et al., 2009; Gong et al., 2011; Patziger et al., 2012; Xanthos et al., 2013; Ramin et al., 2014).

In the previous studies with circular sedimentation tank, few of velocity and concentration calibrations were reported inside the inlet zone, where the Reynolds number can be very high (turbulent flow). Moreover, the SKE model is valid only for fully turbulent flow and performs poorly for complex flows involving strong streamline curvature (Das et al., 2016; Fluent, 2017). Therefore, two modified versions of the SKE model (RNG k-ε and Realizable k-ε models) have been applied in recent sedimentation tank studies (Laine et al., 1999; Tamayol et al., 2008; Tarpagkou and Pantokratoras, 2013; Patziger and Kiss, 2015a; Das et al., 2016). However, in these studies, the RNG k-ε model was applied in the studies of sedimentation tanks either in potable water treatment or primary sedimentation tanks in wastewater treatment, where the buoyancy effect can be ignored in the flow field. To the best of our knowledge, none of the published SSTs papers simulated the density stratified flow with the application of RNG k-ε model. Only Das et

al. (2016) has applied the Realizable *k*-ε model to simulate the turbulent flow in their complex three-dimensional (3D) model, but they had no field observations to show the reliability and superiority of the Realizable *k*-ε model.

Therefore, because of (1) the limitation of the widely applied SKE model, (2) the superior of the RNG and Realizable k-ε models in predicting the turbulence flow involving strong streamline curvature and (3) the recent applications of the RNG and Realizable k-ε models in the related CFD study areas, these three models are selected to compare their prediction performance in two different SSTs.

In this chapter, the influences of the SKE, RNG *k*-ε and Realizable *k*-ε models on the performance of a circular SST are compared using data from the Witney wastewater treatment plant (WWTP) from Burt (2010), and the Darvill WWTP from Griborio (2004). Firstly, the computational meshes with different number of cells are applied to ensure the solutions are mesh-independent. Next, the Witney SST simulation results are compared to the measured velocity and concentration profiles. The comparisons show reasonable agreement on the scale of the entire SST. For Darvill only the effluent suspended solids (ESS) concentration and RAS concentrations are available but they also agree well with the simulations. Next the validated models are used with the three different turbulence models to compare the prediction of the hydrodynamics, such as velocity and concentration patterns, especially in the inlet zone and in the near-field zone of the sludge hopper, where significant differences are observed among the three models. Additionally, the predictions of the maximum loading rate by these turbulence models are compared for the

Witney SST.

3.2. Methodology

3.2.1. The mathematical model

3.2.1.1. General information

Since the dominant hydrodynamics processes of circular SSTs take place in the radial direction, it can reasonably be simplified to a 2-D axisymmetric approach (Zhou and McCorquodale, 1992b; Vitasovic et al., 1997; Lakehal et al., 1999; Griborio, 2004; Tamayol et al., 2009; Patziger et al., 2012; Patziger and Kiss, 2015a; Patziger, 2016; Gao and Stenstrom, 2017)

Table 3-1. Loading conditions of the SSTs

	Inflow parameters			Settling parameters			Dry solids density
SSTs	MLSS g/L	RAS ratio	Q_{inlet} m^3/d	V_o m/h	r_h L/g	r_p L/g	ρ_p kg/m^3
Witney Darvill	4.187	1.09	4,372	12.64	0.340	12.25	1450
Test 1	4.6	0.80	35,986	7.71	0.390	10.00	1450
Test 2	4.3	0.97	32,529	7.71	0.390	10.00	1450
Test 3	3.6	0.79	40,726	7.71	0.390	10.00	1450

3.2.1.2. Governing equations

The equations describing 2-D, steady, turbulent, and density stratified flow in a circular SST are as follows:

Continuity equation:

$$\frac{\partial \mathrm{ru}}{\partial \mathrm{r}} + \frac{\partial \mathrm{rv}}{\partial \mathrm{y}} = 0 \tag{3.1}$$

r -Momentum component:

$$u\frac{\partial u}{\partial r}+v\frac{\partial u}{\partial y}=-\frac{1}{\rho}\frac{\partial p}{\partial r}+\frac{1}{r}\frac{\partial}{\partial r}\left[r(\vartheta+\vartheta_t)\frac{\partial u}{\partial r}\right]+\frac{1}{r}\frac{\partial}{\partial y}\left[r(\vartheta+\vartheta_t)\frac{\partial u}{\partial y}\right]+S_u \quad (3.2)$$

y -Momentum component:

$$u\frac{\partial v}{\partial r}+v\frac{\partial v}{\partial y}=-\frac{1}{\rho}\frac{\partial p}{\partial y}+\frac{1}{r}\frac{\partial}{\partial r}\left[r(\vartheta+\vartheta_t)\frac{\partial v}{\partial r}\right]+\frac{1}{r}\frac{\partial}{\partial y}\left[r(\vartheta+\vartheta_t)\frac{\partial v}{\partial y}\right]-g\frac{\rho-\rho_r}{\rho}+S_v \quad (3.3)$$

where

$$S_u=\frac{1}{r}\frac{\partial}{\partial r}\left[r(\vartheta+\vartheta_t)\frac{\partial u}{\partial r}\right]+\frac{1}{r}\frac{\partial}{\partial y}\left[r(\vartheta+\vartheta_t)\frac{\partial v}{\partial r}\right]-2\frac{\vartheta+\vartheta_t}{r^2}u \quad (3.4)$$

$$S_v=\frac{1}{r}\frac{\partial}{\partial r}\left[r(\vartheta+\vartheta_t)\frac{\partial u}{\partial y}\right]+\frac{1}{r}\frac{\partial}{\partial y}\left[r(\vartheta+\vartheta_t)\frac{\partial v}{\partial y}\right] \quad (3.5)$$

u and v are the mean velocity components in the r (radial) and y (axial) directions, respectively. p is the general pressure less the hydrostatic pressure at reference density ρ_r; ρ is the density of mixture, g is the acceleration of gravity, ϑ is the viscosity of the sludge mixture, ϑ_t is the turbulent eddy viscosity. For density-driven flows, the local fluid density is related to the local values of the sediment concentration by the following relationship:

$$\rho=\rho_r+C\left(1-\frac{\rho_r}{\rho_p}\right) \quad (3.6)$$

in which C is the SS concentration, ρ_p is dry particle density assumed to be 1450 kg/m^3 (Larsen, 1977), ρ_r is reference density (clear water) and ρ is the density of the fluid-solid mixture.

The sludge settling velocity is expressed using the Takács et al. (1991) double exponential function, which is

$$V_s=\max(0,V_o(e^{-r_p(C-C_{min})}-e^{-r_h(C-C_{min})})) \quad (3.7)$$

where V_o is Stokes velocity, r_p and r_h account for rapidly and poorly settling floc, respectively. The constant C_{min} is the concentration of on-settleable solids in the effluent of the SST. The settling parameter values are shown in Table 3.1.

The solids transport equation in the model is

$$u\frac{\partial \mathrm{C}}{\partial r}+v\frac{\partial \mathrm{C}}{\partial y}=\frac{1}{r}\frac{\partial}{\partial r}\left[r\left(\vartheta+\frac{\vartheta_{\mathrm{t}}}{\sigma_{\mathrm{r}}}\right)\frac{\partial \mathrm{C}}{\partial r}\right]+\frac{1}{r}\frac{\partial}{\partial y}\left[r\left(\vartheta+\frac{\vartheta_{\mathrm{t}}}{\sigma_{\mathrm{y}}}\right)\frac{\partial \mathrm{C}}{\partial \mathrm{y}}-r\mathrm{V_s C}\right] \quad (3.8)$$

in which C is the concentration of SS, ϑ is the viscosity of the sludge mixture, ϑ_{t} is the turbulent eddy viscosity, σ_{r} and σ_{y} are the turbulent Schmidt numbers in the r and y directions, respectively. Both of them are assumed to be 0.7 in this study. $\mathrm{V_s}$ is the sludge settling velocity.

The sludge rheological model is proposed by Bokil (1972):

$v = 1\times10^{-6}e^{1.386C}$ for $C \le 1\ \mathrm{g/L}$

and

$v = 2.9\times10^{-6}e^{0.322C}$ for $C \ge 1\mathrm{g/L}$ (3.9)

in which C is the concentration of SS.

In Reynolds-averaged Navier Stokes equations, TKE can be calculated based on the turbulence closure method. In this study, three types of turbulence closure approaches (SKE, RNG *k*-*ε* and Realizable *k*-*ε* models) are applied and compared. The major differences in these models are (1) the turbulent Schmidt numbers governing the turbulent diffusion of TKE and TDR, (2) the source term in the *ε* and, (3) the method of calculating turbulence (Fluent, 2017).

The standard *k*-*ε* model is a semi-empirical model based on the transport equations for the TKE (*k*) and TDR (*ε*) (Rodi, 1980). It is assumes that the flow is fully turbulent and the effect of molecular viscosity is negligible (Tamayol et al., 2008). The TKE and TDR are calculated from the following transport equations:

$$u\frac{\partial k}{\partial r}+v\frac{\partial k}{\partial y}=\frac{\partial}{\partial r}\left[\left(\vartheta+\frac{\vartheta_{\mathrm{t}}}{\sigma_k}\right)\frac{\partial k}{\partial r}\right]+\frac{\partial}{\partial y}\left[\left(\vartheta+\frac{\vartheta_{\mathrm{t}}}{\sigma_k}\right)\frac{\partial k}{\partial y}\right]+G_k+G_b-\rho\varepsilon \quad (3.10)$$

and:

$$u\frac{\partial \varepsilon}{\partial r}+v\frac{\partial \varepsilon}{\partial y}=\frac{\partial}{\partial r}\left[\left(\vartheta+\frac{\vartheta_t}{\sigma_\varepsilon}\right)\frac{\partial \varepsilon}{\partial r}\right]+\frac{\partial}{\partial y}\left[\left(\vartheta+\frac{\vartheta_t}{\sigma_\varepsilon}\right)\frac{\partial \varepsilon}{\partial y}\right]+C_1\frac{\varepsilon}{k}(G_k-C_3G_b)-C_2\rho\frac{\varepsilon^2}{k} \quad (3.11)$$

G_k represents the generation of TKE due to the mean velocity gradients, and G_b corresponds to the generation of TKE due to buoyancy.

$$G_k=\vartheta_{\mathrm{t}}\left[2\left(\frac{\partial u}{\partial r}\right)^2+2\left(\frac{\partial v}{\partial y}\right)^2+2\left(\frac{u}{r}\right)^2+\left(\frac{\partial u}{\partial y}+\frac{\partial v}{\partial r}\right)^2\right] \quad (3.12)$$

$$G_b=-g\frac{\vartheta_{\mathrm{t}}}{\sigma_t}\frac{\partial \rho}{\partial y} \quad (3.13)$$

The turbulent viscosity, ϑ_{t}, is then determined as a function of TKE and TDR by

$$\vartheta_{\mathrm{t}}=C_\mu\frac{k^2}{\varepsilon} \quad (3.14)$$

The dimensionless empirical constants are given the standard values suggested by (Rodi, 1993). $C_\mu=0.09$, $C_1=1.44$, $C_2=1.92$, $\sigma_k=1.0$, and $\sigma_\varepsilon=1.3$. The value of the empirical constant C_3 related to the buoyancy source term G_b depends on the flow situation (Lakehal et al., 1999). Different researches applied different C_3 values in their specific cases (Lyn et al., 1992; Dahl et al., 1994; Lakehal et al., 1999; Gong et al., 2011; Ramin et al., 2014). Rodi (1993) suggested that C_3 is in the range of 0.8–1.0 for stable stratification that prevails in SSTs and tends toward zero for unstable stratification.

The RNG *k*-*ε* model is derived using a statistical technique called the "renormalization group (RNG) theory''. The analytical derivation results in a model with constants different from those in the SKE model, and additional terms and functions in the transport equations for TKE and TDR. The RNG *k*-*ε* model has a similar form to the SKE model:

$$u\frac{\partial k}{\partial r}+v\frac{\partial k}{\partial y}=\frac{\partial}{\partial r}\left(\alpha_k\mu_{eff}\frac{\partial k}{\partial r}\right)+\frac{\partial}{\partial y}\left(\alpha_k\mu_{eff}\frac{\partial k}{\partial y}\right)+G_k+G_b-\rho\varepsilon \quad (3.15)$$

and:

$$u\frac{\partial \varepsilon}{\partial r}+v\frac{\partial \varepsilon}{\partial y}=\frac{\partial}{\partial r}\left(\alpha_{\varepsilon}\mu_{eff}\frac{\partial \varepsilon}{\partial r}\right)+\frac{\partial}{\partial y}\left(\alpha_{\varepsilon}\mu_{eff}\frac{\partial \varepsilon}{\partial y}\right)+C_1\frac{\varepsilon}{k}(G_k-C_3G_b)-C_2\rho\frac{\varepsilon^2}{k}-R_{\varepsilon} \quad (3.16)$$

In these equations, G_k and G_b are the same as in the SKE model. The quantities α_k and α_{ε} are the inverse effective Prandtl numbers:

$$\left|\frac{\alpha-1.3929}{\alpha_o-1.3929}\right|^{0.6321}\left|\frac{\alpha+2.3929}{\alpha_o+2.3929}\right|^{0.3679}=\frac{\mu_{mol}}{\mu_{eff}} \quad (3.17)$$

where α_o=1.0.

The main difference between RNG and SKE models appears in the additional term R_{ε} in the TDR equation, which is more responsive to the effects of rapid strain and streamline curvature than the SKE model and may have a superior performance in the simulation of sedimentation tank model with a complex inlet geometry. The definition of the R_{ε} and its effects on the prediction of the TDR are illustrated in the ANSYS Fluent Theory Guide, equations 4.48 to 4.50 (Fluent, 2017). The dimensionless model constants are:

$C_1 = 1.42$, $C_2 = 1.68$

Another modified *k-ε* model is the Realizable *k-ε* model. It involves a modified transport equation for the TDR, which has been derived from an exact equation for the transport of the mean-square vorticity fluctuation. Compared with SKE, Realizable *k-ε* model gives a much more accurate prediction of Reynolds stresses for flow with rotation and recirculation (Das et al., 2016). The modeled transport equations for TKE and TDR in the Realizable *k-ε* model are

$$u\frac{\partial k}{\partial r}+v\frac{\partial k}{\partial y}=\frac{\partial}{\partial r}\left[\left(\vartheta+\frac{\vartheta_t}{\sigma_k}\right)\frac{\partial k}{\partial r}\right]+\frac{\partial}{\partial y}\left[\left(\vartheta+\frac{\vartheta_t}{\sigma_k}\right)\frac{\partial k}{\partial y}\right]+G_k+G_b-\rho\varepsilon \quad (3.18)$$

and:

$$u\frac{\partial \varepsilon}{\partial r}+v\frac{\partial \varepsilon}{\partial y}=\frac{\partial}{\partial r}\left[\left(\vartheta+\frac{\vartheta_t}{\sigma_\varepsilon}\right)\frac{\partial \varepsilon}{\partial r}\right]+\frac{\partial}{\partial y}\left[\left(\vartheta+\frac{\vartheta_t}{\sigma_\varepsilon}\right)\frac{\partial \varepsilon}{\partial y}\right]-C_1\frac{\varepsilon}{k}C_3G_b+\rho C_1S\varepsilon-\rho C_2\frac{\varepsilon^2}{k+\sqrt{\vartheta\varepsilon}} \quad (3.19)$$

where

$$C_1=\max\left[0.43,\frac{\eta}{\eta+5}\right],\eta=\frac{Sk}{\varepsilon} \quad (3.20)$$

The turbulent viscosity has the same form as in SKE model:

$$\vartheta_{\mathrm{t}}=C_\mu\frac{k^2}{\varepsilon} \quad (3.21)$$

However, C_μ is no longer constant and is a function of the mean strain and rotation rates, the angular velocity of the system rotation, and the turbulent fields.

Table 3-2. Dimensions of SSTs

Geometry	Values	
	Witney	Darvill
Diameter of the clarifier	18.3 m	35.0 m
Surface area	263 m^2	962 m^2
Radius of the inlet pipe	0.4 m	0.5 m
Depth of side wall	1.8 m	4.1 m
Tank floor slope	7.5%	10%
Hopper floor slope	60°	/
Stilling/Center well diameter	5.49 m	6.0 m
Stilling/Center well depth	0.8 m	2.7 m
Stamford baffle depth	/	0.6m
Stamford baffle length	/	1.7m
Outboard launder	Peripheral launder	Peripheral launder

3.2.1.3. Boundary conditions

Velocity inlet boundary condition is applied to inlet and sludge bottom boundaries, which assumes a uniform distribution of all the dependent variables at the boundary face. For the surface outlet, a pressure outlet boundary condition is applied, which assumes a uniform pressure and zero-gradient for all transport variables. Instead of estimating the TKE and TDR, turbulent intensity

and hydraulic diameter are used as the turbulence specification method on the inlet and outlet boundaries. For the free ambient water surface, the rigid-lid approximation for all velocity components with full slip shear condition is assumed (Wang et al., 2008; Tarpagkou and Pantokratoras, 2013). And the free surface boundary is treated as a symmetry condition. The solid boundaries are specified as stationary walls with a no slip-shear condition and standard wall function is used with the turbulence models.

3.2.1.4. Solution procedure

The governing equations are numerically solved by the commercial CFD code ANSYS Fluent v.17.2. A first-order upwind method is used for interpolation of variables to cell faces for the convective terms, whereas diffusive terms are discretized using second order central differencing. Pressure-velocity coupling is achieved using the SIMPLE method.

The solution procedures which are accomplished in meshes with different grid numbers can be summarized in the following steps:

(1) The flow filed with pure water is firstly solved in the absence of turbulence. Convergence is reached when normalized residuals are less than 10^{-4};

(2) The converged solution is interpolated into the pure water flow field, coupled with SKE model to calculate the steady state turbulence flow field. None of the buoyancy damping terms to the TKE and TDR are included. Convergence is reached when normalized residuals are less than 10^{-4};

(3) The solids transport equation defined in the User Define Scalar is coupled to the model;

(4) The buoyancy damping term (G_b) is included to the TKE equation to describe the turbulent and density stratified flow;

(5) The buoyancy damping term (G_b) associated with C_3 is added to the TDR equation to complete the procedure.

In the steps 3 to 5, convergence is achieved when the following three criteria are all achieved:

(1) Normalized residuals are less than 10^{-3} or the solution no longer changes with subsequent iterations;

(2) The net flux imbalance is less than 1% of the smallest flux through the domain boundary;

(3) Other monitored key physical quantities no longer change with subsequent iterations.

The velocity profiles as a function of depth for Witney and Darvill SSTs, are calculated from meshes with different grid numbers at three radial locations. After achieving grid independence tests, the second-order upwind method is used to calculate a more accurate solution for the final step described in the previous solution procedures.

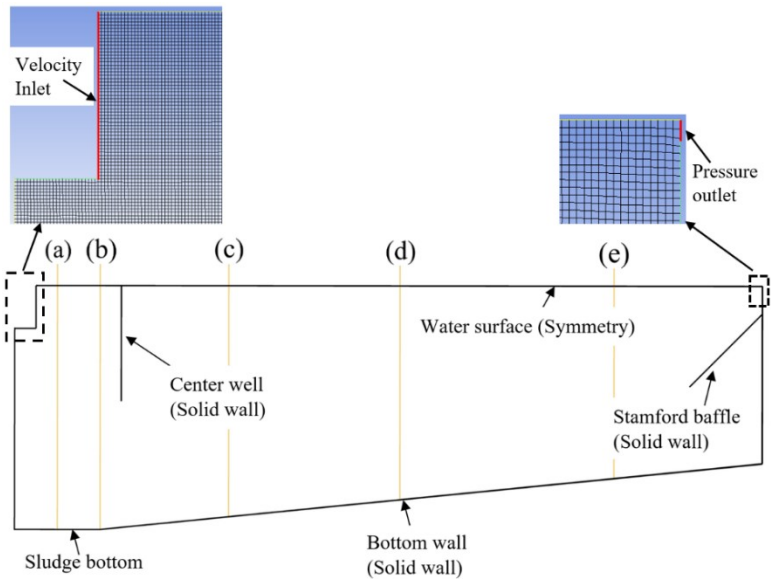

Figure 3-2. Darvill SST Diagrams with representative computed locations and boundary conditions. (a)-(e) refer to the radial locations for the grid independent tests and model comparisons.

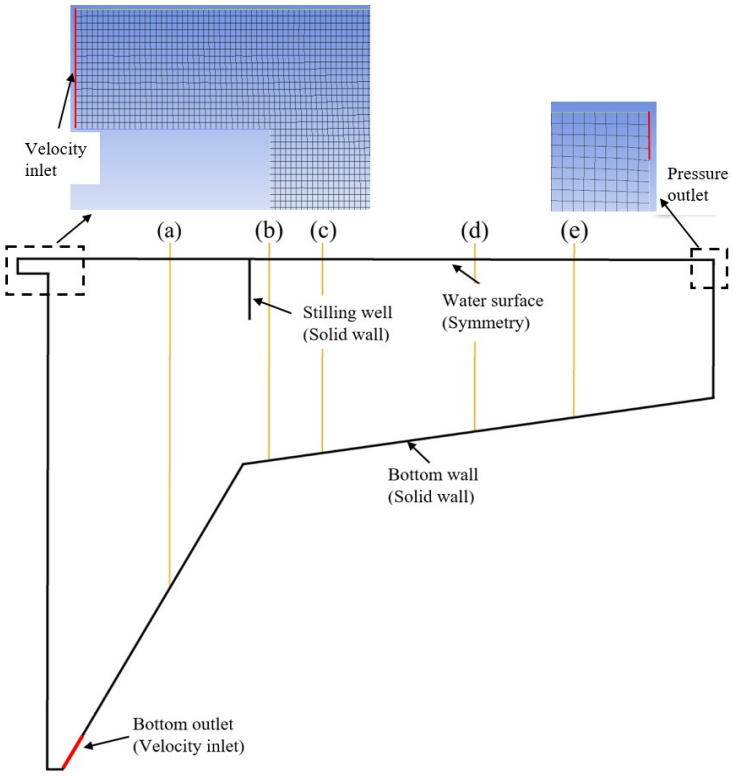

Figure 3-3. Witney SST Diagrams with representative computed locations and boundary conditions. (a)-(e) refer to the radial locations for the grid independent tests and model verification.

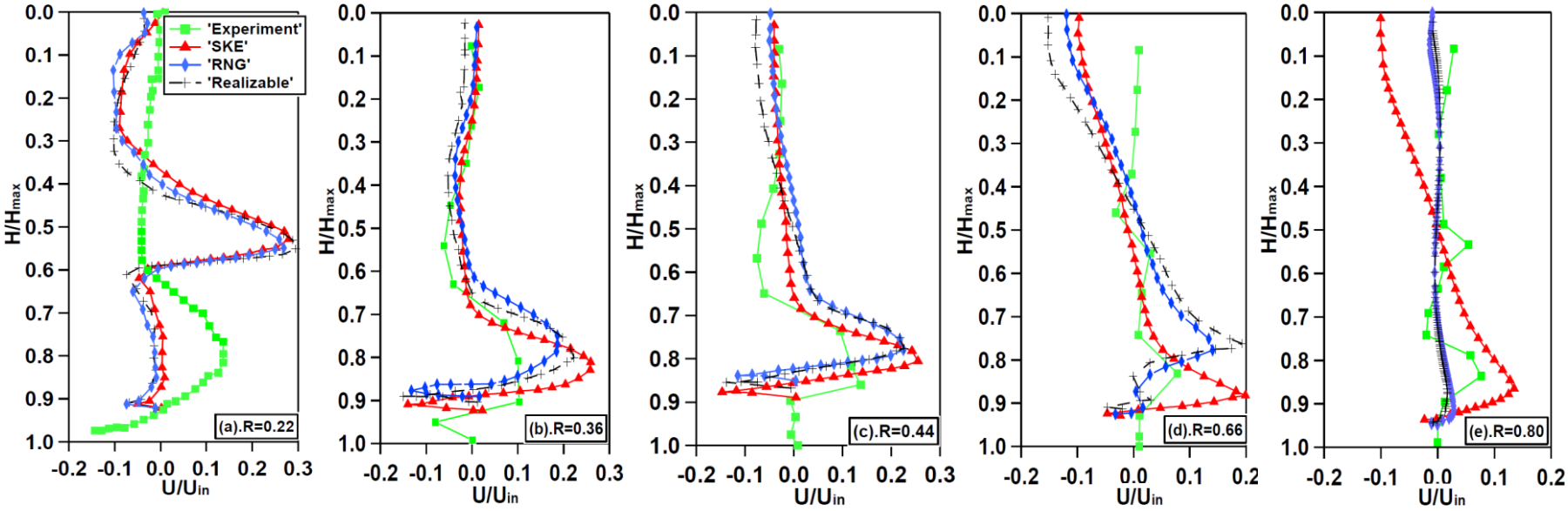

Figure 3-4. Comparison of radial velocity profiles by various turbulence models with field measurements for Witney SST. R is the ratio between the radial distance of the vertical measurement location to the radius of tank.

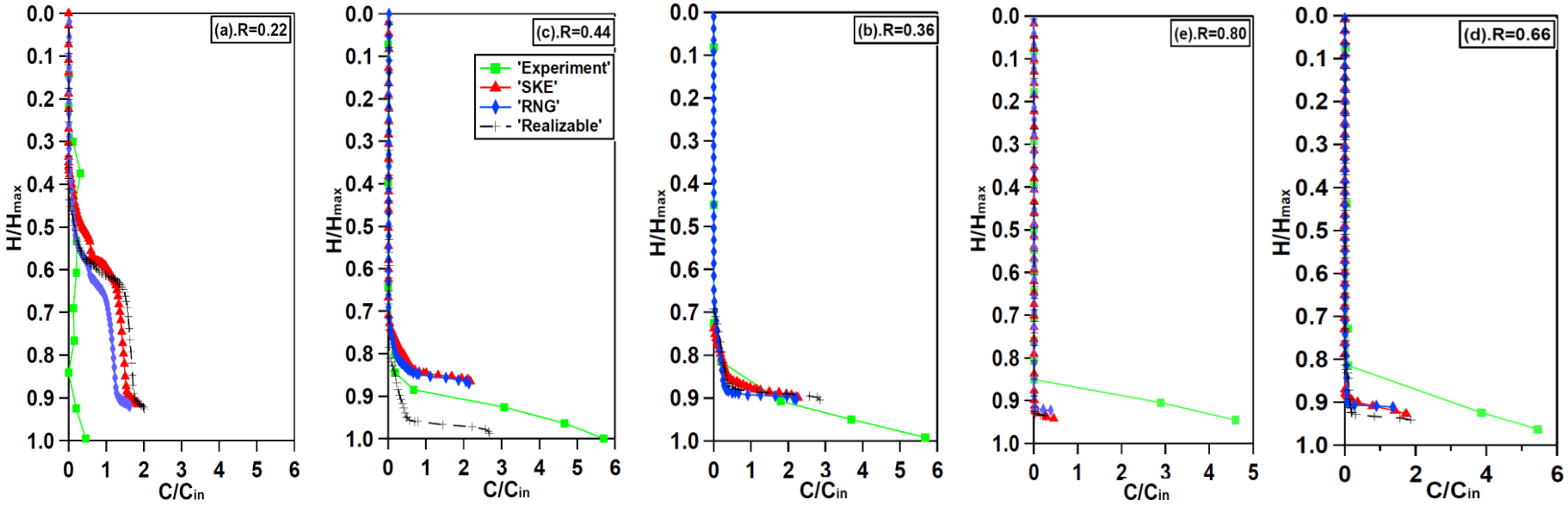

Figure 3-5. Comparison of concentration profiles by various turbulence models with field measurements for Witney SST. R is the ratio between the radial distance of the vertical measurement location to the radius of tank.

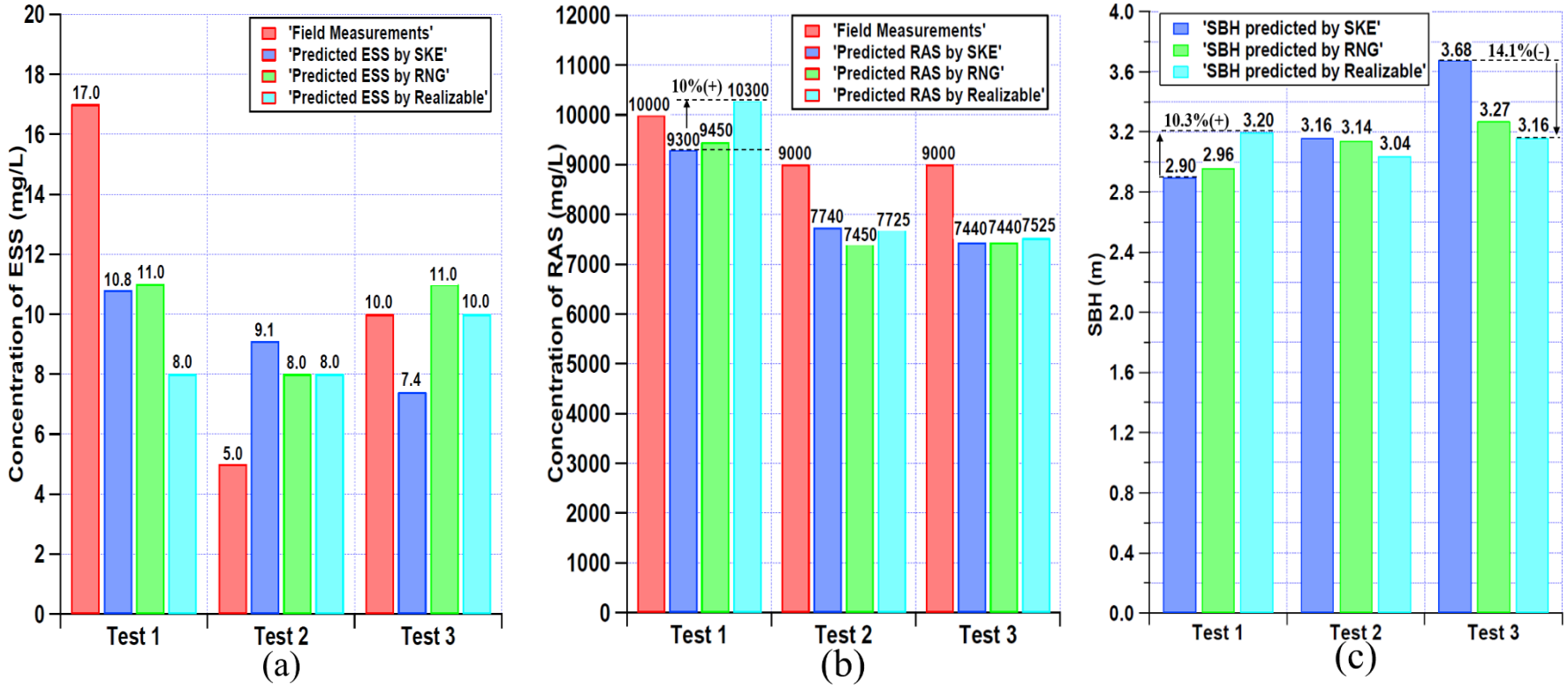

Figure 3-6. Predictions of the performance indicators with SKE, RNG *k-ε*, Realizable *k-ε* turbulence models and field data for Darvill SST.

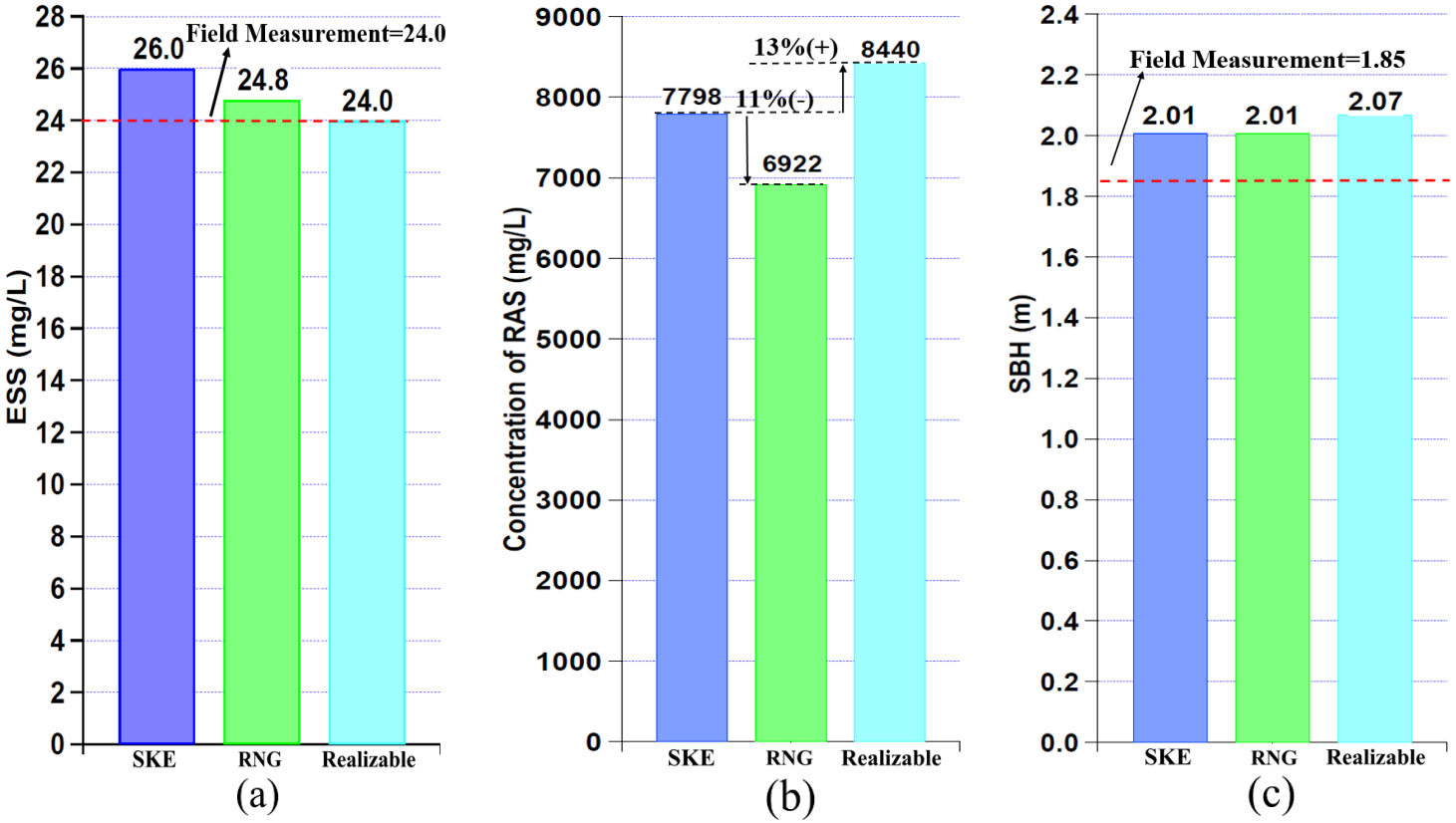

Figure 3-7. Comparison among the predictions of the performance indicators with SKE, RNG *k-ε*, Realizable *k-ε* turbulence models and field data for Witney SST.

3.2.2. Geometry and meshing

The geometries and meshes are generated using Ansys Meshing v.17.2. The general geometry of the Witney SST with the computational mesh (Fine mesh) that is used in the simulations after achieving grid independent test consists of 428,000 cells. In order to ensure that the solution is mesh-independent, three additional meshes are used, one coarse consisting of 123,096 cells, a medium one consisting of 225,284 cells and a finer one consisting of 901,136 cells. The results show that the difference between the prediction of the coarse mesh to other three finer (medium, fine and finer) meshes is significant, but the difference among the prediction of the three finer meshes is negligible. Therefore, the solution from the mesh of 428,000 cells is considered mesh-independent.

The general geometry of the Darvill SST with the computational mesh that is used in the simulations after achieving grid independent test consists of 218,700 cells. In order to ensure that the solution is mesh-independent, two additional finer meshes are used, one consisting of 389,428 cells and another one consisting of 874,800 cells. The results show that the difference among the prediction of these three meshes is negligible. Therefore, the solution from the mesh of 218,700 cells is considered mesh-independent and has the benefit of increased computational speed.

The general geometry of the Witney and Darvill SSTs are displayed in Figures. 3.2 and 3.3, respectively. Since the outlet is extremely small compared with inlet, the grids near the outlet zone are enlarged to show the outlet boundary condition clearly. The dimensions of the Witney and Darvill SSTs are shown in Table 3.2.

3.2.3. Model verification

Since only the measurements of the velocity and concentration profiles for the Witney SST are available in Burt (2010), they are used to compare the model predictions for the Witney SST. The comparisons of the velocity and concentration profiles along the SST radial direction between the model predictions and the field measurements are shown in Figures. 3.4 and 3.5, respectively. However, the predictions of Darvill SST are compared with the observed performance indicators, such as ESS and RAS concentrations, of three tests in Ekama and Marais (2002) and Griborio (2004). The investigated loading conditions for Witney and Darvill SSTs are shown in Table 3.1.

Figures. 3.4 and 3.5 show the velocity and concentration profiles comparison along the radial direction of Witney SST between the model predictions and the field measurements, respectively. In Figure. 3.4, the overall stream curvatures outside of the stilling well are reasonably predicted, but less well predicted inside the stilling well. Figure. 3.5 indicates that the predictions of the bed transition (0.85 g/L contour followed by Burt (2010)) agree reasonably well with the measurements, but sludge blanket concentration is less well predicted.

3.3. Results and discussion

3.3.1. Performance indicators

Comparisons among the predictions of the performance indicators by the different turbulence models and the field data in Darvill and Witney SSTs are shown in Figures. 3.6 and 3.7, respectively. Figures. 3.6 and 3.7 show that the predictions of ESS by the three models are quite similar. All the models show fair agreement with the field data of the Darvill SST and show good

agreement with the field data of the Witney SST.

For the RAS concentration, Figure. 3.6 shows that all the turbulence models give a similar prediction of RAS concentration and show reasonable agreement with the field data in Tests 2 and 3. However, in the Test 1, Realizable k-ε model gives a 10% higher of RAS concentration prediction than the SKE model. Additionally, the difference among the prediction of RAS concentration for the Witney SST is also significant as shown in Figure. 3.7.

The predictions of SBH by the three turbulence models for the Darvill SST are also varied. The largest prediction difference is shown in Test 3, where the Realizable k-ε produces a 14.1% lower SBH than the prediction by SKE.

The predicted RAS concentration in the local area of inlet zone, as shown in Figures. 3.6 and 3.7, and the SBH in Figure. 3.6, show remarkable disagreement, indicating that the influence of turbulence is important.

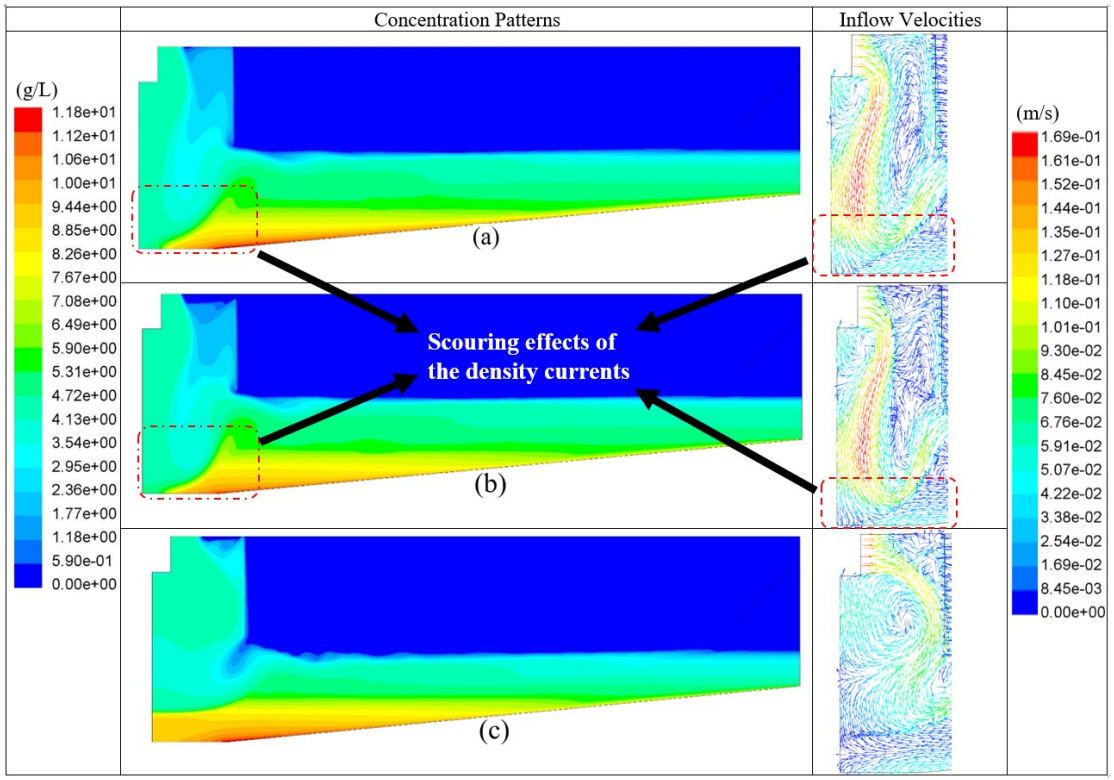

Figure 3-8. Flow and concentration contours for the Test 1 of Darvill SST predicted by (a) SKE, (b) RNG *k*-*ε* and (c) Realizable *k*-*ε* turbulence models.

3.3.2. Velocity and concentration contours for Darvill SST

Figure. 3.8 (a-c) presents the predictions of the velocity magnitude vectors in the inlet zone and concentration contours by the SKE (a), RNG *k*-*ε* (b) and Realizable *k*-*ε* (c) models for the Test 1 of Darvill SST, respectively. It shows that the predicted turbulent flow contours by the SKE and RNG *k*-*ε* models are similar. Both models show the influent flows into the center well immediately turns sharply downward without impinging the baffle, and then changes its direction towards the baffle in the near-field zone above the sludge hopper and finally flows as a horizontal jet from the bottom lip of the baffle outside the inlet zone. Additionally, both SKE (a) and RNG *k*-*ε* (b) models

predict the formation of a small eddy below the inlet port and a large eddy between the downward jet and baffle, from the surface to the turning point of jet at the bottom.

However, the flow contour predicted by Realizable k-ε inside the inlet zone is totally different from the simulation result using SKE and RNG k-ε turbulence models. The Realizable k-ε model predicts that the horizontal inflow jet impinges on the center of the baffle and is then forced in the opposite direction before reversing directions to form a horizontal jet from the lip of the baffle outside the inlet zone. Additionally, Realizable k-ε (c) predicts a larger eddy below the inlet port and a compressed eddy in the triangulated area bounded by the surface, baffle and downward jet. Moreover, the region of the high downward flow (shown as red in Figure. 3.8 a, b) predicted by the Realizable k-ε is much smaller than the region predicted by the other two models.

The prediction of the magnitude and the location of the peak velocity is also different. Results of the Realizable k-ε also show that the location of the peak velocity (0.131m/s) is at the inlet port, while both SKE (0.149m/s) and RNG k-ε (0.183m/s) models predict it is at the center of the core of the high downward flow.

Figure. 3.9 presents the quantitative comparisons of the velocity magnitude of the three models inside and outside the inlet zone for Test 1 of Darvill SST. Consistent with the qualitatively comparisons in Figure. 3.8, SKE and RNG k-ε models have similar velocity magnitude distribution from the surface to bottom, although the peak velocity prediction and the vertical position of the peak velocity have some small differences. However, large disagreement of the velocity magnitude distribution can be found between Realizable k-ε and SKE/RNG k-ε in the inlet zone. Outside of

the inlet zone, the difference reduces gradually along the radial direction as the energy is dissipated.

The flow contours predicted by the SKE and RNG k-ε models are similar which creates similar concentration profiles. In both cases the concentrations in inlet, outlet, main settling and bottom sludge zones and the SBH are all similar. However, the velocity and concentration predictions of SKE and RNG k-ε models of the sludge in the near-field zone of the sludge hopper are quite different than predicted by the Realizable k-ε model. The differences in concentrations predicted by the Realizable k-ε are caused by the high downward velocities inside the center well, as shown in Figure. 3.8c. The magnitude and pattern of the velocities near the middle of the center well are quite different. The downward velocity predicted by the Realizable k-ε model at R=1.0m is lower and does not closely approach the sludge hopper, as observed in the SKE and RNG k-ε results. Figure. 3.8 shows that the concentration above the sludge hopper ranges from 4 to 11 g/L (green to red) for the SKE and RNG k-ε model results, while the Realizable k-ε predictions for concentrations in this area range from 8 to 11 g/L (yellow-orange to red).

The Realizable k-ε model results show a similarity of the overall concentration contour within the SST but produces a more homogeneous, highly concentrated sludge blanket in the near-field zone of the sludge hopper and a shallower sludge blanket (Figure. 3.8c), as compared to the SKE and RNG k-ε results. This is because the high downward flow predicted by SKE and RNG k-ε in the inlet zone swirls up the settled sludge, which results in drifting of the settled sludge particles and insufficient transport towards sludge hopper (Patziger et al., 2016); therefore, elevating the entire sludge blanket.

3.3.3. Velocity contour for Witney SST

Figure. 3.10 indicates that these three turbulence models predict the similar flow contour on the scale of the entire Witney SST; therefore, the similar concentration contour. All the models predict that the inflow turns sharply downward as a density current without reaching the stilling well. However, the SKE model predicts a 15.8% longer length of the bottom horizontal jet flow than the prediction of the RNG and Realizable k-ε models, which indicates the SKE model predicts a stronger horizontal jet than the prediction of the RNG and Realizable k-ε models. Also, the Figure. 3.4(b-e) shows the prediction of the bottom horizontal jet by SKE model is deeper and closer to the sludge blanket surface. Since the strong and deep horizontal flow jet can easily drift and swirl up the settled sludge (Patziger, 2016), the SKE model predicts a higher ESS than the prediction of the RNG and Realizable k-ε models (shown in Figure. 3.7a). As the increase of the influent rate, the SKE model may predict the failure of SST when the RNG and Realizable k-ε models still predict the well-operated SST.

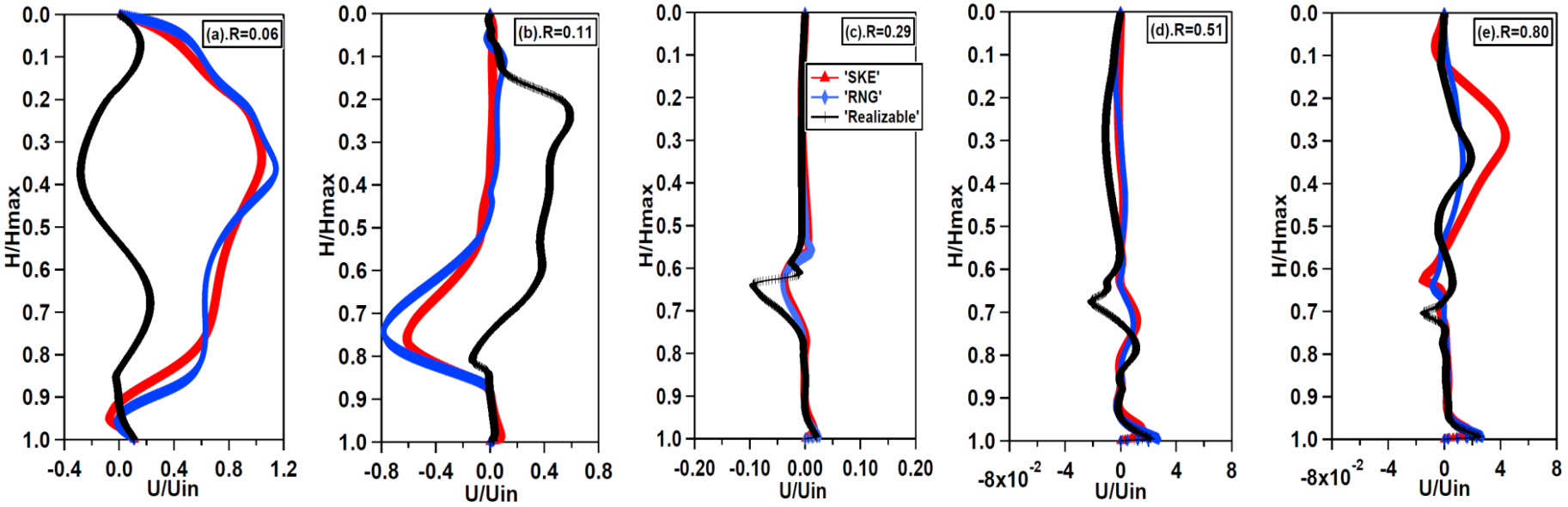

Figure 3-9. Comparison among the predictions of radial velocity profiles (m/s) by various turbulence models for the Test 1 of Darvill SST. R is the ratio between the radial distance of the vertical measurement location to the radius of tank.

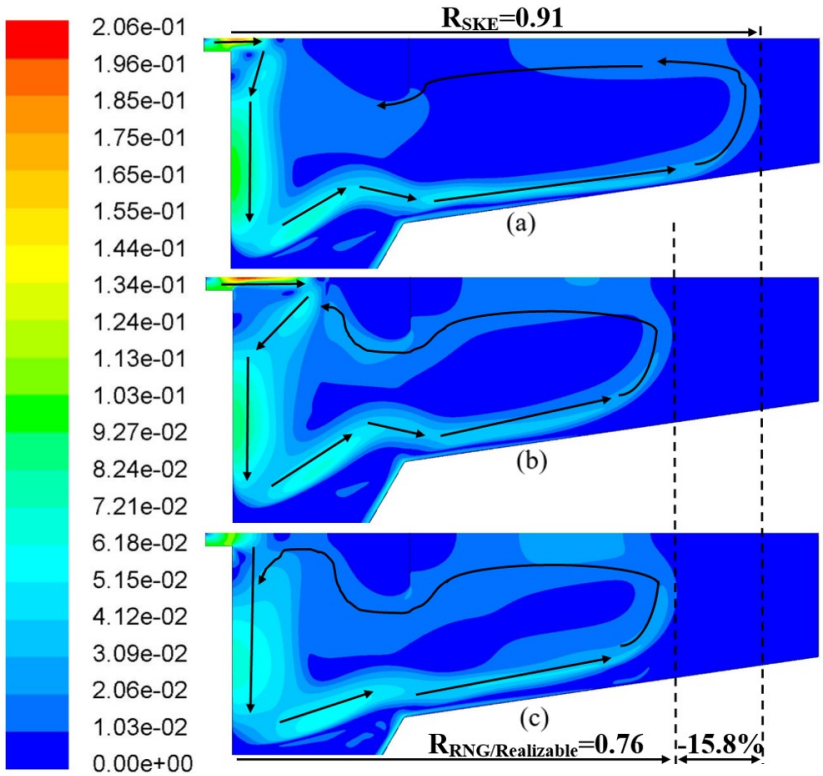

Figure 3-10. Predictions of flow patterns (m/s) for the Witney SST by the turbulence models: (a) SKE model, (b) RNG model, (c) Realizable *k*-*ε* model.

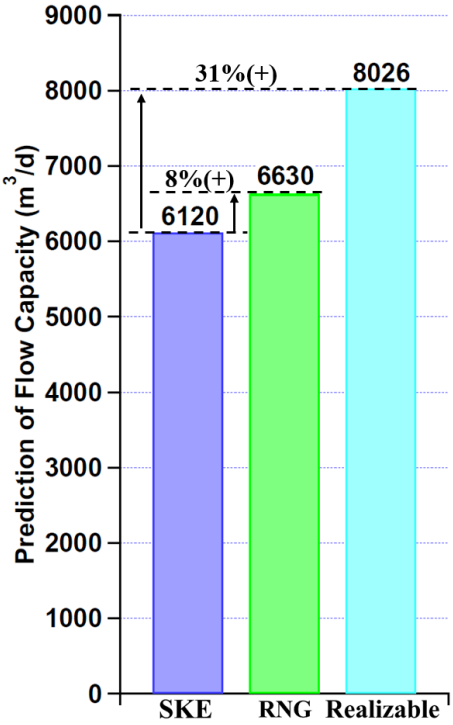

Figure 3-11. Prediction of the flow capacity by the SKE, RNG and Realizable *k*-*ε* turbulence models.

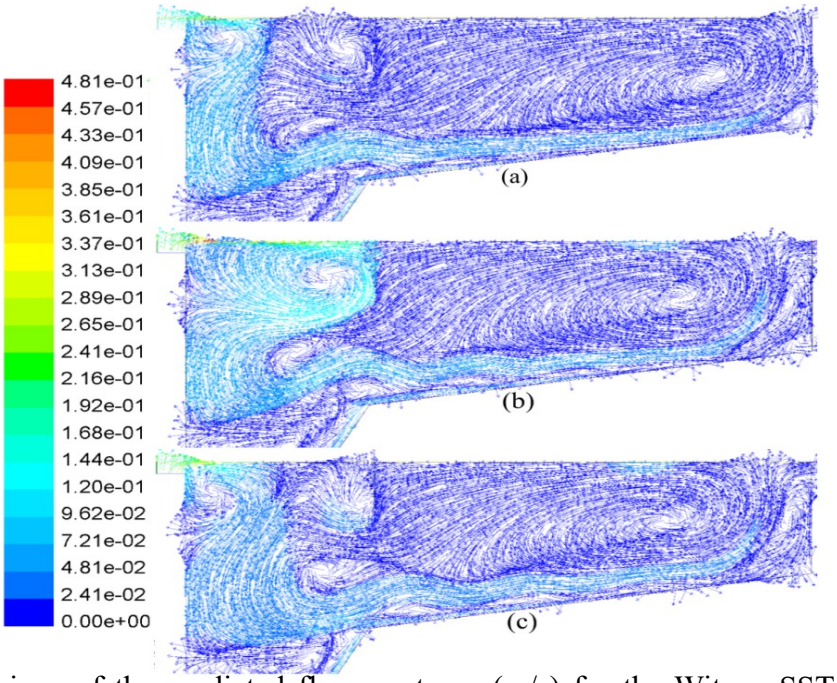

Figure 3-12. Comparison of the predicted flow contours (m/s) for the Witney SST under the maximum hydraulic loading condition: (a) SKE model, (b) RNG model, (c) Realizable *k*-*ε* model.

Table 3-3. Prediction similarity and difference by these turbulence models under the original and maximum loading rates

	Velocity and concentration profiles under the original loading rate	Flow capacity	Velocity and concentration profiles under the maximum loading rate
SKE	+	-	+
RNG	+	+	-
Realizable	+	+	+

Same symbol in a column indicates the prediction similarity by these turbulence model.

3.3.4. CFD stress tests for the Witney SST

3.3.4.1 Predictions of the flow capacity

In order to compare the prediction of the Witney SST capacity by these turbulence models, stress tests are simulated by increasing the influent rate. The failure of the SST is accepted as ESS>30 mg/L. MLSS and RAS ratio keep constant. Figure. 3.11 shows the prediction of the ESS under the original influent rate and the limiting influent rate by these turbulence models. The limiting influent rate (or the maximum loading rate) predicted by the SKE model is 6120 m^3/d (surface overflow rate, SOR= 0.464 m/h) when ESS reaches 30 mg/L, while the predictions of the limiting influent rates are 6630 (SOR=0.502 m/h) and 8026 m^3/d (SOR=0.608 m/h), respectively, by the RNG and Realizable k-ε models. The limiting influent rates predicted by the RNG and Realizable k-ε models are about 8% and 31% higher than predicted by the SKE model, respectively. This indicates that the turbulence model selection strongly influences the prediction of the Witney SST's flow capacity.

3.3.4.2 Comparison of the predicted velocity contours under the maximum loading rate

Figure. 3.12 shows the prediction of the velocity contours by these turbulence models when

their prediction of the ESS reaches 30 mg/L. The RNG model does not predict the downward density current that the other two models predict as shown in Figure. 3.10. At lower loading rates, simulations with all three models predict similar flow contours. In Figure. 3.12, the SKE and Realizable k-ε models similarly predict the density currents from the inlet without reaching the stilling well, while the RNG model predicts a strong horizontal jet impinging on the baffle.

Based on the similarity and difference predicted by these turbulence models under the original and maximum loading rates, especially in the inlet zone, Table 3.3 shows a diagnostic approach to select the most accurate turbulence model. The same symbol in a column indicates that the predictions of the turbulence models are similar. The first column indicates that the predictions of the velocity and concentration fields by these turbulence models are all similar under the original loading rate and one cannot decide the most accurate turbulence model. Next, the second column shows that the predictions of the flow capacity by the SKE model are significantly different from the RNG and Realizable k-ε models. If the experimental data show the actual maximum flow capacity is close to the prediction of the SKE model, the SKE model is the optimal turbulence model. Otherwise, the velocity and concentration profiles under the maximum loading rate, especially in the inlet zone, need to be measured to select the optimal model from the RNG and Realizable k-ε models.

3.4. Conclusions

In this chapter, a Fluent-based 2D axisymmetric numerical model is used to analyze the hydrodynamics and turbulent flow, such as flow and concentration patterns of two different SSTs.

The previous numerical studies did not study the effect of different turbulent models on the turbulent flow and concentration pattern in the inlet zone, where they can have major impacts. In the present work numerical simulations with three advanced turbulent models (SKE, RNG k-ε and Realizable k-ε) are performed on two different SSTs to study the influence of turbulent models on the flow and concentration patterns and operation parameters, such as ESS, RAS concentration and SBH. Also, the predictions of the SST capacity are compared using the three turbulence models.

For the case studied by various turbulence models, the following conclusions are made:

- Turbulence model selection can have a strong influence on the prediction of hydrodynamics of an SST, such as flow and concentration patterns. The difference is remarkable inside the inlet zone, where the high flow energy is dissipated, resulting in high turbulence.
- The remarkable different predictions of the hydrodynamics inside the inlet zone cause significant differences (more than 10%) in predicting RAS concentration and SBH, which can greatly influence the operation of sludge return concentration.
- Turbulence model selection also can have a strong influence on the prediction of flow capacity. The RNG and Realizable k-ε models predict 8% and 31% higher of the flow capacity than the SKE model, respectively, for the Witney SST.
- The significant difference among the predictions of the turbulence models inside the inlet zone of Darvill SST under the original loading rate and of Witney SST under the maximum

loading rate suggest that more observations are required in this area for model verification and turbulence model selection.

The turbulence models as shown with these simple geometries have a strong influence on the prediction of the SST hydrodynamics inside the inlet zone. For geometries with complex inlet baffling structures, such as the LA or tangential energy dissipating inlet structure which cannot be easily simplified to a 2-D axisymmetric mesh, it is especially necessarily to study the influence of the turbulence model. Such complex geometries use will likely require 3-D meshes to better predict SST performance, and turbulence model selection should have a major impact.

Future work should include non-steady state simulations to better understand the hydrodynamics predicted by these turbulence models during transient conditions. Other advanced turbulence models, such as the large eddy simulation model by Al-Sammarraee and Chan (2009), should also be considered in the future turbulence model comparisons.

Chapter 4 Evaluation of turbulence and inter-phase mass diffusion assumptions on the performance of a secondary settling tank

4.1. Introduction

In conventional wastewater treatment plants (WWTPs), bioreactors are connected to secondary settling tanks (SSTs) to remove organic matter and reduce nutrients such as nitrogen and phosphorus by gravity sedimentation (Ramin et al., 2014). Secondary settling tanks (SSTs), also known as sedimentation tanks or secondary clarifiers, have two different functions: clarification and thickening (Parker, 1983). Clarification is used to separate the suspended biomass from the effluent. Thickening is used to concentrate the sludge in order to recycle or dispose of it in less volume (Gao and Stenstrom, 2017). In SSTs the clarification process happens in the upper layer while thickening occurs near the bottom. This results in an effluent with a low concentration of suspended solids (SS) flowing out from the top and a second stream with highly concentrated sludge from the bottom (Li and Stenstrom, 2014).

Previously, design procedures for SSTs were more empirical, which were based on hydraulic criteria such as surface overflow rate (SOR) and hydraulic retention time (HRT) (Coe, 1916). Without understanding the internal flow field and solids distribution, SSTs' performance can suffer unanticipated fluctuations, which may reduce performance and increase the risks of failure. Therefore, computational fluid dynamics (CFD) models of SSTs have been developed to illuminate the 'black box' and to understand the different influential processes in the SSTs (Larsen, 1977; Imam et al., 1983; Zhou and McCorquodale, 1992b).

Since flow in SSTs is driven by density, experiments have been performed to understand the nature of the flow in SSTs, and different mathematical models have been proposed to describe this phenomenon (Devantier and Larock, 1986; 1987; Stamou et al., 1989; Lyn et al., 1992; Zhou and McCorquodale, 1992a; c; Lakehal et al., 1999). Larsen (1977) was the pioneer in the CFD study of SSTs and set the framework of the CFD study for the future SST research. Since then, research has mostly focused on (1) improving the prediction accuracy of the CFD models by understanding the hydrodynamics of the SSTs (Tarpagkow et al.; Adams and Rodi, 1990; Lyn et al., 1992; Zhou and McCorquodale, 1992b; Lakehal et al., 1999); (2) optimizing the operation (e.g. inflow rate, inlet mixed liquor suspended solids (MLSS), returned activated sludge (RAS) ratio) and internal geometry of the SSTs (Zhou and McCorquodale, 1992a; Krebs et al., 1995; Deininger et al., 1996; Vitasovic et al., 1997; Griborio, 2004; Patziger, 2016).

Devantier and Larock (1986) were the first researchers to study the effects of buoyancy term (G_b) in the standard k-ε turbulence model (SKE). However, because of the strong local numerical instabilities along the reaction baffle, the flow in the inlet zone was not modeled and the opening under the bottom baffle lip was chosen as the inlet boundary. Additionally, due to a coarse mesh caused by limited computational storage, the SKE model was locally divergent. Also, due to the convergence difficulty for the flow with high mixed liquor suspended solids (MLSS) concentration, the modeled inlet concentration of solids was very low (only 750 mg/L). In the follow-on study, DeVantier and Larock (1987) overcame these difficulties by decoupling the buoyancy term. This improved the simulation results but ignored the buoyancy effects on the

turbulence model.

Zhou and McCorquodale (1992a; b) also ignored the buoyancy term in turbulence model when analyzing the hydrodynamics of SSTs. However, the modeled inlet concentration of MLSS in their studies was low (only 1400 mg/L). Hence, their simulation results may be limited to SSTs operating with low inlet solids concentrations.

Vitasovic et al. (1997) applied a two-dimensional (2D) model to study the effects of surface overflow (SOR) rate and to optimize the internal structure of the SST. The buoyancy term was also ignored in their turbulence model. Some of their predictions were opposite to the simulation results predicted by the Quasi-3D (Q3D) model in Gao and Stenstrom (2017).

The latest CFD SST model decoupled the buoyancy term in turbulence model was in Tamayol et al. (2009). In this study, effects of Froude (Fr) and Reynolds (Re) numbers on the flow field and optimal baffle location were studied. However, no calibration procedure of their model was reported; therefore, the reliability of their model results was doubtful.

More recent studies, essentially after the 1990s, have included the buoyancy term in their models, and many have compared their simulation results with field data (Lyn et al., 1992; Dahl, 1993; Lakehal et al., 1999; Xanthos et al., 2010; Shahrokhi et al., 2013; Ramin et al., 2014). However, none have compared simulation results with and without coupling the buoyancy term. Therefore, none of the previous studies confirmed the need to couple the buoyancy term in turbulence model. Also, the buoyancy coefficient (C_3) applied in the turbulent dissipation rate (TDR) equation varied widely among the studies. Interpreting the results are further complicated

using a wide range of the turbulent Schmidt numbers (σ_c). Table 4.1 shows the wide range of buoyancy coefficients and turbulent Schmidt numbers used previously.

In this chapter, sensitivity tests using the Realizable *k-ε* model are performed to understand (1) the necessity of coupling the buoyancy term in turbulence kinetic energy (TKE) equation, and (2) the effects of two model parameters (the coefficient of buoyancy term (C_3) in the turbulent dissipation rate (TDR) equation and the turbulent Schmidt number (σ_c) in the sludge transport equation). Firstly, simulation results are presented by coupling and decoupling the buoyancy term in the TKE equation and compared. Next, the effects of inlet MLSS concentration and sludge settling properties are illustrated without coupling the buoyancy term in TKE equation. Finally, the effects on the hydrodynamics of SST of varying the C_3 and the σ_c are compared.

Table 4-1. Applications of the two model parameters: (1) coefficient of buoyancy term (C_3) in TDR equation; (2) turbulent Schmidt number in sludge transport model in the literature

Turbulent Schmidt Number		References
σ_y	σ_r	
0.5	0.5	(Stamou et al., 1989)
0.7	0.7	
1.0	1.0	
1.0	0.5	(Zhou and McCorquodale, 1992a)
1.0	1.0	(Zhou and McCorquodale, 1992c)
0.5	1.0	
1.0	1.0	(Dahl, 1993)
0.7	0.7	(Lakehal et al., 1999)
0.5-0.9	0.7	(Saffarian et al., 2010)
1.0	1.0	(Ramin et al., 2014)
Coefficient of Buoyancy Term (C_3)		
0.15		(Ramin et al., 2014)
0.2		(Dahl, 1993; Shahrokhi et al., 2013)
0-0.2		(Lakehal et al., 1999; Saffarian et al., 2010)
0.8		(Xanthos et al., 2010)

4.2. Methodology

4.2.1 The numerical model

The geometry and the boundary conditions have been shown in Figure 3.2. Since the current research focus on the parameters in the turbulence model and the sludge transport model, only these two models are shown below. A more detailed description of CFD model non-Newtonian flow behavior of the activated sludge and buoyancy effects are shown in Gao and Stenstrom (2018a).

The Realizable k-ε model is:

$$\frac{\partial k}{\partial t} + u\frac{\partial k}{\partial r} + v\frac{\partial k}{\partial y} = \frac{\partial}{\partial r}\left[\left(\vartheta + \frac{\vartheta_t}{\sigma_k}\right)\frac{\partial k}{\partial r}\right] + \frac{\partial}{\partial y}\left[\left(\vartheta + \frac{\vartheta_t}{\sigma_k}\right)\frac{\partial k}{\partial y}\right] + G_k + G_b - \rho\varepsilon \tag{4.1}$$

and:

$$\frac{\partial \varepsilon}{\partial t} + u\frac{\partial \varepsilon}{\partial r} + v\frac{\partial \varepsilon}{\partial y} = \frac{\partial}{\partial r}\left[\left(\vartheta + \frac{\vartheta_t}{\sigma_\varepsilon}\right)\frac{\partial \varepsilon}{\partial r}\right] + \frac{\partial}{\partial y}\left[\left(\vartheta + \frac{\vartheta_t}{\sigma_\varepsilon}\right)\frac{\partial \varepsilon}{\partial y}\right] - C_1\frac{\varepsilon}{k}C_3G_b + \rho C_1 S\varepsilon - \rho C_2\frac{\varepsilon^2}{k+\sqrt{\vartheta\varepsilon}} \tag{4.2}$$

G_k represents the generation of TKE due to the mean velocity gradients, and G_b corresponds to the generation of TKE due to buoyancy.

$$G_k = \vartheta_t\left[2(\frac{\partial u}{\partial r})^2 + 2(\frac{\partial v}{\partial y})^2 + 2(\frac{u}{r})^2 + (\frac{\partial u}{\partial y} + \frac{\partial v}{\partial r})^2\right] \tag{4.3}$$

$$G_b = -g\frac{\vartheta_t}{\sigma_t}\frac{\partial \rho}{\partial y} \tag{4.4}$$

$$C_1 = max\left[0.43, \frac{\eta}{\eta+5}\right], \eta = \frac{Sk}{\varepsilon} \tag{4.5}$$

The turbulent viscosity, ϑ_t, is then determined as a function of TKE (k) and its TDR (ε) by

$$\vartheta_t = C_\mu\frac{k^2}{\varepsilon} \tag{4.6}$$

However, C_μ is no longer constant and is a function of the mean strain and rotation rates, the angular velocity of the system rotation, and the turbulent fields.

The sludge transport model is

$$u\frac{\partial C}{\partial r}+v\frac{\partial C}{\partial y}=\frac{1}{r}\frac{\partial}{\partial r}\left[r\left(\vartheta+\frac{\vartheta_t}{\sigma_r}\right)\frac{\partial C}{\partial r}\right]+\frac{1}{r}\frac{\partial}{\partial y}\left[r\left(\vartheta+\frac{\vartheta_t}{\sigma_y}\right)\frac{\partial C}{\partial y}-rV_sC\right] \quad (4.7)$$

in which C is the sludge concentration, ϑ is the viscosity of the sludge mixture, ϑ_t is the turbulent eddy viscosity, σ_r and σ_y are the turbulent Schmidt numbers in the r and y directions, respectively. V_s is the particle settling velocity determined by the Takacs equation (Takács et al., 1991).

Table 4-2. Loading conditions for the three test cases on the Darvill SST

Loading conditions*	Test 1	Test 2	Test 3
Averaged SOR (m/h)	0.866	0.715	0.985
Averaged $Q_{effluent}$ (m^3/h)	833	688	948
Recycle ratio	0.80	0.97	0.79
Averaged MLSS (mg/L)	4600	4300	3600

* Values were reported by Ekama and Marais (2002), and used by Griborio (2004).

4.2.2 Boundary conditions

The velocity inlet boundary condition is applied to inlet and sludge bottom boundaries. A pressure outlet boundary condition is applied for the surface outlet boundary, which assumes a uniform pressure and zero-gradient for all transport variables. For the free ambient water surface, the rigid-lid approximation for all velocity components with full slip shear condition is assumed. The free surface boundary is treated as a symmetry condition. The solid boundaries are specified as stationary walls with no shear.

4.2.3 Model verification

The simulation results are compared with the field data from Griborio (2004) and shown

in other paper (Gao and Stenstrom, 2018a). ESS and RAS concentration are fitting parameters.

4.3. Results and discussion

4.3.1 The effects of buoyancy term G_b in TKE equation

4.3.1.1 Effects on performance indicators

In Griborio's dissertation, four Darvill SST test cases (Tests 1 to 4) from Ekama and Marais (2002) were compared. The loading conditions for these four tests are shown in Table 4.2. The field observations of the ESS and SBH for the Test 4 are not available, but the field observations of the ESS and SBH for the Tests 1 to 3 are available and compared with the predictions of the buoyancy-decoupled/coupled turbulence models. The comparisons are shown in Table 4.3. Additionally, the predictions of the ESS for Tests 1 to 3 by the SettlerCAD model and the 2Dc model (Griborio, 2004) are also included in Table 4.3. The SettlerCAD model was developed based on the CFD model of Zhou and McCorquodale (1992b). This model uses an SKE model without coupling the buoyancy terms. 2Dc model was developed at the University of New Orleans (UNO). The turbulence model is based on the mixing length theory. Comparisons for the Tests 1 to 3 are based on a "safe/fail" basis. SST failure is defined as the ESS greater than 30mg/L or the sludge blanket rising to the SST surface.

Table 4.3 shows that the buoyancy-coupled turbulence model not only correctly predicts the safe operation for all three tests, but also predicts similar ESS to the field observations for all three tests. However, the buoyancy-decoupled turbulence model not only predicts the failure for all three tests, but the predicted ESS are significantly different from the field observations. The

SettlerCAD model also predicts the failure for Tests 1 and 2 due to high ESS, and the predictions are remarkably different from the field observations. The results of the buoyancy-decoupled/coupled turbulence models in our study and the results of the SettlerCAD model show that coupling/decoupling the buoyancy term in the TKE equation has significant influence on the prediction of the SST performance. The application of the buoyancy-coupled turbulence model is more reliable.

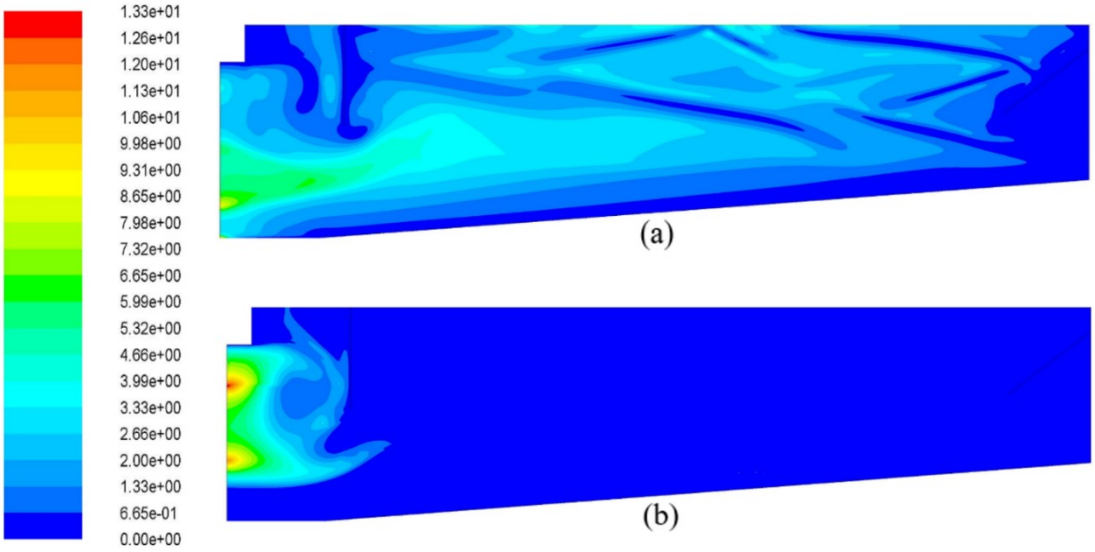

Figure 4-1. Distribution of turbulent viscosity (kg/m-s): (a) buoyancy-decoupled; (b) buoyancy-coupled TKE equation (Q=1500 m^3/h, MLSS=4600 mg/L, RAS=0.8).

4.3.1.2 Effects on turbulent viscosity

Figure. 4.1(a, b) compares the distributions of turbulent viscosity (ϑ_t) with buoyancy-decoupled/coupled TKE equations when inflow rate (Q) is 1500 m^3/h, MLSS is 4600 mg/L, and returned activated sludge (RAS) ratio is 0.8 (Q=1500 m^3/h, MLSS=4600 mg/L, RAS=0.8). Without coupling the buoyancy term in TKE equation (Figure. 4.1a), the highly turbulent viscosity

is extended from the inlet zone to the entire main settling zone and from the surface of the SST to the bottom sludge outlet. However, coupling the buoyancy term in TKE equation (Figure. 4.1b) reduces the highly turbulent viscosity and is only presented inside the inlet zone. Outside the inlet zone, the turbulent viscosity (turbulent mixing) is globally reduced due to the density stratification in the SST. A decrease in ϑ_t, in turn, causes a decrease of the turbulent diffusive transport of all quantities (Lakehal et al., 1999).

Table 4-3. Comparison among the results of the actual stress tests, the prediction results of the SettlerCAD model, and the prediction results of the G_b-decoupled/G_b-coupled turbulence models.

Actual Stress Tests[1]	Test 1	Test 2	Test 3
SBH[2] (m)	2.20	2.60	2.70
ESS (mg/L)	17	5	10
SettlerCAD Results[1]	Test 1	Test 2	Test 3
ESS (mg/L)	495	933	2.1
Test Outcome[3]	Fail	Fail	Safe
Fluent Model[4]	Test 1	Test 2	Test 3
SBH[2] (m): G_b-decoupled	0	0	0
/G_b-coupled	3.2	3.0	3.2
ESS (mg/L): G_b-decoupled	2650	2792	1550
/G_b-coupled	8	8	10
Test Outcome[3] for the G_b-decoupled	Fail	Fail	Fail
Test Outcome[3] for the G_b-coupled	Safe	Safe	Safe

1: Values were reported by Ekama and Marais (2002), and used by Griborio (2004).
2: SBH is the depth between the water surface and the sludge blanket surface.
3: SST failure is defined as the ESS≥30mg/L or the sludge blanket rising to the SST surface.
4: G_b-decoupled and G_b-coupled turbulence models are applied in our simulations.

Table 4-4. Effects of the coefficient of buoyancy term (C_3) on different performance indicators at the original inflow rate (Q) and 20% increase of inflow rate (1.2Q)

	Turbulent intensity (%)		TKE (m^2/s^2)		Turbulent viscosity (kg/m-s)		ESS (mg/L)		RAS (mg/L)		SBH (m)	
C_3	Q	1.2Q	Q	1.2Q	Q	1.2Q	Q	1.2Q	Q	1.2Q	Q	1.2Q
0	3.02	2.82	1.36	1.20	15.0	2.70	8.2	12.0	10400	10200	3.2	2.7
0.2	2.96	2.84	1.31	1.21	15.0	3.31	8.0	10.7	10300	10100	3.2	2.7
0.4	2.91	2.91	1.27	1.27	11.9	5.33	10.5	11.0	10200	10000	3.2	2.8
0.6	2.74	2.82	1.13	1.19	10.5	3.59	10.0	9.5	10100	10300	3.2	2.5
0.8	2.70	2.81	1.10	1.19	10.1	5.31	9.5	8.5	10000	10200	3.2	2.5
1.0	2.66	2.82	1.01	1.19	9.7	9.10	12.3	10.6	10000	10300	3.2	2.5

4.3.1.3 Effects on settling velocity

Figure. 4.2 (a, b) shows the settling velocity profiles with buoyancy-coupled/decoupled in the TKE equation (Q=1500 m^3/h, MLSS=4600 mg/L, RAS=0.8). Without coupling the buoyancy term in the TKE equation, the distribution of large turbulent viscosity is present over the entire SST, as shown in Figure. 4.1a, and causes the poor particle settling (Figure. 4.2a), even with good particle settling properties. The maximum settling velocity occurs at the surface of the SST but is much lower than the maximum settling velocity in the coupled result, which occurs at the surface of the sludge blanket.

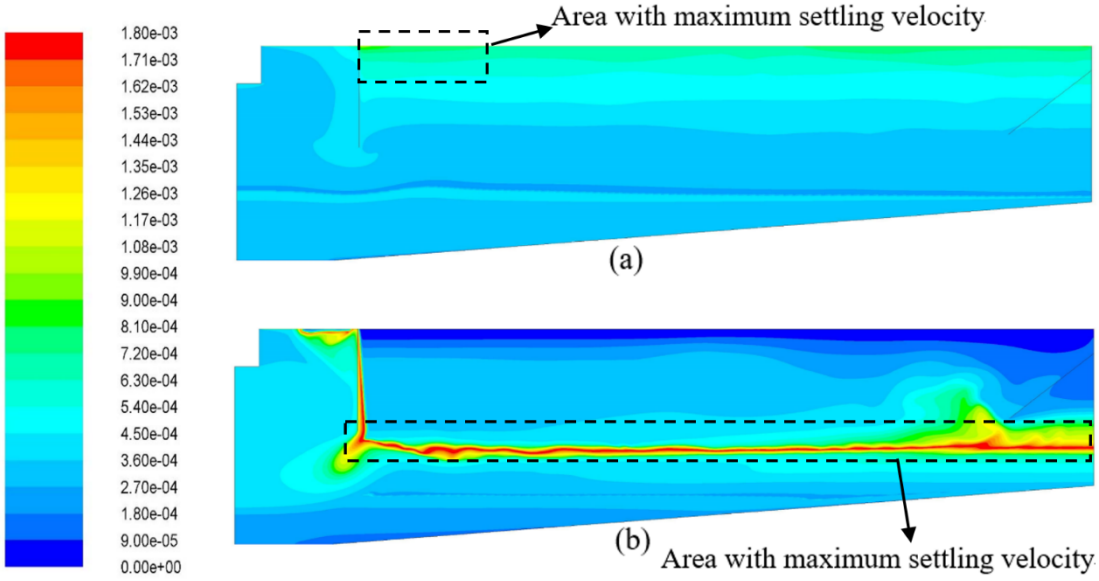

Figure 4-2. Distribution of sludge settling velocity (m/s): (a) buoyancy-decoupled; (b) buoyancy-coupled TKE equation (Q=1500 m^3/h, MLSS=4600 mg/L, RAS=0.8).

4.3.1.4 Effects on sludge concentration

Figure. 4.3 (a, b) shows the sludge concentration profiles by buoyancy-coupled and buoyancy-decoupled TKE equation (Q=1500 m^3/h, MLSS=4600 mg/L, RAS=0.8). Without the buoyancy term coupled in TKE equation (Figure. 4.3b), the sludge does not settle well and is

stratified vertically and well mixed horizontally throughout the radius of the SST. This is opposite to Lyn's results (Lyn et al., 1992), which showed very little vertical stratification. However, with the buoyancy term coupled in TKE equation, the turbulent mixing is globally damped, and the sludge blanket exhibits a distinct interface at the upper clarification zone and bottom thickening zone (Figure. 4.3a).

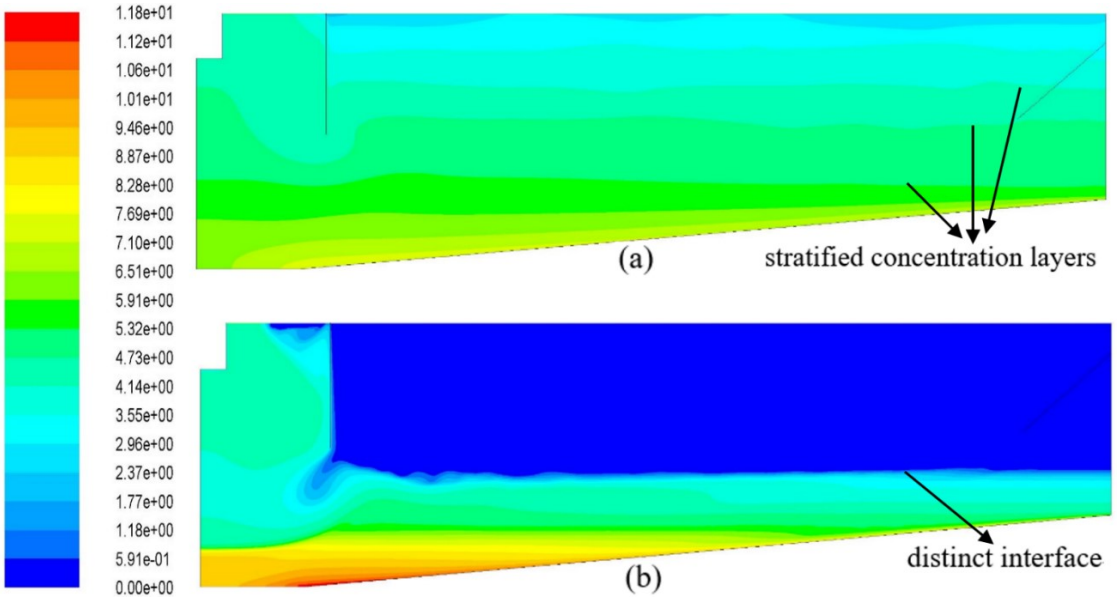

Figure 4-3. Distribution of sludge concentration (g/L): (a) buoyancy-decoupled; (b) buoyancy-coupled TKE equation (Q=1500 m^3/h, MLSS=4600 mg/L, RAS=0.8).

4.3.2 The effects of sludge concentration and settling velocity with buoyancy-decoupled/ coupled TKE equation

To confirm whether the buoyancy term in the TKE equation can be neglected when the MLSS concentration is low or the settling velocity is significantly large, coupled and decoupled simulations are performed with four gradually decreasing MLSS concentrations and five gradually increasing settling velocities (Q=1500 m^3/h, RAS=0.8). All the predicted effluent suspended solid (ESS) concentrations are summarized in Figure. 4.4(a, b). Since Zhou and McCorquodale (1994)

showed that the usual range of settling velocity (V_s) in SSTs is from 7.0 to 11.0 m/h, which means the Stokes velocity constant (V_o) in the Takacs equation (Takács et al., 1991) is from 8.0 to 13.0 m/h corresponding to the current sludge empirical coefficients for rapid and slow settling (r_p=0.39 L/g; r_h=10 L/g (Griborio, 2004)), sensitivity tests of sludge settling velocity on ESS start from V_o= 7.7m/h (the original Stokes velocity) and extends to an extremely high V_o (30m/h), the maximum velocity reported in previous research (Zhou and McCorquodale, 1992b).

In the original case (MLSS=4600 mg/L), the buoyancy-coupled TKE equation (Figure. 4.4a) predicts an ESS concentration similar to the field observations (7 to 8 mg/L simulated compared to 17mg/L observed). In the buoyancy-decoupled TKE equation (Figure. 4.4b) there is a large divergence between field observations and simulation results; the simulation shows failure of the SST. With a decrease of MLSS concentration or an increase of sludge settling velocity, the ESS predicted by the buoyancy-coupled TKE equation shows a negligible change of ESS concentration and all the simulations show the SST is operating well, compared to excessive ESS predicted by the buoyancy-decoupled TKE equation. The predicted ESS at 4600 mg/L MLSS concentration averaged over the five settling velocities is approximately 7 to 8 mg/L. Figure. 4.4b shows excessive ESS at 4600 mg/L MLSS which decreases with increasing settling velocity but remains excessive. The ESS decreases with decreasing MLSS concentration under the same sludge settling velocity but also remain excessive.

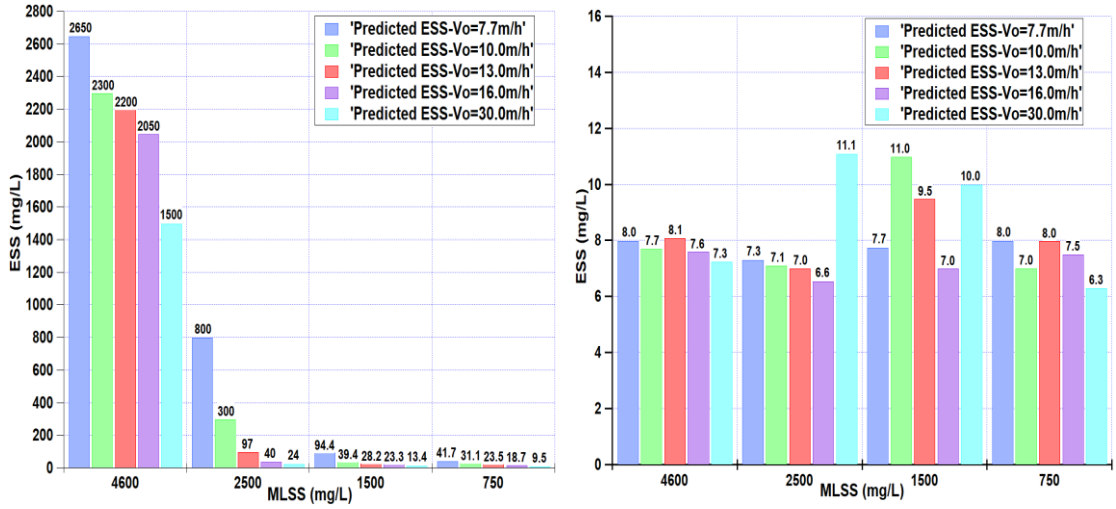

Figure 4-4. Predicted ESS with four different MLSS concentrations and five Stokes velocities V_o: (a) buoyancy-decoupled; (b) buoyancy-coupled. (Q=1500 m^3/h, RAS=0.8).

The buoyancy-coupled TKE equation predicts reasonable ESS for all MLSS concentrations and settling velocities. The decoupled TKE equation rarely predicts reasonable ESS, and then only for MLSS concentrations of 1500 mg/L or less with settling velocities of 13 m/h or greater. All predictions of ESS by the buoyancy-coupled TKE equation (Figure. 4.4a) are reasonable, while the predictions of ESS by buoyancy-decoupled TKE equation show the failure of SST even with an extremely high settling velocity. The buoyancy-decoupled TKE predicts plausible results only when the MLSS is below 1500 mg/L with settling velocities of 13m/h or greater. The buoyancy-decoupled TKE equation is of limited value, being useful only at low MLSS concentrations with high settling velocities. This is a severe limitation since SST operating with low MLSS and well settling sludge rarely fail and there is less incentive to model them. Cases with high MLSS and poorer settling are more likely candidates for modeling.

4.3.3 The effects of coefficient ($\boldsymbol{C_3}$) of buoyancy term in TDR equation

Lakehal et al. (1999) showed that the sludge blanket height (SBH), the magnitude and the

location of the peak horizontal velocity and peak gradients of both horizontal and concentration are sensitive to the value of C_3, but did not show the effects of C_3 on performance indicators, such as ESS and RAS concentrations. To understand the potential impacts of C_3 on ESS and RAS concentrations, a sensitivity study is made by varying C_3 using two flow rates. The results are shown in Table 4.4.

At the original inflow rate (Q=1500m^3/h, MLSS=4600 mg/L, RAS=0.8), the simulation predicts that increasing C_3 causes a gradual decrease of all the turbulent quantities. This occurs because increasing C_3 in the TDR equation causes an increase in TDR. The increase in TDR, in turn, causes a decrease of the turbulent eddy viscosity ϑ_t, decreasing of the turbulent diffusive transport parameters, consistent with Lakehal et al. (1999) results.

The effects of decreased turbulent diffusion can also be demonstrated by comparing the velocity contours in Figure. 4.5 (a, b) and the concentration contours in Figure. 4.6 (a, b). Each contour in these two figures shows the profile predicted with C_3 =0 and C_3 =1, respectively. In Figure. 4.5 (a, b), since the eddy diffusion is more intense with C_3 =0, a series of small eddies along the horizontal jet is generated (highlighted in six black rectangular boxes in Figure. 4.5a). As C_3 increases, the small eddies gradually decline and finally disappear. Therefore, the sludge blanket exhibits smoother concentration gradient at the interface as shown in Figure. 4.6b.

However, different from the simulation results in Lakehal et al. (1999), Table 4.4 shows the SBH does not present a significant variation with the change of C_3. Additionally, little change of ESS and RAS concentration show these two performance indicators are also insensitive to the

change of C_3.

However, the 20% increase in the original inflow rate (1.2Q=1800m^3/h, MLSS=4600 mg/L, RAS=0.8) changes the pattern for all turbulent quantities (turbulent intensity (TI), TKE and turbulent viscosity) from a decrease in turbulent quantities with increasing C_3 to a variable pattern, decreasing and increasing turbulent quantities with increasing C_3. The Equation. 6 shows the C_μ of the Realizable k-ε model is not a constant as it in the SKE model, but a function of the mean strain and rotation rates, the angular velocity of the system rotation, and the turbulent fields. Therefore, the uncertainty of C_μ may result in the unexpected changes of turbulent viscosity. Additionally, variations of SBH, ESS and RAS concentrations as the variation of C_3 at 1.2Q are negligible. Therefore, the effects of C_3 on the SBH, ESS and RAS concentrations at the different inflow rates are minimal.

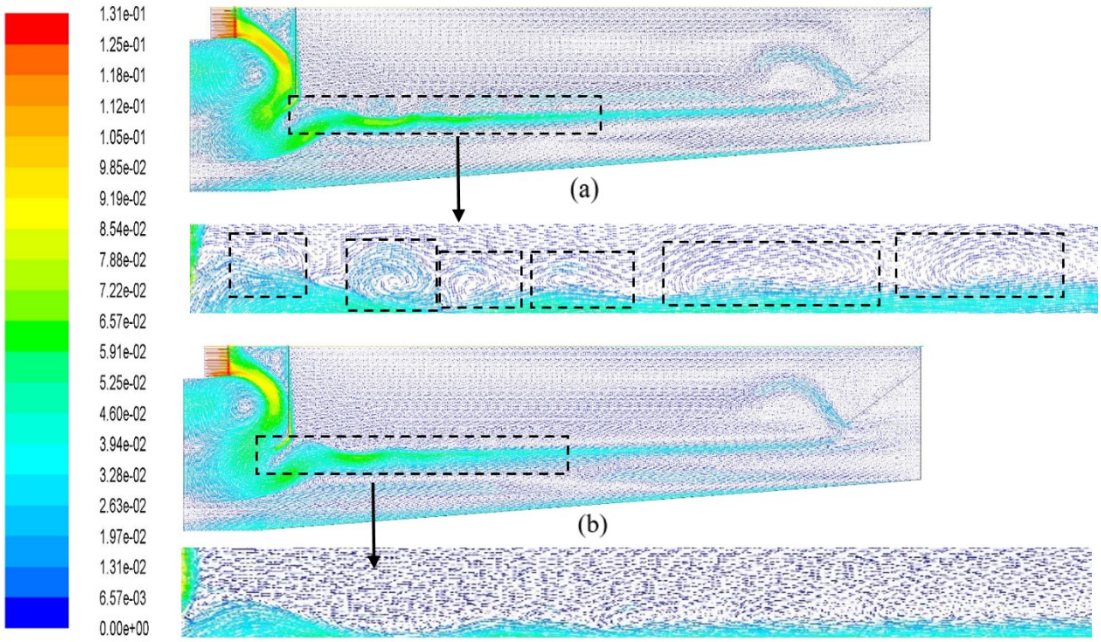

Figure 4-5. Effects of coefficient of buoyancy term (C_3) on velocity distribution (m/s) with the original inflow rate (Q=1500 m^3/h, MLSS=4600 mg/L, RAS=0.8): (a) C_3=0, presence of a series

of eddies along the horizontal jet; (b) C_3=1.0, absence of eddies along the horizontal jet.

4.3.4 The effects of turbulent Schmidt number $\boldsymbol{\sigma_c}$

To understand the effects of the turbulent Schmidt number on the performance of an SST, simulations are run with three turbulent Schmidt numbers (0.5, 0.7, 1.0) at two inflow rates (Q and 1.2Q, MLSS=4600 mg/L, RAS=0.8) and two values of C_3. The ESS, RAS concentration and SBH predicted at the two inflow rates and two C_3 coefficient values are shown in Figure. 4.7 (a-f). They show that the ESS and RAS only change slightly with the increase of turbulent Schmidt number. This is consistent with the results in Stamou et al. (1989), who concluded that the ESS is insensitive to the change of turbulent Schmidt number. However, the variation of SBH predicted with different σ_c is significant. Figure. 4.7e shows the SBH increases by 0.5m (18.5%) with an increase in the turbulent Schmidt number from 0.5 to 0.7. Figure. 4.7f shows the SBH increases by 0.6m (24%) as the turbulent Schmidt number increases from 0.5 to 1.0. Due to space limits, the concentration profiles predicted with only two turbulent Schmidt numbers (0.5 and 1.0) at 1.2Q are presented in Figure. 4.8 (a, b) to show the difference of the SBH.

Table 4-5. Effects of each influential factor on the performance indicators

	ESS	SBH	RAS
G_b in TKE equation	√	√	√
C_3 in the TDR equation	×	×	×
σ_c in the sludge transport equation	×	√	×

√: Strong Influence ×: No Strong Influence

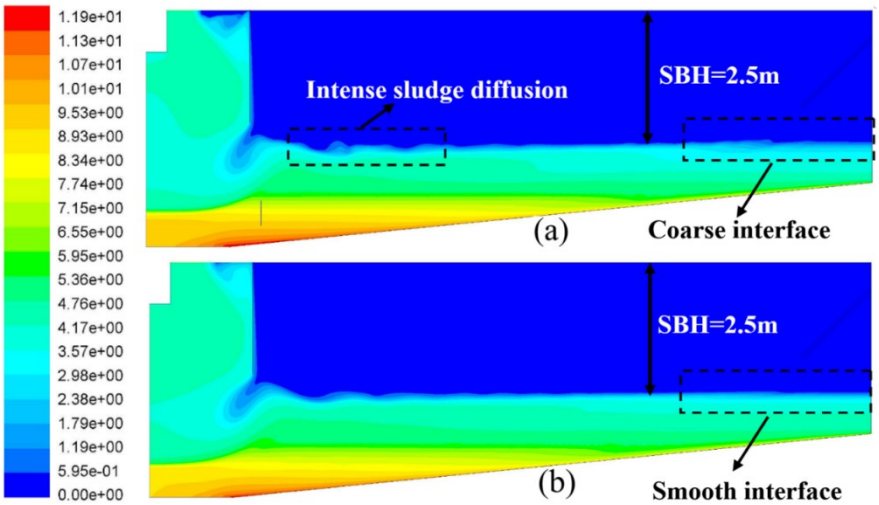

Figure 4-6. Effects of coefficient of buoyancy term (C_3) on sludge concentration (g/L) with the original inflow rate (Q=1500 m^3/h, MLSS=4600 mg/L, RAS=0.8): (a) C_3=0; (b) C_3=1.0

4.4. Conclusions

In this chapter, a Fluent-based 2D axisymmetric numerical model is used to study the effects of buoyancy terms in the TKE equation, and the effects of the two model parameters (the coefficient of buoyancy term (C_3) in the TDR equation and the turbulent Schmidt number (σ_c) in the sludge transport equation) on the performance of an SST.

Unlike the early numerical studies that were limited by the performance of computer hardware and convergence difficulties of SST models with high MLSS concentrations, this chapter provides a sensitivity analysis. The advanced SST numerical model accounts for the effects of these influential factors on the hydrodynamics and performance indicators of an SST, such as turbulent viscosity, TKE, TI, SBH, ESS and RAS concentrations.

Based on the simulation results the following conclusions are made and are briefly summarized in Table 4.5:

1. The buoyancy term should be coupled in TKE to correctly predict the ESS unless both the

MLSS is very low (below 1500 mg/L) and sludge settling is high (above 13m/h). The field observations and results predicted by buoyancy-coupled TKE equation at higher MLSS and poorer sludge settling show the SST is operating well; however, the buoyancy-decoupled TKE equation shows failure of the SST due to rising SBH for these same conditions

2. ESS, RAS concentrations and SBH are all insensitive to the variation of the coefficient C_3 of the buoyancy term in TDR equation. Therefore, the C_3=0 can be set to zero, which will remove the buoyancy term in the TDR equation, improving rate of convergence and reducing computing time.
3. ESS and RAS concentration are insensitive to the effects of turbulent Schmidt number σ_c, whereas SBH is strongly influence by the variation of turbulent diffusion caused by the change of σ_c. Therefore, the turbulence Schmidt number can be used to adjust the SBH, when ESS and RAS concentrations are well calibrated to the field data, but the SBH does fit field observations.
4. It is recommended that for the application of a SST numerical model, both the prediction results of the buoyancy-decoupled and buoyancy-coupled TKE equations should be verified with the field data, before the further applications of the model.

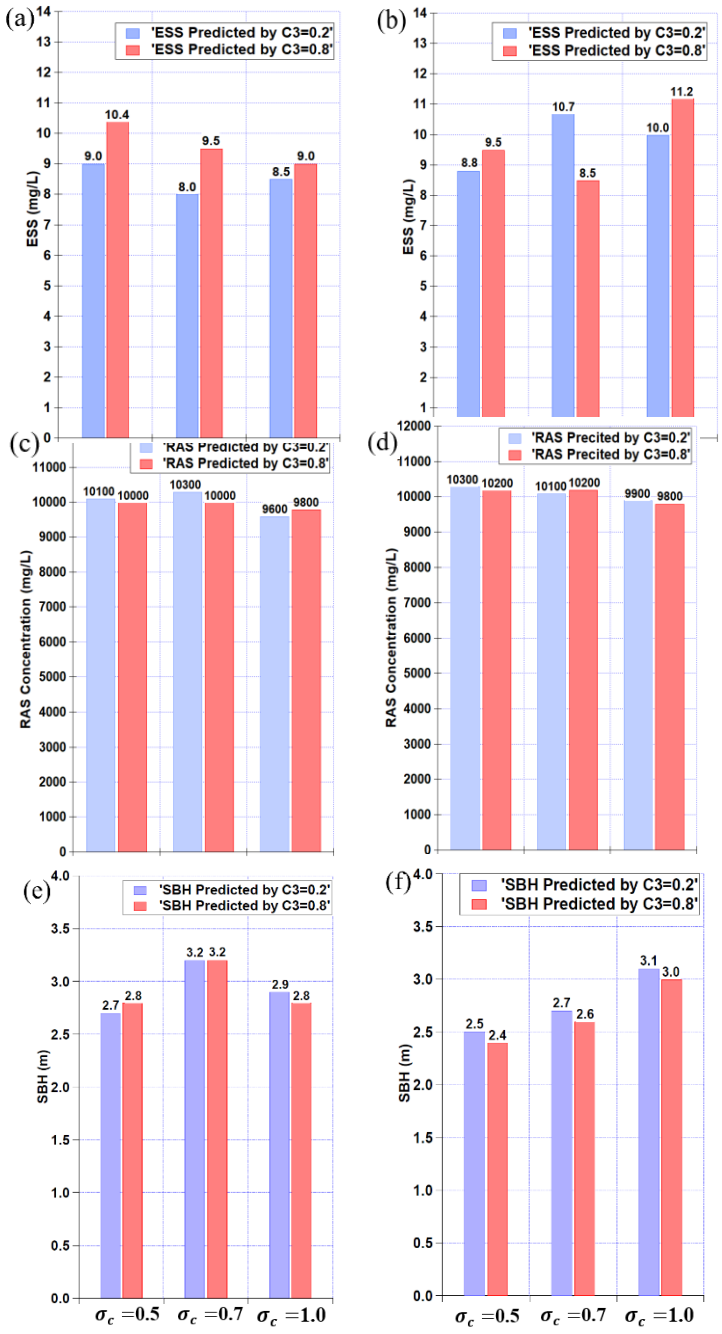

Figure 4-7. Effects of turbulent Schmidt number on the prediction of ESS, RAS concentration and SBH at different inflow rates and different C_3: (a) ESS-original inflow rate (Q); (b) ESS-20% increment of inflow rate (1.2Q); (c) RAS concentration- Q; (d) RAS concentration-1.2Q; (e) SBH-Q; (f) SBH- 1.2Q (Q=1500 m^3/h, 1.2Q=1800 m^3/h, MLSS=4600 mg/L, RAS=0.8).

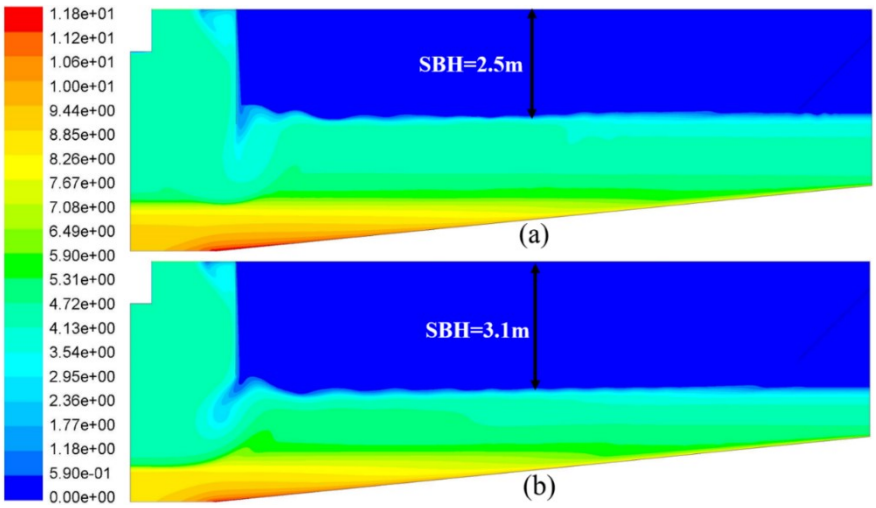

Figure 4-8. Effects of turbulent Schmidt number on the sludge concentration (g/L) at 20% increment of inflow rate (1.2Q=1800m3/h, MLSS=4600 mg/L, RAS=0.8): (a) $\sigma_c = 0.5$; (b) $\sigma_c = 1.0$

Chapter 5 Generalizing the effects of the baffling structures on the buoyancy-induced turbulence in secondary settling tanks with eleven different geometries using CFD models

5.1. Introduction

In conventional wastewater treatment plants (WWTPs), the activated sludge process (ASP) is the most popular technique to remove organic matter and reduce nutrients such as nitrogen and phosphorus (Li and Stenstrom, 2014). After the bio-reaction in the aeration tank, the effluent has a highly concentrated biomass and must be separated by secondary settling tank (SST), also known as secondary clarifier or secondary sedimentation tank.

In order to study the flow field and solids distribution in an SST, computational fluid dynamics (CFD) simulations have been developed in the last 30 years and have become a practical approach. Larsen (1977) was the pioneer in applying CFD to predict the hydrodynamics in settling tanks and set the framework for future CFD settling tank research. Since then, applications of CFD in settling tanks have become popular and have been used to (1) understand the hydrodynamics in the SST (Zhou and McCorquodale, 1992a; b; c; Ekama et al., 1997; Tamayol et al., 2009); (2) optimize internal structures (Gong et al., 2011; Patziger et al., 2012; Ramalingam et al., 2012; Xanthos et al., 2013; Das et al., 2016; Patziger, 2016; Gao and Stenstrom, 2017) and (3) adjust operation process (Parker et al., 2008; Patziger et al., 2008; 2012).

Compared with the experimental study, the main advantages of CFD simulations are less expense and less time commitment. However, because of the limited computational speed and storage in many of the early studies, simple turbulence models, such as constant eddy viscosity

model and mixing length theory model were used to qualitatively study the turbulence flow in the SST (Imam et al., 1983; Krebs, 1991; Krebs et al., 1992; Krebs et al., 1995). However, the constant eddy viscosity model needs a constant value to estimate the turbulence effects on the flow. The mixing-length model requires an accurate estimate of the mixing length. Neither parameter can be measured directly which means that both models require additional information to estimate these two parameters (McCorquodale et al. 2004). Since the disadvantages of these two models, more advanced turbulence models such as standard k-ε (SKE) model, RNG k-ε model and Realizable k-ε model, have been applied in recent settling tank studies (Zhou and McCorquodale, 1992a; b; c; Vitasovic et al., 1997; Lakehal et al., 1999; Weiss et al., 2007; Patziger and Kiss, 2015; Das et al., 2016).

Gao and Stenstrom (2018a) compared the influences of SKE, RNG k-ε and Realizable k-ε models on the performance of a circular SST using data from Burt (2010), and McCorquodale et al. (2004). Their results showed that turbulence model selection has a strong influence on the prediction of SST capacity and the SST hydrodynamics, especially inside the inlet zone and near the sludge hopper.

Additionally, the applications of turbulence models lack consensus of the use of the buoyancy term (G_b) in the turbulent kinetic energy (TKE). In some early applications of the SKE model, this term was decoupled in the TKE equation. Devantier and Larock (1986) explained that coupling G_b in the TKE equation required solving numerically stiff equations and difficulty in obtaining solution convergence. Some other researches also ignored G_b in the TKE equation (Zhou

and McCorquodale, 1992a; b; Vitasovic et al., 1997; Tamayol et al., 2009). Comments on these researches were briefly summarized in Gao and Stenstrom (2018b).

On the contrary, G_b was also widely applied in many other SST studies (Lyn et al., 1992; Dahl, 1993; Lakehal et al., 1999; Xanthos et al., 2010; Shahrokhi et al., 2013; Ramin et al., 2014). Gao and Stenstrom (2018b) studied the effects of the buoyancy-induced turbulence on Darvill SST under varied MLSS concentrations and sludge settling velocities. Only a vertical inlet baffle was installed in the Darvill SST to dissipate the inflow energy. The results showed that installing the inlet dissipating baffle alone cannot reduce the effect of buoyancy on turbulence. For this case and cases like it, the effect of buoyancy on turbulence are negligible only when the loading conditions are limited, often outside of normal operating range.

Since flow in the SST is the turbulent, density-driven flow, understanding the effect of buoyancy on turbulence in different SST geometries is very important. Additionally, decoupling buoyancy in the turbulence model makes the numerical model converge faster than the buoyancy coupled turbulence model; therefore, saving computing time. A predictive tool to show when a decoupled approach will work is of value in saving computing resources and effort.

In this chapter, 11 different types of the SST geometries, including 4 circular SSTs types and 7 rectangular SSTs types are evaluated to generalize the effects of the internal baffling structures on the buoyancy-induced turbulence in SSTs with different geometries. The following two questions are answered: (1) What parameter can be used to quantify the effects of the baffling structure and to indicate if the G_b-decoupled turbulence model will work under a normal flow

conditions? (2) If the G_b-decoupled turbulence model tends to work as the G_b-coupled turbulence model under a normal flow condition in different SST geometries, which parameter can be used to differentiate the performance of the G_b-decoupled/coupled turbulence models, and is useful to compare in different SST geometries?

Firstly, the measurements of the velocity profiles and performance indicators, such as effluent suspended solids (ESS), sludge blanket height (SBH) in the original and the modified Witney SST geometries are used to verify the model predictions. Both the G_b-decoupled/coupled SKE models are verified. Next, the predictions of the ESS by the G_b-decoupled/coupled SKE models for all eleven geometries are compared. Then, the effects of the varied baffling structures on the turbulence properties by the G_b-decoupled/coupled SKE models are analyzed and quantified. Additionally, stress tests are simulated on the Zones B and C by both models.

5.2. Methodology

5.2.1 The mathematical model

The commercial CFD code ANSYS Fluent (v.17.2) is used to determine the steady-state, turbulent, and density stratified flow in the different SSTs. Consistent with the previous research (Gao and Stenstrom, 2018a, b), the circular SSTs in this research are also investigated by the two-dimensional axisymmetric approach. The major difference is the G_b-decoupled turbulence model is also applied with the G_b-coupled turbulence model. Since the current study focus on the effect of buoyancy on turbulence, only the applied turbulence model is shown below. A more detailed description of CFD model non-Newtonian flow behavior of the activated sludge and sludge settling

properties are shown in Gao and Stenstrom (2018a).

The standard k-ε (SKE) model is applied in this study. The transport equations for the turbulent kinetic energy (k) and the turbulent dissipation rate (ε) are shown below:

$$u\frac{\partial k}{\partial r}+v\frac{\partial k}{\partial y}=\frac{\partial}{\partial r}\left[\left(\vartheta+\frac{\vartheta_{\mathrm{t}}}{\sigma_k}\right)\frac{\partial k}{\partial r}\right]+\frac{\partial}{\partial y}\left[\left(\vartheta+\frac{\vartheta_{\mathrm{t}}}{\sigma_k}\right)\frac{\partial k}{\partial y}\right]+G_k+G_b-\rho\varepsilon \tag{5.1}$$

and:

$$u\frac{\partial \varepsilon}{\partial r}+v\frac{\partial \varepsilon}{\partial y}=\frac{\partial}{\partial r}\left[\left(\vartheta+\frac{\vartheta_t}{\sigma_\varepsilon}\right)\frac{\partial \varepsilon}{\partial r}\right]+\frac{\partial}{\partial y}\left[\left(\vartheta+\frac{\vartheta_t}{\sigma_\varepsilon}\right)\frac{\partial \varepsilon}{\partial y}\right]+C_1\frac{\varepsilon}{k}G_k-C_2\rho\frac{\varepsilon^2}{k} \tag{5.2}$$

G_k represents the generation of turbulent kinetic energy (TKE) due to the mean velocity gradients, and G_b corresponds to the buoyancy-induced TKE. The SKE model without or with the implementation of the G_b term is named buoyancy-decoupled (G_b-decoupled) or buoyancy-coupled (G_b-coupled) SKE model, respectively.

$$G_k=\vartheta_{\mathrm{t}}\left[2\left(\frac{\partial \mathrm{u}}{\partial \mathrm{r}}\right)^2+2\left(\frac{\partial \mathrm{v}}{\partial \mathrm{y}}\right)^2+2\left(\frac{\mathrm{u}}{\mathrm{r}}\right)^2+\left(\frac{\partial \mathrm{u}}{\partial \mathrm{y}}+\frac{\partial \mathrm{v}}{\partial \mathrm{r}}\right)^2\right] \tag{5.3}$$

$$G_b=-g\frac{\vartheta_{\mathrm{t}}}{\sigma_t}\frac{\partial \rho}{\partial y} \tag{5.4}$$

The turbulent viscosity, ϑ_{t}, is then determined as a function of k and ε by

$$\vartheta_{\mathrm{t}}=C_\mu\frac{k^2}{\varepsilon} \tag{5.5}$$

The dimensionless empirical constants are given the standard values suggested by Rodi (1993). $C_\mu=0.09$, $C_1=1.44$, $C_2=1.92$, $\sigma_k=1.0$, and $\sigma_\varepsilon=1.3$.

Additionally, inlet densimetric Froude number (Fr) is applied in this study to describe the inertial and density gravity force in the SSTs in terms of initial momentum and buoyancy flux. It was applied in the previous studies to describe the effects of the bottom density current in SSTs (Zhou et al., 1992) and to optimize the inlet-structure design (Krebs et al., 1995). Since Fr is

dimensionless, it can be used to compare the SST performance in difference geometries or loading conditions in this study.

$$F_r = \left(\frac{u_o^2}{gH_{in}\frac{\rho-\rho_r}{\rho_r}}\right)^{1/2} \quad (5.6)$$

Where u_o is the inlet velocity; ρ_r is the clear water density; and ρ is the local density of mixture.

Table 5-1. Loading conditions of the different cases and their relevant geometries numbers

Different Cases	Relevant Geometries shown in Figure. 1	Inflow parameters			Settling parameters*			Dry solids density
No.	No.	MLSS g/L	RAS ratio	SOR m/h	V_o m/h	r_h L/g	r_p L/g	ρ_p kg/m^3
Circular SSTs	Circular SSTs							
1	1	4.600	0.80	0.866	7.710	0.390	10.00	
2	2	4.187	1.09	0.332	12.64	0.340	12.25	
3a	3	3.384	1.09	0.332	13.32	0.386	13.00	
3b	3	2.904	0.83	0.673	13.32	0.386	13.00	
3c	3	4.187	1.09	0.332	13.32	0.386	13.00	
4	4	4.187	1.09	0.332	13.32	0.386	13.00	1450
Rectangular SSTs	Rectangular SSTs							
5	5							
6	6							
7	7							
8	8	4.187	0.91	1.01	12.64	0.340	12.25	
9	9							
10	10							
11	11							

*: V_o is Stokes velocity. r_h and r_p account for rapidly and poorly settling floc, respectively.

Table 5-2. Dimensions of Circular SSTs

Geometry	Values		
Geometry No.*	No. 1	No. 2	No. 3, 4
Diameter of the clarifier	35.0 m	18.3 m	18.3 m
Surface area	962 m^2	263 m^2	263 m^2
Radius of the inlet pipe	0.5 m	0.4 m	0.4 m
Depth of side wall	4.1 m	1.8 m	1.8 m
Tank floor slope	10%	7.5%	7.5%
Hopper floor slope	/	60°	60°
Stilling/Center well diameter	6.0 m	5.49 m	1.65 m
Stilling/Center well depth	2.7 m	0.8 m	1.8 m
Stamford baffle depth	0.6m	/	/
Stamford baffle length	1.7m	/	/
Outboard launder	Peripheral launder	Peripheral launder	Peripheral launder

*: Different SST geometries are numbered in Figure 5.1.

Table 5-3. Dimension of Rectangular SSTs

Geometry No.*	Tank length (m)	Tank depth (m)	Inlet height (m)	Outboard launder	Height of all the vertical baffles (m)	Length of all the horizontal baffles (m)	Horizontal distance of the vertical baffles (m)
No. 5	60	4.5	0.5	Peripheral launder	/	/	/
No. 6					2	3	/
No. 7							/
No. 8							/
No. 9							3
No. 10					/		
No. 11							

*: Different SST geometries are numbered in Figure 5.1.

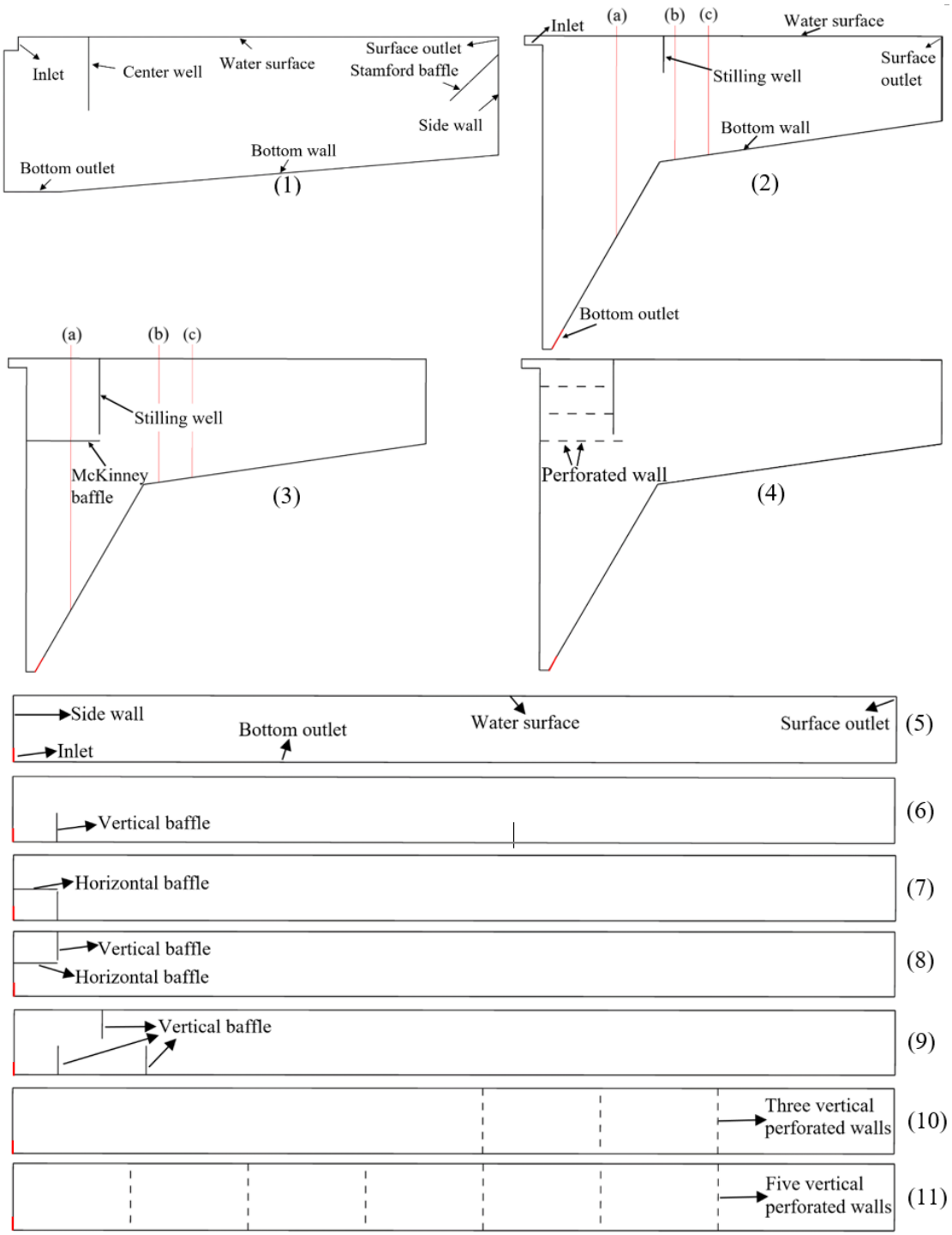

Figure 5-1. Different SST geometries. (a)-(c) in second and third geometries refer to the radial locations for the model verification shown in Figure 5-3. Since the geometries No. (3) and (4) are similar to No. (2), only the differences are named in the geometries No. (3) and (4). Similarly, because the geometries No. (6-11) are similar to No. (5), only the differences are named in the geometries No. (6-11).

5.2.2 Geometries and meshing

Figure 5.1 shows 11 different SST geometries. The circular SSTs, geometry No. 1 is the Darvill SST described in McCorquodale et al. (2004), and one loading condition is run for this geometry (Case 1). No. 2 is the old Witney SST, and one loading condition is run with this geometry (Case 2). No. 3 is the new Witney SST, and three loading conditions are run for this geometry (Cases 3a, 3b, 3c). Both the old and modified Witney SSTs are described by Burt (2010). No. 4 is a new Witney SST created in this study and one loading condition is run for this geometry (Case 4). Therefore, 6 cases are run with these 4 circular SSTs.

For the rectangular SSTs, geometry No. 5 is the Krebs SST (Krebs et al, 1996). No. 6 to 11 are the modified Krebs SSTs created in this study. One loading condition is run with each rectangular SST. Therefore, 7 cases are run with these 7 rectangular SSTs (Cases 5 to 11). Totally, 13 cases are run with these 11 SSTs. Each geometry run one case, except for the geometry No. 3, which run three cases (Cases 3a, 3b, 3c). The loading conditions of these 13 different cases and their relevant geometries numbers are listed in Table 5.1. The dimensions of the four circular and seven rectangular SSTs are shown in Tables 5.2 and 5.3, respectively.

In this study, the computational grids for the Darvill SST are approximately 218,700 cells; the Witney SSTs required approximately 428,000 cells and rectangular SSTs require 230,000 cells. These sizes are selected after grid independent tests. The results of grid independent tests on geometries No. 1 and 2 are described in our previous study (Gao and Stenstrom, 2018a). Since the G_b-decoupled turbulence model provide similar, accurate predictions with the G_b-coupled

turbulence model on both geometries No. 3 and 4, in order to ensure that the buoyancy effects are reasonably resolved, one coarser mesh (225,000 cells) and one finer mesh (900,000 cells) are used. The differences in the concentration field along the radial direction of circular SSTs on geometries No. 3 and 4 for the original and finer mesh size are negligible. Similarly, since G_b-decoupled turbulence model predicts successful SST operation but not as the predictions are accurate predicted by the G_b-coupled turbulence model for geometries No. 10 and 11, two additional finer meshes (460,000 and 890,000 cells) are used for both geometries No. 10 and 11. Results show that the difference among the three mesh sizes are negligible for geometries No .10 and 11, respectively.

5.2.3 Model verification

Since the measurements of the performance indicators (ESS and SBH) and velocity profiles for the Cases 2, 3a, 3b are available in Burt (2010), they are used to verify the model predictions.

5.2.3.1 Performance indicators comparisons

Figure 5.2 (a, b) shows the predictions of the ESS (Figure 5.2a) and SBH (Figure 5.2b) by the G_b-decoupled/coupled turbulence models for the Cases 2, 3a, 3b, respectively. It indicates that only the G_b-coupled turbulence model correctly predicts the performance indicators for the Case 2, while both the G_b-decoupled/coupled turbulence models correctly predict the performance indicators for the Cases 3a and 3b. Therefore, the predictions of the velocity profiles by the G_b-decoupled turbulence model for the Cases 3a and 3b are also added to compare the field measurements. The results are discussed in the next section.

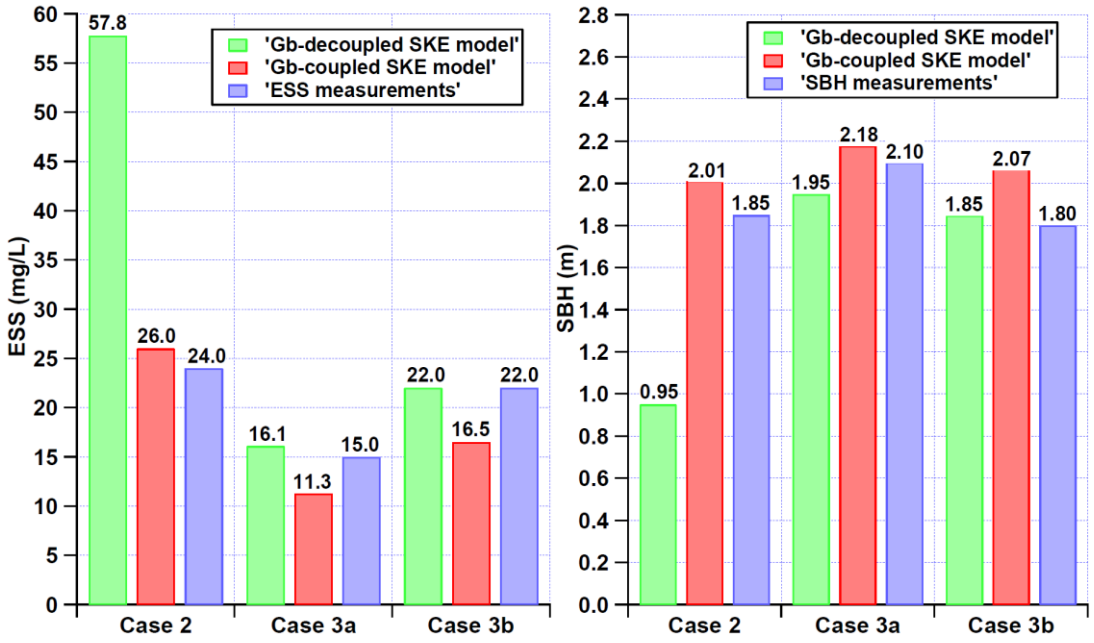

Figure 5-2. Comparisons of the performance indicators (a: ESS; b: SBH) between the model predictions and field observations for Cases 2, 3a, 3b, respectively.

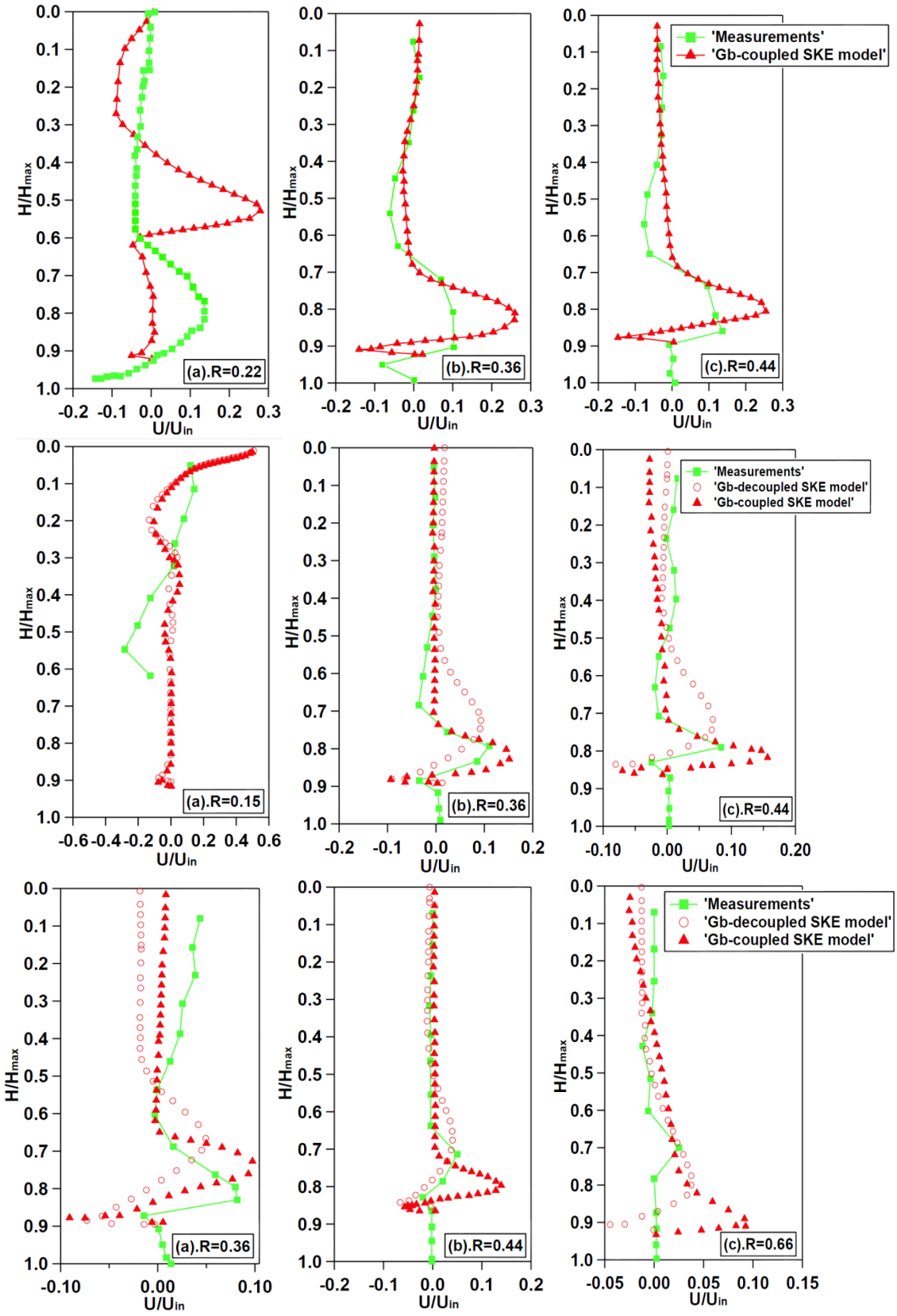

Figure 5-3. Comparisons of radial velocity profiles (m/s) between the model predictions and field

measurements for Cases 2, 3a, 3b, respectively. R is the ratio between the radial distance of the vertical measurement location to the radius of tank. Case 2 (first row), Case 3a (second row), Case 3b (third row). The profiles of R=0.22 for the Case 2 and R=0.15 for the Case 3a are inside the stilling well. Other seven profiles are outside the stilling well. For Cases 3a and 3b, the predictions of the buoyancy-decoupled turbulence model are also included.

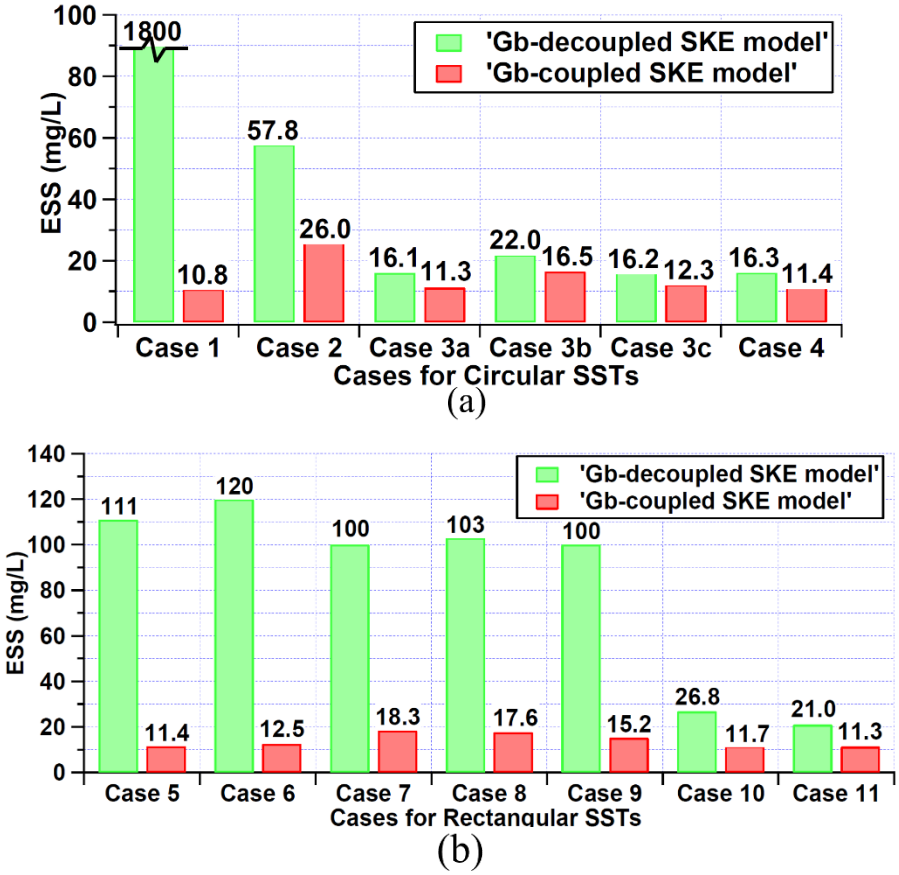

Figure 5-4. Predictions of the ESS by the G_b-decoupled/coupled turbulence models with these 13 cases (a: circular SSTs; b: rectangular SSTs)

5.2.3.2 Velocity profiles comparisons

Figure 5.3 shows the comparisons between the prediction of the velocity profiles and the field measurements for Cases 2, 3a, 3b. Top, medium and bottom rows in the Figure 5.2 represent the velocity profiles comparison for Cases 2, 3a, 3b, respectively. The predictions of the velocity profiles by the G_b-decoupled/coupled turbulence models are similar. Both the G_b-decoupled/coupled turbulence models reasonably predict the overall stream curvatures outside the stilling well.

5.3. Results and discussion

5.3.1 Comparisons of predicted ESS by the G_b-decoupled/coupled turbulence models

The predictions of the ESS by the $\boldsymbol{G_b}$-decoupled/coupled turbulence models with these 13 cases are shown in Figure 5.4. It shows that the change of the internal baffling structure, impacts the need for a coupled model, the results are divided into three different zones, based upon the dissipation in turbulence. Cases in Zone A the baffling produces only limited reductions in the effect of buoyancy on turbulence and simulations require a coupled model. In Zone C where there are larger reductions in the effect of buoyancy on turbulence, either model can be used. Cases in Zone B may require a coupled model and the criteria are discussed later.

For the geometries No. 1, 2, 5 to 9, Cases 1, 2, 5 to 9, the predicted differences between the $\boldsymbol{G_b}$-decoupled/coupled turbulence models are significant, and only the $\boldsymbol{G_b}$-coupled turbulence model correctly predicts the ESS for these 7 cases. This implies that the effect of buoyancy on turbulence is strong in these geometries (Zone A).

For the geometries No. 10 and 11, Cases 10 and 11, the predictions of the ESS by both models are below the ESS limiting (30mg/L), but the predictions differ by approximately 15 mg/L. The predictions of the ESS by the G_b-coupled turbulence model are approximately 12 mg/L while the predictions of the ESS by the G_b-decoupled turbulence model are close to the limiting ESS, 30 mg/L. This implies that the effect of buoyancy on turbulence is partially dissipated by the internal baffling (Zone B).

For the geometries No. 3, Cases 3a, b, c and the geometries No. 4, Case 4, the predictions of the ESS by both models are similar, within 5 mg/L. This implies that the effect of buoyancy on turbulence is largely dissipated by the internal baffling (Zone C).

Additionally, the results of the geometries No. 1 and 2 are consistent with Gao and Stenstrom (2018b), where an inlet dissipating baffle alone cannot reduce the effect of buoyancy on turbulence under the normal loading conditions. Also, comparisons among the predicted ESS by the G_b-coupled turbulence model for the geometry No. 5 (the original rectangular geometry) and the geometries No. 6 to 9 (the first four modified rectangular geometries) show that a poor baffling structure can increase the ESS.

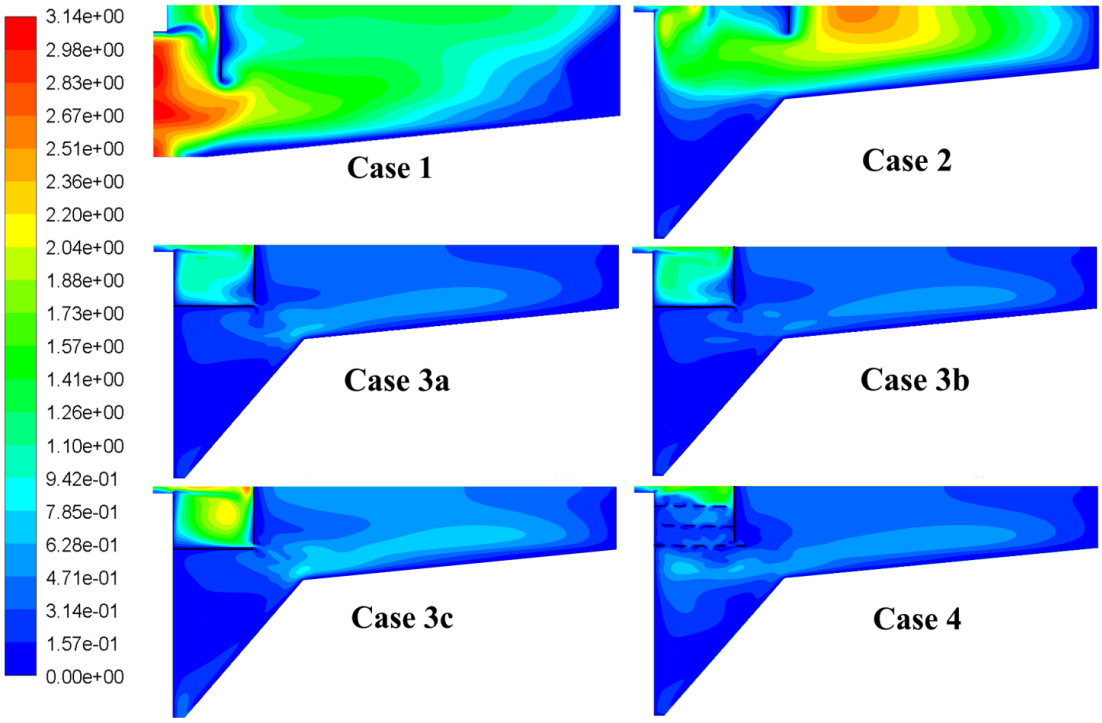

Figure 5-5. Predictions of the turbulent viscosity (kg/m-s) by the buoyancy-decoupled SKE models for the circular SSTs (Cases 1 to 4, respectively).

5.3.2 Analyzing the effects of the internal baffling structures on turbulence

In order to analyze the effects of the different baffling structures on turbulence, turbulent viscosity profiles are compared for these 13 different cases. Figures 5.5 and 5.6 show the predictions of the turbulent viscosity by the G_b-decoupled turbulence model on the circular and rectangular SSTs, respectively. As shown in Figure 5.5 for Cases 3a to 3c and Case 4 in Zone C, the turbulence is reduced significantly by forcing the influent to flow through the baffling structure created by both the vertical and horizontal baffles. However, without the horizontal baffle (Cases 1 and 2), the turbulence is not dissipated and extends to the entire SST.

Also, in Figure 5.6 for the Cases 10 and 11 in Zone B, the turbulence is reduced significantly by forcing the influent to flow through several vertical perforated walls on the depth

of entire SST. However, without a baffling structure or with a poor baffling structure (Cases 5 to 9), the turbulence is prevailing in the SSTs and the strongest area is near the effluent weir.

The predictions of the turbulence viscosity profiles by the G_b-decoupled turbulence model directly show that the effects of the baffling structures on turbulence are varied. Good baffling structures can significantly dissipate the effect of buoyancy on turbulence, while the effect of buoyancy on turbulence is strong in the SSTs without a baffling structure or with poor baffling structures.

In order to quantitatively describe the influence of the baffling structure on the turbulence, the averaged turbulent kinetic energy (TKE) by the G_b-decoupled/coupled turbulence models for these 13 cases are calculated and the differences of the averaged TKE predicted by the G_b-decoupled/coupled turbulence models are compared. The results are shown in Table 5.4 and indicate the differences of the averaged TKE by the G_b-decoupled/coupled SKE models. The differences between predicted TKE for both Cases 1 and 2 (Zone A) of the circular SSTs are 38-41%. For Cases 3a to 3c and Case 4 (Zone C), the differences in TKE are less, 14-18%. The larger differences for Cases 1 and 2 indicate the need for a coupled model, but the smaller differences in Cases 3a to 3c and Case 4 show that both models produce similar results.

For the rectangular SSTs, the differences of the averaged TKE by the G_b-decoupled/coupled SKE models for the Cases 5 to 9 are more than 90% (Zone A), and for the Cases 10 and 11 are approximately 80% (Zone B). These differences among the two sets of cases are much smaller than in the previous example.

The differences of the averaged TKE shown in Table 5.4 explain the prediction differences of the ESS by the G_b-decoupled/coupled SKE models for these 13 cases shown in Figures 5.5 and 5.6. For the circular SSTs, since the averaged TKE is significantly dissipated for the cases in Zone C, the averaged TKE by the G_b-decoupled SKE model is similar to it predicted by the G_b-coupled SKE model. Therefore, both models predict similar ESS. For the rectangular SSTs, since the differences among the cases in Zones A and B are much smaller than the differences in the circular SSTs, the predictions of the ESS by the G_b-decoupled/coupled SKE models only show qualitatively agreement. For the cases in Zone A, which the difference of the averaged TKE by the G_b-decoupled/coupled SKE models is large, the ESS can only be correctly predicted by the G_b-coupled SKE model. Therefore, the difference of averaged TKE by the G_b-decoupled/coupled turbulence models can be used as the indicator to quantify the effects of the baffling structures and to show the G_b-decoupled turbulence model tends to work. Also, further study is needed to differentiate the performance of the G_b-decoupled/coupled SKE models for the geometries in Zones B and C and is illustrated in the next section.

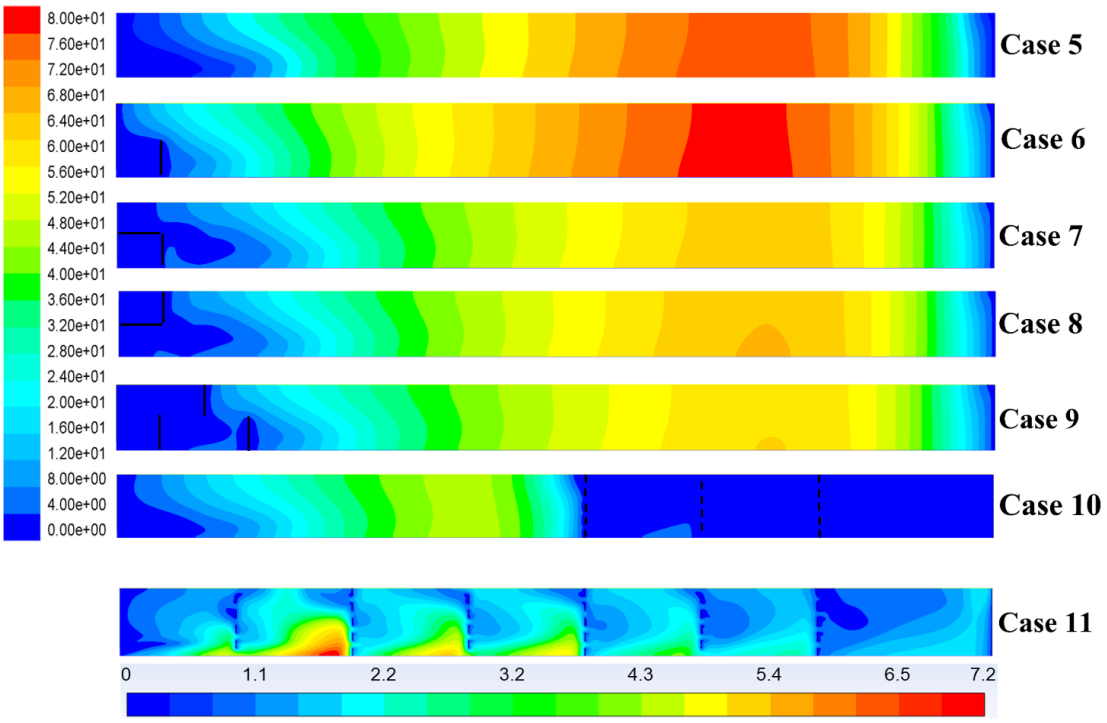

Figure 5-6. Predictions of the turbulent viscosity (kg/m-s) by the buoyancy-decoupled SKE models for the rectangular SSTs (Cases 5 to 11, respectively). The maximum turbulent viscosity in the Case 11 is less than 10% of it in the Cases 5 to 10. Therefore, in order to show the turbulence dissipation in the Case 11 clearly, a different colormap below the turbulent viscosity profile of the Case 11 is also applied in the Figure. 5.6

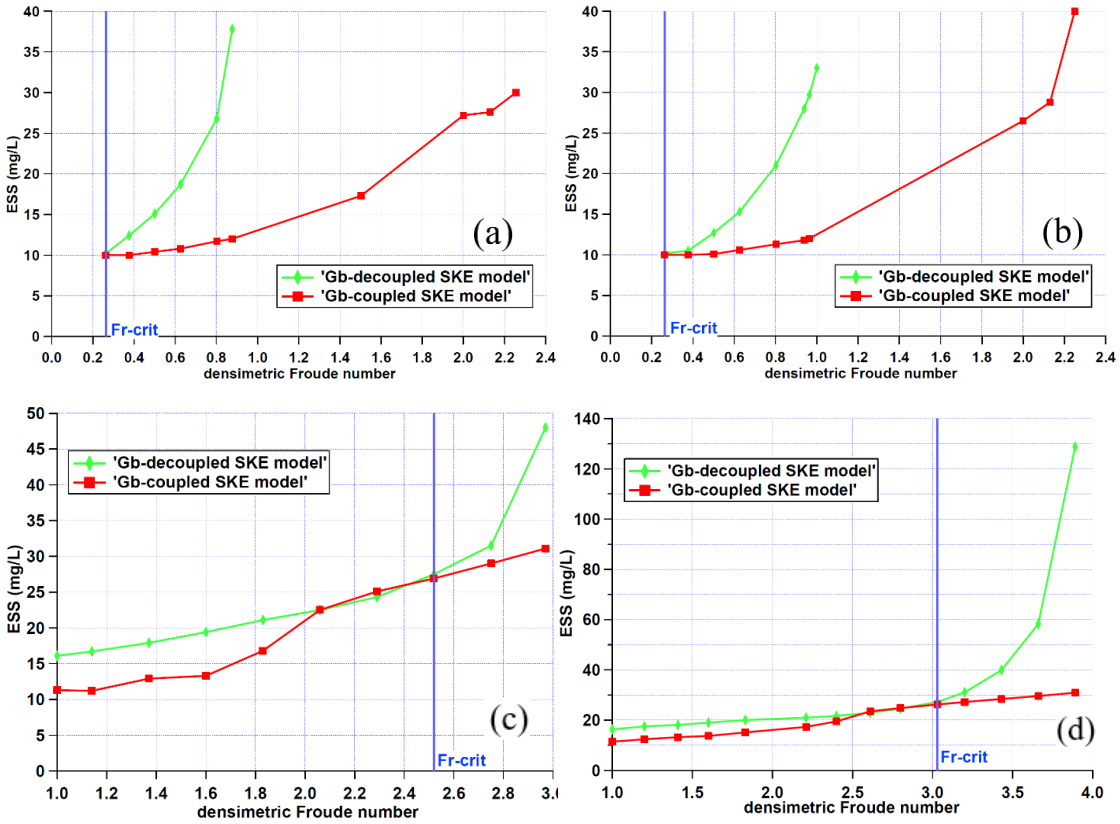

Figure 5-7. Predictions of the ESS as a function of inlet Fr in Zone B (geometries No. 10 (a) and 11 (b)) and in Zone C (geometries No. 3 (c) and 4 (d)).

5.3.3 CFD stress tests

Since Figure 5.4 shows that the G_b-decoupled turbulence model can also predict reasonable ESS for the SST geometries in Zones B and C, stress tests are simulated for these geometries by both models to compare the prediction of the SST capacities and to further distinguish the performance of the models. The stress tests are simulated by increasing the inlet densimetric Froude number (Fr).

Since the lowest surface overflow rate (SOR) applied for the cases in the Zones B and C is 0.332 m/h shown in Table 5.1, it is applied as the initial SOR for the CFD stress tests. Fr is then increased as the increase of the SOR and other conditions are kept constant.

Figure 5.7(a) to 5.7(d) shows the predicted ESS as a function of inlet Fr for the geometries in Zones B and C. It shows that as the inlet Fr increases, there is a critical Fr (Fr-crit). Below Fr-crit, the predictions of the G_b-decoupled/coupled turbulence models are similar. As the inlet Fr exceeds the Fr-crit, the predicted ESS by these two models begins to diverge. Therefore, the inlet Fr can be used as the second indicator (indicator No. 2) to further differentiate the performance of these two models for the Zones B and C.

Figure 5.7(a) and 5.7(b) shows that for geometries in Zone B, the values of the Fr-crit are both 0.263. The small value of Fr-crit indicates the predictions of the ESS by these two models are similar only when the Fr is very small and the predicted ESS diverges quickly with increasing Fr. When the G_b-decoupled turbulence model predicts the ESS over the limiting (30 mg/L) for the geometries in Zone B, the G_b-coupled turbulence model predicts approximately 12 mg/L ESS. For geometries in Zone C shown in Figure 5.7(c) and 5.7(d), the values of the Fr-crit are 2.52 and 3.03. Figure 5.7(c) and 7(d) shows that the predicted ESS by these two models respect to the Fr-crit are close to the ESS limiting (30mg/L), which indicates that both models can correctly predict the ESS before it reaches the limiting value.

The CFD stress tests show that both models work in Zone C from the low flow conditions to the limiting flow conditions, whereas the G_b-decoupled turbulence model works well when the buoyancy-coupled turbulence model for low flow conditions in Zone B. The results are consistent with the reduction of the difference of the averaged TKE (indicator No. 1) showing in Table 5.4, which the geometries in Zone C fully dissipate the effect of buoyancy on turbulence, while the

geometries in Zone B partially dissipate the effect of buoyancy on turbulence.

5.4. Conclusions

In this chapter, a Fluent-based 2D SST model is used to generalize the effects of internal baffling structures on the buoyancy-induced turbulence. Eleven SST geometries, including four circular SST geometries and seven rectangular SST geometries, are evaluated. Predictions of the ESS by the buoyancy-decoupled and buoyancy-coupled SKE models on these eleven SST geometries are compared, and the effects of the internal baffling structures on the turbulence properties, such as turbulent viscosity and averaged TKE, are analyzed and quantified. The results show that the effects of the baffling structures can be divided into three different zones, which negligibly (Zone A), partially (Zone B), and fully (Zone C) dissipate the turbulence. Furthermore, CFD stress tests are simulated on the geometries in the Zones B and C by both buoyancy-decoupled and buoyancy-coupled turbulence models and the inlet densimetric Froude number is applied to further differentiate the performance of these two models in Zones B and C.

Based on the simulation results on these different SST geometries, the following conclusions are made:

- The effects of the SST baffling structures on the buoyancy-induced turbulence are varied on both circular and rectangular SSTs. Good baffling structures can significantly dissipate the effect of buoyancy on turbulence, while the effect of buoyancy on turbulence is strong in the SST without a baffling structure or with poor baffling structures.

- The difference of the averaged TKE by the buoyancy-decoupled/coupled SKE models can be used as the first indicator (indicator No. 1) to quantify the influence of the baffling structure on the effect of buoyancy on turbulence and to differentiate the performance of these two turbulence models.
- The inlet densimetric Froude number can be used as the second indicator (indicator No. 2) to further distinguish the performance of the buoyancy-decoupled/coupled SKE models for the SST geometries in Zones B and C. Below the critical inlet Fr (Fr-crit), both models predict similar results. As soon as the inlet Fr exceeds Fr-crit, the predictions of the models gradually diverge.
- Only the buoyancy-coupled turbulence model can correctly predict the performance of the SST geometries in Zone A, while the buoyancy-decoupled turbulence model works as well as the buoyancy-coupled turbulence model under the low flow conditions in Zone B, and both models work from the low flow conditions to the limiting flow conditions in Zone C. This point is also summarized in Table 5.5.

5.5. Future Research

The applicability of some more advanced turbulence models, such as Reynold stress and LES models, have not yet been validated for SSTs partially due to the development of their damping term on the effect of buoyancy on turbulence. However, for the geometries which can also be correctly predicted without implementation the G_b in the turbulence model, the performance of these more advanced turbulence models can be compared with the turbulence

models in the k-epsilon family in the future research.

Table 5-4. Predictions of the averaged TKE (m^2/s^2) by the G_b-decoupled/coupled SKE models and calculations of their difference for each case. Three difference zones are classified based on the difference of the averaged TKE.

Cases No.	Geometry No. (Figure 1)	Averaged TKE (m^2/s^2) $\times 10^{-4}$		Difference (%)	Different Zones
Circular SSTs	Circular SSTs	G_b-decoupled	G_b-coupled		
1	1	3.39	2.10	38%	A
2	2	8.50	5.00	41%	A
3a	3	3.46	2.93	15%	C
3b	3	7.90	6.60	16%	C
3c	3	3.60	3.10	14%	C
4	4	3.65	3.00	18%	C
Rectangular SSTs	Rectangular SSTs				
5	5	6.33	0.37	94%	A
6	6	7.00	0.66	90%	A
7	7	6.20	1.10	82%	A
8	8	6.00	1.00	83%	A
9	9	5.70	0.60	89%	A
10	10	4.40	0.91	79%	B
11	11	1.10	0.27	75%	B

Table 5-5. Summary of all the cases and relevant geometries which can be correctly predicted by the G_b-decoupled or G_b-coupled turbulence models

Correct predictions by G_b-decoupled or -coupled models	Zones	Cases No.	Geometries No.
G_b-coupled turbulence model only	A	1, 2, 7-11	1, 2, 5-9
G_b-decoupled turbulence model (partially*) & G_b-coupled turbulence model	B	12, 13	10, 11
G_b-decoupled turbulence model (fully*) & G_b-coupled turbulence model	C	3-6	3, 4

Chapter 6 The influence of model parameters and inlet turbulence boundary specification methods in secondary settling tanks-A computational fluid dynamics study

6.1. Introduction

In conventional wastewater treatment plants (WWTPs), secondary settling tanks (SST), also known as secondary sedimentation tanks or secondary clarifiers are used in the activated sludge process (ASP) to remove organic matter and reduce nutrients such as nitrogen and phosphorus (Li and Stenstrom, 2014). SST performance is important for overall plant efficiency and techniques to improve performance have been evaluated and modeling using computational fluid dynamics (CFD) is being used, especially with the availability of greater computing resources. Since Larsen (1977) set the framework for CFD modeling of settling tanks, CFD has become a popular tool for the researchers and engineers to understand the hydrodynamics of SSTs and to optimize their internal geometry and process efficiency (Zhou and McCorquodale, 1992a, b, c; Samstag et al., 1992; Krebs et al., 1996; Vitasovic et al., 1997; McCorquodale et al., 2004; Xanthos et al., 2011; Patziger et al., 2012; Xanthos et al., 2013; Das et al., 2016; Patziger, 2016; Gao and Stenstrom, 2017).

Despite the successes of CFD modelling of SSTs, a significant shortcoming of the CFD modeling is the lack of a generally accepted SST modeling framework (assumptions for turbulence, settling velocity, sludge rheology). The different assumptions implemented in the model framework still do not fully conform to experimental observations and improvements are still needed.

In the CFD modelling for SST, one of the major constraints is the lack of a consistent way of calculating sludge settling properties which are needed to accurately describe clarification, settling, and compression of the sludge over the range of concentrations routinely found in SSTs (Plósz et al., 2012). Li and Stenstrom (2014) in their one-dimensional SST modeling paper, reviewed 15 different functions of settling velocity versus concentration. Although many model improvements have been achieved based on the Takács settling equation (Takács et al., 1991; Bürger et al., 2011; Guyonvarch et al., 2015; Xu et al., 2017), they have not been widely accepted by engineers. Therefore, Takács model (Equation. 6.1) is still the most popular sludge settling equation being implemented in CFD SST models.

$$V_s = V_o(e^{-r_h(C-C_{min})} - e^{-r_p(C-C_{min})}) \quad (6.1)$$

where V_o is Stokes velocity, r_h and r_p account for rapidly and poorly settling floc, respectively. The constant C_{min} is the concentration of on-settleable solids in the effluent of the SST (Vitasovic et al., 1997). While the value of r_h can be obtained from a series of batch tests over a concentration range, by measuring the zone settling velocities as the linear descending rate of the liquid/solid interface in academic projects (Burt 2010, Ramin, 2014) and can also be correlated with sludge volume index (SVI), stirred sludge volume index (SSVI), and diluted sludge volume index (DSVI) in many consulting projects (Wahlberg and Keinath (1988); Daigger (1995); Ozinsky and Ekama (1995); Griborio and McCorquodale (2016)), there is not a guidance to obtain the value of r_p. Table 6.1 shows that differences among values of r_p used in previous studies are significant. Since Ekama and Marais (2004) stated that value of $\boldsymbol{r_p}$ in the Takács settling model

affects the CFD prediction of ESS, its effect will be quantified in this study.

The second constraint is the lack of a generally accepted sludge rheological model. Lakehal et al. (1999) and Saffarian et al. (2010, 2011) conducted sensitivity studies for previously published sludge rheological models, such as the Bokil, Casson Bingham, Herschel-Bulkley and modified Herschel-Bulkley models. The results showed that the application of different sludge rheological models has significant impacts on the prediction of concentration and velocity fields. Additionally, since there is no consensus of the comprehensive and repeatable rheological measurement procedure (Ratkovich et al., 2013), these different rheological models should be applied cautiously.

The third constraint is the applications of turbulence models. Although standard k-ε model (SKE) has been widely applied in the CFD SST modelling over the last 30 years because of its robustness, economy and reasonable accuracy for the prediction of turbulent flow in SSTs, two modified versions of the SKE model (RNG k-ε model and Realizable k-ε model) have been used in several recent settling tank studies (Tamayol et al., 2009; Tarpagkou et al., 2013; Das et al., 2016; Patziger, 2016). Gao and Stenstrom (2018a) compared the performance of these three turbulence models and the results showed that the prediction difference of flow and concentration fields among these models is significant. The predicted sludge blanket height (SBH) and concentration of returned activated sludge (RAS) are more than 10% among different turbulence models.

Also, the inlet turbulence boundary condition can be specified using the estimated turbulent kinetic energy (TKE) and turbulent dissipation rate (TDR) or turbulent intensity (TI) and hydraulic

diameter. Table 6.1 summarizes three turbulence specification methods for the inlet turbulence boundary condition. The first two methods (No. 14 and 15) estimate the TKE and TDR at the inlet boundary and the third method (No. 16) uses TI and hydraulic diameter to define the turbulence profile at the inlet boundary. With the same inflow conditions and internal structure, the prediction of the inlet TKE and TDR can be more than one and two orders of magnitude among these three different turbulence specification methods. Therefore, different inlet turbulence specification methods may have strong effects on the prediction of SST performance.

Additionally, there are uncertainties of model parameters, such as (1) the turbulent Schmidt number ($\boldsymbol{\sigma_c}$) in the sludge transport equation; (2) the coupling of the buoyancy term ($\boldsymbol{G_b}$) in the TKE equation; (3) the coefficient of the buoyancy term ($\boldsymbol{C_3}$) in the TDR equation and (4) the dry solids density ($\boldsymbol{\rho_p}$). The effects of the uncertainties of the first three model parameters have been investigated previously by Gao and Stenstrom (2018b), and the effects of $\boldsymbol{r_p}$ and $\boldsymbol{\rho_p}$ are discussed in this study. Since the $\boldsymbol{\rho_p}$ is coupled within every governing equation, the variation of $\boldsymbol{\rho_p}$ will influence the entire flow and concentration fields.

Table 6.1 shows key model parameter values and boundary conditions used in previous studies. There is a large range in values and there is no systematic way of predicting the impact of the parameter uncertainties and different inlet turbulence boundary conditions. The hydrodynamics of the entire SST are very sensitive to the changes of the inlet boundary condition and parameters, which means it is important to understand the effects of varied conditions on SST performance.

In this chapter, sensitivity studies are conducted to understand the effects of the

uncertainties of r_p and ρ_p as well as the different inlet turbulence specification methods. Three different conditions varying flow rate, solids concentration and recycle rate for the SSTs of the Wintey WWTP, described by Burt (2010), are used in the sensitivity study. Trial 1 is applied to the original circular SST, and the Trials 2 and 3 are applied to the modified circular SST. The performance indicators (ESS, RAS concentration and SBH) and the sludge settling velocity, flow and concentration profiles are observed as a function of the different values of the model parameters. For brevity, only the trial showing the largest discrepancy between the prediction and measurement of the performance indicator are presented as the representative trial to illustrate the differences in the profiles.

Table 6-1. Range of key model parameters used previous studies: settling parameter accounting for the particle with poor settling property (r_p, Takacs settling model), dry solids density (ρ_p) and turbulence specification method for the inlet boundary condition

No.	Parameters and definitions	References
#	r_p (L/g)	
1	4	McCorquodale et al. (2004)
2	5	McCorquodale et al. (2004)
3	10	Vitasovic et al. (1997); Ekama and Marais (2004)
4	$10r_h$*	Ekama et al. (1997); Weiss et al. (2007)
5	15-30	Zhou and McCorquodale (1992a)
6	20	Tamayol et al. (2009)
	ρ_p (kg/m^3)	
7	1100	Deininger et al. (1998)
8	1450	Larsen (1977); Saffarian et al. (2010)
9	1500	Tarpagkou and Pantokratoras (2013)
10	1600	Weiss et al. (2007)
11	1360-1660	Zhou and McCorquodale (1992a)
12	1700-1800	Kinnear (2002)
13	1907/1743/2070	Xu et al. (2017)
	Inlet turbulence-boundary conditions	
14	$k_{in} = 1.5(I_u v_{in})^2$ $\varepsilon = \frac{C_\mu^{3/4} k_{in}^{3/2}}{\kappa L_u}$	Lakehal et al. (1999); Saffarian et al. (2010, 2011)
15	$k_{in} = \alpha u_o^2$ $\varepsilon = \frac{C_\mu^{3/4} k_{in}^{3/2}}{L_m}$	Zhou and McCorquodale (1992a); Kleine and Reddy (2005)
16	TI Hydraulic diameter	Gao and Stenstrom (2018a, 2018b, 2019a, 2019b)

*: r_h is the exponential term accounting for the particle with good settling property.

Table 6-2. Inputs for the Trials in this study

	Inflow parameters			Settling parameters			Dry solids density
Trials	MLSS	RAS Ratio	Q_{in}	V_o	r_h	r_p	ρ_p
#	g/L	-	m^3/s	m/h	L/g	L/g	kg/m^3
1	4.187	1.09	0.0506	12.64	0.340	3.4-30	1000-2100
2	3.384	1.09	0.0506	13.32	0.386	3.8-30	1000-2100
3	2.904	0.83	0.0900	13.32	0.386	3.8-30	1000-2100

6.2. Materials and methods

6.2.1 The numerical model

A two-dimensional (2D) CFD SST model is developed to conduct the sensitivity tests and provides a detailed insight into the complex flow and transport processes in the SST. This method can largely reduce the number of cells and calculation time without deteriorating the accuracy of the simulation compared with the three-dimensional (3D) simulations (Patziger, 2016). The turbulent flow is modelled by the Reynolds-averaged Navier-Stokes equations with a SKE model closure (Rodi, 1980). The solids transport process is calculated by user defined advection-diffusion equation with terms describing settling and thickening based on the Takács settling function (Takács et al., 1999; Patziger et al., 2012). All the governing equations are numerically solved by the commercial CFD code ANSYS Fluent (v.18.2). A more detailed description of CFD model non-Newtonian flow behavior of the activated sludge and buoyancy effects were illustrated in Gao and Stenstrom (2018a).

6.2.2 Model calibration and validation

Three different trials are compared using Burt (2010) data for two different SSTs at the Wintey WWTP for the model calibration. Trial 1 used the original SST with a large stilling well; Trials 2 and 3 are tested in a modified SST with the addition of McKinney baffle below the stilling well. The baffle was added in anticipation of improving ESS, even at higher flow rates. The main inputs for these three trials are shown in Table 6.2. The numerical velocity profiles and the corresponding experimental data show reasonable agreements.

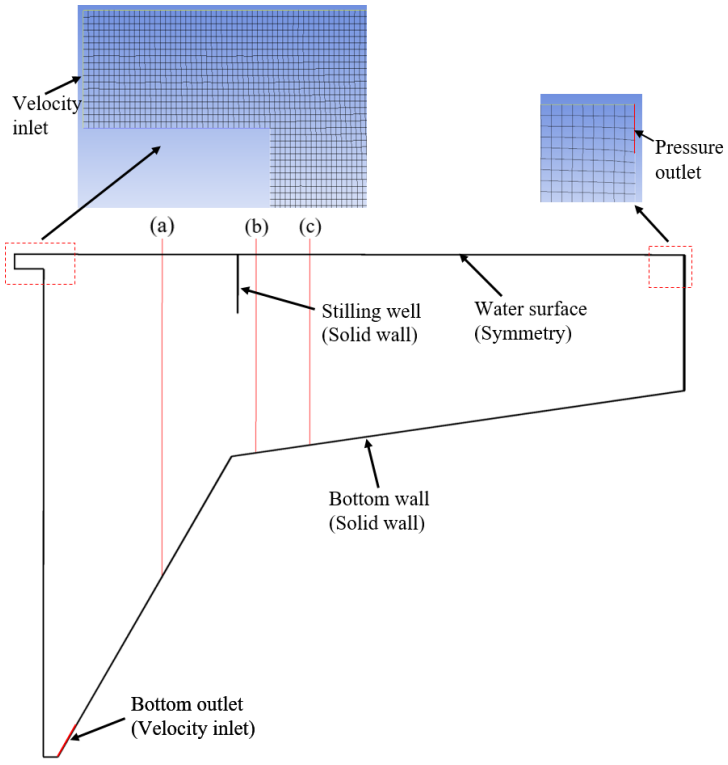

Figure 6-1. Original SST Diagram with representative computed locations and boundary conditions for Trial 1. (a)-(c) refer to the radial locations for the model calibration.

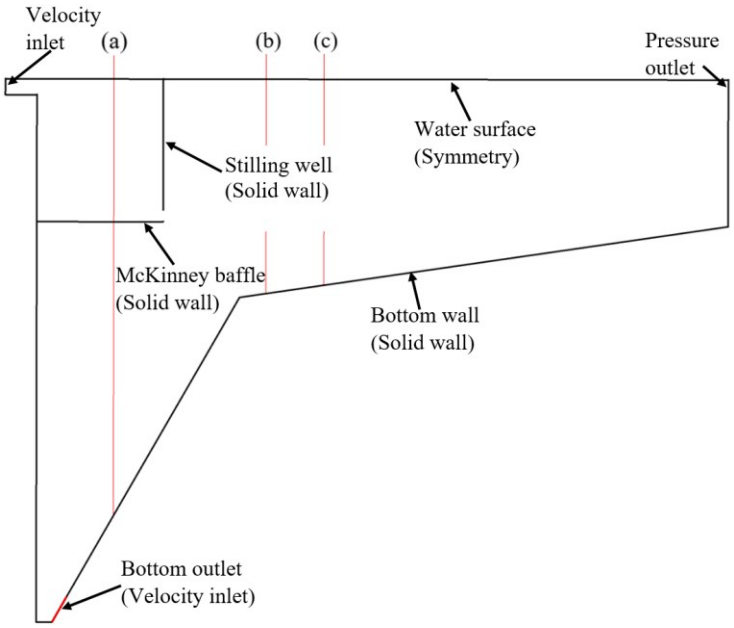

Figure 6-2. Modified SST Diagram with representative computed locations and boundary conditions for Trials 2 and 3. (a)-(c) refer to the radial locations for the model calibration.

6.3. Results and discussion

To evaluate the effects of the turbulence specification methods of the inlet boundary conditions and the values of the parameters r_p and ρ_p, sensitivity tests are conducted for different turbulence specifications and parameter values. Table 6.1 shows the parameter ranges used by previous researchers. Based upon these ranges, simulations are made from r_p =3.4 to 30 L/g for Trial 1 and 3.86 to 30 L/g for Trials 2 and 3. Also, ρ_p is varied from 1100 to 2100 kg/m^3 for all trials. The results are shown in Table 6.3.

Additionally, the neutral density condition is simulated to compare with the results of density-coupled conditions for each trial. All the parameter values and turbulence specification methods are summarized in the second column in Table 6.3.

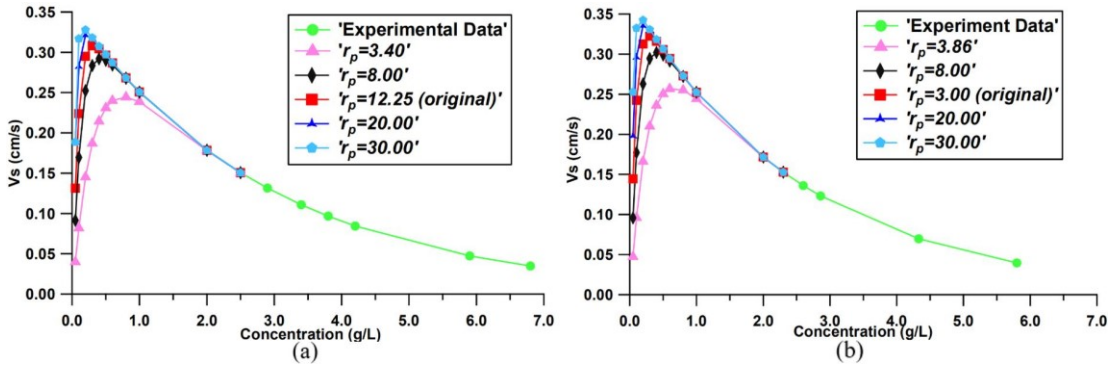

Figure 6-3. Settling velocity curves with the variation of r_p (a (Left): Trial 1; b (Right): Trials 2, 3).

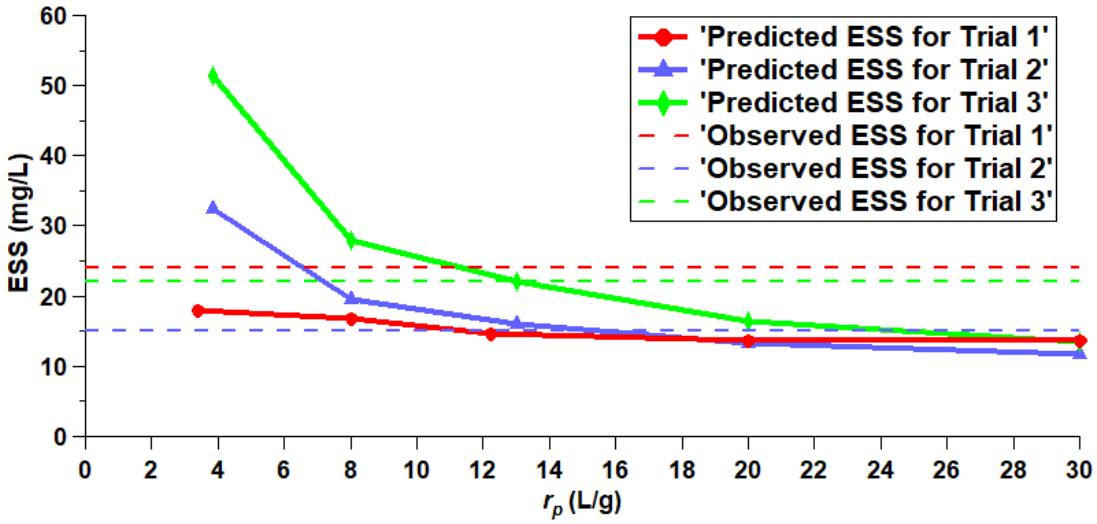

Figure 6-4. Predictions of ESS (mg/L) respect to r_p (L/g) for Trials 1 to 3.

6.3.1 Effects of sludge settling parameter (r_p)

The settling velocity curves with varied r_p are shown in Figure 6.3. The value of r_p controls the settling velocity with small particles (for concentration <1.0 g/L), which shows an exponential increase, finally reaching a maximum. The peak settling velocity increases more than 30% as r_p increases from 3.4 to 30 L/g.

The field measurements and the predictions of each model for the performance indicators (SBH, ESS and RAS concentrations) are summarized in Table 6.3. The field measurements (Table

6.3 and Figure 6.4) show that the ESS is acceptable for all three trials, although the ESS for Trial 2 is somewhat less. Trials 1 and 2/3 differ because of the addition of the McKinney baffle for Trials 2 and 3. The flow rates are the same in Trials 1 and 2 but the MLSS concentrations is approximately 20% less in Trial 2. Also, the flow rate in Trial 3 is 80% larger than in Trial 1. The McKinney baffle is the primary reason for the improved performance of Trials 2 and 3 over Trial 1. Unfortunately, there are no observations for ESS at this higher flow without the McKinney baffle.

Model predictions for Trial 1 are always better than actual performance and are insensitive to r_p. Trials 2 and 3 are much more sensitive to r_p and predict failure due to high ESS at low values of r_p, even when the field observations show success. As r_p increases (better settling performance for small particles), ESS is reduced in each trial but especially in Trials 2 and 3, as shown in Figure 6.4. The variation of the ESS with respect to r_p is large and causes remarkably different ESS predictions, even to the extent of predicting clarification failure (ESS > 30 mg/L). However, Table 3 shows that r_p has little influence on the sludge thickening, and its effects on thickening are not likely to important.

The results show that comparison to field data is required for Trials 2 and 3 and that Trial 1 simulation is independent of field observations. Without field measurements for Trials 1 and 2, selecting the wrong value of r_p can lead to the opposite conclusion, where the model predicts that the original SST performs better than the modified SST. Selecting too large a value of r_p may significantly overpredict the clarification performance of the SST. Therefore, r_p should be well-calibrated based on the predictions of the ESS and field measurements of multiple SSTs to not only

fulfill the calibration for each SST, but also show the correct performance difference among the SSTs.

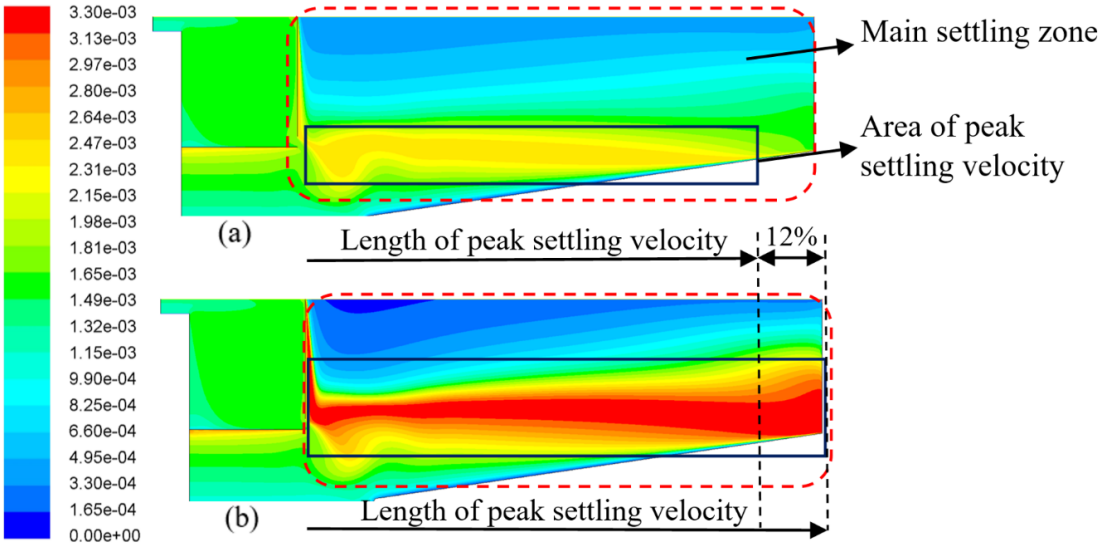

Figure 6-5. Predictions of settling velocity profiles (m/s) for the Trial 3 (a (top): r_p =3.86 L/g; b (bottom): r_p =30.00 L/g).

Figures 6.5 (a) and 6.5 (b) show the predictions of settling velocity profiles for Trial 3 with the smallest and the largest values of r_p (r_p =3.86 (a) and 30.00 (b) L/g, respectively). It shows that the prediction of settling velocity for r_p =30 L/g is higher than the prediction for r_p =3.86 L/g in the entire main settling zone (circled in red dash line). This difference becomes more significant near the side wall, where the settling velocity is one order of magnitude greater. Additionally, the region of the peak settling velocity (circled in black solid line) in Figure 6.5 (b) is 12% longer in the radial direction and 50% larger in overall size than that in Figure 6.5 (a). With greater sludge settling velocity (higher r_p value), the region of peak settling velocity exists in the entire main settling zone (from the stilling well to the side wall).

Figures 6.6 (a) and 6.6 (b) show the prediction of sludge concentration profiles for Trial 3

with the smallest and the largest values of r_p (r_p =3.86 (a) and 30.00 (b) L/g, respectively). Only the regions with sludge concentration higher than 30 mg/L are shown. The Figure 6.6b shows that with larger r_p, the higher settling velocity in the main settling zone results in a lower suspended solids concentration at the upper region of the main settling zone. The 30 mg/L iso-concentration contour is 0.65m below the water surface on the side wall. On the contrary, the concentration profile predicted with small r_p (as shown in Figure 6.6a) shows the sludge concentration is above 30mg/L in the entire SST.

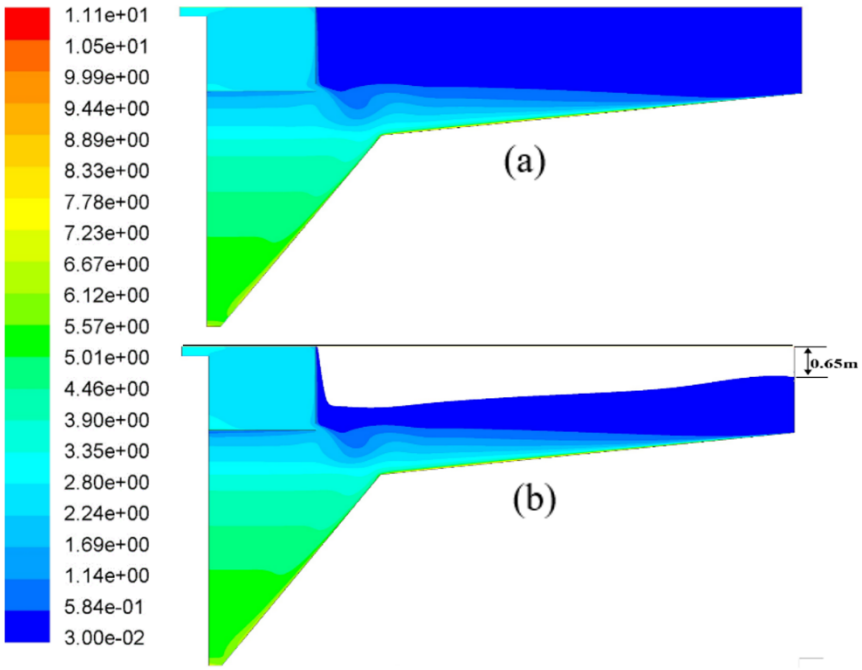

Figure 6-6. Predictions of sludge concentration profiles (g/L) for the Trail 3 (a (top): r_p =3.86 L/g; b (bottom): r_p =30.00 L/g). Only the regions with sludge concentration higher than 30 mg/L are shown.

6.3.2 Effects of dry solids density (ρ_p)

Table 6.3 shows that as the value of ρ_p increases in Trials 1 to 3, the predictions of ESS by the density-coupled model are reduced by 42.4%, 14.3%, and 11.7%, respectively. However, compared with the absolute difference between the smallest and the largest ESS predicted by

different values of r_p as shown in Figure 6.7, the variation of dry solids density still predicts the ESS value in an acceptable range, even if value of solids density is almost doubled. Similarly to the results of varying r_p, the change in the value of ρ_p in the density-coupled condition has little influence on the sludge thickening performance (SBH and RAS concentration). Therefore, a medium value of ρ_p, such as 1450 kg/m^3, is a good assumption.

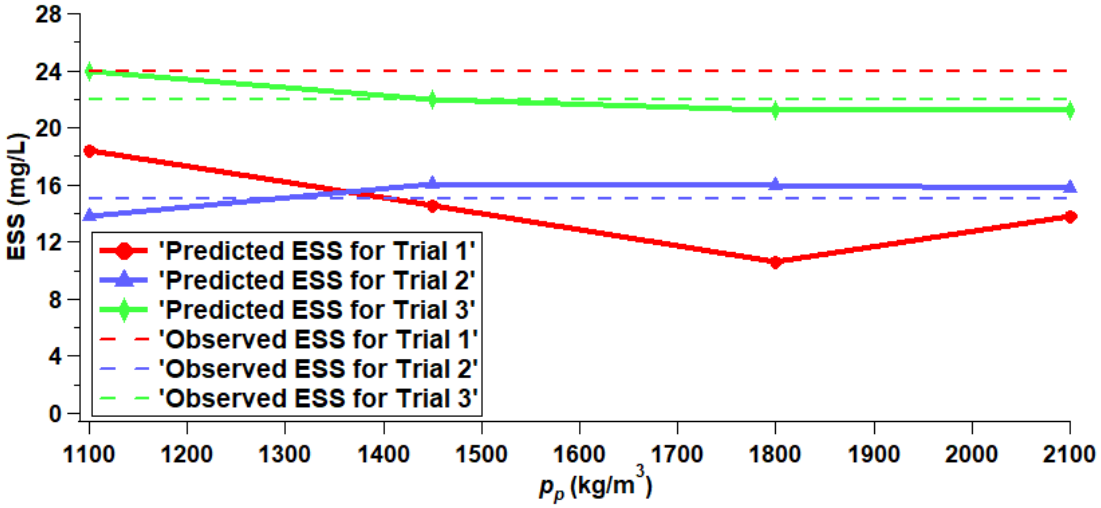

Figure 6-7. Prediction of ESS (mg/L) respect to ρ_p (kg/m^3) for Trials 1 to 3.

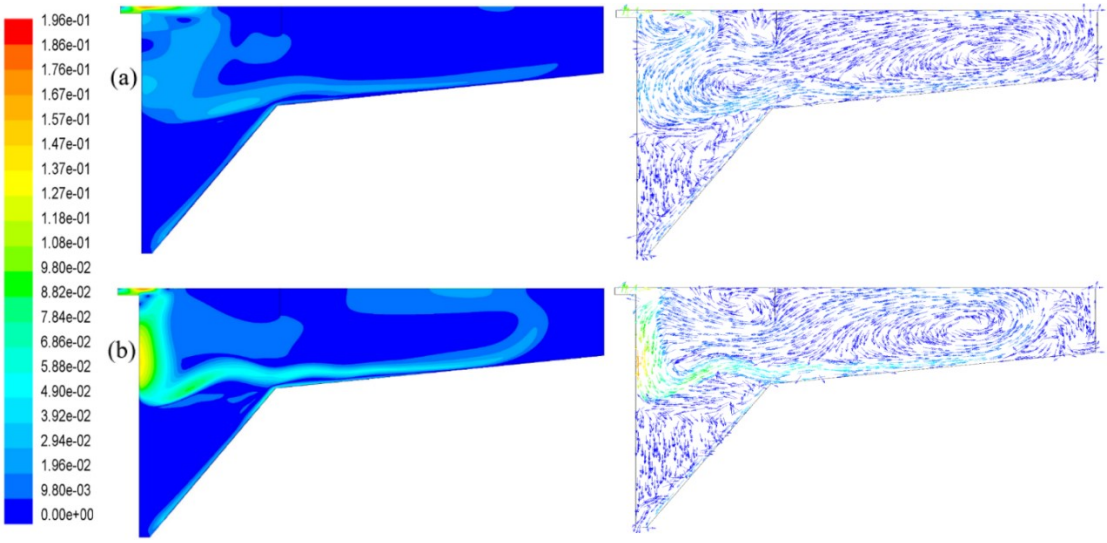

Figure 6-8. Predictions of velocity magnitude (Left) and vector profiles (Right) (m/s) with two

different dry solids densities for Trial 1 (a (top): 1100 kg/m^3; b (bottom): 2100 kg/m^3).

Figures 6.8 (a, b) and 6.9 (a, b) show the predictions of velocity and sludge settling velocity profiles with two different dry solids densities (a: 1100 kg/m^3; b: 2100 kg/m^3) for Trial 1. The prediction of velocity profile with lower dry solids density (Figure. 6.8a) shows that the stronger initial momentum from the inlet results in a longer horizontal jet at the water surface. Along the horizontal jet, the velocity is gradually reduced as the energy is dissipated. At the same time, the sludge settling velocity (Figure. 6.9a) gradually increases along the horizontal jet and reaches a maximum at the end of the jet. Conversely, the prediction of velocity profile with higher dry solids density (Figure. 6.8b) shows a shorter horizontal jet, but a stronger density current in the vertical direction. Therefore, Figure. 6.9b shows the peak sludge settling velocity is closer to the inlet location. Additionally, at the center of the main settling zone, the settling velocity with higher dry solids density is one order of magnitude higher than with a lower dry solids density, which leads to better clarification at the upper layer.

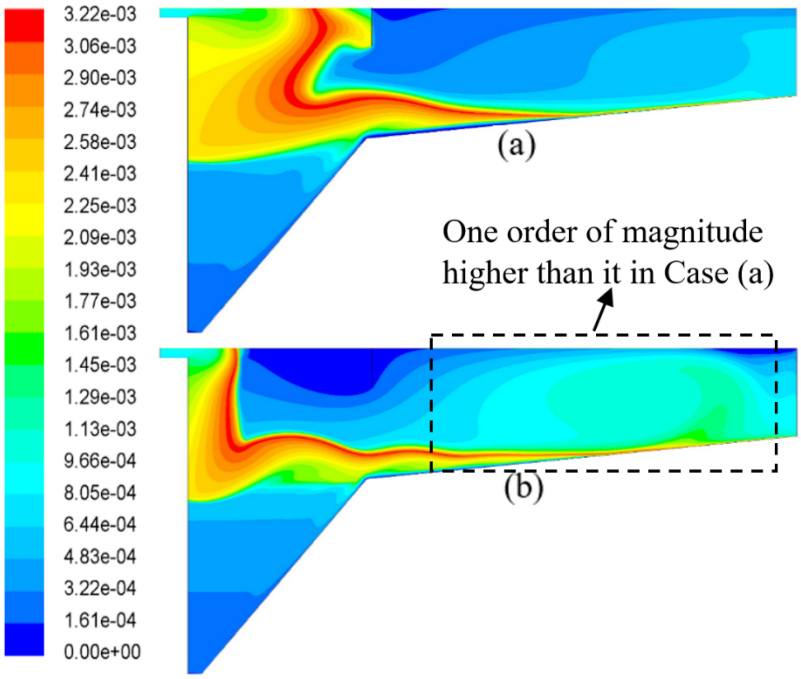

Figure 6-9. Predictions of sludge settling velocity magnitude profiles (m/s) with two different dry solids densities for Trial 1 (a (top): 1100 kg/m^3; b (bottom): 2100 kg/m^3).

If the solids density is ignored (e.g., the neutral density condition), the SBH reaches the effluent weir and the ESS is dramatically over-predicted. Figures 6.10 (a) and 6.10 (b) compare the sludge concentration profiles predicted by density-coupled condition and neutral density condition, respectively. Compared with density-coupled condition, which correctly predicts the sludge thickening at the bottom and clarification at the upper layer, the neutral density condition fails to predict sludge distribution correctly. Therefore, the hydrodynamics of SST should be predicted using density-coupled conditions.

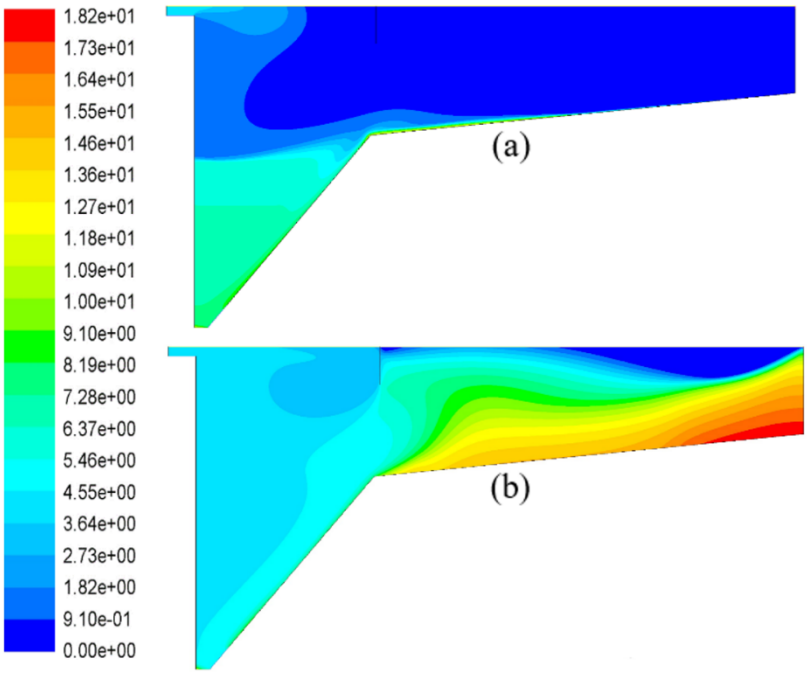

Figure 6-10. Comparison of sludge concentration profiles (g/L) predicted by (a) density-coupled condition and (b) neutral density condition

6.3.3 Effects of inlet-turbulence specification methods

Table 6.1 (rows numbered 14-16) shows the three different, commonly used turbulence specification methods for the inlet boundary condition. The calculation of the initial TKE and TDR at the inlet for the three trials are shown in Table 6.4 under the "Inlet boundary values" columns. The calculation of the averaged TKE and TDR on the scale of entire SST for the three trials are shown in Table 6.4 under the "Averaged values" columns. The results in Table 6.4 show that although the differences in the initial values of TKE and TDR calculated using the different specification methods can differ by as much as one to four orders of magnitude, respectively, the difference in the turbulence field calculated by the different boundary specification methods on the scale of entire SST is negligible. Table 6.3 also shows that the difference of each performance indicator predicted by these three different turbulence specification methods is minimal. Hence,

the different turbulence specification methods can only cause local effects in the near area of inlet boundary and have few effects on the prediction of variables outside of the inlet zone.

6.4. Conclusions

In this chapter, a Fluent-based 2D SST model is used to analyze the impacts of using three different turbulence specification methods for the inlet boundary condition and ranges of two model parameters: (1) exponential term accounting for the small particle settling (r_p) in the Takács settling model, and (2) dry solids density (ρ_p) in the density-coupled conditions. Sensitivity tests are conducted to compare the predictions of the performance indicators (ESS, RAS and SBH) and different variable fields (sludge settling velocity, velocity and sludge concentration fields). The effects of the neutral density condition are also studied, and the prediction results are compared with the density-coupled results.

Based on the simulation results of the sensitivity tests, the following conclusions are made:

- The exponential term accounting for the small particle (r_p) in the Takács settling model is one of the key parameters to correctly predict the ESS. The small values of the r_p may incorrectly predict the clarification failure of the SST, when the field measurements show the SST is functioning well. However, r_p has little influence on the sludge thickening. Therefore, r_p can be used to adjust the ESS, when SBH and RAS concentration are well calibrated to the field data, but the ESS does not fit field observations.
- The field observations show the modified SST with the addition of a McKinney baffle performs better than the original SST, whereas using an incorrect value of r_p may result in

an opposite prediction.

- It is recommended that r_p be adjusted to conform to ESS field measurements at multiple SSTs to not only satisfy the calibration of ESS for each SST, but also show the correct performance difference among the SSTs.
- The dry solids density (ρ_p) also effects on the prediction of ESS, but the effects are small compared to the effects of r_p, on predicted ESS. Doubling the value of ρ_p still produces acceptable comparisons to field data. Therefore, a medium value of r_p, such as 1450 kg/m^3, is a good assumption.
- Since inflow to the SST is driven by density, using neutral density assumptions in the SST model can cause wrong prediction for the SST performance.
- Different turbulence specification methods for the inlet boundary have only local effects on the hydrodynamics near the inlet and have little influences on the prediction of the overall performance of SST. Therefore, each turbulence specification method can be applied to obtain similar predictions.

Table 6-3. Effects of model parameters accounting for the particle with poor settling property in the Takács settling model settling (r_p), dry solids density (ρ_p) and turbulence specification methods on the inlet boundary condition on the performance indicators

	Geometries	Original SST			Modified SST					
	Trials	No. 1			No. 2			No. 3		
Exp #	Model uncertainties	ESS mg/L	SBH m	RAS mg/L	ESS mg/L	SBH m	RAS mg/L	ESS mg/L	SBH m	RAS mg/L
Measure-ment		24.0	1.85	-	15.0	2.10	-	22.0	1.80	-
	r_p (L/g)									
1	3.40[1]/3.86[2,3]	**18.0**	1.90	7790	**32.4**	1.90	6366	**51.4**	1.85	5800
2	8.00	**16.8**	1.93	7800	**19.6**	1.92	6280	**28.0**	1.85	5825
3	12.25[1]/13.00[2,3]	**14.6**	2.01	7798	**16.1**	1.95	6482	**22.0**	1.85	6230
4	20.00	**13.6**	2.00	7830	**13.3**	2.03	6378	**16.4**	1.85	5820
5	30.00	**13.6**	2.04	7800	**11.7**	1.96	6455	**13.5**	1.85	5823
Difference (%)*		**24.4**	6.87	0.5	**63.9**	6.40	3.11	**73.7**	0	6.50
	ρ_p (kg/m^3)									
6	1000	*2400*	*0.00*	*5197*	*3329*	*0.01*	*4388*	*2542*	*0.00*	*3253*
7	1100	**18.4**	2.00	7835	**13.8**	1.98	6483	**24.0**	1.86	5848
8	1450	**14.6**	2.01	7798	**16.1**	1.95	6482	**22.0**	1.85	6230
9	1800	**10.6**	2.20	7800	**16.0**	1.93	6468	**21.2**	1.85	5812
10	2100	**13.8**	2.12	7789	**15.8**	1.93	6438	**21.2**	1.85	5809
Difference (%)*		**42.4**	9.10	5.87	**14.3**	2.53	0.69	**11.7**	0.53	6.76

	Inlet boundary									
11	No. 14[a]	14.6	2.01	7848	16.2	1.96	6532	21.8	1.85	5843
12	No. 15[b]	14.6	2.01	7804	16.4	1.95	6483	21.5	1.85	5834
13	No. 16[c]	14.6	2.01	7798	16.1	1.95	6482	22.0	1.85	6230
Difference (%)*		0	0	0.63	1.22	0.51	0.77	2.27	0	6.36

SBH: Defined as the vertical distance from the top effluent to the location with 850 mg/L sludge concentration, which is the same definition applied in the Burt (2010).

1-3: Trials 1 to 3, respectively. 3.40 is 10 times the value of r_h (0.34 L/g) used in the Trial No. 1 and 3.86 is 10 times the value of r_h (0.386 L/g) used in the Trials No. 2 and 3. Also, 12.25 is the value of r_p used in the Trial No. 1 in the original literature and 13.00 is the value of r_p used in the Trials No. 2 and 3 in the original literature.

*: Percentage reduction between the maximum and minimum value of the performance indicator as the variation of the value of each model uncertainty

a-c: Rows numbered 14 to 16 from Table 6.1, respectively.

Bond values: Results of the performance indicator, which is greatly influenced (more than 10% difference between the smallest and the largest value) by the sensitivity tests in each trial.

Italic values: Results of the performance indicators with neutral density condition in each trial.

Table 6-4. Calculation of initial TKE and TDR with different turbulence specification methods on the inlet boundary condition and the averaged TKE and TDR on the scale of entire SST.

	Trial-1				Trial-2				Trial-3			
No.	Inlet boundary Values		Averaged Values		Inlet boundary values		Averaged values		Inlet boundary values		Averaged values	
#	TKE	TDR	TKE	TDR	TKE	TDR	TKE	TDR	TKE	TDR	TKE	TDR
14[a]	7.60×10^{-4}	5.75×10^{-6}	5.40×10^{-5}	3.80×10^{-6}	7.60×10^{-4}	8.62×10^{-6}	4.38×10^{-5}	2.58×10^{-6}	2.41×10^{-3}	4.85×10^{-5}	9.44×10^{-5}	9.78×10^{-6}
15[b]	2.03×10^{-4}	1.67×10^{-3}	5.37×10^{-5}	3.69×10^{-6}	2.03×10^{-4}	1.67×10^{-3}	3.28×10^{-5}	2.28×10^{-6}	6.42×10^{-3}	9.38×10^{-3}	7.42×10^{-5}	8.62×10^{-6}
16[c]	3.80×10^{-5}	6.88×10^{-7}	5.21×10^{-5}	3.45×10^{-6}	3.75×10^{-5}	6.74×10^{-7}	3.46×10^{-5}	2.13×10^{-6}	1.20×10^{-4}	3.87×10^{-6}	7.90×10^{-5}	8.46×10^{-6}

b-c: Rows numbered 14 to 16 are from Table 1.

Chapter 7 Computational Fluid Dynamics Applied to Secondary Clarifier Analysis

7.1. Introduction

Effluent suspended solids (ESS) from biological processes, such as the activated sludge process, are affected by the performance of secondary clarifiers or secondary settling tanks (SSTs). Since escaping solids contain contaminants, like BOD, COD, heavy metals, nitrogen and phosphorus, the removal efficiency of SSTs is fundamental to the overall performance of a wastewater treatment plant (Parker et al., 1996).

As noted by Kleine and Reddy (2005), there are two different functions of SSTs: clarification and thickening. Clarification is used to separate the suspended solids (SS) from the effluent; thickening is the process to concentrate the sludge in order to recycle or dispose of it in a small volume. The failure in clarification or the thickening processes, which usually results from not understanding of the two-phase nature of the flow, will result in violations of the effluent permits and biomass loss (Ben and Stenstrom, 2014). Moreover, it may be more complicated with the existence of hydrodynamic and physical effects, such as density currents and flocculation (Kleine and Reddy, 2005). Therefore, SSTs designed by a simple rule such as surface overflow rate (SOR) and hydraulic retention time (HRT) are problematic, and many other influential factors, such as inlet and outlet structures, tank geometry, wind movement, rainfall, concentration of mixed liquor suspended solids or density gradients, and temperature should be taken into account (Wang et al., 2011).

To consider all these characteristics and understand the underflow hydrodynamics and

solids distribution, computational fluid dynamics (CFD) models of SSTs has been developed and enriched our knowledge to the SSTs in the last 40 years (e.g. Larsen, 1977; Imam et al., 1983; Zhou and McCorquodale, 1992a, b, c).

In this chapter, the 2Dc (Quasi 3-D axisymmetric) unsteady state SST model package from New Orleans University is used for simulation and the outputs are displayed using TECPLOT (Bellevue, WA 98015). The general information for the computer used for this study are shown below:

CPU--Intel Core i7, 5500U, @ 2.40GHz 2.40GHz.

RAM--16.0GB

OS—windows 10, 64-bit.

A total of 82 simulations are performed, and it takes the computer 12 minutes to get the result of each simulation. The objectives of this chapter are to understand the effect of several influential factors, for instance SOR, sludge loading rate (SLR), tank geometry variation and density currents on the concentration of ESS and to analyze the modeling outputs by comparing the simulation results with the field data and the simulation outcomes.

7.2. Description of Conditions and the Tested SST

A full-scale, center-feed, peripheral withdrawal circular tank (Figure 7.1) is tested using a number of conditions provided by Vitasovic et al. (1997) and Wahlberg et al. (1998). Firstly, the verification of the 2Dc model is performed with the results presented in Table 7.1 and plotted in Figure 7.2. The simulations show good agreement with the field data.

Next, the effect of SOR, SLR, K_1 (empirical coefficient for rapid settling) and size of the flocculating well on ESS are evaluated and summarized in Figures 7.3 to 7.7. The simulation time for all the conditions is 400 minutes, which is the same as the simulation time in Vitasovic et al. (1997). "NA" means the model fails to output the results for the specific condition. A bond value means the result does not reach the equilibrium and ESS is still rising after 400 minutes of steady input.

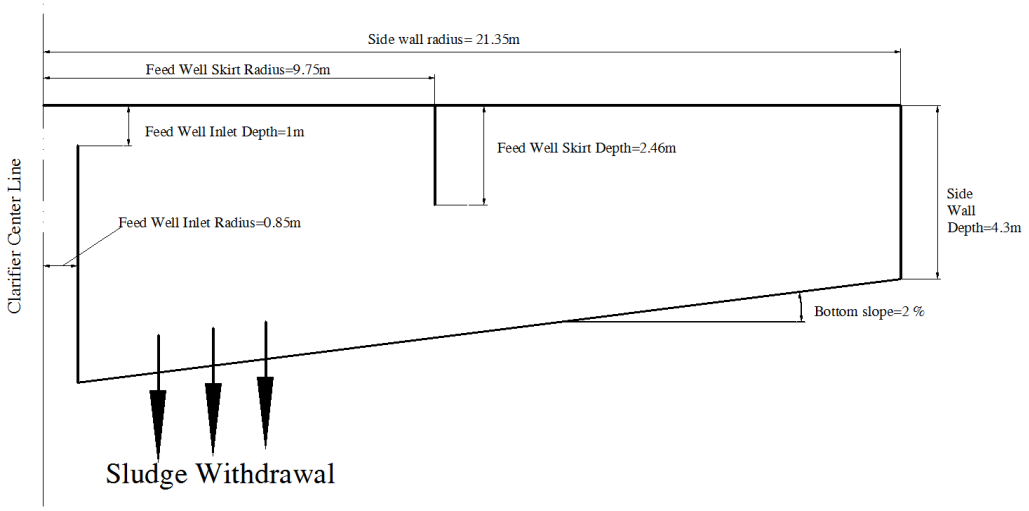

Figure 7-1. Geometry of the tested SST

Table 7-1. Selected SST simulation results used for modeling verification (Vitasovic et al., 1997)

Simulations	1	2	3	4	5
Returned Activated Sludge Concentration Predictions (g/L)					
Previous Experimental Results	5.42	6.70	5.78	5.28	8.76
2Dc Modeling Results (this study)	6.20	7.10	4.60	5.40	7.70
Effluent Suspended Solids Predictions (mg/L)					
Previous Experimental Results	13.50	7.80	10.50	12.80	11.30
2Dc Modeling Results (this study)	14.25	8.97	16.26	18.00	9.90

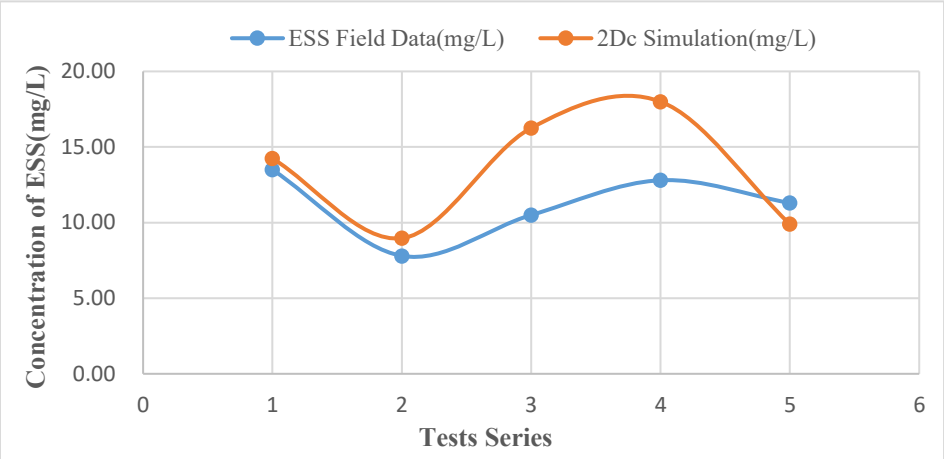

Figure 7-2. CFD Simulations Compared to Field Observations (Vitasovic, 1997).

Table 7.2 shows the results of ESS as the function of surface overflow rate (SOR) and solids loading rate (SLR) for K_1=0.62. Five simulations (simulations 6 to 10) are shown in the table. Compared with the previous simulation of ESS, the 2Dc model is more stable and reliable. The 2Dc simulation results of Table 7.2 are plotted in the Figure 7.3.

Table 7-2. Simulated results of ESS as the function of surface overflow rate and solids loading rate, K_1=0.62 (Vitasovic et al., 1997).

Simulations	6	7	8	9	10
Returned Activated Sludge Concentration Predictions (g/L)					
Previous Modeling Results	6.707	6.761	6.248	5.711	5.124
2Dc Modeling Results (this study)	6.600	6.620	6.610	6.590	6.550
Effluent Suspended Solids Predictions (mg/L)					
Previous Modeling Results	7.00	9.00	162.00	87.00	591.00
2Dc Modeling Results (this study)	9.50	12.84	15.80	19.89	**29.00**

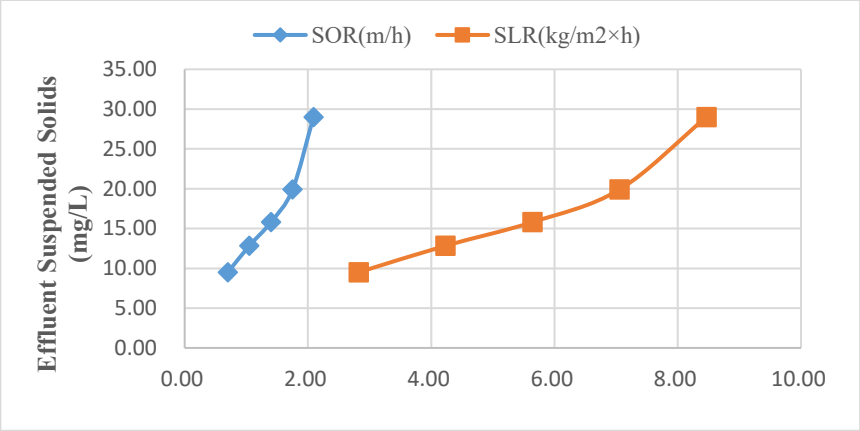

Figure 7-3. Predicted effluent suspended solids concentration as a function of surface overflow rate and solids loading rate shown in Table 7.2.

Similarly with Table 7.2, Table 7.3 shows the simulation results of ESS as the function of surface overflow rate (SOR) and solids loading rate (SLR) for lower K_1 (K_1=0.42). Five simulations (simulations 11 to 15) are shown in the table. The 2Dc simulation results of Table 7.3 are plotted in Figure 7.4.

Table 7-3. Simulated results of ESS as the function of surface overflow rate and solids loading rate, K_1=0.42 (Vitasovic et al., 1997).

Simulations	11	12	13	14	15
Returned Activated Sludge Concentration Predictions (g/L)					
Previous Modeling Results	6.704	6.711	6.695	6.641	6.507
2Dc Modeling Results (this study)	6.690	6.690	6.680	6.680	7.000
Effluent Suspended Solids Predictions (mg/L)					
Previous Modeling Results	6.00	9.00	15.00	26.00	62.00
2Dc Modeling Results (this study)	9.31	12.61	15.36	15.36	21.02

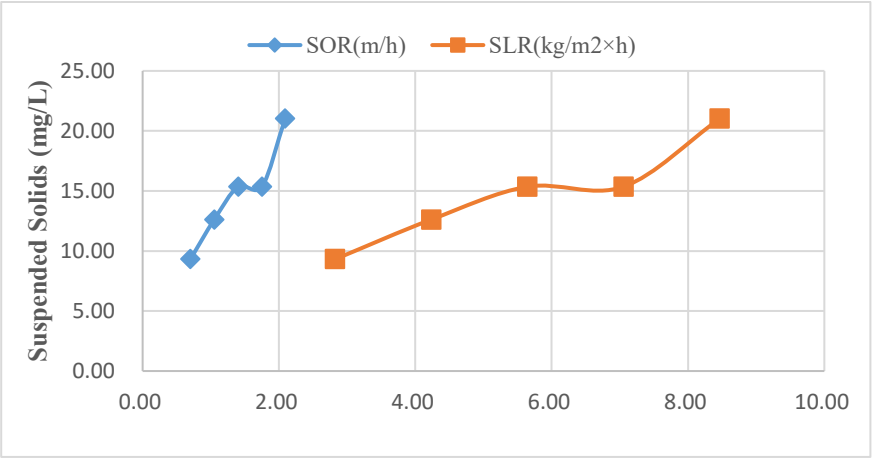

Figure 7-4. Predicted effluent suspended solids concentration as a function of surface overflow rate and solids loading rate for conditions shown in Table 7.3.

Table 7.4 shows the performance of the SST as a function of the size of flocculating well. Twenty-five simulations (simulations 6 to 10 and simulations 16 to 35) are shown in the table. The twenty-five data sets are divided into five groups. The size of the flocculating well is fixed in each group; therefore, the trend of ESS for varied SORs can be observed in each group. In addition, the five groups show the change of performance as a function of the size of flocculating well; therefore, the change of ESS for different sizes of flocculating wells can be observed by comparing the ESS for the same SOR but different flocculation well size ratios. Since simulations 6 to 10 are simulated using the original size of the flocculating well, the results are included in Table 7.4 again to complete the comparison. The simulation results of Table 7.4 are plotted in Figure 7.5.

The simulations based on the data set from the Wahlberg et al. (1998) are listed in Table 7.5 below, which summarizes the influence of SOR and SLR on the performance of the SST. In matrix 1, simulations 36 through 51 are divided into four groups. The four groups have four different SLRs, but within each group the SLR is constant. The change of ESS can be observed

with the increase of SOR in each group in Matrix 1. The change of ESS with the increase of SLR can be found by comparing the ESS with the same SOR but different SLR in different groups in the Matrix 1. In the Matrix 2, simulations 52 to 67 are also divided into four groups of data. Differ with the Matrix 1, the four groups in the Matrix 2 have different SORs, rather than SLRs, and they are constant in each group. Figures 7.6 and 7.7 show the ESS as a function of SOR and SLR based on the data in the two matrixes of Table 7.5.

Table 7-4. Predicted effluent suspended solids concentration as a function of geometry modifications.

K_1 $(g/L)^{-1}$	K_2 $(g/L)^{-1}$	Cmin (g/L)	Vo (m/h)	MLSS (g/L)	Vc (m/h)	Kc $(g/L)^{-1}$	RAS Ratio	peripheral baffle depth (m)
0.61	10.00	0.005	13.00	2.52	6.50	0.31	0.60	0.50
Simula -tions	radius of the flocculation well (m)	Ratio between the flocculation well diameter and total diameter	SOR (m/h)	SLR $(kg/m^2 \times h)$	Influent flow (m^3/h)	RAS flow (m^3/h)	RAS Conc (g/L)	ESS (mg/L)
16	5.978	28%	0.7	2.82	1000	600	6.61	14.09
17	5.978	28%	1.05	4.23	1500	900	6.58	20.67
18	5.978	28%	1.4	5.64	2000	1200	6.54	28.44
19	5.978	28%	1.75	7.05	2500	1500	6.48	38.36
20	5.978	28%	2.09	8.46	3000	1800	N/A	N/A
21	7.4725	35%	0.7	2.82	1000	600	6.64	12.43
22	7.4725	35%	1.05	4.23	1500	900	6.56	18.57
23	7.4725	35%	1.4	5.64	2000	1200	6.58	25.20
24	7.4725	35%	1.75	7.05	2500	1500	6.54	34.47
25	7.4725	35%	2.09	8.46	3000	1800	6.43	**54.02**

26	8.54	40%	0.7	2.82	1000	600	6.65	11.58
27	8.54	40%	1.05	4.23	1500	900	6.62	17.31
28	8.54	40%	1.4	5.64	2000	1200	6.58	22.68
29	8.54	40%	1.75	7.05	2500	1500	6.55	31.61
30	8.54	40%	2.09	8.46	3000	1800	6.47	**46.80**
6	9.75	46%	0.7	2.82	1000	600	6.60	9.50
7	9.75	46%	1.05	4.23	1500	900	6.62	12.81
8	9.75	46%	1.4	5.64	2000	1200	6.61	15.80
9	9.75	46%	1.75	7.05	2500	1500	6.59	19.89
10	9.75	46%	2.09	8.46	3000	1800	6.55	29.00
31	10.675	50%	0.7	2.82	1000	600	10.14	6.64
32	10.675	50%	1.05	4.23	1500	900	6.63	14.46
33	10.675	50%	1.4	5.64	2000	1200	6.59	18.35
34	10.675	50%	1.75	7.05	2500	1500	6.60	23.91
35	10.675	50%	2.09	8.46	3000	1800	6.53	39.44

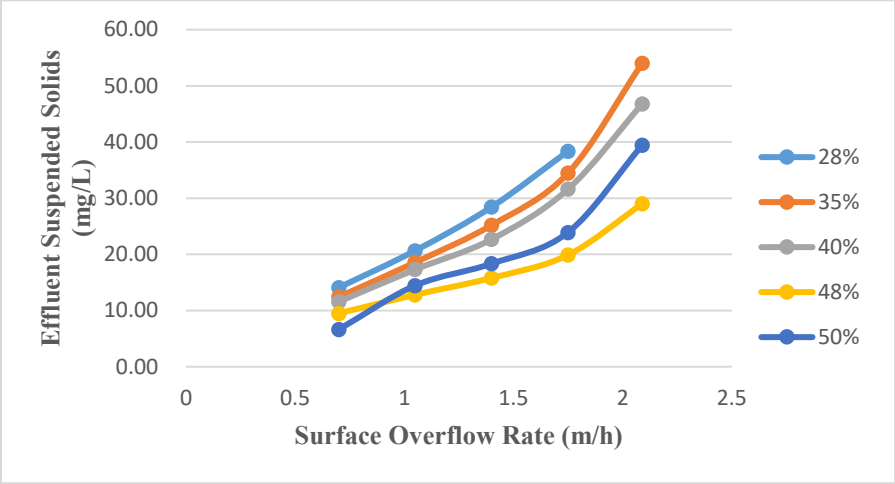

Figure 7-5. Effect of Surface Overflow Rate on Concentration of Effluent Suspended Solids for Different Size of Flocculating Well

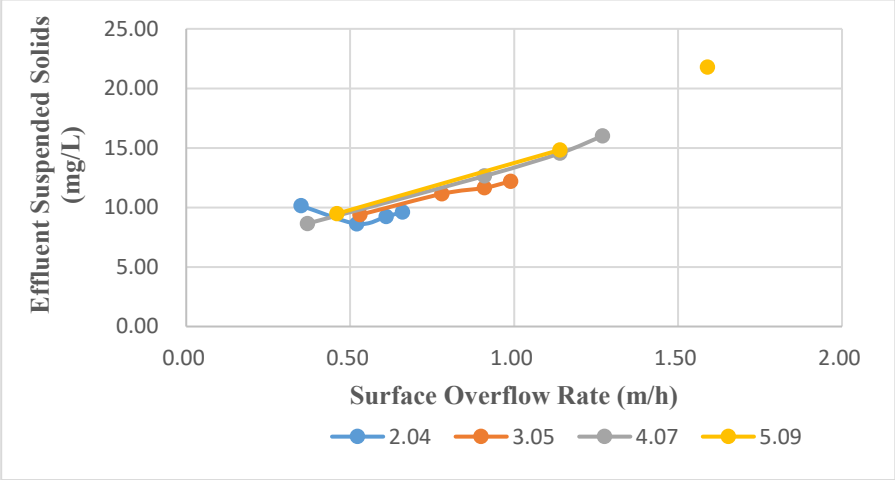

Figure 7-6. Predicted effluent suspended solids concentration as a function of surface overflow rate for simulations 36 to 51 in Table 7.5.

Table 7-5. Summary of simulation and predicted effluent suspended solids concentrations as the function of surface overflow rate and solids loading rate (Wahlberg et al., 1998).

$K_1(g/L)^{-1}$	$K_2(g/L)^{-1}$	$C_{min}(g/L)$	$V_o(m/h)$	MLSS(g/L)	$V_c(m/h)$	$K_c(g/L)^{-1}$	
0.607	10.00	0.005	11.10	2.363	5.55	0.304	
Matrix 1	SOR (m/h)	SLR (kg/m^2-h)	Influent flow (m^3/h)	RAS flow (m^3/h)	RAS Ratio	RAS Conc (g/L)	ESS (mg/L)
36	0.35	2.04	503	729	1.45	6.64	10.14
37	0.52	2.04	746	486	0.65	5.84	8.63
38	0.61	2.04	869	364	0.42	7.48	9.24
39	0.66	2.04	842	292	0.35	8.32	9.63
40	0.53	3.05	757	1092	1.44	3.99	**9.39**
41	0.78	3.05	1120	729	0.65	5.94	11.14
42	0.91	3.05	1303	546	0.42	7.94	11.65
43	0.99	3.05	1412	437	0.31	9.89	12.20
44	0.37	4.07	524	1942	3.71	3.00	8.65
45	0.91	4.07	1301	1164	0.89	4.98	12.64
46	1.14	4.07	1634	831	0.51	6.79	14.55
47	1.27	4.07	1819	647	0.36	8.44	16.01
48	0.46	5.09	655	2428	3.71	3.00	9.48
49	1.14	5.09	1626	1456	0.90	4.96	14.84
50	1.43	5.09	2043	1039	0.51	NA	NA
51	1.59	5.09	2241	841	0.38	8.10	**21.80**
Matrix 2							
52	0.46	1.34	655	158	0.24	9.45	7.88
53	0.46	2.05	655	584	0.89	4.96	8.21
54	0.46	3.17	655	1262	1.93	3.58	7.84
55	0.46	4.99	655	2366	3.61	3.01	9.46
56	1.14	3.57	1626	536	0.33	8.80	14.54
57	1.14	3.73	1626	631	0.39	8.07	14.51
58	1.14	4.77	1626	1262	0.78	5.33	14.72
59	1.14	5.89	1626	1940	1.19	4.33	14.94
60	0.70	2.05	1000	240	0.24	9.84	9.77
61	0.70	3.13	1000	890	0.89	4.99	10.64

62	0.70	4.85	1000	1930	1.93	3.58	11.25
63	0.70	7.63	1000	3610	3.61	3.01	11.55
64	0.90	2.64	1286	309	0.24	9.86	11.87
65	0.90	4.02	1286	1145	0.89	4.98	12.55
66	0.90	6.23	1286	2482	1.93	3.58	13.00
67	0.90	9.80	1286	4643	3.61	NA	NA

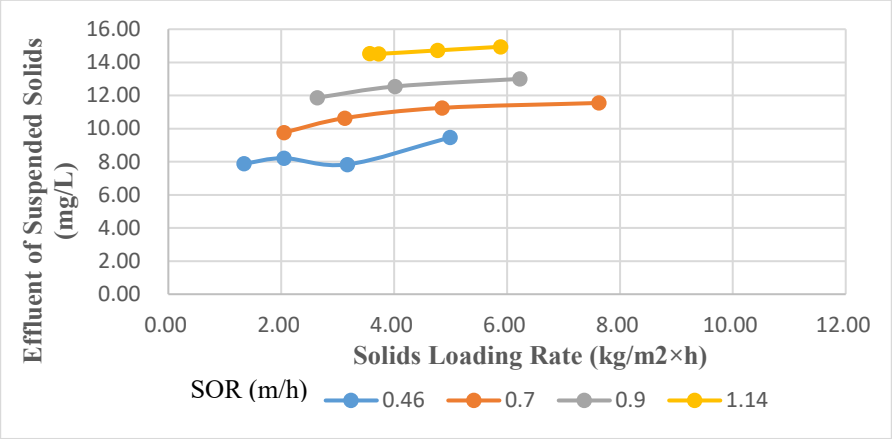

Figure 7-7. Predicted effluent suspended solids concentration as a function of solids loading rate for simulations 52 to 67 in Table 7.5.

7.3. Results and Discussion

7.3.1 Effect of density currents on the performance of SSTs

Figures 7.8 to 7.12 present five flow patterns that are produced by performing simulations corresponding to the conditions from Table 7.1 defined as simulations 1 to 5. In Figures 7.9 and 7.12, the horizontal inflow does not reach the flocculating well, but turns sharply downward as a density waterfall. When this happens, the entrainment of low concentration fluids from the main settling zone flows back to the high concentration flocculating well and forms a strong recirculation eddy (Zhou et al., 1992). In the withdrawal zone, an eddy is formed by the bottom sludge reverse flow. Some researchers believe the density waterfall can deteriorate the

performance of clarifiers by reducing the volume usage efficiency of flocculating well (Krebs, P., 1991; Vitasovic et al., 1997) and increasing the upward flow in the withdrawal zone corresponding to increase effluent suspended solid (Zhou et al., 1992). However, the simulations of 2 and 5 show the formation of the density waterfall and the lowest ESS, compared with the results in simulations 1, 3 and 4. The Figures 7.9 and 7.12 show that the density difference between the comparatively heavy fluid at the main settling zone and the relatively lighter fluid at the outlet zone causes a stable stratification. Samstag et al. (1992) revealed that the stable density stratification in the settling and effluent zone contributes to a significant damping of vertical mixing. Therefore, the density currents do not bring about side effects on the ESS removal efficiency of the SST unless the upward currents can flow to the exit directly.

The Figures 7.9 and 7.12 are shown here due to their similar streamline.

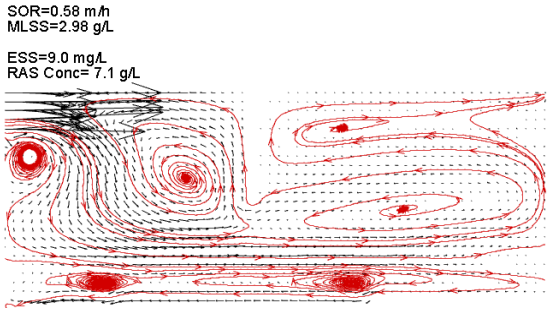

Figure 7-8. Streamline for simulation 2.

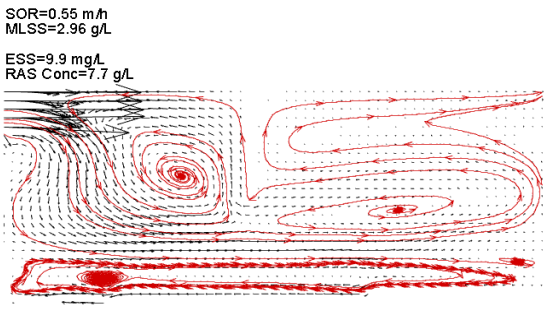

Figure 7-9. Streamline for simulation 5.

Figures 7.8, 7.10 and 7.11 show differences from Figures 7.9 and 7.12, indicating that the influent flow with higher SOR/SLR and lower MLSS concentration is deflected downward by impinging on the flocculating well. The downward flow splits to form an eddy inside the inlet zone and a forward bottom current in the settling zone.

The Figures 7.8, 7.10 and 7.11 are shown here due to their similar streamline.

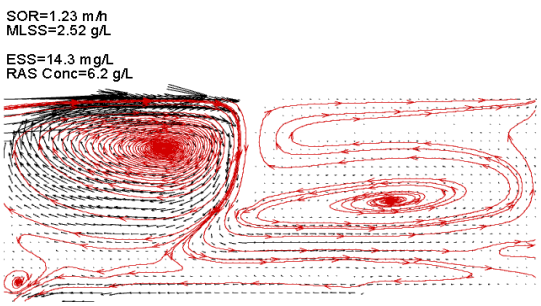

Figure 7-10. Streamline for simulation 1.

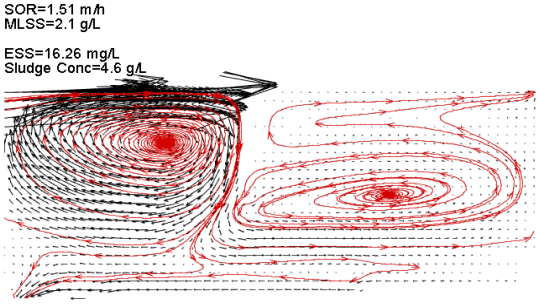

Figure 7-11. Streamline for simulation 3

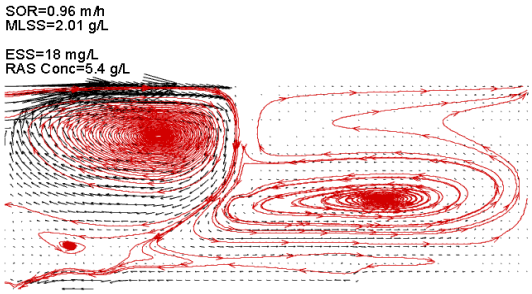

Figure 7-12. Streamline for simulation 4

The similarity from Figures 7.8 to 7.12 illustrates that the currents in the withdrawal zone, all the bottom currents flow counterclockwise towards to the flocculating well and then flow clockwise to the exit, instead of flowing upward to the effluent weir directly.

7.3.2 Effect of Surface overflow rate (SOR) and Solids loading rate (SLR)

Vitasovic et al. (1997) used the data in the Tables 7.2 and 3 to study the influence of SOR and SLR on ESS. Based on the data in the Tables 7.2 and 7.3, the relationships between SOR, SLR and ESS are shown in Figures 7.3 and 7.4 already, and the ESS seems more sensitive with the variations of SOR than with SLR. However, since the SLR and SOR changed at the same time, it is better to keep one of the two parameters at a specific value and only change the left one. Hence, simulations 13 to 15 from Table 7.3 are selected and three new Tables are generated. Each table

uses different SOR values with a specific SLR value, all the other parameters in Table 7.3 are fixed in the new Tables. Figure 7.13 summarizes the outcomes of the three new tables.

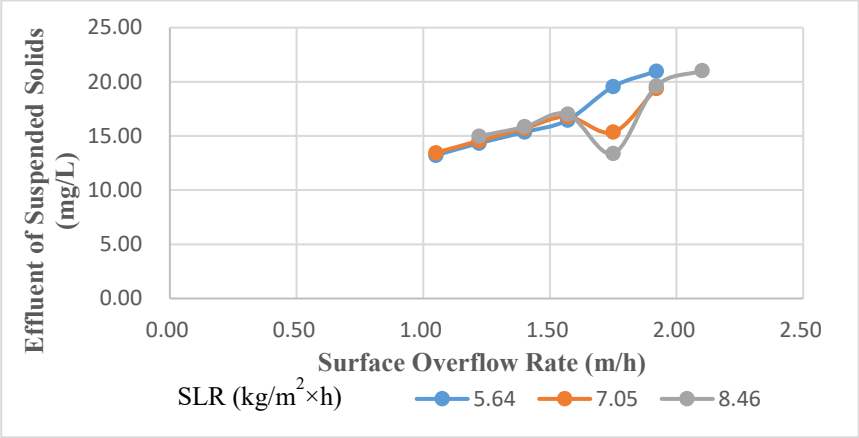

Figure 7-13. Predicted effluent suspended solids concentration as a function of surface overflow rate and solids loading rate for Table 7.6a, b, c

The data sets in the Figure 7.13 demonstrates that based on the 2Dc model, the SOR has a greater impact on ESS than the SLR. What is more, an interesting phenomenon is the ESS reaches to the minimum as the SOR increased to 1.57 m/h when the SLR=7.05 g/L and 8.46 g/L. Mccorquodale et al. (2004) explained that this may be caused by the improvement of hydrodynamics and the increase of flocculation process due to higher collision frequency of sludge particles.

In addition, the simulations based on the data set from the Wahlberg et al. (1998) are listed in Table 7.5. Figures 7.6 and 7.7 show the ESS as a function of SOR and SLR based on the data in the two matrixes of Table 7.5. The results reveal that the SOR that has greater contribution to ESS, which is opposite to Wahlberg et al.'s findings. There are three possible reasons for this contradiction.

Firstly, the disagreement may be caused by the differences of fundamental mathematical equations, such as continuity equation and turbulent equation, applied in the two models. In the 2Dc model, in order to include three dimensional effects, like swirl momentum and turbulence created by inlet and rotating scraper mechanisms, a third direction (θ direction) is included (McCorquodale et al., 2004). The governing equations of motion for three dimensional, incompressible, unsteady, stratified, incompressible, and turbulent- average flow in cylindrical coordinate (r, θ, y) in the 2Dc model are listed below (Jensen et al., 1979; McCorquodale et al., 2004):

Continuity equation

$$\frac{\partial ru}{\partial r}+\frac{\partial rv}{\partial y}+\frac{\partial rv_\theta}{r\partial\theta}=0 \tag{7.1}$$

r -Momentum component:

$$\frac{\partial \rho u}{\partial t}+u\frac{\partial \rho u}{\partial r}+\frac{v_\theta}{r}\frac{\partial \rho u}{\partial \theta}-\frac{\rho v_\theta^2}{r}+v\frac{\partial \rho u}{\partial y}=-\frac{\partial p}{\partial r}$$
$$+\frac{1}{r}\frac{\partial}{\partial r}\left(r\mu_{eff}\frac{\partial u}{\partial r}\right)+\frac{1}{r^2}\frac{\partial}{\partial \theta}\left(\mu_{eff}\frac{\partial u}{\partial \theta}\right)-\frac{2}{r^2}\mu_{eff}\frac{\partial v_\theta}{\partial \theta}+\frac{\partial}{\partial y}\left(\mu_{eff}\frac{\partial u}{\partial y}\right)+\rho g_r \tag{7.2}$$

θ-Momentum component:

$$\frac{\partial \rho v_\theta}{\partial t}+u\frac{\partial \rho v_\theta}{\partial r}+\frac{v_\theta}{r}\frac{\partial \rho v_\theta}{\partial \theta}+\frac{\rho v_\theta u}{r}+v\frac{\partial \rho v_\theta}{\partial y}=-\frac{1}{r}\frac{\partial p}{\partial \theta}+\frac{1}{r}\frac{\partial}{\partial r}\left(r\mu_{eff}\frac{\partial v_\theta}{\partial r}\right)+\frac{1}{r^2}\frac{\partial}{\partial \theta}\left(\mu_{eff}\frac{\partial v_\theta}{\partial \theta}\right)+$$
$$\frac{1}{r^2}\mu_{eff}\frac{\partial u}{\partial \theta}+\frac{\partial}{\partial y}\left(\mu_{eff}\frac{\partial v_\theta}{\partial y}\right)+\rho g_\theta \tag{7.3}$$

y -Momentum component:

$$\frac{\partial \rho v}{\partial t}+u\frac{\partial \rho v}{\partial r}+\frac{v_\theta}{r}\frac{\partial \rho v}{\partial \theta}+v\frac{\partial \rho v}{\partial y}=-\frac{\partial p}{\partial y}+\frac{1}{r}\frac{\partial}{\partial r}\left(r\mu_{eff}\frac{\partial v}{\partial r}\right)+\frac{1}{r^2}\frac{\partial}{\partial \theta}\left(\mu_{eff}\frac{\partial v}{\partial \theta}\right)+\frac{\partial}{\partial y}\left(\mu_{eff}\frac{\partial v}{\partial y}\right)+$$
$$\frac{\rho-\rho_r}{\rho}g_y \tag{7.4}$$

In which u, v, and v_θ are temporal mean velocity components in the r, θ, y directions

respectively. μ_{eff} is the effective viscosity; p is the general pressure less the hydrostatic pressure at reference density ρ_r; ρ is the fluid-solid mixture density; g is the gravitational acceleration and $(\frac{\rho-\rho_r}{\rho}g)$ is a density gradient term for the simulation of buoyant effects. In order to understand more details of the mathematical equations (e.g. solids transport equation, and turbulent equations) coupled in the 2Dc model, the readers are suggested to read McCorquodale et al. (2004).

For the comparison, the governing equations of motion for two-dimensional, unsteady, turbulent, and density stratified flow in the Vitasovic et al. (1997) are as follows:

Continuity equations:

$$\frac{\partial ru}{\partial r}+\frac{\partial rv}{\partial y}=0 \tag{7.5}$$

r -Momentum component:

$$\frac{\partial u}{\partial t}+u\frac{\partial u}{\partial r}+v\frac{\partial u}{\partial y}=-\frac{1}{\rho}\frac{\partial p}{\partial r}+\frac{1}{r}\frac{\partial}{\partial r}\left(r\vartheta_t\frac{\partial u}{\partial r}\right)+\frac{1}{r}\frac{\partial}{\partial y}\left(r\vartheta_t\frac{\partial u}{\partial y}\right)+S_u \tag{7.6}$$

y -Momentum component:

$$\frac{\partial v}{\partial t}+u\frac{\partial v}{\partial r}+v\frac{\partial v}{\partial y}=-\frac{1}{\rho}\frac{\partial p}{\partial y}+\frac{1}{r}\frac{\partial}{\partial r}\left(r\vartheta_t\frac{\partial v}{\partial r}\right)+\frac{1}{r}\frac{\partial}{\partial y}\left(r\vartheta_t\frac{\partial v}{\partial y}\right)-g\frac{\rho-\rho_r}{\rho}+S_v \tag{7.7}$$

where

$$S_u=\frac{1}{r}\frac{\partial}{\partial r}\left(r\vartheta_t\frac{\partial u}{\partial r}\right)+\frac{1}{r}\frac{\partial}{\partial y}\left(r\vartheta_t\frac{\partial v}{\partial r}\right)-2\frac{\vartheta_t}{r^2}u \tag{7.8}$$

and

$$S_v=\frac{1}{r}\frac{\partial}{\partial r}\left(r\vartheta_t\frac{\partial u}{\partial y}\right)+\frac{1}{r}\frac{\partial}{\partial y}\left(r\vartheta_t\frac{\partial v}{\partial y}\right) \tag{7.9}$$

All the same symbols shown in the two different references have the same mean, except ϑ_t shown in the Vitasovic et al. (1997) is eddy viscosity.

Secondly, the method used to analyze the relationship between these parameters might be

a problem. The equation used for connecting SLR, SOR and ESS is

$$SLR=SOR \times (1+RAS\ Ratio) \times MLSS \quad (7.10)$$

Usually the relationship between these three parameters is just simply studied by keeping one of the SLR and SOR constant to study the effect of another parameter on ESS. However, we cannot ignore the impact of RAS ratio on the performance of clarifier. For example, the SOR and ESS is usually studied by keeping SLR and MLSS constant. However, as the SOR increases, the RAS ratio will decrease. Both changes of the two parameters will cause negative effect on the ESS concentration of the SST. At the same time, the increase of RAS ratio will reduce the MLSS concentration flowing to the SST. In another case, in order to study the SLR and ESS, usually the SOR and MLSS will be kept constant. Therefore, the RAS ratio will rise as the increase of SLR. As a result, the impact of rising the RAS ratio will offset the negative contribution of the SLR on the ESS. Also, increasing the RAS ratio will increase the concentration of MLSS flowing to the SST. Therefore, the study of the SOR/SLR on ESS of secondary clarifier by keeping MLSS concentration and one of the SOR/SLR constant is problematic and other methods are needed to illustrate the relationship between the parameters.

Thirdly, there might be no relationship between SOR, SLR and ESS when the secondary clarifier is well designed and well operated. Therefore, it is meaningless to study the relationship between SOR, SLR and ESS in the well designed and operated secondary clarifier.

7.3.3 Effect of the size of flocculating well on the SS removal efficiency of the SST

To exemplify the effect of tank design on the performance of the tank, a modification in

clarifier geometry is simulated for different SOR values. All the other inputs (size alteration of flocculating well, K_1, Stokes velocity, MLSS and RAS ratio) are equal to the values in the Vitasovic et al. (1997). Outputs shown in Table 7.4 indicate that after adjusting the size of the flocculating well from 46% to 28% of the tank diameter, the modified tank produces even higher ESS. The simulation of the last test for the 28% of tank diameter modification cannot be simulated by the 2Dc model, so there are only four results for the 28% of tank diameter modification. The figures of both modified and unmodified tanks show that the rise of sludge blanket interface will ultimately contributes to the break of limitation of ESS concentration. For the retrofitted tank, the break comes out even earlier than the original tank. The examples of streamline profiles for the unmodified and modified tanks are shown from Figures 7.14, 7.15 and Figures 7.16, 7.17, respectively. The comparisons for streamline profiles in both of the tanks display a same trend: when the SLR increases with SOR at a constant RAS ratio, the strong eddy in the main settling zone becomes smaller and finally disappears. The currents, which are found to form the eddy, flow out directly from the end of the flocculating well lip.

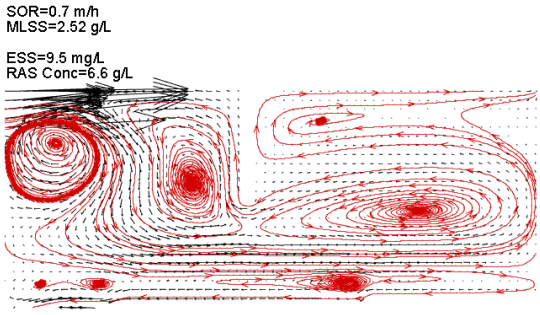

Figure 7-14. streamline before geometry modification (simulation 6)

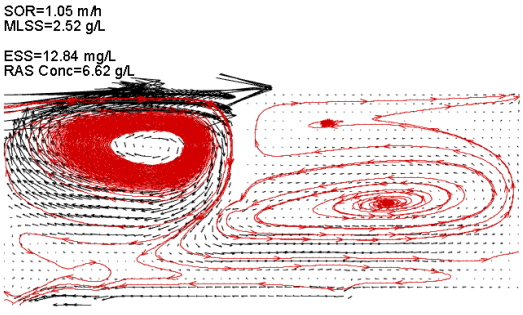

Figure 7-15. streamline before geometry modification (simulation 7)

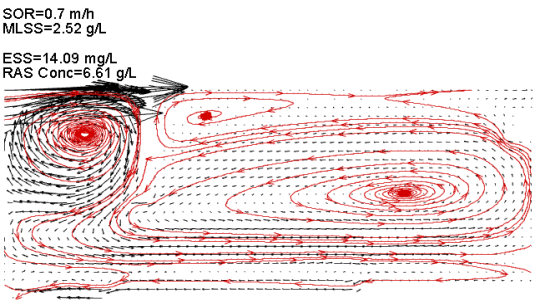

Figure 7-16. streamline after geometry modification (simulation 16)

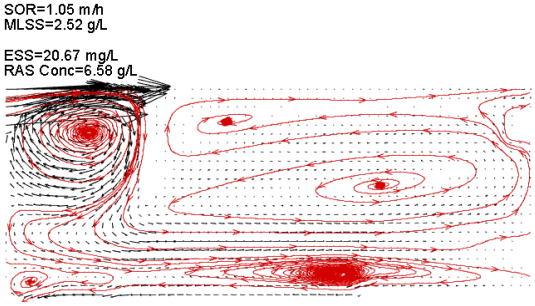

Figure 7-17. streamline after geometry modification (simulation 17)

Later on, in order to convince the modeling results, addition simulations are performed at 35%, 40% and 50% of the tank diameter. The results of these modifications are shown in Table 7.4 and Figure 7.5. The results indicate that the smaller flocculating well produces higher ESS. Although this outcome is opposite to the result of the simulation provided by Vitasovic et al. (1997), it is consistent with the conclusion of Parker et al. (1971) that larger flocculation wells usually create better flocculation condition and less ESS. The simulations demonstrate that the optimal size of the flocculating well is 46% of the tank diameter, which is the original size of the well. This may be the reason why the effect of changing the K_1 from 0.62 to 0.42 L/g is small compared with the conclusions in the Vitasovic et al. (1997). The conclusions of the literature illustrate that changing the value of settling parameter K_1 may decrease the ESS concentration when the geometry of the tank is not optimal.

In addition, the comparison of the last simulation (simulations 10, 20, 25, 30 and 35) in each specific size of the flocculating well shows that equilibrium cannot be reached after 400 minutes of steady input when the size of the flocculating well is comparatively small. Therefore,

simulations with larger flocculating well achieve equilibrium earlier in ESS and may improve numerical accuracy.

7.4. Conclusions

This chapter has evaluated the concepts of using a mechanic SST model to SST performance. A more advanced model (Q3D) is compared to an older, less advanced model (2D) which does not include swirl velocity. Based on the application of the Q3D clarifier model and using the data from the literature, the following conclusions are made:

- There are differences between the model predictions made by the Quasi 3-D(Q3D) axisymmetric model package and the 2-D model developed by Vitasovic et al (1997). This might be caused by the deviations of mathematical equations, such as continuity equation and turbulent equation, as applied in the two models. The Q3D model is more powerful and accurate, considering its inclusion of three-dimensional effects, such as like swirl momentum and the more precise description of viscosity.
- Simulation results confirm the existence of density waterfall in the cases with low flow rate and high MLSS (as shown in simulations 2 and 5 in Figure 7.9 and 12, respectively). However, the data do not show the side effect of density currents on the SST removal efficiency, because stable stratification in the main settling and outlet zones resists the upward dispersion of suspended solids. The bottom currents in the withdrawal zone, instead of flowing upward to the effluent weir directly, flow counter clockwise towards to the flocculating well and then flow clockwise to the exit. Therefore, the density waterfall

does not reduce the hydraulic efficiency if stable stratification is existed in the main settling zone and effluent zone.

- The results of the Q3D numerical model reveal that the impact of surface overflow rate (SOR) on effluent suspended solid (ESS) is more significant than solids loading rate (SLR). This is opposite to the simulation results in the Vitasovic et al (1997). The analyses were arranged to evaluate the different impacts of SOR and SLR on ESS using the relationship SLR=SOR×(1+RAS ratio)×MLSS. Different results may be possible if the MLSS is varied independently of SOR or SLR, and this is a topic for future research.
- The effect of changing the settling parameter K_1 from 0.42 to 0.62 L/g on the performance of SST is insignificant when the geometry has been optimized.
- The simulation results show that increasing the flocculating well size from 28% to 50% of the tank diameter resulted in lower ESS concentration. At smaller well sizes, the simulation took much longer to reach equilibrium, suggesting that there may be some uncertainty in the numerical method for these conditions that merits future work.
- A numerical model can be used to predict or verify the hydraulic efficiency of the SST. The present model package is capable of solving complex analysis of clarifier for different operating and design conditions, such as influent flow rate, inlet solids concentration, flocculation, temperature, settling property, internal SST geometry (for example, energy dissipating baffle, flocculation well, and withdrawal arrangements).

Chapter 8 Evaluating the effects of inlet geometry on the flux capacity of secondary settling tanks with computational fluid dynamics model and one-dimensional flux theory model

8.1. Introduction

The state point analysis (SPA) developed by Keinath et al. (1977) and Keinath (1985) is one of the most practical approaches to analyze the behavior of existing secondary settling tanks (SSTs) as well as improving the operation of full-scale SSTs (Clarifier Design). It is based on one-dimensional flux theory (1DFT), and the flux curve can be easily developed by on-site observations. However, since it simplifies the SSTs to the idealized steady-state 1D model, it ignores the non-ideal effects of (1) hydrodynamics, such as turbulence, density currents, flocculation, wind and temperature, and the effects of (2) the arrangement of the internal geometry, such as energy dissipation inlet (EDI), flocculation well, McKinney baffle, Stamford baffle etc. (Ekama and Marais, 2004). Therefore, the actual flux capacities of SSTs are lower than the prediction of the 1DFT and the applications of 1DFT without considering a proper safety factor can cause incorrect design and operation of the SST.

In order to understand the effects of hydrodynamics and the arrangement of internal features on the performance of the SST, computational fluid dynamics (CFD) models have been developed in the last 30 years and have been used to (1) understand the hydrodynamics in the SST (Zhou and McCorquodale, 1992a, b, c; McCorquodale, 2004); (2) optimize internal structures (Xanthos et al., 2011; 2013); (3) adjust operation process (Vitasovic et al., 1997; Wahlberg et al., 1998; Ekama and Marais, 2004; Parker et al., 2008; Patziger et al., 2012; Gao and Stenstrom, 2017)

and improve sub-models (Lakehal et al., 1999; Clercq, 2003; Ramalingam et al., 2012; Ramin, 2014).

Wahlberg et al. (1998) stated that the limiting flux obtained from 1DFT should be considered a theoretical limit, often greater or much greater than actual capacity. With the help of CFD models, the hydrodynamics of SST and the arrangement of internal features can be optimized, and the actual limiting flux can be increased more closely to the theoretical flux limit.

Ekama and Marais (2004) analyzed the effects of Stamford baffles on SST limiting flux in two different wastewater treatment plants (WWTPs) by using the SettlerCAD program (Zhou et al., 1992). In their study, the operation parameters such as recycle rate (Q_r) and concentration of mixed liquor suspended solids (MLSS) were kept constant. The SST was stressed by increasing the flow rate (Q), which had the effect of increasing the surface overflow rate (SOR) and the solids loading rate (SLR). Their simulation results showed that the difference between the CFD predicted limiting flux of the SST with and without the Stamford baffle was only 2%, and the capacities were both around 80% of the maximum flux limit obtained from 1DFT. Therefore, they concluded that the baffling has only a small influence on the capacity of an SST, and 80% of the maximum flux limit obtained from 1DFT is a reasonable value to apply in the design and operation of full-scale SSTs.

However, since the Stamford baffle is only one of the internal features of an SST, the effect of other internal features on the SST's limiting flux need to be studied before making a final conclusion. Also, since grid specification and refinement of SettlerCAD cannot be changed by the

user, the numerical diffusion caused by the grid may result in inaccurate prediction results. Moreover, because all constants in the governing equations are coded in the program and cannot be changed by the users, they cannot be used to adjust the prediction results to better calibrate the field measurement.

McCorquodale (2004) developed a Quasi-three-dimensional (Quasi-3D) SST model and used it to evaluate Ekama and Marais's recommended "80% of the flux limit calculated by IDFT." He adjusted the operation parameters (Q, SLR, returned activated sludge (RAS) ratio, and MLSS) in two ways: (1) keeping the Q and RAS ratio constant while changing SLR by changing the MLSS concentration; (2) keeping the RAS ratio and MLSS constant while changing SLR and SOR by increasing flow rate (Q). Their results showed that 80% of the flux limit calculated by the IDFT was an accurate correction factor when adjusting the operation parameters using the second method, whereas the 80% of the flux limit calculated by the 1DFT under-predicted the SST real capacity when adjusting the operation parameters using the first stress testing method.

Since the stress testing methods, geometry of SSTs, sludge settling properties and CFD programs used by McCorquodale (2004) and Ekama et al. (2004) were different, it is not surprising that their conclusions were different. Therefore, there is a need to compare the limiting flux predicted by the CFD model and 1DFT using these three different stress testing methods in the same SST, sludge settling properties and the CFD program.

In this chapter, a Fluent-based two-dimensional (2D) SST CFD model is used to conduct a series of CFD stress tests. The SSTs of Wintey WWTP described in the Burt (2010) are simulated.

A total of 116 simulations are performed in this study. The objectives of this study are to (1) understand the effects of different stress testing methods and (2) the effect of another internal feature-McKinney baffle-on the limiting flux of two different SSTs.

8.2. Methodology

8.2.1 Governing equations and boundary conditions

The commercial CFD code ANSYS Fluent (v.18.2) is used to determine the steady-state, turbulent, and density stratified flow in the circular SSTs. Consistent with the previous research Gao and Stenstrom (2018 a, b), the circular SSTs in this research are also investigated by an axisymmetric approach. For circular SSTs with axisymmetric internal features, this approach can dramatically reduce the computational time without deteriorating the simulation accuracy compared with three-dimensional (3D) model as shown by Patziger et al. (2012).

Velocity inlet boundary condition is applied to inlet and sludge bottom boundaries, which assumes a uniform distribution of all the dependent variables at the boundary face. For the surface outlet, a pressure outlet boundary condition is applied. Using this type of boundary condition, all flow quantities at the outlets are extrapolated from the interior domain. For the free ambient water surface, the rigid-lid approximation for all velocity components with full slip shear condition is assumed (Wang et al., 2008; Tarpagkou and Pantokratoras, 2013). And the free surface boundary is treated as a symmetry condition. The solid boundaries are specified as stationary walls with a no slip-shear condition and a standard wall function is used with the turbulence models.

8.2.2 Geometry and meshing

The general geometries of original and modified Wintey SSTs and computational meshes with a nearly uniform cell size of 0.00625×0.00625m and approximately 900,000 cells are shown in Figures 6.1 and 6.2, respectively. The radius of the Wintey SST is 18.3m with a 1.8m minimum side water depth. The tank floor slope and hopper floor slope are 7.5% and 60%, respectively. Gao and Stenstrom (2018a, 2019a) showed the results of mesh-independent tests for the original and modified SSTs, respectively. Since the surface outlet is extremely small compared with the inlet, the meshes near the surface outlet are enlarged in the figure to show the outlet meshes more clearly.

8.2.3 Model verification

Three different tests (different flow conditions and sludge settling properties) shown in Burt (2010) are used to predict the performance indicators, such as effluent suspended solids (ESS), sludge blanket height (SBH), and the velocity profiles and to compare with his field measurements.

Figure 8.1 shows the model calibration and it shows that the predictions of the CFD model have good agreements with the field data. The model verification using a medium mesh (428,000 cells) has been completed in Gao and Stenstrom (2019a); a larger mesh (approximately 900,000 cells) was used in these simulations and is also accurate.

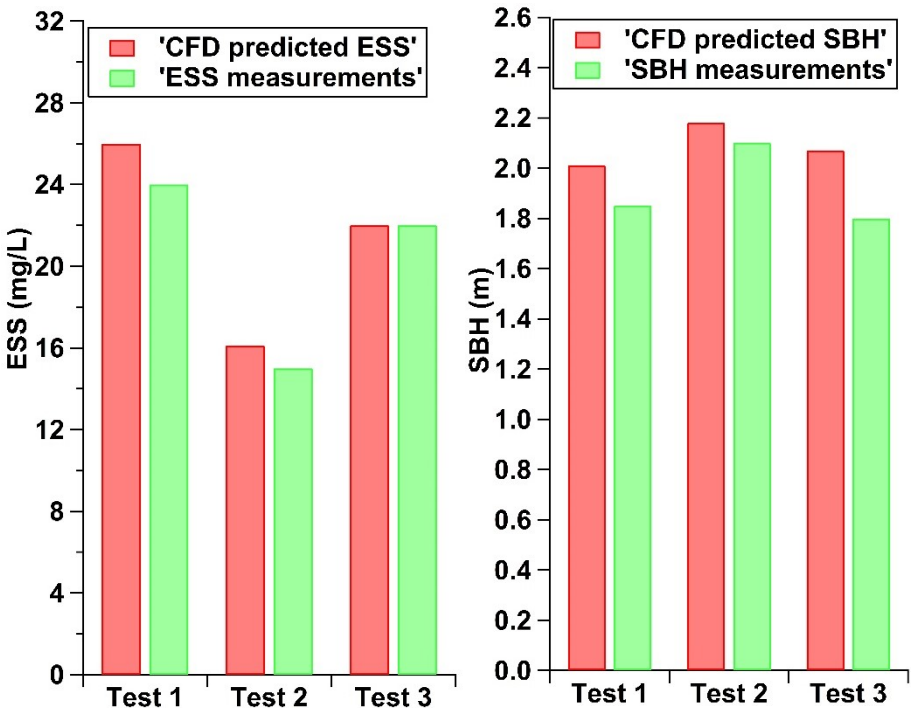

Figure 8-1. Comparison between the predictions of performance indicators with the CFD model and field data for the Wintney SSTs

8.2.4 Stress test initialization

Since the model verification studies shows that the CFD model results closely fit the observations, the CFD model can be used for the CFD stress tests. For the stress tests, the flow conditions of these three tests are used to initialize the CFD stress tests on each stress testing method used in McCorquodale et al. (2004) and Ekama and Marais (2004). However, the sludge settling properties used in Test 1 are used for all the stress tests to prevent the variation of sludge properties on the prediction of the limiting flux. Therefore, only flow conditions and the internal baffling structure vary during the CFD stress testing. Table 8.1 shows the three inputs used for CFD stress tests.

The first stress test method is to increase the SLR and SOR by increasing the flow rate (Q),

while keeping the RAS ratio and inlet MLSS concentration constant (McCorquodale et al., 2004). The second stress test method is to increase the SLR and SOR by increasing the flow rate but keeping the returned flow rate (Q_r) and inlet MLSS concentration constant (Ekama and Marais, 2004). The third stress method is to increase the SLR by increasing the MLSS concentration, while keeping the influent flow (Q) and recycle flow (Q_r) constant (McCorquodale et al., 2004).

Table 8-1. Main inputs for CFD stress tests

	Inflow parameters			Settling parameters*			Dry solids density
Trials No.	MLSS	RAS	SOR	V_o	r_h	r_p	ρ_p
	g/L	ratio	m/h	m/h	L/g	L/g	kg/m^3
1	4.187	1.09	0.332	12.64	0.340	12.25	1450
2	3.384	1.09	0.332	12.64	0.340	12.25	1450
3	2.904	0.83	0.673	12.64	0.340	12.25	1450

*: V_o is Stokes velocity. r_h and r_p account for rapidly and poorly settling floc, respectively.

8.2.5 Prediction of the 1DFT limiting flux

The 1DFT limiting flux for each stress test method are the same as used by McCorquodale et al. (2004) and can be summarized in the following steps:

(1) The conditions shown in Table 8.1 are used as the starting points of three stress method;

(2) The operating conditions (SOR, SLR, RAS ratio, MLSS) shown in Table 8.1 are varied according to the stress test methods described previously;

(3) The stress test ends with SST failure when the ESS exceeds 30 mg/L or when the sludge blanket height (SBH) rising to the effluent weir. The downward flow velocity (U_b) is calculated at the failure point and is called the limiting U_b.

(4) The limiting U_b is then used to calculate the bulk flux and total flux of the 1DFT.

(5) Steps 1 to 4 are performed for SSTs with and without the McKinney baffle.

The addition of the McKinney improves SST performance and the predicted limiting U_b increases for all conditions. Figure 8.2 shows and example of the flux diagram for the original (top) and improved (bottom) SSTs. The limiting fluxes are estimated from the CFD simulations for Trial 1 in Table 8.1 using the first stress test method.

8.3. Results and discussion

Tables 8.2 to 8.4 summarize the major results of the CFD stress tests, including (1) the limiting flux predicted by both the CFD modeling and the 1DFT analysis; (2) the limiting flux predicted by CFD as a percentage of the 1DFT limit; and (3) the failure reasons of SSTs, using the three stress methods. The starting points for each stress test method are the conditions shown in Table 8.1. Stress tests are performed with and without the McKinney baffle.

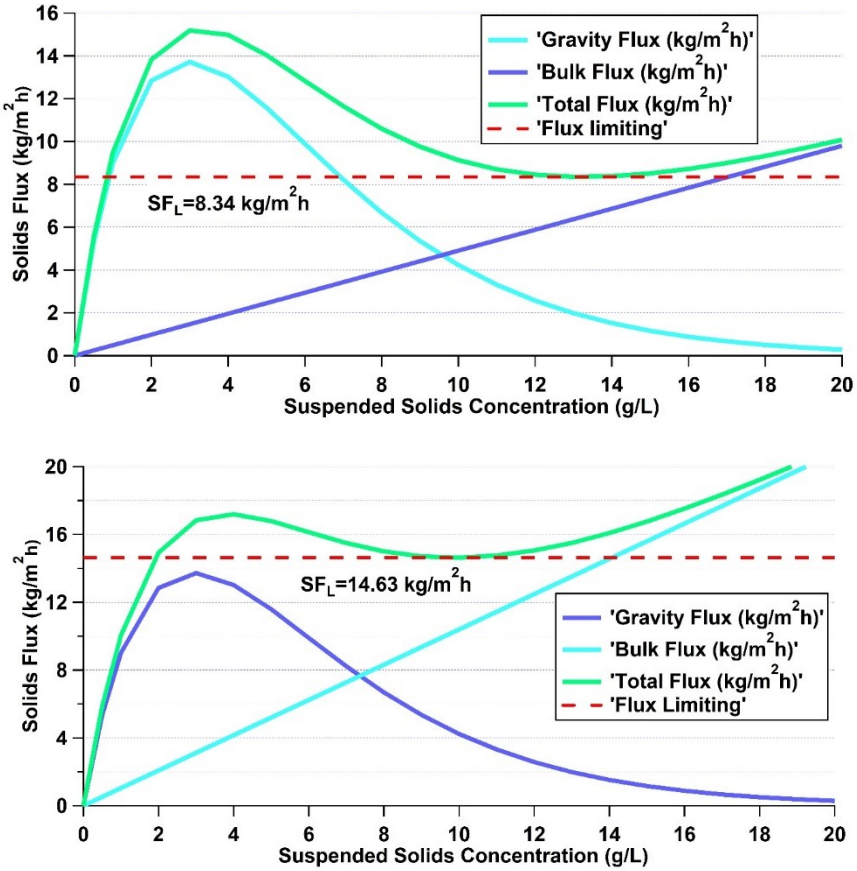

Figure 8-2. Flux diagram for the SST without the McKinney baffle(top) and with the McKinney baffle (bottom). Flow conditions are initialized from Trial 1 and modified using the first stress test method.

Table 8-2. Summary of the limiting flux predicted by the 1DFT and CFD modeling using the first stress testing method

1st stress method (increasing Q with constant MLSS)								
Trial No.	Presence of the McKinney Baffle	SLR-1DFT (kg/m^2h)[1]	SLR-CFD (kg/m^2h)	SLR%	SOR[2] (m/h)	MLSS (g/L)	RAS Ratio	Failure Reason
1	No	8.3	3.9	47.2	0.45	4.187	1.09	Excessive carry over of SS by the upward current towards the effluent weir
	Yes	14.6	7.9	54.1	0.91	4.187	1.09	
2	No	9.8	3.9	39.8	0.55	3.384	1.09	
	Yes	15.6	7.4	47.4	1.05	3.384	1.09	
3	No	9.5	3.8	40.1	0.72	2.904	0.83	
	Yes	13.5	5.9	43.8	1.12	2.904	0.83	

1: 1 kg/m^2h=0.2 $lb/(ft^2h)$

2: Limiting SOR used to calculate the limiting flux predicted by the 1DFT and CFD models

Table 8-3. Summary of the limiting flux predicted by the 1DFT and CFD modeling using the second stress testing method

2nd stress method (increasing Q with constant Q_r and MLSS)								
Trials No.	Presence of the McKinney Baffle	SLR-1DFT (kg/m^2h)[1]	SLR-CFD (kg/m^2h)	SLR%	SOR[2] (m/h)	MLSS (g/L)	RAS Ratio[2] (R)	Failure Reason
1	No	6.6	3.5	52.5	0.47	4.187	0.75	Excessive carry over of SS by the upward current towards the effluent weir
	Yes	6.6	5.3	80.1	0.90	4.187	0.40	
2	No	6.6	3.1	46.9	0.54	3.384	0.65	
	Yes	6.6	4.7	72.2	1.04	3.384	0.347	
3	No	9.2	3.4	36.6	0.75	2.904	0.55	
	Yes	9.2	4.8	52.2	1.10	2.904	0.51	

1: 1 kg/m^2h=0.2 $lb/(ft^2h)$

2: Limiting SOR and RAS Ratio used to calculate the limiting flux predicted by the 1DFT and CFD models

Table 8-4. Summary of the limiting flux predicted by the 1DFT and CFD modeling using the third stress testing method

3rd stress method (increase SLR as the increase of MLSS)								
Trials No.	Presence of the McKinney Baffle	SLR-1DFT (kg/m^2h)[1]	SLR-CFD (kg/m^2h)	SLR%	SOR (m/h)	MLSS[2] (g/L)	RAS Ratio	Failure Reasons
2	No	6.6	5.2	80.0	0.33	7.6	1.09	A
	Yes	6.6	5.5	85.0	0.33	8.0	1.09	B
3	No	9.2	4.0	42.7	0.67	3.2	0.83	A
	Yes	9.2	6.6	71.0	0.68	5.3	0.83	A

1: 1 kg/m^2h=0.2 $lb/(ft^2h)$

2: Limiting MLSS used to calculate the limiting flux predicted by the 1DFT and CFD models

A: Excessive carry over of SS by the upward current towards the effluent weir

B: Rising of sludge blanket to the effluent weir

8.3.1 Stress testing using the first method

Table 8.2 shows the predicted limiting fluxes and the most obvious results are that the CFD analysis predicts much lower limiting fluxes than the 1DFT analysis. The addition of the McKinney baffle increases the predicted limiting flux using both methods and the increases are substantial, increasing by 160 to 200% for both methods; for example, the limiting flux increases from 8.3 to 14.6 kg/m^{2}h or by 176% using the 1DFT analysis. There are still large differences in the predicted limiting fluxes between the 1DFT and CFD methods, but the percent differences are lightly less with the McKinney baffle for all three trials. For example, the CFD-predicted limiting flux is 47% of the 1DFT liming flux without the McKinney baffle and 54% with the McKinney baffle.

The failure mode for all three trials using the first stress testing method is the excessive ESS. In all cases the SBH is acceptable. Figure 8.3 shows one example of acceptable SBH during the stress test even when the ESS is excessive. Left side shows the last safe run and the right side shows the first failure run using the first stress testing method. The 1DFT analysis does not conservatively predict ESS, which is understandable since the original goal of SST flux analysis was to predict thickening performance (Dick, 1970).

Figure 8.4 shows the predicted ESS calculated by CFD as a function of the SLR (kg/(m^{2}h)) for stress testing method 1. The most obvious result is the improvement provided by the McKinney baffle. Limiting flux increases from approximately 5.5 to 8.0 kg/m^{2}h depending on the trial number of initial conditions. The trial number matters little for the results without the McKinney baffle,

with all three trials having a limiting flux at approximately 4.0 kg/m^{2}h. An interesting question is why do the different trials produce different limiting fluxes? Trial 3 produces the most conservative result while Trial 1 predicts the greatest SST capacity, and all trials fail due to excessive ESS. Trial 1 has the greatest MLSS concentration and the higher influent MLSS creates a more compact, lower height SBH, which creates lower ESS. Therefore, if the stress test is conducted using the first stress test method, starting from a comparatively higher inlet MLSS concentration and lower influent flow rate will predict the greatest capacity.

Figure 8.5 compares the velocity profiles for the original and modified SSTs under the limiting loading condition of the original SST. It shows that without the McKinney baffle (Left), the density current forms a strong horizontal jet at the surface of the sludge blanket and flows upward to the effluent weir. Therefore, the original SST fails due to the excessive ESS stirred up from the surface of the sludge blanket to the effluent weir. With the addition of the McKinney baffle in the modified SST (Right), inflow energy is significantly dissipated inside the inlet zone, and the horizontal jet outside the inlet zone is weaken. Therefore, the predicted ESS for the modified SST under the limiting loading conditions of the original SST is only 18 mg/L and the modified SST has larger capacity than the original SST with the addition of the McKinney baffle.

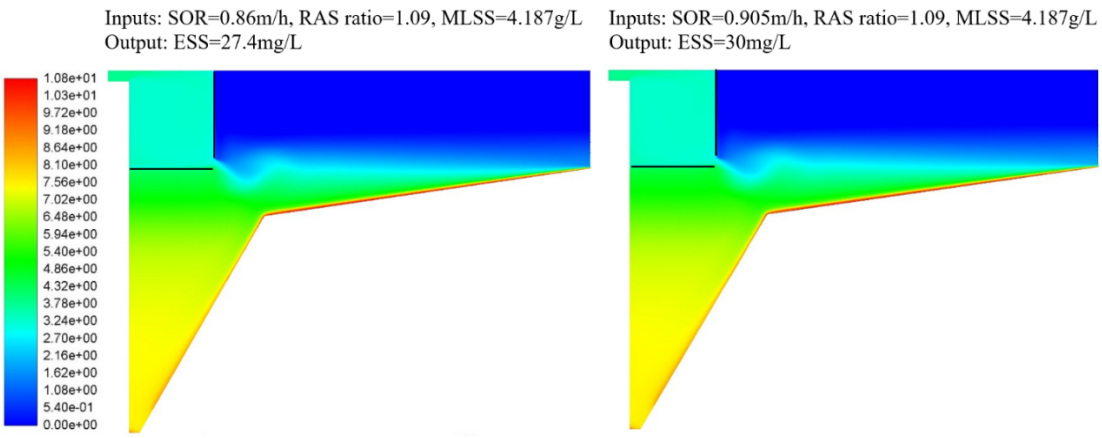

Figure 8-3. Example concentration profiles (g/L) shown the acceptable SBH even when the ESS is excessive. Left side shows the last safe run and the right side shows the first failure run using the first stress testing method.

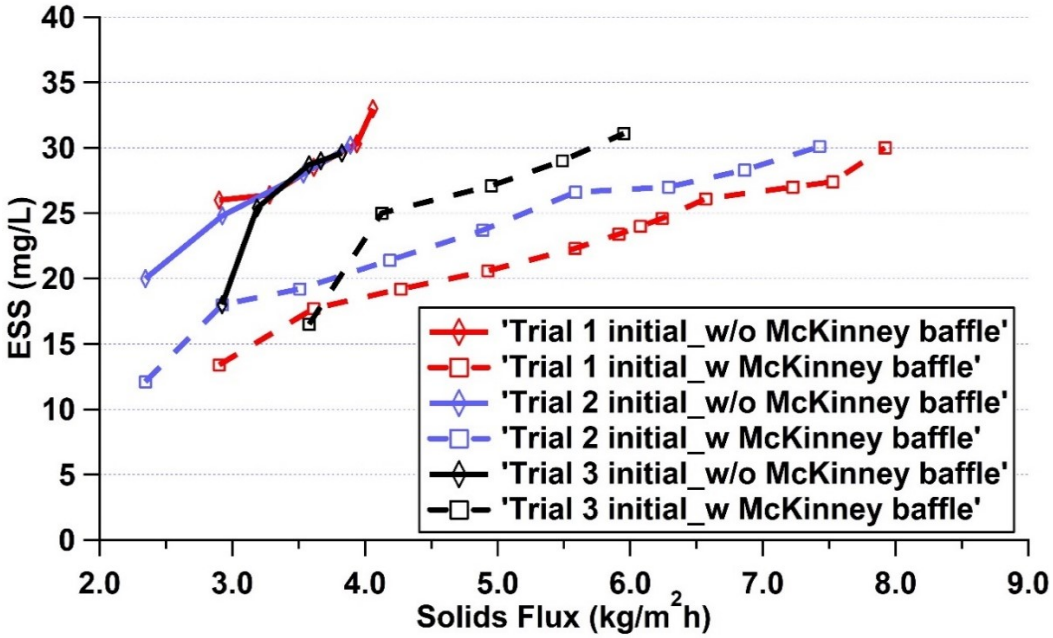

Figure 8-4. ESS as a function of SLR (kg/(m^{2}h)) when CFD stress tests are conducted using the 1st stress testing method

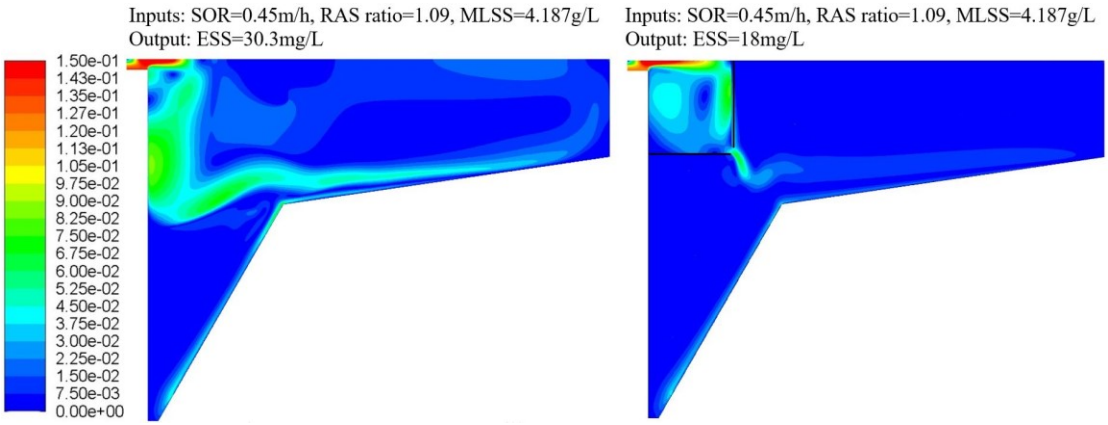

Figure 8-5. Comparison of velocity profiles (m/s) for the original and modified SSTs when original SST fails due to clarification failure.

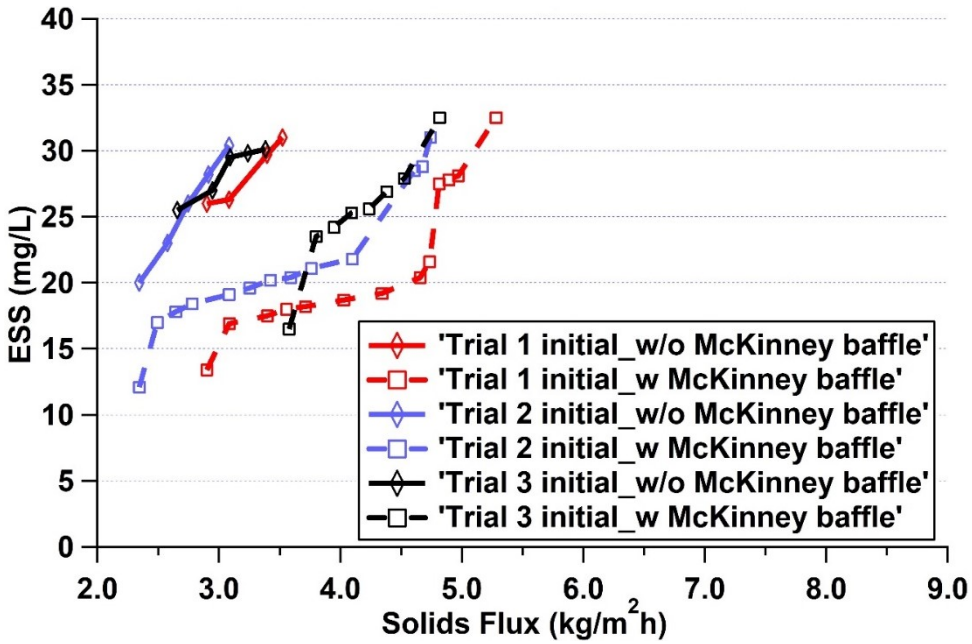

Figure 8-6. ESS as a function of SLR (kg/(m^{2}h)) when CFD stress tests are conducted using the 2nd stress testing method.

8.3.2 Stress testing using the second method

Stress test method 2 maintains a constant return flow rate (Q_r); therefore, the predicted 1DFT flux limit is the same for the original and improved SSTs. Therefore, the CFD predicted limiting flux as a percentage of 1DFT limit is proportional to the CFD predicted limiting flux and

can be used to correctly describe the improvement of the modified SST. Table 8.3 shows that with the addition of McKinney baffle, the CFD predicted limiting flux as a percentage of the 1DFT flux limit is approximately 1.4 to 1.5 times as large for the SST without the McKinney baffle. It increases from 53%, 47% and 37% to 80%, 72% and 52%, when the stress test is initialized under the flow conditions of Trials 1 to 3, respectively. Among these six CFD predicted limiting fluxes, only the CFD predicted limiting flux initialized from flow conditions of Trial 1 for the modified SST reaches 80% of 1DFT limit. The other five limiting fluxes are much lower than 80% of 1DFT limit. Table 8.3 also shows that the maximum CFD predicted limiting flux (3.5 and 5.3 kg/(m^2h)) are also reached by initializing with a comparatively higher inlet MLSS concentration and lower inflow rate, which is consistent to the results of stress tests using the first stress testing method.

Figure 8.6 shows the prediction of the ESS as a function of the CFD predicted SLR (kg/(m^2h)) tested using the second stress testing method. Similar to the results shown in Figure 8.4, the prediction of ESS is gradually increased above 30 mg/L and the failure of SSTs is also caused by excessive carry over of SS by the upward current towards the effluent weir.

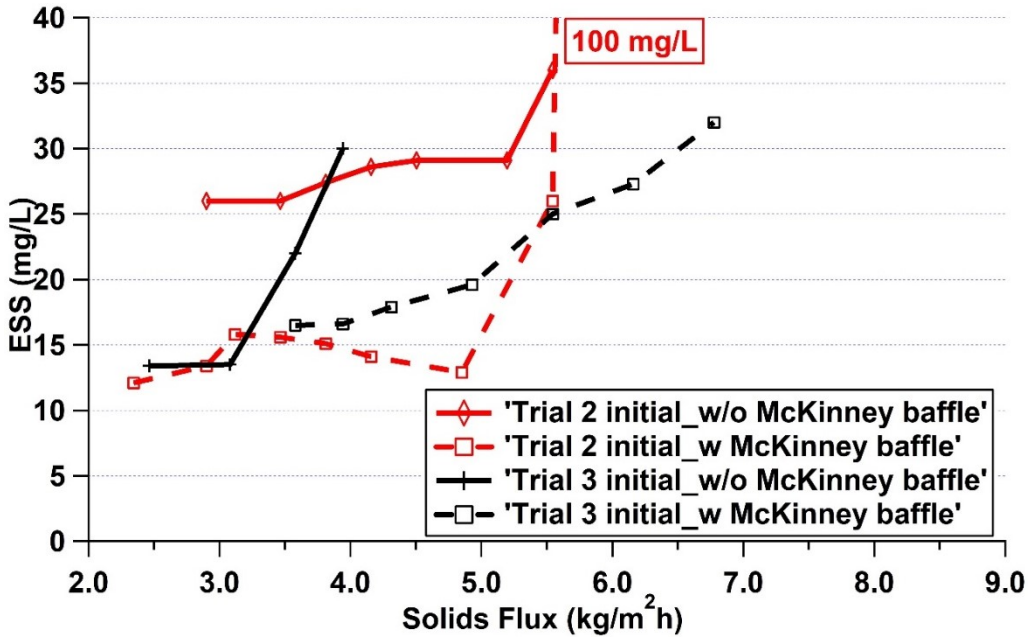

Figure 8-7. ESS as a function of SLR (kg/(m^{2}h)) when CFD stress tests are conducted using the 3rd stress testing method.

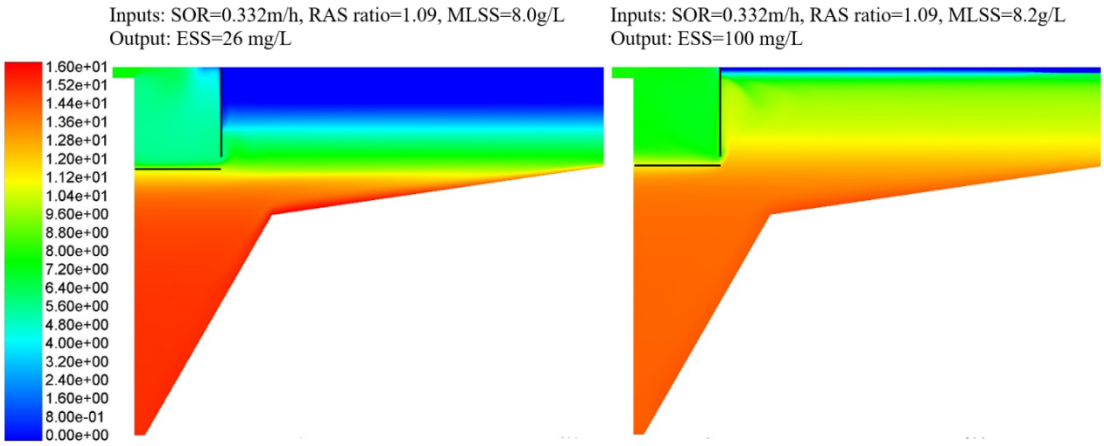

Figure 8-8. Concentration profiles (g/L) shown the SST failure caused by rising of sludge blanket to the effluent weir. Left side shows the last safe run and the right side shows the first failure run using the third stress testing method

8.3.3 Stress testing using the third method

Since flow conditions of Trials 1 and 2 are the same, except that the inlet MLSS concentration for Trial 2 is lower than in Trial 1, the stress test conducted on the third stress method

is only started from the flow conditions of Trials 2 and 3. Also, since the Q_r remains constant when the stress test is started under the same flow conditions, the prediction of the 1DFT limit for the SSTs is the same. Therefore, describing the CFD predicted limiting flux as a percentage of 1DFT limit can correctly evaluate the performance improvement of the SST.

Table 8.4 shows that the stress test conducted using the third stress testing method increases the CFD predicted limiting flux as a percentage of 1DFT limit after the addition of the McKinney baffle. It increases from 80% and 43% to 85% and 71% when the stress test is initialized under the flow conditions of Trials 2 to 3, respectively. Among these four CFD predicted limiting flux, only the CFD predicted limiting flux initialized from flow conditions of Trial 2 for both SSTs reaches 80% of 1DFT limit. Figure 8.7 shows the prediction of the ESS as a function of the CFD predicted SLR (kg/(m^2h)) tested on the third stress method. It shows that the failure of both SSTs is caused by clarification failure when the flow conditions of the stress test are initialized with Trial 3; whereas the failure of the original SST is caused by clarification failure while the failure of the modified SST is caused by solids overloading when the flow conditions of the stress test are initialized with Trial 2. Before the solids is overloaded, the performance of the SST is improved with an increase of the flux until a certain point (flux=5.4 kg/m^2h), where it starts to perform poorly until it suddenly failed by solids overload at 5.5 kg/(m^2h).

When the modified SST is solids overloaded, the inlet MLSS concentration is as much as 8.2 g/L. Figure 8.8 shows the concentration profiles for the modified SST under the last safe run and the first failure run initialized with flow conditions of Trial 2. It shows that the increasing of

the inlet concentration of MLSS from 8.0 to 8.2 g/L causes the exaggerated rise of the sludge blanket to the water surface and the SST is failed by the solids overload.

8.4. Conclusions

In this chapter, effects of the McKinney baffle on the limiting flux of SSTs are studied on a Fluent-based CFD model. CFD stress tests are performed on three different stress testing methods. In each method, different flow conditions are used to initialize the stress test. The prediction of flux capacities of SSTs with and without the McKinney baffle are initialized with different flow conditions under each stress testing method. This study gives a detailed procedure to analyze the performance of McKinney baffle and can be applied to study the effect of other internal geometries.

Compared with the prediction results of the stress test initialized with different flow conditions and conducted using different stress testing methods, only three of the ten CFD predicted limiting flux (30%) reach the 80% of the 1DFT limit under the 2nd and 3rd stress methods. The 80% of the 1DFT limit is reached for (1) the original SST without McKinney baffle when the CFD stress test is started with relatively higher inlet MLSS concentration and lower inflow rate (Trial 1), conducted using the 2nd stress method, and for (2) both original and modified SSTs when the CFD stress test is started with a higher inlet MLSS concentration and lower inflow rate (Trial 2), conducted using the 3rd stress method. Therefore, different internal baffling structures, initial flow conditions and different stress testing methods all contribute to the CFD predicted limiting flux and it is improper to use 80% reduction of the 1DFT for all SSTs.

Also, the prediction results of the stress test by using different stress methods (shown in

Figures 8.4, 8.6 and 8.7) indicate that the McKinney baffle significantly improves the performance of the SST. The predicted ESS for the modified SST with the McKinney baffle is at least 5 mg/L or 30% lower than the prediction of ESS for the original SST under every solid flux. Also, the addition of the McKinney baffle extends the SST limiting flux. The limiting flux in the modified SST can be approximately 1.4 to 2 times of it in the original SST.

Additionally, since the limiting flux predicted by CFD model for the original SST without McKinney baffle is reached by conducting the CFD stress test using the third stress method (increasing MLSS alone), and the limiting flux predicted by CFD model for the modified SST with McKinney baffle is reached by conducting the CFD stress test under the first stress method (increasing flow rate alone), for the engineering consulting project, which is usually limited by the budget hours and do not have enough time to run many cases for CFD stress tests on SSTs with different geometries, it is recommended increasing the flow rate (Q) and MLSS alternatively, while keeping RAS ratio constant.

Based on the simulation results, the following conclusions are made:

1. The McKinney baffle greatly improves the limiting flux of an SST.

2. When stress testing an SST, a preferred strategy is to increase the inflow rate (Q) and MLSS alternatively, while keeping RAS ratio constant.

3. Since initial flow conditions, internal geometries and stress testing methods influence the prediction of the SST limiting flux, the limiting flux prediction ranges from approximately 36% to 80% of the 1DFT limit for the original SST, and ranges from approximately 43% to 85% for the

modified SST; therefore, a flux rating of 80% of the 1DFT limiting is not recommended for all SSTs and evaluating the reduction rate of the 1DFT should be tested case-by-case.

Chapter 9 The influence of wind in secondary settling tanks for wastewater treatment- A computational fluid dynamics study

9.1. Introduction

Secondary settling tanks (SSTs), also known as sedimentation tanks or secondary clarifiers are used in wastewater treatment plants (WWTPs) to remove organic matter and reduce nutrients such as nitrogen and phosphorus (Ramin et al., 2014). It has two different functions: clarification and thickening (Parker, 1983). Clarification separates the suspended solids from the effluent while thickening concentrates the solids at the tank bottom in order to recycle or dispose with less volume (Gao and Stenstrom, 2017).

McCorquodale et al. (2004) summarized that the efficiency of the SSTs depends mainly on the (1) hydrodynamics, (2) particle settling velocity, (3) turbulence, (4) sludge rheology, (5) flocculation, (6) heat exchange and temperature changes. Also, these six processes depend on several influential factors, including (1) tank geometry, (2) flow conditions (surface overflow rate (SOR), returned activated sludge (RAS) ratio, concentration of mixed liquor suspended solids (MLSS) and (3) atmospheric conditions, such as water temperature and wind velocity.

In the last three decades, many researchers and engineers have developed and applied computational fluid dynamics (CFD) models to optimize SST internal geometry to improve process efficiency, and to understand the effects of influential factors on the efficiency of SSTs (Zhou and McCorquodale, 1992a, b, c; Samstag, 1992; Ekama et al., 1997; Vitasovic et al., 1997; De Clercq, 2003; Weiss et al., 2007; Patziger et al., 2012; Ramalingam et al., 2012; Das et al.,

2016). Most of the previous researches focused on the influential factors inside the SST, such as tank geometry, energy dissipating inlet structures, other baffle configurations, and flow conditions. However, the effects of the atmospheric conditions, such as wind, have rarely been studied.

Larsen (1977) identified that the wind shear at the free surface transfers energy to the SST and affects the flow field. McCorquodale et al. (2004) noted the wind is one of the influential factors on the performance of an SST. However, their Q3D model did not include the wind shear effects because of limited computing resources, and they concluded that SST models should be expanded to three-dimensional (3D) to accurately predict wind effects.

In the recent years, several researches have studied the wind effects on rectangular settling tanks in water treatment plants (WTPs) (Khezri et al., 2012; Stamou and Gkesouli, 2015; Gkesouli et al., 2016; Goodarzi et al., 2017; Gkesouli and Stamou, 2018). Table 9.1 shows the major conclusions of these studies. In most cases the predicted effects on removal efficiency are negative, with the exception of low counter-current wind velocity, which increased ESS removal. However, the applicability of these studies to SSTs in WWTPs is limited since the particle concentration in the influent of the settling tank in WTPs is very low. The effects of particles on the flow field are negligible, whereas the high particle concentration in the influent of SSTs in WWTPs make the flow currents density-driven.

Additionally, settling tanks in WTPs are usually rectangular tanks, whereas circular tanks are often used in large SSTs in WWTPs. Also, the internal baffling structures for rectangular and circular settling tanks are different. Therefore, the flow and concentration fields for settling tanks

in WTPs and SSTs in WWTPs are different, and results concluded for settling tanks in WTPs may not be appropriate for SSTs in WWTPs. To the best of our knowledge, none of the published papers simulated the wind effects on SSTs in WWTPs.

The study shows in this chapter differs from the previous wind studies on settling tanks in WTPs in that high total suspended solids concentrations (TSS) concentrations which causes density currents are considered. Both circular and rectangular SSTs in WWTPs are studied under different flow rates and wind directions. Table 9.2 summarizes the loading conditions of the SSTs. The geometries of SSTs and flow conditions are adapted from McCorquodale et al. (2004) and Krebs et al. (1996). The CFD package ANSYS Fluent is used to simulate the wind effects on the circular SST along the inlet port direction (along X axis) and at 45^{o} to the inlet direction and Tecplot 360 (Bellevue, Washington) is used for postprocessing. For the rectangular SST, the wind effects are simulated co-current, counter-current and perpendicular to the SST longitudinal direction.

Ideally, a transient, 3D and three-phase SST model is needed to simulate an SST that take into account the effect of wind. However, a single run of such simulation may require a few months with our computer (Xeon Sliver 4114). Gkesouli and Stamou (2018) provided an alternative, but more economical and faster approach, which is to determine a typical value of the flow velocity at the water surface (*Us*) and set it as a boundary condition along the water surface. The *Us*, is expected to depend on the velocity of the wind that is usually defined at a height of 10 m (U_{10}) or "tree top" wind velocities.

Under each tested wind direction, the flow velocity at the water surface (U_s) increases from

zero to two mildly windy conditions (U_s= 0.125 and 0.25 m/s), and one extreme condition (U_s= 0.50 m/s), which correspond to 8.35, 16.69, and 33.39 miles/hr for the wind velocities at 10 m height (U_{10}) or "tree top" wind velocities, respectively. Equation (1) shows the conversion between U_s and U_{10} (Gkesouli and Stamou, 2018).

$$U_s = (0.9\sim5.8\%)\ U_{10} \tag{9.1}$$

Performance indicators, such as effluent suspended solids (ESS), and sludge blanket height (SBH) from the tank surface, and 3D hydrodynamics profiles are compared as in the range of different wind velocities and wind directions. The SBH is defined as the depth of sludge bed contour 1000 mg/L to the water surface.

Table 9-1. Summary of major contributions of previous studies on wind effects on rectangular water treatment plant settling tanks

References	Wind Speed (U_{10})/ Surface Flow Speed (Us)	Major conclusions
Khezri et al. (2012)	U_{10}=2.5-7.0m/s (both co-current and counter-current)	Co-current wind causes increase flow field velocity resulting in reduced particle removal efficiency.
		Counter-current wind causes flow field velocity decrease that improve particle removal efficiency at low wind velocities (0-2.5m/s), but reduced removal efficiency at high velocity (>2.5m/s).
Stamou and Gkesouli (2015)	Us=0.5m/s (co-current only)	Co-current wind causes negligible effects on particle removal efficiency.
Gkesouli et al. (2016)	U_{10}=0, 5, 7.5m/s (both co-current and counter-current)	Co-current wind slightly reduces particle removal efficiency (<0.3%).
		Counter-current wind slightly increases particle removal efficiency by up to 1%.
Goodarzi et al. (2017)	U_{10}=5.0m/s (co-current only)	Co-current wind causes strong negative effects on particle removal efficiency.
Gkesouli and Stamou (2018)	U_{10}=15~25m/s (co-current only)	Co-current wind causes strong negative effects on removal efficiency

Table 9-2. Loading conditions of the circular and rectangular SSTs

	Inflow parameters			Settling parameters			Dry solids density
Cases No.	MLSS g/L	RAS ratio	$Q_{effluent}$ m^3/h	V_o m/h	r_h L/g	r_p L/g	ρ_p kg/m^3
Case 1	4.60	0.80	833	7.71	0.39	10.00	1450
Case 2	4.30	0.97	688	7.71	0.39	10.00	1450
Case 3	3.60	0.79	948	7.71	0.39	10.00	1450
Case 4	3.50	0.91	360	18.00	0.70	30.00	1450
Case 5	3.50	0.91	540	18.00	0.70	30.00	1450

9.2. Theoretical model

9.2.1 General information

The hydrodynamics characteristics of settling tanks in WTPs were studied by using the standardized multiphase model based on a theoretical solution for slip velocity based on particle size. (Stamou and Gkesouli, 2015; Gkesouli et al., 2016; Goodarzi et al., 2017). However, since the flow in SST is driven by density current, the particle transport model based on sludge settling velocities perform better than the standardized multiphase model (Wicklein and Samstag, 2009). Therefore, the particle transport model based on sludge settling velocities used in our previous SST studies (Gao and Stenstrom, 2018a, 2018b, 2019a, 2019b) is also coupled in this current study.

9.2.2 Governing equations

The equations describing 3-D, steady, turbulent, and density stratified flow in a circular SST are as follows (Das et al., 2015):

9.2.2.1 Continuity equation:

$$\nabla \cdot (\rho \overrightarrow{u_i}) = 0 \tag{9.2}$$

9.2.2.2 Momentum equation:

$$\nabla \cdot (\rho \overrightarrow{u_i}\, \overrightarrow{u_i}) = -\nabla p + \nabla \cdot \bar{\bar{\tau}} + \vec{F} \tag{9.3}$$

9.2.2.3 Standard *k*-*ε* turbulence model:

$$\rho \nabla (\overrightarrow{u_i} k) = \rho \nabla \left[\left(v + \frac{v_t}{\sigma_k} \right) \nabla k \right] + G_k + G_b - \rho \varepsilon \tag{9.4}$$

$$\rho \nabla (\overrightarrow{u_i} \varepsilon) = \rho \nabla \left[\left(v + \frac{v_t}{\sigma_\varepsilon} \right) \nabla \varepsilon \right] + C_1 \frac{\varepsilon}{k} (G_k - C_3 G_b) - C_2 \rho \frac{\varepsilon^2}{k} \tag{9.5}$$

9.2.2.4 Sludge transport equation:

$$\frac{\partial \rho(\overrightarrow{u_i}+V_s)C}{\partial x_i} = \rho \frac{\partial}{\partial x_i}(\frac{v_t}{\sigma_c}\frac{\partial C}{\partial x_i}) \quad (9.6)$$

9.2.2.5 Sludge settling equation (Takács et al., 1991):

$$V_s = \max(0, V_o(e^{-r_p(C-C_{min})} - e^{-r_h(C-C_{min})})) \quad (9.7)$$

9.2.2.6 Sludge rheological model (Bokil, 1971):

$$v = 1 \times 10^{-6} e^{1.386C} \text{ for } C \leq 1 \text{ g/L} \quad (9.8)$$

and

$$v = 2.9 \times 10^{-6} e^{0.322C} \text{ for } C \geq 1 \text{g/L}$$

9.2.2.7 Local fluid density:

$$\rho = \rho_r + C(1 - \frac{\rho_r}{\rho_p}) \quad (9.9)$$

where ρ is the local fluid density, t is time, $\overrightarrow{u_i}$ is the absolute velocity vector, p is the general pressure less the hydrostatic pressure at reference density ρ_r, $\bar{\bar{\tau}}$ is viscous stress, $\vec{F}$ is body force, k in equation (4) and ε in equation (5) are turbulent kinetic energy (TKE) and turbulent dissipation rate, respectively. G_k represents the generation of TKE due to the mean velocity gradients, and G_b corresponds to the generation of TKE due to buoyancy. ϑ is the viscosity of the sludge mixture, ϑ_t is the turbulent eddy viscosity. In equation (6), C is the sludge concentration and V_s is the sludge settling velocity in the vertical direction, and σ_c is the turbulent Schmidt number. The value of σ_c is assumed to be 0.7 in this study and its effects on the performance of SSTs were studied in Gao and Stenstrom (2018b). r_p and r_h account for rapidly and poorly settling floc, respectively. They were calibrated in the original study of this circular SST

(McCorquodale et al., 2004).

9.2.3 Computational fluid dynamic boundary conditions

Velocity inlet boundary conditions are applied to inlet and sludge bottom boundaries, which assumes a uniform distribution of all the dependent variables at the boundary face. For the surface outlet, a pressure outlet boundary condition is applied. Using this type of boundary condition, all flow quantities at the outlets are extrapolated from the interior domain. For the calm condition, the free ambient water surface is treated as a free slip wall. For the windy conditions, a constant horizontal velocity is used on the free surface along the wind direction (Stamou and Gkesouli, 2015; Gkesouli and Stamou, 2018). The solid boundaries are specified as stationary walls with a no slip-shear condition and standard wall function is used with the turbulence models.

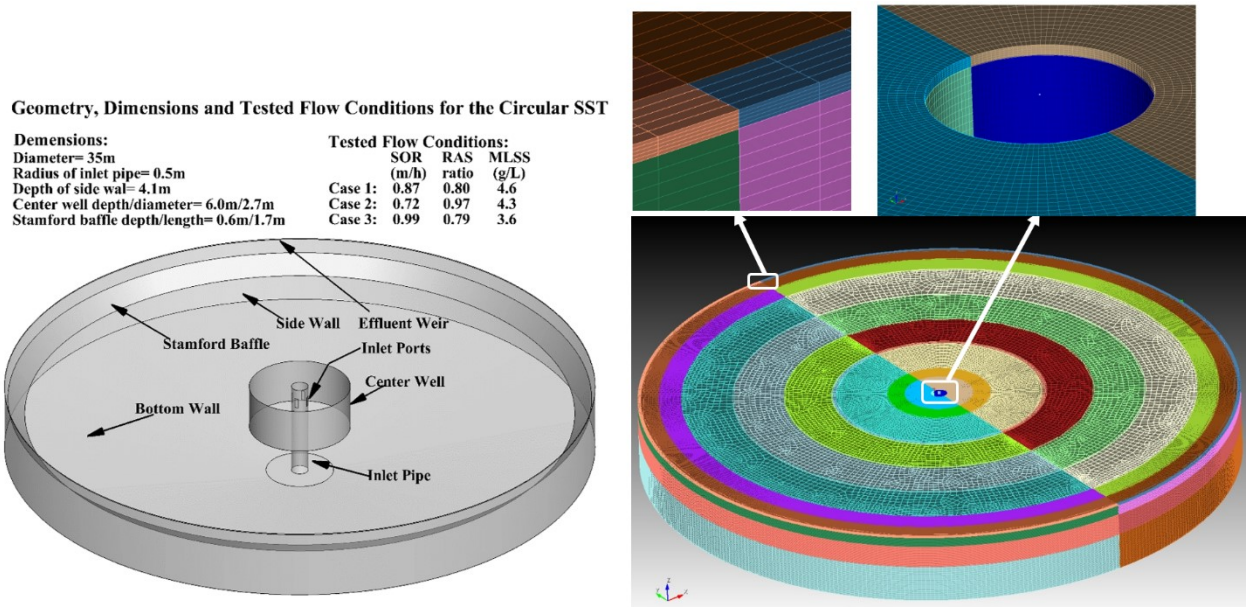

Figure 9-1. Geometry, dimensions, the tested flow conditions (left) and mesh (right) for the circular SST

9.2.4 Geometry and meshing

Figures 9.1 and 9.2 show the geometries, dimensions, the tested flow conditions and meshes for the circular and rectangular SSTs. The computational meshes are generated from Trelis 16.5 (American Fork, Utah) and consist of a total number of 4.8 and 2.0 million hybrid cells for circular and rectangular SSTs, respectively. The geometry of the circular SST was cut axi-symmetrically, and automatically shown with different colors. Next, the geometry with half SST was cut into different sections along the radial direction and meshed in each section independently. The sections with different colors along the radial direction represent the mesh in different sizes, with finer meshes in the field near the inlet and outlets and coarser meshes in the main settling zone. Finally, the mesh for half of the geometry was duplicated to automatically generate the mesh for another half of the geometry. It should be noted that there are four inlet ports at the very center of the SST and the direction of these ports are significant as shown in the simulations. The rectangular SST shown in Figure 9.2 is meshed in the similar fashion to the circular SST shown in Figure 9.1.

In order to ensure that the solutions are mesh-independent, two additional meshes are used for both tanks. For the circular SST, one coarser mesh consisting of 3 million cells, and a finer one consisting of 6 million cells. For the rectangular SST, one coarser mesh consisting of 1 million cells, and a finer one consisting of 4 million cells. Since the prediction difference using the medium and fine meshes is negligible for both tanks, the solutions from the mesh of 4.8 million cells for the circular SST and 2 million cells for the rectangular SST are considered mesh-independent and

have the benefit of increased computational speed.

9.2.5 Model validation

The predictions of effluent suspended solids (ESS) and returned activated sludge (RAS) are compared with the measured results (McCorquodale et al. 2004) and previous two-dimensional (2D) simulation results shown in Gao and Stenstrom (2018a). Figure 9.3 shows that predictions of the current 3D model are consistent to the previous 2D results and measured results. The case numbers in Figure 9.3 are listed in Figure 9.1.

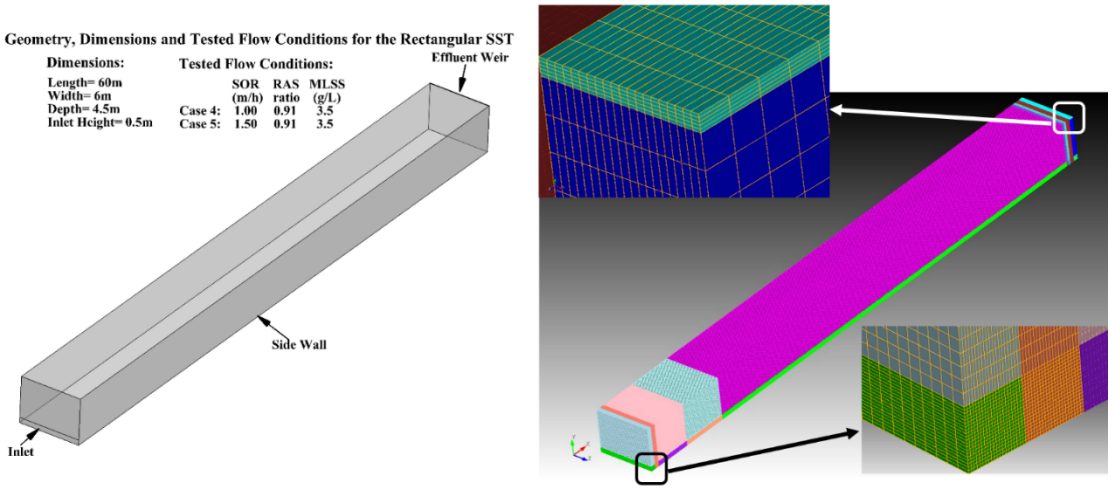

Figure 9-2. Geometry, dimensions, the tested flow conditions (left) and mesh (right) for the rectangular SST

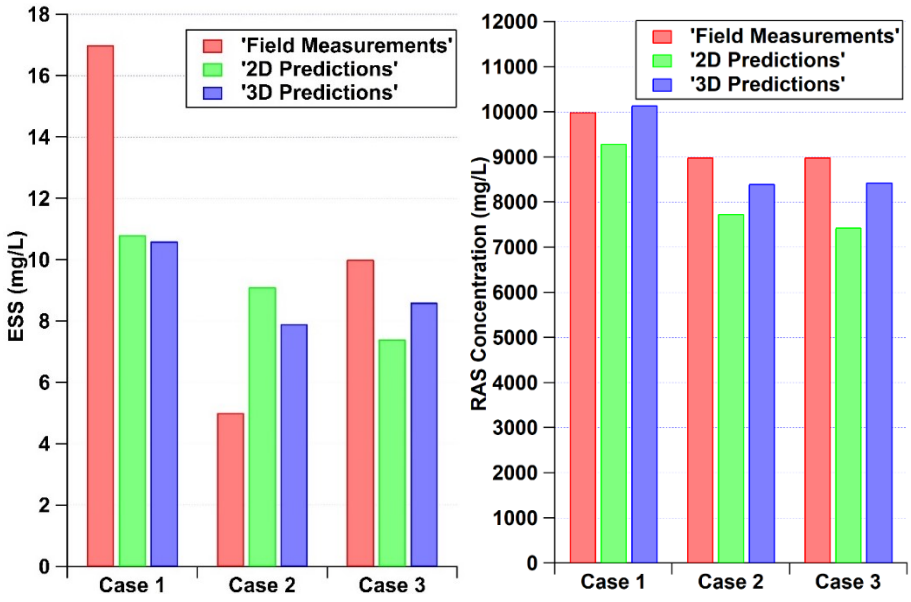

Figure 9-3. Comparisons among the predictions of performance indicators with 2D, 3D models and field data.

9.3. Results and discussion

9.3.1 Impact of the wind on the circular SST

9.3.1.1 Performance indicators

Figure 9.4 shows comparisons of predictions of area-weighted performance indicators among different flow velocities at the water surface for Cases 1 to 3. It shows that the wind deteriorates the SST clarification performance, whereas it has little impact on sludge thickening until under the extreme windy condition. Also, wind along the inlet port direction has a stronger impact than a 45° to the inlet direction.

The SST clarification is very sensitive to the wind, especially when the concentration of MLSS is high. The prediction of ESS is approximately doubled as the increase of the flow velocity at the water surface (U_S) to 0.125m/s (U_{10}= 8.35 miles/hr) in each case. As the increase of the flow

velocity at the water surface (U_S) to 0.25m/s (U_{10}= 16.69 miles/hr), the SST fails in Case 1 due to the excessive of ESS and is under the limiting condition in both Cases 2 and 3.

Since the effects of turbulence and wind, the flow and concentration distribution are not uniform in the SST; therefore, the distribution of ESS is not uniform. Table 9.3 shows the predictions of ESS range among different flow velocity at the water surface (U_S) for Cases 1 to 3. Although Figure 9.4 shows that the area-weighted ESS in Case 1 under the calm and mild windy condition (0.125m/s) are much lower than the ESS limit (30 mg/L), Table 9.3 shows that the ESS is close to the limit in Case 1 under the calm condition and exceeds the ESS limit (highlighted in red) under the mild windy condition (0.125m/s) at a certain location. Table 9.3 also indicates that the wind along the inlet port direction has a stronger impact on the SST clarification.

Table 9-3. Predictions of performance indicators range among different surface flow velocities on water surface for Cases 1 to 3

Surface Flow Speeds	Wind Direction	Averaged ESS (mg/L)	Lowest ESS (mg/L)	Highest ESS (mg/L)	Averaged RAS (mg/L)	Averaged SBH (m)
Case 1						
U_s=0		10.6	5.4	27.0	10151	3.2
U_s=0.125 m/s	A	21.6	9.6	67.0	10191	3.1
U_s=0.125 m/s	B	18.6	10.0	44.0	10262	3.2
U_s=0.25 m/s	A	34.5	17.8	80.0	10170	3.0
U_s=0.25 m/s	B	33.9	17.9	78.3	10180	3.1
U_s=0.50 m/s	A	96.7	43.3	208	9885	3.0
U_s=0.50 m/s	B	86.4	41.0	167	10056	3.0
Case 2						
U_s=0		7.9	5.7	11.3	8410	3.7
U_s=0.125 m/s	A	14.1	9.0	25.0	8756	3.7
U_s=0.125 m/s	B	13.7	8.7	23.0	8870	3.7
U_s=0.25 m/s	A	30.0	17.5	55.0	8876	3.7
U_s=0.25 m/s	B	27.5	16.3	55.8	8691	3.7
U_s=0.50 m/s	A	85.8	38.3	196	8600	3.4
U_s=0.50 m/s	B	74.8	35.9	177	8640	3.5
Case 3						
U_s=0		8.6	3.0	14.0	8440	3.8
U_s=0.125 m/s	A	15.2	9.0	25.8	8532	3.7
U_s=0.125 m/s	B	14.5	9.0	23.4	8633	3.7
U_s=0.25 m/s	A	29.2	16.8	81.3	8815	3.7

U_s=0.25 m/s	B	27.4	16.6	51.6	8674	3.7
U_s=0.50 m/s	A	93.0	43.8	173	8652	3.2
U_s=0.50 m/s	B	79.0	39.0	162	8652	3.4

Wind directions:

A: Along the inlet port direction

B: 45° to the inlet port direction

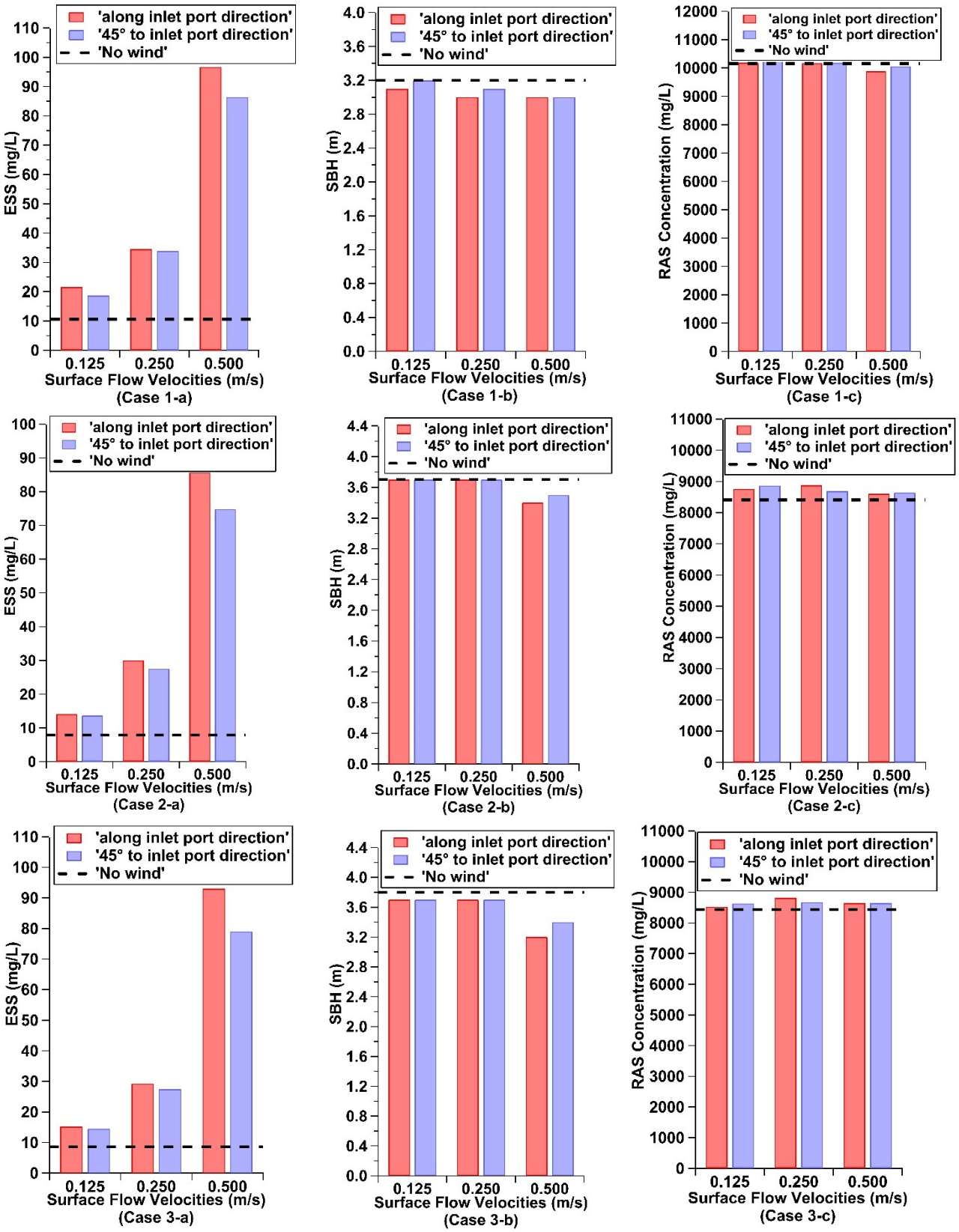

Figure 9-4. Predictions of area-weighted performance indicators among different flow velocities on the water surface for Cases 1 to 3. (Top: Case 1; Medium: Case 2; Bottom: Case 3).

9.3.1.2 Concentration iso-surfaces

In order to better illustrate the prediction results shown in Table 9.3, sludge concentration iso-surfaces at 30 mg/L under calm and the first two windy conditions for the Case 1 are shown in Figures 9.5 to 9.7, respectively. Table 9.3 and Figure 9.4 show that the ESS exceeds 30mg/L on the entire effluent weir under the extreme windy condition; therefore, the concentration iso-surface at 30 mg/L under the extreme windy condition does not exist and cannot be shown here.

Figure 9.5 shows that due to the high concentration of MLSS, the 30 mg/L iso-surface is generally close to the Stamford baffle. At some peripheral areas of the SST, the iso-surface is above the Stamford baffle and is very close to the effluent weir. Therefore, the predicted ESS is close to 30 mg/L at these areas. Figure 9.6 shows that under the first mild windy condition (0.125m/s), the elevation of the iso-surface on the entire upwind side of the SST rises above the Stamford baffle. At some peripheral areas of the SST, the iso-surface is at the effluent weir. Therefore, the SST clarification partially fails. As the increase of the wind shear induced flow velocity at the water surface (U_S=0.25 m/s) shown in Figure 9.7, the 30 mg/L iso-surface on the entire upwind side of the SST is at the water surface. Also, the flow velocity at the water surface (U_S) caused by the wind shear drifts the suspended solids on the upwind side of the SST to the downwind side of the SST. Therefore, the SST clarification on the entire effluent weir fails.

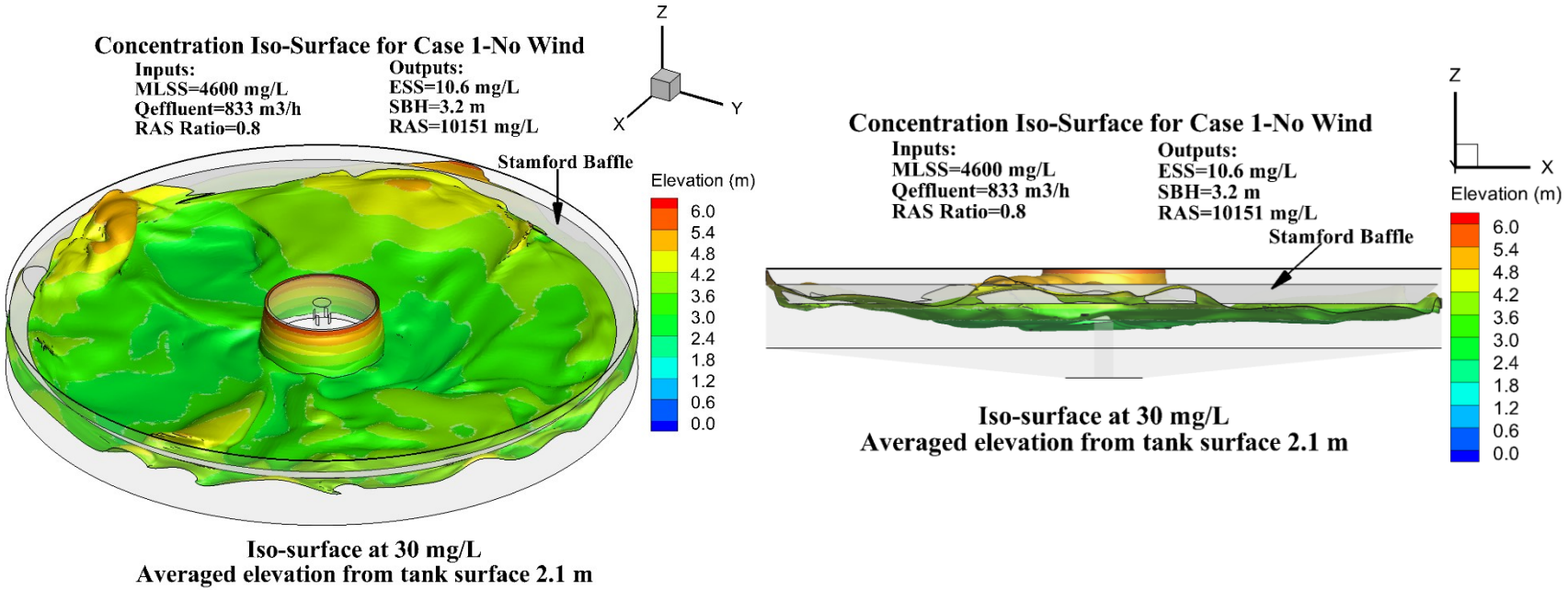

Figure 9-5. Concentration iso-surface at 30 mg/L under the calm condition for the Case 1. Note the four inlet ports in the very center of the SST.

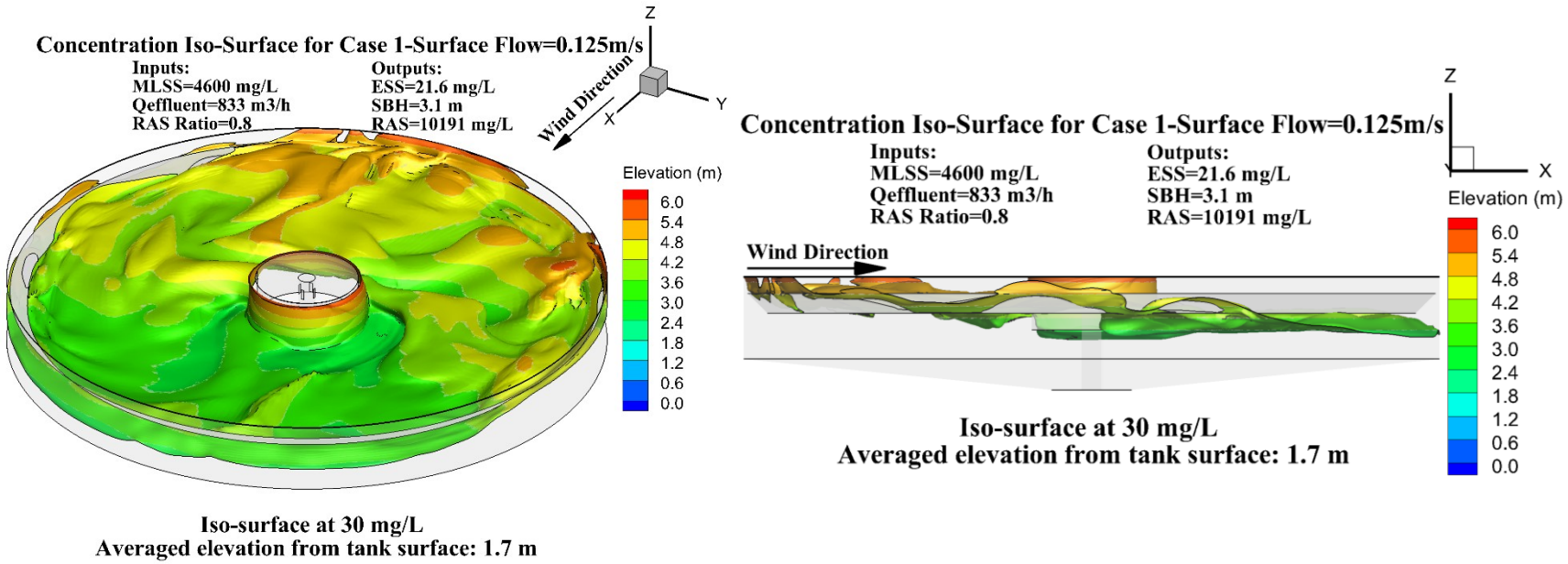

Figure 9-6. Concentration iso-surface at 30 mg/L under the first windy condition (0.125m/s) for the Case 1

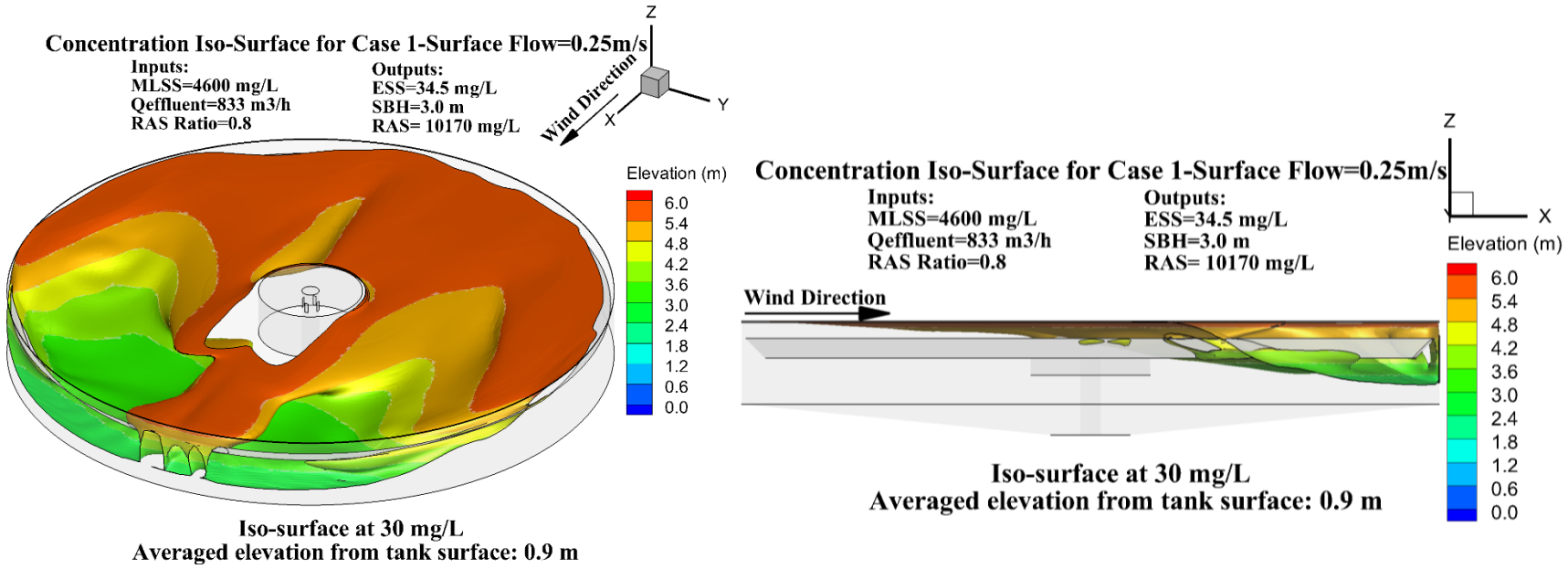

Figure 9-7. Concentration iso-surface at 30 mg/L under the second windy condition (0.25m/s) for the Case 1

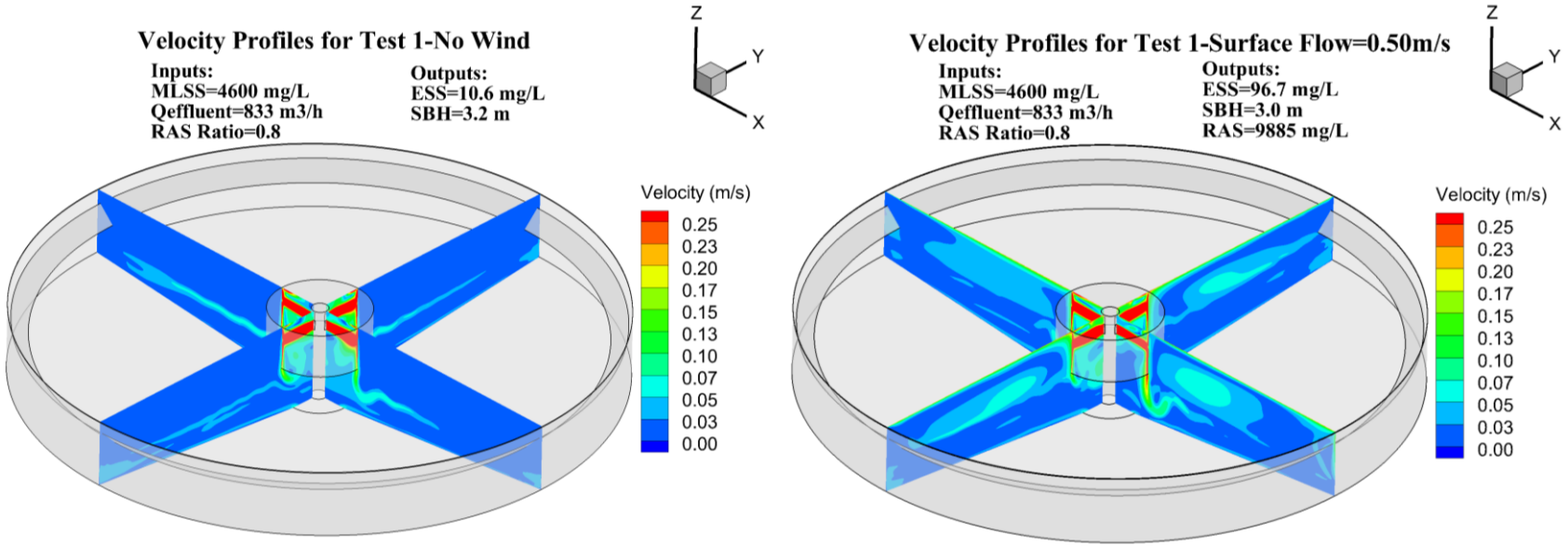

Figure 9-8. Velocity profiles without (left) and with (right) the wind effect

Table 9-4. Predictions of ESS range among different surface flow velocities on water surface for Cases 4 and 5

Surface Flow Speeds	Wind Direction	Averaged ESS (mg/L)	Lowest ESS (mg/L)	Highest ESS (mg/L)
Case 4				
U_s=0		10.8	10.3	11.4
U_s=0.125 m/s	Co-current	10.7	10.2	10.8
U_s=0.25 m/s	Co-current	11.6	10.5	12.0
U_s=0.50 m/s	Co-current	23.7	14.0	31.0
U_s=0.125 m/s	Counter-current	11.0	11.0	11.6
U_s=0.25 m/s	Counter-current	12.2	12.0	13.0
U_s=0.50 m/s	Counter-current	29.0	18.9	56.6
U_s=0.125 m/s	Perpendicular	10.8	10.0	11.0
U_s=0.25 m/s	Perpendicular	10.9	10.0	11.4
U_s=0.50 m/s	Perpendicular	11.0	10.3	11.4
Case 5				
U_s=0		16.6	14.3	21.0
U_s=0.125 m/s	Co-current	15.6	10.0	23.0
U_s=0.25 m/s	Co-current	16.0	11.0	20.0
U_s=0.50 m/s	Co-current	50.6	19.6	69.4
U_s=0.125 m/s	Counter-current	16.8	15.0	32.0
U_s=0.25 m/s	Counter-current	17.4	15.8	22.5
U_s=0.50 m/s	Counter-current	74.0	49.0	136
U_s=0.125 m/s	Perpendicular	16.0	13.0	19.0
U_s=0.25 m/s	Perpendicular	17.3	12.4	25.0
U_s=0.50 m/s	Perpendicular	16.9	12.5	27.7

9.3.1.3 Velocity profiles without/with the wind effect

Figure 9.8a and 9.8b show the velocity profiles without/with the wind effect, respectively. Without the wind effect (left), inflows on both sides of the SST impinge on the center well and are then forced downward before reversing directions to form horizontal jets towards the side wall. In

a vertical section of the SST, the horizontal jet in the main settling zone recirculates the flow clock-wise and counter-clock-wise on both sides of the SST.

The existence of the wind shear (right) increases the circulation on the upwind side of the SST and causes a large and strong recirculation in the main settling zone. The horizontal jet flows along the radial direction to the side wall where it turns vertically and then turns back towards the center well. Therefore, the liquid in main settling zone of the upwind side of the SST is mixed, reducing clarification efficiency.

On the downwind side of the SST, the flow velocity at the water surface caused by the wind effect create opposite recirculation flows compared to the upwind side. The recirculation flow is along the surface, to the side wall then downward and back along the SST bottom to the center well. The wind flows against the horizontal flow to the center well. Therefore, the horizontal jet becomes weaker and the recirculation magnitude in the main settling zone is reduced compared to the upwind side. Also, the strong wind on the downwind side of the SST produces strong surface velocity to the effluent weir. The SS on the upwind side of the SST can be transported to the downwind side by the strong surface jet, the overall ESS removal efficiency of the SST decreases.

9.3.2 Impact of the wind on the rectangular SST

9.3.2.1 Performance indicators

Figure 9.9 compares the predicted area-weighted ESS and SBH among different flow velocities on the water surface for Cases 4 and 5. Compared with the impact of wind on the performance of the circular SST, which doubled the ESS under the first mild windy condition

(U_s=0.125 m/s), the rectangular SST is generally more resistant to the effect of the wind. Moreover, Figure 9.9 shows that among these three different types of wind directions (co-current, counter-current, perpendicular to SST longitudinal direction), counter-current wind has the most significant negative impact on the SST clarification, while co-current wind slightly reduces the ESS under the first mild windy condition, but performance gradually deteriorates with increasing wind speed. The wind flowing perpendicular to the SST's longitudinal direction has the least negative effect on the SST clarification. However, neither these three types of wind have strong impact on the sludge thickening under the mild conditions (U_s=0.125 and 0.25 m/s), and only co-current and counter-current wind has strong impact on the sludge thickening under the extreme windy condition.

Table 9.4 shows the range of ESS predictions in the clam and different windy conditions for Cases 4 and 5. It also shows that under the first mild windy condition (U_s=0.125 m/s), co-current wind slightly improves clarification of the SST along the entire length of the effluent weir, whereas the counter-current wind increases ESS to more than 30 mg/L at certain location along the effluent weir. Also, when wind increases perpendicularly to SST longitudinal direction, the highest ESS increases gradually to 30 mg/L at the extreme windy condition.

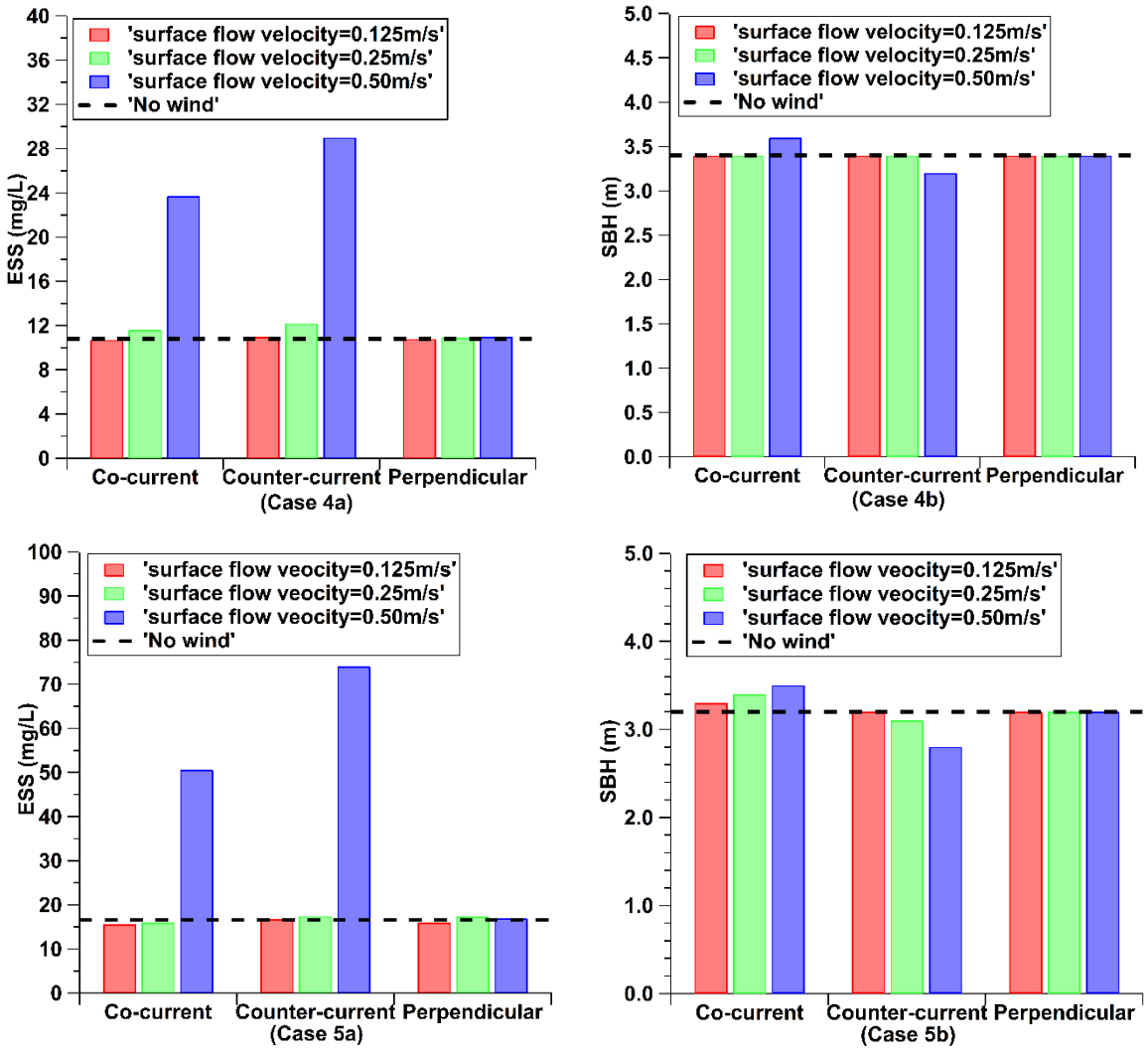

Figure 9-9. Predictions of area-weighted ESS and SBH among different surface flow velocities on water surface for Cases 4 and 5

9.3.2.2 Variation of the hydrodynamics as the existence of co-current wind

Figure 9.10 compares the velocity profiles under the calm and co-current wind conditions for the Case 5. Under the calm condition (Figure 9.10a), the inflow generates a strong horizontal jet from the inlet to the rear of the tank, which creates a current flowing counter-clock-wise over the length of the entire SST and forms a small eddy recirculating clock-wise near the effluent weir.

However, the existence of co-current wind (Figure 9.10b) changes the flow pattern above the horizontal inflow jet. It changes the recirculation over the entire SST to flow clock-wise and enhances the size and turbulence intensity of the eddy near the effluent weir. Since the recirculation direction above the horizontal inflow jet is opposite to the eddy near the effluent weir, it suppresses the upward flow of the suspended solids to the effluent weir. As the increase of flow velocities on the water surface (Figure 9.10c and 9.10d), recirculation over the entire SST and near the effluent weir are intensified. When flow velocities on the water surface increases to 0.5 m/s (extreme condition), the flow velocity on the entire water depth near the rear wall increases to the same magnitude of the inlet velocity. The strong flow velocity near the rear wall stirs up the suspended solids to the effluent weir and causes the SST to fail.

Figure 9.11 shows the comparison of concentration iso-surfaces at 30 mg/L under the calm and co-current wind conditions. Similar to the velocity patterns shown in Figure 9.10, Figure 9.11a shows that under the calm condition, the elevation of the concentration iso-surface reduces gradually as the sedimentation of suspended solids along the longitudinal direction. However, the existence of surface flow velocity caused by co-current wind (Figure 9.11b) intensifies the eddy near the effluent weir; therefore, stirring up the suspended solids near the effluent weir to a higher elevation. As the increase of surface flow velocity (Figure 9.11c and 9.11d), the intensification of the recirculation above the horizontal jet and the eddy near the effluent weir stir up the suspended solids over the entire SST; therefore, the entire elevation of the iso-surface is increased. Figure 9.11d shows that the eddy near the effluent weir is so strong that the ESS concentration along the

entire length of the effluent weir is more than 30mg/L (ESS limiting).

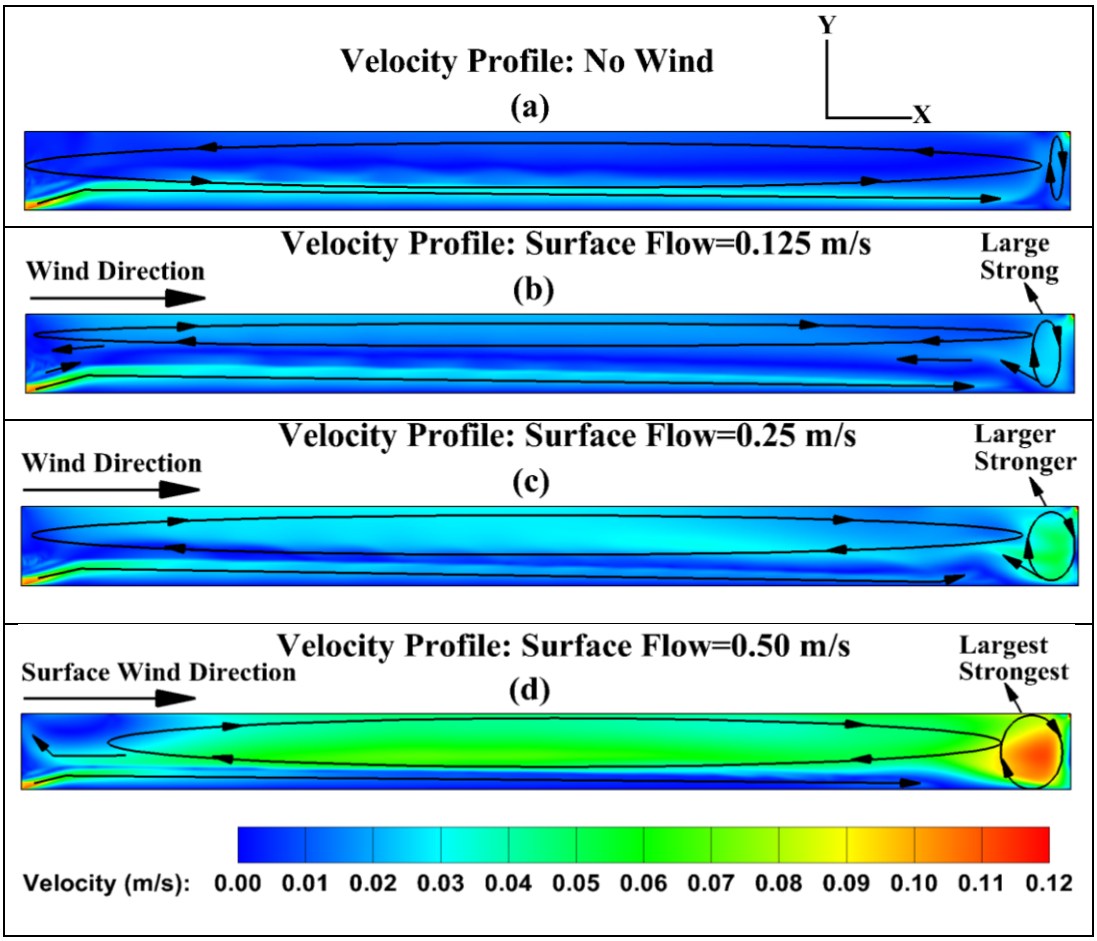

Figure 9-10. Comparison of velocity profiles under the calm and co-current wind conditions for the Case 5

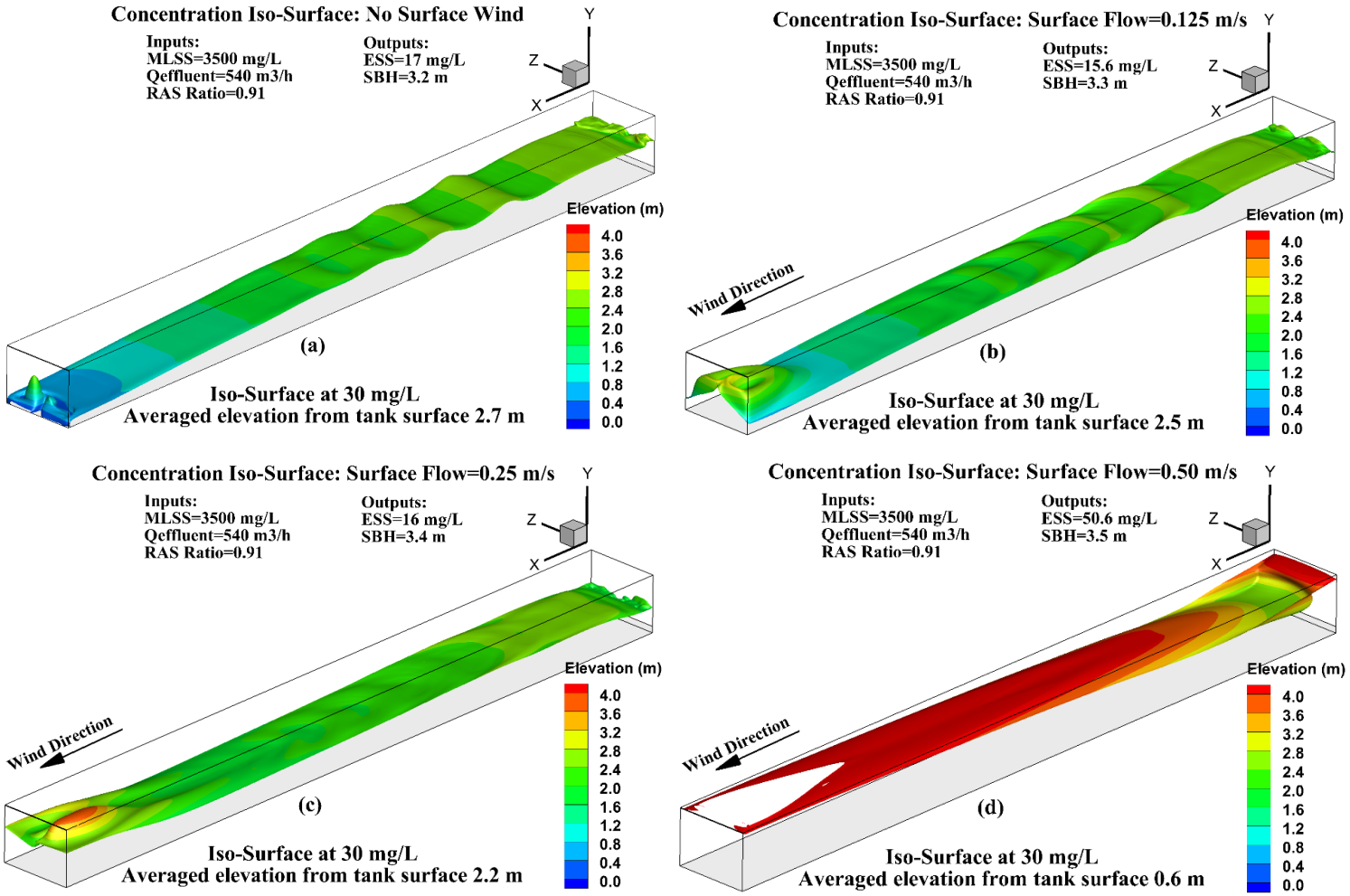

Figure 9-11. Comparison of concentration iso-surfaces at 30 mg/L under the calm and co-current wind conditions for the Case 5.

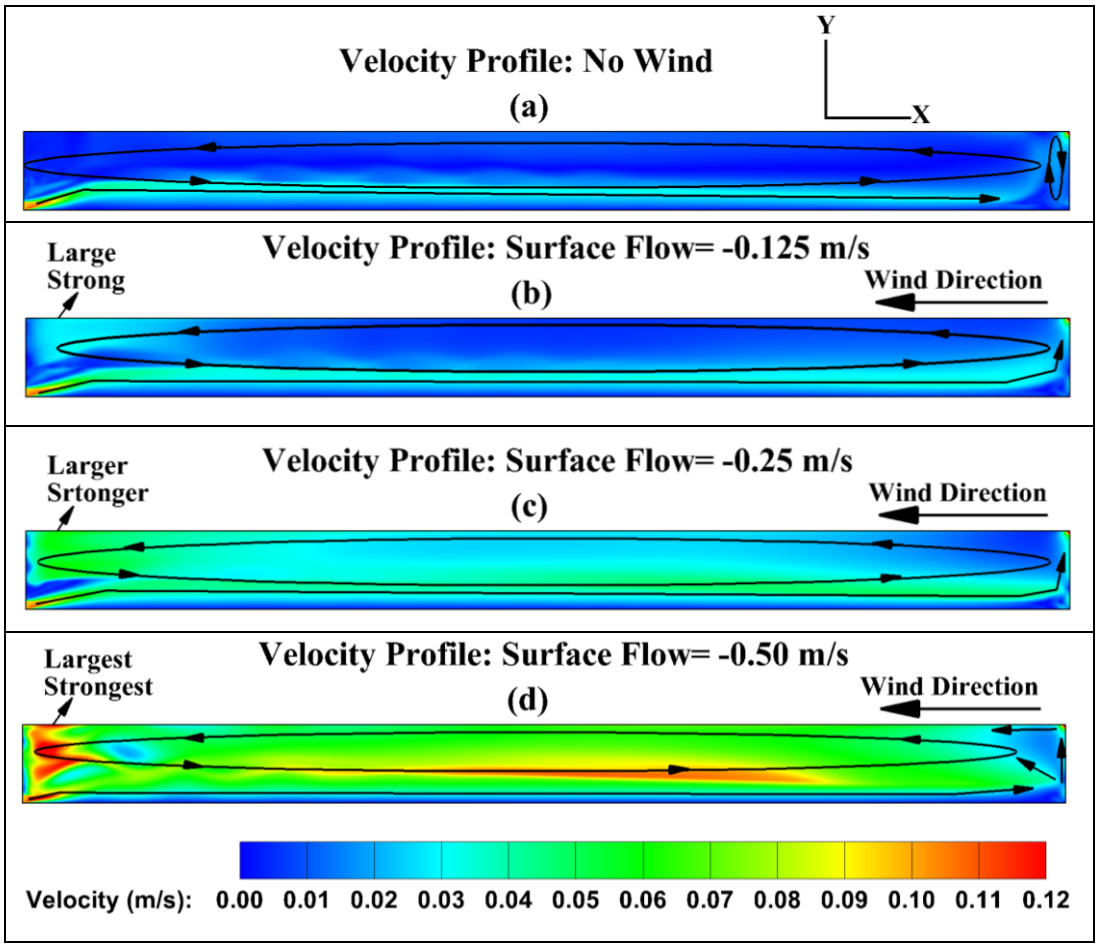

Figure 9-12. Comparison of velocity profiles under the calm and counter-current wind conditions for the Case 5.

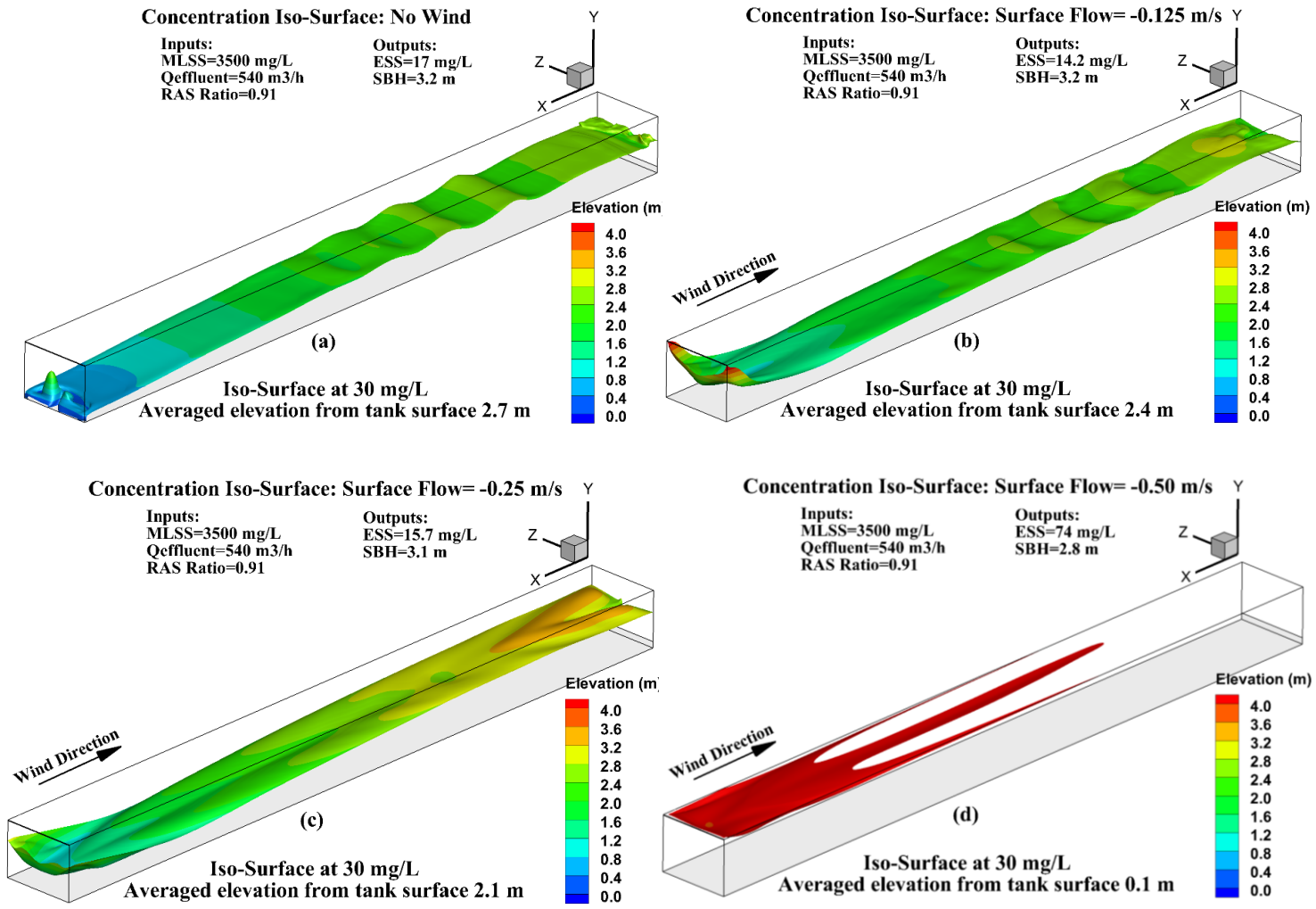

Figure 9-13. Comparison of concentration iso-surfaces at 30 mg/L under the calm and counter-current wind conditions for the Case 5.

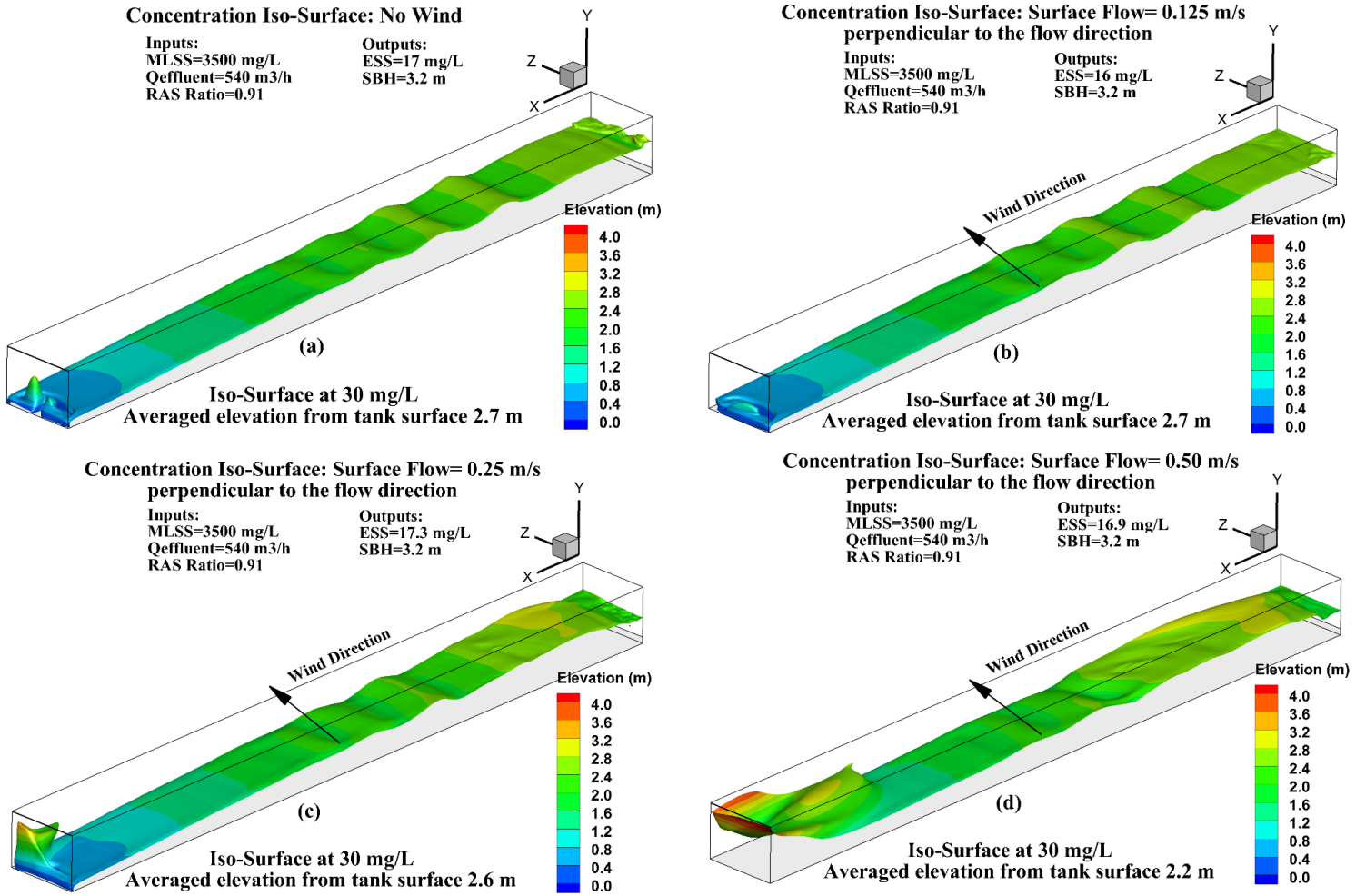

Figure 9-14. Comparison of concentration iso-surfaces at 30 mg/L under the calm condition and wind flows perpendicular to the tank longitudinal direction for the Case 5.

9.3.2.3. Variation of the hydrodynamics as the existence of counter-current wind

Figure 9.12 compares the velocity profiles under the calm and counter-current wind conditions for the Case 5. It shows that the existence of surface flow velocity caused by the counter-current wind enhances the horizontal inflow jet flowing to the rear wall and then flowing upward to the effluent weir. The stronger upward flow carries the suspended solids to the effluent weir; therefore, counter-current wind has stronger negative impacts than the co-current wind. Also, different from the flow pattern under co-current wind, counter-current wind strengthens the counter-clock-wise flow pattern over the entire SST, especially near the front wall. As the counter-current wind increases to the extreme condition (Figure 9.12d), the flow velocity on the entire water depth near the front wall increases to the same magnitude of the inlet velocity.

Figure 9.13 shows the comparison of concentration iso-surfaces at 30 mg/L under the calm and counter-current wind conditions. Similar to the velocity patterns shown in Figure 9.12, the stronger upward flow near the rear wall (Figure 9.13b) carries suspended solids to the effluent weir; therefore, the elevation of the concentration iso-surface near the rear wall increases. As the increase of surface flow velocity caused by the counter-current wind (Figure 9.13c and 9.13d), suspended solids on the entire SST is stirred up and the entire elevation of the concentration iso-surface is increased. Figure 9.13d shows that the concentration of the suspended solids is more than 30 mg/L (ESS limiting) on a significantly larger scale of SST surface area than under the same velocity of co-current wind (Figure 9.11d), which also indicates that the counter-current wind has stronger negative impacts than the co-current wind on the SST.

Compared with the wind study of Gkesouli et al. (2016) for a settling tank in the WTP which shows that co-current wind has negligible negative effects and counter-current wind has positive effects on the particle removal efficiency, the current study shows that the SST fails with only 0.125 m/s increase of surface flow velocity caused by the counter-current wind velocity and 0.25 m/s increase of surface flow velocity caused by the co-current wind velocity.

9.3.2.4 Variation of the hydrodynamics as the existence of wind flows perpendicular to the SST longitude direction

Figure 9.14 shows the comparison of concentration iso-surfaces at 30 mg/L under the calm condition and wind flows perpendicular to the tank longitudinal direction for the Case 5. It shows that the concentration of the iso-surfaces at 30 mg/L under the first windy condition (U_s=0.125 m/s) and under the calm condition are similar, which indicates that the suspended solids distribution in the rectangular SST is insensitive to the wind velocity less or equal than this mild windy condition. As the flow velocity on the water surface increase to 0.25 m/s, the suspended solids on the downwind side of the effluent weir is stirred up and elevated close to the effluent weir. When the surface flow velocity increases to 0.50 m/s (extreme condition), the concentration iso-surface is elevated close to the effluent weir on the entire width of the SST.

9.4. Conclusions

In this chapter, Fluent-based 3D numerical models are used to analyze the impact of wind on the performance of both circular and rectangular SSTs in the WWTP. The wind with different wind speeds and wind directions are studied under different flow conditions.

The circular SST is tested under three different flow conditions (Cases 1 to 3). Three different surface flow speeds on the water surface as well as two different wind directions (along the inlet port direction and at 45^o to the inlet port direction) are evaluated at each flow condition. The rectangular SST is tested under two different flow conditions (Cases 4 and 5). Under each flow condition, three different surface flow speeds on the water surface as well as three different wind directions (co-current, counter-current wind and wind flowing perpendicular to the SST long axis) are tested. Therefore, 18 simulations are run for both circular and rectangular SSTs.

The predictions of performance indicators, such as ESS and SBH and 3D hydrodynamics profiles are compared among different wind velocities and the calm condition. Additionally, predictions under different wind directions are also compared.

For the cases studied under various flow conditions, wind speeds and wind directions, the following conclusions are made:

- Wind deteriorates the SST clarification performance under every wind direction and speed in both circular and rectangular SSTs, except with mild co-current wind (U_s≤0.125m/s), which slightly improves the clarification of the rectangular SST.
- Wind under the mild windy conditions (U_s≤0.25m/s) has little effect on the sludge thickening under every wind direction in both circular and rectangular SSTs, while it deteriorates the sludge thickening under the extreme windy condition (U_s=0.50m/s).

- Wind has stronger negative impacts on the circular SST than the rectangular SST. The existence of mild windy condition (U_s=0.125m/s) can double the ESS for the circular SST, while the rectangular SST is less sensitive to the effect of wind under mild windy condition.
- For the circular SST, wind along the inlet port direction has stronger negative impact on the SST than the wind at 45^o to the inlet direction. For the rectangular SST, counter-current wind has strongest negative impacts on the SST while the wind flowing perpendicular to the SST longitudinal direction has the least negative impacts.
- These results suggest that in windy climates covering SSTs or protecting them from strong winds may be justified.

Chapter 10 Summary

This dissertation focuses on the CFD modeling of secondary settling tanks (SSTs), including the evaluation of different turbulence sub-models and investigation the impact of different parameters in modeling structures and the application of CFD models on the design and operation of SSTs. Specific conclusions of this dissertation can be made as follows:

1. Turbulence model selection can have a strong influence on the prediction of flow capacity and hydrodynamics of an SST. The difference of velocity and concentration patterns is remarkable inside the inlet zone, where the high flow energy is dissipated, resulting in high turbulence. Therefore, more observations are required inside the inlet zone for model verification and turbulence model selection.
2. The prediction difference between buoyancy-decoupled and buoyancy-coupled turbulence models is significant in an SST with poor baffling structures but negligible in an SST with good baffling structures. Therefore, G_b is a buoyancy correction term to correctly predict the performance of an SST with poor baffling structures.
3. For the studies of different parameters in the modeling structures, the results showed that (1) the buoyancy term in the turbulent dissipation rate equation can be removed to improve the rate of convergence and reduce computing time; (2) the turbulence Schmidt number can be used to adjust the SBH, when ESS and RAS concentrations are well calibrated to the field data, but the SBH does fit field observations; (3) the exponential term accounting for the small particle (r_p) in the Takács settling model can be used to adjust the ESS, when

SBH and RAS concentration are well calibrated to the field data, but the ESS does not fit field observations; (4) a medium value of dry solids density (r_p), such as 1450 kg/m^3, is a good assumption; (5) different turbulence specification methods for the inlet boundary condition predict similar predictions.

4. Influent temperature variations, surface heat exchange, and MLSS concentrations are all major factors affecting the performance of SSTs. Also, high MLSS concentrations, typically occurring in ASPs, will overcome the effect of inlet temperature, resulting in bottom currents. Therefore, MLSS concentration is the dominate factor in producing density currents in SSTs.
5. The controversy over the relationship between SOR and SST performance can be largely explained by the SST geometry. Shallow SSTs (< 4m) have poorer performance relative to deep SSTs (> 4m). The shallow SSTs have density currents which scour particles to the effluent zones of the SST, which makes the area available for sedimentation more important. Deep SSTs do not scour particles into the effluent zones and the area available for sedimentation is less important.
6. When stress testing an SST, a preferred strategy is to increase the inflow rate and the concentration of mixed liquor suspended solids (MLSS) alternatively, while keeping returned activated sludge (RAS) ratio constant.
7. Flux rating of 80% of the 1DFT limiting is not recommended for all SSTs and evaluating the reduction rate of the 1DFT should be tested case-by-case. Also, the McKinney baffle

can greatly improve the limiting flux of an SST.

8. Wind has generally strong negative impacts on both circular and rectangular SSTs, but the circular SST is more sensitive to the impact of wind than the rectangular SST. Therefore, in windy climates covering circular SSTs or protecting them from strong winds may be justified.
9. For the circular SST, wind deteriorates its clarification performance under every wind direction and speed, while wind causes strong negative impact on the sludge thickening performance only under the extreme windy condition. Also, wind along the inlet port direction has stronger negative impact on the SST than the wind at 45^{o} to the inlet direction.
10. Wind deteriorates the SST clarification performance under every wind direction in the rectangular SST, except with mild co-current wind, while it causes strong negative impact on the sludge thickening performance only under the extreme windy condition. Also, counter-current wind has strongest negative impacts on the SST while the wind flowing perpendicular to the SST longitudinal direction has the least negative impacts.

References

Abdel-Gawad, S. and McCorquodale, J. 1985. Numerical simulation of rectangular settling tanks. J. Hydraul. Res. 23(2), 85-100.

Abdel-Gawad, S.M. and McCorquodale, J.A. 1984a. Hydrodynamic of circular primary clarifiers. Can. J. Civil. Eng. 11(2), 299-307.

Abdel-Gawad, S.M. and McCorquodale, J.A. 1984b. Strip integral method applied to settling tanks. J. Hydraul. Eng. 110(1), 1-17.

Adams, E.W. and Rodi, W. 1990. Modeling flow and mixing in sedimentation tanks. J. Hydraul. Eng. 116(7), 895-913.

Al-Sammarraee, M., Chan, A., Salim, S.M and Mahabaleswar, U.S. 2009. Large-eddy simulations of particle sedimentation in a longitudinal sedimentation basin of a water treatment plant. Part I: Particle settling performance, J. Chem. Eng. 152, 315–321.

Armbruster, M., Krebs, P. and Rodi, W. 2001. Numerical modelling of dynamic sludge blanket behaviour in secondary clarifiers. Water Sci. Technol. 43(11), 173-180.

Bretscher, U., Krebs, P. and Hager, W.H. 1992. Improvement of flow in final settling tanks. J. Environ. Eng. 118(3), 307-321.

Bokil, S. D. 1972. Effect of mechanical blending on the aerobic digestion of the waste activated sludge. Ph.D. thesis, Department of Civil and Engineering, University of Windsor, Ontario, Canada.

Burt, D.J. 2010. Improved Design of Settling Tanks Using an Extended Drift Flux Model. Ph.D.

thesis, University of Bristol, UK.

Bürger, R., Diehl, S., and Nopens, I. 2011. A consistent modelling methodology for secondary settling tanks in wastewater treatment. *Wat. Res*. 45, 2247-2260.

Coe, H.; Clevenger, G.H. 1916. Method for Determining the Capacities of Slime Settling Tanks. *Trans. Am. Inst. Min. Metallurgical En*g. 55, 356-384.

Dahl, C. 1993. Numerical Modelling of Flow and Settling in Secondary Settling Tanks. Ph.D. diss. Dep. Civil. Eng. Aalborg Univ., Denmark.

Dahl, C., Larsen, T. and Petersen, O. 1994. Numerical modelling and measurement in a test secondary settling tank. Water Sci. Technol. 30(2), 219-228.

Daigger, G.T. 1995. Development of Refined Clarifier Operating Diagrams Using an Updated Settling Characteristics Database. Water Environ Res. 67(1), 95-100.

Das, S., Bai, H., Wu, C., Kao, J.-H., Barney, B., Kidd, M. and Kuettel, M. 2016. Improving the performance of industrial clarifiers using three-dimensional computational fluid dynamics. Eng. Appl. Comp. Fluid. 10(1), 130-144.

De Clercq, B. 2003. Computational fluid dynamics of settling tanks: development of experiments and rheological, settling, and scraper submodels. BIOMATH. Ghent, University of Ghent.

Deininger, A.; Günthert, F. W.; Wilderer, P. A. 1996. The Influence of Currents on Circular Secondary Clarifier Performance and Design. *Water Sci. Technol.* 34 (3-4), 405-412.

Deininger, A., Holthausen, E., and Wilderer, P.A. 1998. Velocity and solids distribution in circular secondary clarifiers: full scale measurements and numerical modelling. *Wat. Res*. 32, 2951-

2958.

Devantier, B. A.; Larock, B. E. 1986. Modelling A Recirculating Density-driven Turbulent Flow. *Int. J. Numer. Methods Fluids.* 6 (4), 241-253.

DeVantier, B. A.; Larock, B. E. 1987. Modeling Sediment-induced Density Currents in Sedimentation Basins. *J. Hydraul. Eng.* 113 (1), 80-94.

Dick, R.I. 1970. Role of activated sludge final settling tanks. *J. Sanit. Engng Div.* ASCE. 96, No. SA2, 423.

Ekama, G. A.; Bernard, J. L.; Gunthert, F.; Krebs, P.; McCorquodale, J.; Parker, D.; Wahlberg, E. 1997. Secondary settling tanks: theory, modelling, design and operation, pp. 187-203.

Ekama, G. and Marais, P. 2002. Hydrodynamic modelling of secondary settling tanks. WRC Rep. No. 835/1/02 Part 1.

Ekama, G.A., and Marais, P. 2004. Assessing the applicability of the 1D flux theory to full-scale secondary settling tank design with a 2D hydrodynamic model. *Wat Res*. 38, 495-506.

Fluent, A. 2017. ANSYS Fluent 18.0 Theory Guide.

Gao, H. and Stenstrom, M.K. 2017. Computational Fluid Dynamics Applied to Secondary Clarifier Analysis, pp. 301-315.

Gao, H. and Stenstrom, M.K. 2018a. Evaluation of three turbulence models in predicting of the hydrodynamics of a secondary sedimentation tank. Water Research. 143, 445–456.

Gao, H. and Stenstrom, M.K. 2018b. Turbulence and interphase mass diffusion assumptions on the performance of secondary settling tanks. Water Environment Research. 91, 1-10.

Gao, H. and Stenstrom, M.K. 2019a. Generalizing the effects of the baffling structures on the buoyancy-induced turbulence in secondary settling tanks with eleven different geometries using CFD models. Chem. Eng. Res. Des. 143, 215-225.

Gao, H. and Stenstrom, M.K. 2019b. Evaluating the effects of inlet geometry on the flux capacity of secondary settling tanks with computational fluid dynamics model and one-dimensional flux theory model. J. Environ. Eng- Special Collection on CFD. 2019, 145(10), 04019065-1-9. DOI: 10.1061/(ASCE)EE.1943-7870.0001582.

Gao, H. and Stenstrom, M.K. 2019c.The influence of wind in secondary settling tanks for wastewater treatment- A computational fluid dynamics study. Part I: circular secondary settling tanks. Water Environment Research. (Under Review-2nd round)

Gao, H. and Stenstrom, M.K. 2019d.The influence of wind in secondary settling tanks for wastewater treatment- A computational fluid dynamics study. Part II: rectangular secondary settling tanks. Water Environment Research. (Under Review-2nd round)

Gao, H and Stenstrom. M. K. 2019e. Uncertainty analysis of the model parameters and inlet turbulence boundary specification methods of secondary settling tank. (Under Review-2nd round).

Gkesouli, A., Nitsa, M., Stamou, A., Rutschmann, P., Bui, M. D. 2016. Modeling the effect of wind in rectangular settling tanks for water supply. Desalination and Water Treatment. 57(54), 26345–26354.

Gkesouli, A. and Stamou, A. 2018. A CFD modeling procedure to assess the effect of wind in

settling tanks. J. Hydroinformatics. 21 (1), 123-135.

Gong, M., Xanthos, S., Ramalingam, K., Fillos, J., Beckmann, K., Deur, A. and McCorquodale, J.A. 2011. Development of a flocculation sub-model for a 3-D CFD model based on rectangular settling tanks. Water Sci. Technol. 63(2), 213-219.

Goodarzi, D., Lari, K.S., Alighardashi, A. 2018. A large eddy simulation study to assess low-speed wind and baffle orientation effects in a water treatment sedimentation basin. Water Science and Technology. 2017 (2), 412-421.

Griborio, A. 2004. Secondary Clarifier modeling: a multi-process approach. Ph.D. thesis, UNO.

Griborio, A., and McCorquodale, J. A. 2016. Lessons learned from 10 years of clarifier CFD modeling- the 2Dc experience. Proceedings of the 89th Annual Water Environment Federation Technical Exhibition and Conference [CD-ROM]; Chicago, Illinois, Sept. 26–30; Water Environment Federation: Alexandria, Virginia.

Guyonvarch, E., Ramin, E., Kulahci, M., and Plósz, B.G. 2015. iCFD: Interpreted Computational Fluid Dynamics-Degeneration of CFD to one-dimensional advection-dispersion models using statistical experimental design-The secondary clarifier. *Wat. Res*. 83, 396-411.

Imam, E. and McCorquodale, J.A. 1983. Simulation of flow in rectangular clarifiers. J. Environ. Eng. 109(3), 713-730.

Imam, E., McCorquodale, J.A. and Bewtra, J.K. 1983. Numerical modeling of sedimentation tanks. J. Hydraul Eng. 109(12), 1740-1754.

Jayanti, S. and Narayanan, S. 2004. Computational study of particle-eddy interaction in

sedimentation tanks. J. Environ. Eng.130(1), 37-49.

Jensen, D. E.; Spalding, D. B.; Tatchell, D. G. 1979. Computation of structures of flames with recirculating flow and radial pressure gradients. *Combustion and Flame*, 34, 309-326.

Keinath, T.M., Ryckman, M.D., Dana, C.H., and Hofer, D.A. 1977. Activated sludge-unified system-design and operation. *J. Environ. Eng. Div*. ASCE 103 (5), 829-849.

Keinath, T.M. 1985. Operational dynamics and control of secondary clarifiers. *J. Water Pollut. Control Fed*. 57 (7), 770-776.

Khezri, S. M., Biati, A., Erfani, Z. 2012. Determination of the effect of wind velocity and direction changes on turbidity removal in rectangular sedimentation tanks. Water Science and Technology. 66 (12), 2814–2820.

Kinnear, D.J. 2002. Biological solids sedimentation: a model incorporating in fundamental settling parameters. Ph.D. Thesis, Department of Civil and Environmental Engineering, University of Utah, 2002.

Kleine, D. and Reddy, B.D. 2005. Finite element analysis of flows in secondary settling tanks. Int. J. Numer. Method. Biomed. Eng. 64(7), 849-876.

Krebs, P. 1991. The hydraulics of final settling tanks. Water Sci. Technol. 23(4-6), 1037-1046.

Krebs, P., Vischer, D. and Gujer, W. 1992. Improvement of secondary clarifiers efficiency by porous walls. Water Sci. Technol. 26(5-6), 1147-1156.

Krebs, P. 1995. Success and shortcomings of clarifier modelling. Water Sci. Technol. 31(2), 181-191.

Krebs, P., Vischer, D. and Gujer, W. 1995. Inlet-structure design for final clarifiers. J. Environ. Eng. 121(8), 558-564.

Krebs, P., Stamou, A., Garcia-Heras, J. L., Rodi, W. 1996. Influence of inlet and outlet configuration on the flow in secondary clarifiers. Water Sci Technol. 34 (5-6), 1-9.

Kynch, G.J. 1952. A theory of sedimentation. Trans. Faraday Soc. 48, 166-176.

Laine, S., Phan, L., Pellarin, P. and Robert, P. 1999. Operating diagnostics on a flocculator-settling tank using fluent CFD software. Water Sci. Technol. 39(4), 155-162.

Lakehal, D., Krebs, P., Krijgsman, J. and Rodi, W. 1999. Computing shear flow and sludge blanket in secondary clarifiers. J. Hydraul. Eng. 125(3), 253-262.

Larsen, P. 1977. On the hydraulics of rectangular settling basins: experimental and theoretical studies, Department of Water Resources Engineering, Lund Institute of Technology, University of Lund.

Li, B. and Stenstrom, M.K. 2014. Research advances and challenges in one-dimensional modeling of secondary settling tanks--a critical review. Water Res. 65, 40-63.

Lyn, D., Stamou, A. and Rodi, W. 1992. Density currents and shear-induced flocculation in sedimentation tanks. J. Hydraul. Eng. 118(6), 849-867.

McCorquodale, J.A., La Motta, E., Griborio, A., Georgiou, I., Homes, J. 2004. Development of Software for Modeling Activated Sludge Clarifier System. Technology Transfer Report Submitted to US EPA, Schielder Urban Environmental System Center, University of New Orleans, New Orleans, LA, USA.

Ozinsky, A. E., and Ekama, G. A. 1995. Secondary settling tank modelling and design Part 1: review of theoretical and practical developments. *Water SA*, 21(4), 325–32.

Parker, D. S.; Kaufman, W. J.; Jenkins, D. 1971. Physical conditioning of activated sludge floc. *Water Pollution Control Federation*, 43(9), 1817-1833.

Parker, D.S. 1983. Assessment of Secondary Clarification Design Concepts. J. Water Pollut Control Fed. 55(4), 349-359.

Parker, D. and Stenquist, R. 1986. Flocculator-clarifier performance. J. Water Pollut Control Fed. 53(3), 214-219.

Parker, D., Butler, R., Finger, R., Fisher, R., Fox, W., Kido, W., Merrill, S., Newman, G., Pope, R. and Slapper, J. 1996. Design and operations experience with flocculator-clarifiers in large plants. Water Sci. Technol. 33(12), 163-170.

Parker, D. S.; Kinnear, D. J.; Wahlberg, E. J. 2001. Review of folklore in design and operation of secondary clarifiers. *Journal of Environmental Engineering*, 127(6), 476-484.

Parker, D.S., Merlo, R.P., Jimenez, J.A., Wahlberg, E.J., 2008. Analyzing wet weather flow management using state of the art tools. Water Sci Technol. 57 (8), 1247-1251.

Patziger, M., Kainz, H., Hunze, M., Jozsa, J., 2008. Analysing sludge balance in activated sludge systems with a novel mass transport model. Water Sci Technol. 57 (9), 1413-1419.

Patziger, M., Kainz, H., Hunze, M. and Jozsa, J. 2012. Influence of secondary settling tank performance on suspended solids mass balance in activated sludge systems. Water Res. 46(7), 2415-2424.

Patziger, M. and Kiss, K. 2015. Analysis of suspended solids transport processes in primary settling tanks. Water Sci. Technol. 72(1), 1-9.

Patziger, M., Gunthert, F.W., Jardin, N., Kainz, H. and Londong, J. 2016. On the design and operation of primary settling tanks in state of the art wastewater treatment and water resources recovery. Water Sci. Technol. 74(9), 2060-2067.

Patziger, M., 2016. Computational fluid dynamics investigation of shallow circular secondary settling tanks: Inlet geometry and performance indicators. Chem. Eng. Res. Des. 112, 122-131.

Plósz, B.G., Nopes, I., Rieger, L., Griborio, A., Clercq, J.D., Vanrolleghem, P.A., Daigger, G.T., Takács, I., Wicks, J., and Ekama, G.A. 2012. A critical review of clarifier modelling: state of the art and engineering practices. In: Proceedings of WWTmod2012-3rd IWA/WEF Wastewater Treatment Modelling Seminar, pp. 27-30, Mont-Sainte-Anne, Quebec, Canada, 2012.

Pitman, A.R 1985. Settling of Nutrient Removal Activated Sludges. *Water. Sci. Technol*. 17(4-5), 493-504.

Ramalingam, K., Xanthos, S., Gong, M., Fillos, J., Beckmann, K., Deur, A., McCorquodale, J.A. 2012. Critical modeling parameters identified for 3D CFD modeling of rectangular final settling tanks for New York City wastewater treatment plants. Water Sci Technol. 65 (6), 1087-1094.

Ramin, E., Wagner, D.S., Yde, L., Binning, P.J., Rasmussen, M.R., Mikkelsen, P.S. and Plosz, B.G.

2014. A new settling velocity model to describe secondary sedimentation. Water Res. 66, 447-458.

Ratkovich, N., Horn, W., Helmus, F.P., Rosenberger, S., Naessens, W., Nopens, I., and Bentzen, T.R. 2013. Activated sludge rheology: a critical review on data collection and modelling. *Wat Res*. 47, 463-482.

Rodi, W. 1980. Turbulent models and their application in hydraulics—a state of the art review. International Association for Hydraulics Research, Delft.

Rodi, W. 1993. Turbulence models and their application in hydraulics, CRC Press.

Samstag, R. W.; Dittmar, D. F.; Vitasovic, Z.; McCorquodale, J. A. Underflow geometry in secondary sedimentation. 1992a. Water environment research. 64, 3, 204-212.

Saffarian, M. R.; Hamedi, M. H.; Shams, M. 2010. Comparison of Various Settling Velocity Functions and Non-Newtonian Fluid Models in Circular Secondary Clarifiers. *Korean J. Chem. Eng.,* 27(5), 1497-1508.

Saffarian, M.R., Hamedi, M.H., and Shams, M. 2011. Numerical simulation of a secondary clarifier in a sewage treatment plant using modified Bingham model. *Can. J. Civ. Eng*. 38, 11-22.

Shahrokhi, M., Rostami, F., Md. Said, M.A., Yazdi, S.R.S. and Syafalni. 2013. Experimental Investigation of the Influence of Baffle Position on the Flow Field, Sediment Concentration, and Efficiency of Rectangular Primary Sedimentation Tanks. *J. Hydraul. Eng.,* **139** (1), 88-94.

Stamou, A., Adams, E. and Rodi, W. 1989. Numerical modeling of flow and settling in primary

rectangular clarifiers. J. Hydraul. Res. 27(5), 665-682.

Stamou, A.I., Theodoridis, G. and Xanthopoulos, K. 2009. Design of secondary settling tanks using a CFD model. J. Environ. Eng. 135(7), 551-561.

Stamou, A. and Gkesouli, A. 2015. Modeling settling tanks for water treatment using computational fluid dynamics. J. Hydroinformatics. 17 (5), 745-762.

Takács, I., Patry, G.G. and Nolasco, D. 1991. A dynamic model of the clarification-thickening process. Water Res. 25(10), 1263-1271.

Tamayol, A., Firoozabadi, B. and Ahmadi, G. 2008. Effects of inlet position and baffle configuration on hydraulic performance of primary settling tanks. J. Hydraul. Eng. 134(7), 1004-1009.

Tamayol, A., Firoozabadi, B. and Ashjari, M. 2009. Hydrodynamics of secondary settling tanks and increasing their performance using baffles. J. Environ. Eng. 136(1), 32-39.

Tarpagkou, R. and Pantokratoras, A. 2013. CFD methodology for sedimentation tanks: The effect of secondary phase on fluid phase using DPM coupled calculations. Appl. Math. Model. 37(5), 3478-3494.

Vitasovic, Z.C., Zhou, S., McCorquodale, J.A. and Lingren, K. 1997. Secondary clarifier analysis using data from the Clarifier Research Technical Committee protocol. Water Environ. Res. 69(5), 999-1007.

Wahlberg, E.J. and Keinath, T.M. 1988. Development of Settling Flux Curves Using SVI. J. Water Pollut Control Fed. 60(12), 2095-2100.

Wahlberg, E. J.; Gerges, H. Z.; Gharagozian, A.; Stenstrom, M. K.; Vitasovic, Z.; Zhou, S. P.; McCorquodale J. A., and Lingren, K. 1998. Of: Secondary Clarifier Analysis Using Data from the Clarifier Research Technical Committee Protocol. *Water Environment Research*. 70(2), 249-253.

Wang, X., Yang, L., Sun, Y., Song, L., Zhang, M and Cao, Y. 2008. Three-dimensional simulation on the water flow field and suspended solids concentration in the rectangular sedimentation tank, J. Environ. Eng. 134(11), 902–911.

Wang, X. L.; Zhou, S. S.; Li, T.; Zhang, Z. Q.; Sun, Y. X.; Cao, Y. B. 2011. Three-dimensional simulation of the water flow field and the suspended-solids concentration in a circular sedimentation tank. *Canadian Journal of Civil Engineering*, 38(7), 825-836.

Water Environmental Federation. Clarifier Design, 2nd ed.; McGraw-Hill: New York, NY, USA, (2006); pp. 507-540.

Weiss, M., Plósz, B.G., Essemiani, K. and Meinhold, J. 2007. Suction-lift sludge removal and non-Newtonian flow behaviour in circular secondary clarifiers: Numerical modelling and measurements. J. Chem. Eng. 132(1-3), 241-255.

Wells, S.A. and LaLiberte, D.M. 1998. Modeling Density Currents in Circular Clarifiers. J. Fluid/Particle Sep. 11(1), 48-54.

Wicklein, E. and Samstag, R.W. 2009. Comparing commercial and transport CFD models for secondary sedimentation. In: Proceedings of WEFTEC 09-82th Annual WEF Technical Exhibition and Conference, pp. 6066-6081. Orlando, FL, USA.

Xanthos, S., Gong, M., Ramalingam, K., Fillos, J., Deur, A., Beckmann, K. and McCorquodale, J.A. 2010. Performance Assessment of Secondary Settling Tanks Using CFD Modeling. *Water Resour. Manage.,* 25 (4), 1169-1182.

Xanthos, S., Ramalingam, K., Lipke, S., McKenna, B. and Fillos, J. 2013. Implementation of CFD modeling in the performance assessment and optimization of secondary clarifiers: the PVSC case study. Water Sci. Technol. 68(9), 1901-1913.

Xu, G., Yin, F.J., Xu, Y.J., and Yu, H.Q. 2017. A force-based mechanistic model for describing activated sludge settling process. *Wat Res*. 127, 118-126.

Zhou, S. and McCorquodale, J.A. 1992a. Influence of skirt radius on performance of circular clarifier with density stratification. Int. J. Numer. Methods Fluid. 14(8), 919-934.

Zhou, S. and McCorquodale, J.A. 1992b. Mathematical modelling of a circular clarifier. Can. J. Civil. Eng. 19(3), 365-374.

Zhou, S. and McCorquodale, J.A. 1992c. Modeling of rectangular settling tanks. J. Hydraul. Eng. 118(10), 1391-1405.

Zhou, S., McCorquodale, J.A. and Vitasovic, Z. 1992. Influences of density on circular clarifiers with baffles. J. Environ. Eng. 118(6), 829-847.

Zhou, S.; McCorquodale, J. A. 1994. Modeling of Rectangular Settling Tanks-closure. *J. Hydraul. Eng.,* 120(2), 279-281.